APPLYING QUALITY CONTROL MEASURES TO VALIDATE AIRBORNE LIDAR BATHYMETRY IN DIVERSE ENVIRONMENTS

KUTALMIS SAYLAM

Thesis submitted to the University of Ottawa
in partial fulfillment of the requirements for the
Doctorate in Philosophy degree in Geography.

Department of Geography, Environment, and Geomatics
Faculty of Arts
University of Ottawa

Abstract

Airborne lidar (light detection and ranging) technology represents an evolution of traditional photogrammetry due to its capability to produce dense and accurate three-dimensional representation of Earth's surfaces. Installed on a variety of mobile platforms, airborne lidar systems (ALS) can generate vast amounts of positional information with high planimetric accuracy and detail, using artificially produced laser pulses, commonly in the near-infrared spectrum (1064 nm). The technology is effective in mapping topographic details, and researchers have applied the information to various applications, such as urban mapping, forestry, environmental assessment, and hazard management. Technological advancements in sensors, auxiliary hardware, and computing software have enabled the manufacturing of more efficient and versatile systems, and the addition of a visible (green) wavelength (515-532 nm) has revolutionized the shallow water mapping industry. Dual wavelength "bathymetric" airborne lidar systems (ALB) can support a wide range of applications in hydrographic surveying, coastal zone monitoring, and riverbed and lake mapping, and has lately also been used in cryospheric studies. With access to a variety of remotely sensed information, researchers can utilize datasets sourced from different sensors and platforms to conduct interdisciplinary studies, contributing to the discovery of new patterns and processes in geomorphology. To use airborne lidar data effectively, researchers need to validate data quality in terms of accuracy, completeness, and consistency. Particularly with airborne lidar bathymetry, measurements require verification by conducting rigorous in-situ campaigns and a comparison to datasets sourced from other applicable methods.

In the research described in this thesis, I utilized two airborne lidar systems with bathymetric capabilities (Leica Chiroptera I and 4X) and conducted a variety of supplemental surveys to investigate the quality control aspects related to measuring topographic and bathymetric surfaces and water depths.

In the Frio River in southwestern Texas, springs provide recharge along the outcrop portion of the Edwards Aquifer, and the river empties into the Nueces River. Because of the recent drought causing environmental concerns related to pathogens and bacteria build-up in non-flowing pool conditions, and the related concerns about recreational business loss, the Texas Water Development Board inquired about and funded an extensive airborne lidar survey. Consequently, in 2017, UT Austin researchers acquired airborne lidar data, supplemented with sonar soundings and GNSS (Global Navigation Satellite System) surveys in the river watershed. The in-situ campaign included sampling of turbidity and water transparency at multiple basins, and the mean turbidity was less than 1 nephelometric unit. Therefore, the

transparency was high, and the river bottom was visible to the observer, creating an ideal environment for mapping with bathymetric lidar. As an unconventional validation method, I conducted waveform analysis to confirm water surface heights and depths, at locations where the river riparian zone was covered with vegetation and blocking the GNSS signals. I further validated the findings with sonar and GNSS measurements, where applicable. The results differed depending on the basin characteristics; however, the mean lidar bathymetry and sonar depths agreed within 16% or better depending on the basin characteristics (0.14 m to 0.24 m). Comparison to sonar soundings produced a mean absolute depth difference of 0.13 m, and the agreement between the measurements was high (R^2=0.72). I concluded the research by verifying the importance of conducting in-situ measurements even in almost ideal environmental conditions and demonstrated the feasibility of conducting waveform analysis at locations where in-situ observations are not feasible.

In the Devils River study, the motivation was to address the potential data gap in stream bathymetry, which was critical to parameterize the physical stream-flow models for mapping the aquatic habitat locations of the Devils River minnow, an endangered species. It was challenging to measure the complete riverbed with an airborne lidar system and confirm depths where submerged vegetation (variable-leaf watermilfoil and emergent American water willow) blocked laser pulses. Therefore, I applied a novel approach and utilized a ground penetrating radar (GPR) from an inflatable boat with a shielded monostatic 200-MHz antenna that was mounted immediately above the water surface. Preliminary GPR measurements revealed a bias of 0.22 m (the mean depth was 1.77 m) to lidar bathymetry using the standard fresh-water permittivity rate (20° Celsius, radio waves propagation speed of 3.3 cm/ns, attenuation constant of 0.1 dB/m). To enhance the results, I adjusted the water-column permittivity (ε, 80 versus 78.4) based on the observed water temperature (24.5° Celsius), resulting in radio waves propagating quicker (3.7 cm/ns), and attenuating more slowly (0.08 dB/m), enhancing the height recordings especially in deeper parts of the river. As a result, the mean depths measured were equal (1.99 m) and agreement between the airborne lidar and GPR measurements was strong (R^2=0.92). To validate the findings, I compared lidar bathymetry to sonar recordings, where applicable. In the upper basin, the comparison algorithm matched lidar bathymetry to sonar recordings at 53% in the user-defined thresholds (1 m radius, 0.5 m vertical spacing) and the mean absolute height difference was 0.11 m where depths were shallower than 2.75 m. In the lower basin, I observed a reduced concentration of submerged vegetation; however, depths were greater and influenced the agreement between the measurements adversely (R^2 = 0.72, versus 0.78 for the upper basin). Overall, the absolute depth difference was less than 0.1 m among comparison of all datasets. Nevertheless, I was able to build a bottom map, and successfully demonstrated the possibility of seamlessly combining datasets sourced from different sensors and confirmed the feasibility of using GPR for mapping riverbeds with submerged vegetation.

Lower Laguna Madre is a shallow, hyper-saline lagoon in southern Texas. It is large (800 km^2) and has a unique seagrass ecosystem that serves as an essential nursery for species found in the Gulf of Mexico. The depth of the lagoon varies due to tides, and transparency is influenced by northerly winds that carry sediment from the surrounding sand dunes. In 2017, an airborne lidar survey was conducted and researchers completed an extensive in-situ campaign to build an updated geomorphic map of the lagoon and the surrounding areas. The in-situ data collection areas were clustered in the southern section of the lagoon; each area was unique in terms of turbidity, depth, and other environmental conditions such as floating and submerged vegetation, and varying bottom properties. My research motivation was to investigate the feasibility of measuring the lagoon bathymetry with airborne lidar at these diverse locations and investigate the accuracy of lidar measurements using satellite imagery and other survey methods. For this purpose, I conducted sonar surveys from a boat, also sampling turbidity and transparency. I adjusted the sonar sound wave propagation speed (1533.9, 1530.7, and 1537.5 m/s) by measuring the mean water temperature and salinity at each in-situ area and computed the sonar recordings accordingly. For the satellite-derived bathymetry, I observed tides that influenced the depths, and adjusted the surface heights to match the satellite sensing times prior to comparing them to the lidar bathymetry. To align all measurements with each other, I converted lidar measurements using the applicable geoid model and adjusted all measurements to NAVD 88 orthometric height. Further, I analyzed the pixel reflectance of the satellite imagery, classified the spectral variability, and excluded excessively turbid locations from further analysis. The lidar bathymetry indicated that 51% of the lagoon had depths greater than 0.4 m, with only 1.1% of the measurements exceeding 2 m. The deepest point recorded was at 3.35 m. Sonar recordings agreed in good confidence (R^2=0.68) with lidar bathymetry and exceeded the Special-Order uncertainty standards (Order 1b) set by the International Hydrographic Organization (IHO), whereas feature detection is not specified, and the total vertical uncertainty (TVU) is less than 0.5 m at depths shallower than 10 m. In the less turbid locations (Area 1), the mean absolute depth difference between lidar bathymetry and sonar recordings was 5 cm, and RMSE was 14 cm. In Area 2, higher levels of turbidity decreased the comparison algorithm matching (40%) and the coefficient of determination (R^2=0.38), resulting in an increased depth difference of 14 cm. Further comparison of lidar bathymetry to satellite imagery-derived depths revealed sufficient correlation (44-66 %) between the measurements due to the coarse pixel density of satellite imagery and the limitations of optical imaging technology in shallow and turbid waters. The mean absolute depth difference between lidar bathymetry and satellite-derived bathymetry was less than 13 cm, and RMSE was 15 cm. As a result, I demonstrated that higher levels of turbidity reduced the correlation rate between sonar and lidar measurements, impacting the depth accuracy adversely. However, the bias (the mean absolute depth difference) between lidar bathymetry, sonar and satellite-derived bathymetry was better than the IHO Order 1b standard. Furthermore, the study results demonstrated that optical imaging technology had depth resolving issues at varying turbid locations with depths exceeding 1 m, where lidar bathymetry was successful measuring deeper bottoms with more detail. Therefore, the study revealed the weaknesses and strengths of both technologies and demonstrated the practical and theoretical limitations of airborne lidar bathymetry and depths derived from satellite imaging in shallow waters with varying environmental conditions, filling a gap in the scientific literature, where both technologies have proven effective under ideal conditions.

In the summer of 2022, UT Austin and National Aeronautics and Space Administration (NASA) researchers participated in the ICESat-2 validation/calibration (Cal/Val 2022) campaign, based in Thule Air Force Base (Thule AB), northwest Greenland. The campaign provided sea ice measurements acquired using airborne lidar systems, a Leica Chiroptera 4X and NASA's Land, Vegetation, and Ice Sensor (LVIS). Both sensors acquired data simultaneously at low altitudes (< 2200 ft.), enabling cross-checking of heights. Despite the Chiroptera's low altitude, slow cruising speed constraints, and other logistical and environmental challenges, measurements almost coincident with those of the ICESat-2 observatory were successfully collected. The principal objective of this research was to align Chiroptera measurements to those of ICESat-2 measurements and compare sea ice heights and bathymetric depths. Because sea ice is dynamic and achieving a 1:1 correspondence of satellite and airborne altimeter measurements (time and location) is not possible, an algorithm was developed to adjust the location of each measured point in the Chiroptera lidar dataset by aligning features with ICESat-2 datasets, using linear regression. The algorithm iteratively adjusted Chiroptera measurements for ice drift speed and bearing combinations within user-defined range and increments, to a theoretical location where ICESat-2 and Chiroptera were coincident. For quality-control purposes, I verified the calibration of the Chiroptera system with GNSS checkpoint heights that were established on the Thule AB runway, and further validated the measurements with ATL03 photon heights. The mean absolute height difference was less than a centimeter on both confirmations. Additionally, I compared LVIS and Chiroptera sea ice measurements in ellipsoidal heights and the results matched with less than 4 cm (mean absolute difference) on a 31 km long data swath, indicating a strong level of agreement (R^2=0.98, RMSE=0.047 m). I segmented the long Chiroptera data swath lines (~ 3 km) and applied geophysical height corrections, identical to NASA's tide free computations, for direct comparison to ATL07 segment heights. The tide free system includes the orthometric heights and excludes permanent tide deformations. I used the least-squares method for absolute height comparison where approximately 300 Chiroptera returns were registered within a 12-m diameter footprint of a single ATL07 beam. Before applying the drift adjustments, the height comparison generated a high bias (RMSE= 0.25 m), and the agreement between the measurements was poor (R^2= 0.24). Results improved with drift adjustment, particularly for the stronger ICESat-2 *r-series* sensor product (mean absolute height difference = 0.015 m, R^2 = 0.73). For bathymetric measurements of melt ponds and occasional leads (fractures in the sea ice), I merged bathymetric lidar data classes (Classes 7, 8 and 10), computed the sea surface and mean ice surface heights, and compared depths in the height domain to the ATL03 photons that registered within a 2 m radius of each lidar return. Overall, depths compared were shallow (< 3 m) and ICESat-2 registered slightly deeper returns (mean absolute depth difference = 1 cm). The RMSE was 16 cm and depths agreed with R^2 = 0.84. As a result, the study quantified the measurement bias between ICESat-2 and Chiroptera airborne lidar measurements and introduced a novel algorithm for adjusting sea ice for in terms of speed and bearing drift, enabling direct comparisons.

This PhD research provides a scientific approach to understanding practical and theoretical limitations of bathymetric airborne lidar surveys and demonstrates the significance of quantifying height and depth differences (biases) using supplementary survey methods, particularly at locations with varying environmental conditions. For this purpose, each case study demonstrates an application of a range of survey methods with the purpose of generating validated datasets to build topographic and bathymetric maps in confidence.

Preface

Thesis format and background

This thesis is drafted in article format and consists of four manuscripts; the contents are included in Chapters 2,3,4 and 5, where each chapter introduces a case study. Chapter 1 presents the overall research methodology, including an outline of the literature review, and defines the research motivation. Chapter 2 (*Quantifying Airborne Lidar Bathymetry Quality-Control Measures: A Case Study in Frio River, Texas*) introduces the applicable in-situ methods, and waveform analysis to validate surface and depth measurements, where an airborne lidar bathymetry system was used to measure the bottom of a heavily vegetated river shed, in southwestern Texas. This article was published in October 2018, in the journal *Sensors,* and as of 06/15/2024 it has been cited 24 times and viewed > 5000 times. Chapter 3 (*Multi-Sensor Approach to Improve Bathymetric Lidar Mapping of Semi-Arid Groundwater-Dependent Streams: Devils River, Texas*) addresses the applicable methods to fill gaps in stream ALB bathymetry, which was critical to parameterize the physical stream-flow models for mapping the aquatic habitat locations of Devils River minnow, an endangered species. The study incorporates the use of an ALB system, sonar, GNSS, and a ground penetrating radar where submerged and floating aquatic vegetation challenged mapping the bottom of the Devils River. The study demonstrates the possibility of seamlessly combining datasets by calibrating the speed of propagation of the radio wavelength traversing the water column. The article was published in June 2020, in the journal *Remote Sensing*, and as of 06/15/2024 it has been cited 6 times and viewed > 5000 times. Chapter 4 (*Analysis of Depths Derived by Airborne Lidar and Satellite Imaging to Support Bathymetric Mapping Efforts with Varying Environmental Conditions: Lower Laguna Madre, Gulf of Mexico*) combines airborne lidar bathymetry and satellite-derived bathymetry (ALB and SDB) technologies to measure the bottom of a shallow and hyper-saline lagoon with diverse and varying environmental conditions. The study utilizes sonar recordings that were modified to match each in-situ location environmental conditions (temperature and salinity) to validate ALB and SDB depths (in the height domain). The article was published in December 2023, in the journal *Remote Sensing*, belonged to the Special Issue: Multi-Source Data Observations of Shallow Water Area - Methods, Ecosystem, Geomorphology and Environment. As of 06/15/2024 it has been cited 1 time and viewed > 1000 times. Chapter 5 (*Airborne lidar to verify ICESat-2 Arctic summer sea ice heights and depths: Calibration and validation campaign, Greenland 2022*) presents results from the calibration and validation campaign of 2022 (Cal/Val 2022), which was a collaborative effort between NASA and UT Austin. An ALB was used to map 11,000 km^2 of Arctic sea ice, supplemented with 4-band imagery. Unconventional in-situ methods were applied to validate the ALB system calibration, and a novel algorithm was introduced to shift and align the lidar data swath to match those of ICESat-2 ATLAS measurements. The study concludes by comparing and validating ALB measurements to ATL07 segments and ATL03 photon heights. This article is submitted to journal *Earth and Space Science on 07/2024*, American Geophysical Union (AGU), and currently in the peer-review process.

Below is the outline of the chapters and the respective publication information.

- Chapter 2:

Saylam, K.; Hupp, J.R.; Andrews, J.R.; Averett, A.R.; Knudby, A.J. Quantifying Airborne Lidar Bathymetry Quality-Control Measures: A Case Study in Frio River, Texas. *Sensors* 2018, *18*, 4153. https://doi.org/10.3390/s18124153

- Chapter 3:

Saylam, K.; R. Averett, A.; Costard, L.; D. Wolaver, B.; Robertson, S. Multi-Sensor Approach to Improve Bathymetric Lidar Mapping of Semi-Arid Groundwater-Dependent Streams: Devils River, Texas. *Remote Sens.* 2020, *12*, 2491. https://doi.org/10.3390/rs12152491

- Chapter 4:

Saylam, K.; Briseno, A.; Averett, A.R.; Andrews, J.R. Analysis of Depths Derived by Airborne Lidar, and Satellite Imaging to Support Bathymetric Mapping Efforts with Varying Environmental Conditions: Lower Laguna Madre, Gulf of Mexico. *Remote Sens.* 2023, *15*, 5754. https://doi.org/10.3390/rs15245754

- Chapter 5:

Saylam, K.; R. Averett, A.; Andrews, J.R.; R. Short, S.; T. Kurtz, N. and L. Tilling, R. Airborne lidar to verify ICESat-2 Arctic summer sea ice heights and depths: Calibration and validation campaign, Greenland 2022 (*in review*, American Geophysical Union (AGU), *Earth and Space Sciences*, 07/2024).

Author contributions

I am (Kutalmis Saylam) the principal author of each chapter in this thesis. I am responsible for preparing the research proposals, seeking acquiring and managing the research funding, designing the research methodology, participating in the field work and data acquisition activities in airborne, marine, and terrestrial environments. I conducted the data analysis, drafted the articles, with valuable guidance and feedback from my advisor, Anders Knudby. Specific contributions of co-authors to the individual chapters (articles) are as follows:

Chapter 2: I conceived and supervised the study, performed the fieldwork, analyzed all data, and authored the article. John Hupp conducted the lidar survey, processed lidar data, and contributed to the overall article. John Andrews performed fieldwork, manipulated lidar data, and contributed to sections of the article. Aaron Averett operated the ALB system, assisted with fieldwork, and contributed to sections of the article. Anders Knudby contributed to the overall article and provided insight.

Chapter 3: I supervised the study as co-principal investigator, performed fieldwork, analyzed data, and drafted the article. Aaron Averett operated the ALB system, assisted with fieldwork, and contributed to sections of the article. Lucie Costard performed fieldwork, operated the GPR, and processed GPR datasets. Brad Wolaver conceived the project as principal investigator, received research funding, contributed to sections of the article, and provided insight. Sarah Robertson initiated the project at Texas Parks and Wildlife and provided research funding.

Chapter 4: I served as the study's principal investigator, conducted data processing and analysis, and drafted the article. Alejandra Briseno analyzed satellite imagery and contributed to the relevant sections of the article. John Andrews modified lidar data, generated raster maps, and contributed to the article. Aaron Averett operated the ALB system and contributed to the data analysis.

Chapter 5: I served as the principal investigator for the study with UT Austin. I conducted the in-situ campaign, processed datasets, operated the ALB system, and drafted the article. Aaron Averett operated the ALB system, assisted with fieldwork, and helped with the mission plan. John Andrews assisted with GNSS data collection and contributed to data analysis. Shelby Short assisted with SAR data analysis and drafted a section of the article. Nathan Kurtz was the principal investigator with NASA and oversaw the project. Rachel Tilling assisted with mission planning and data analysis.

Table of Contents

List of Tables

List of Figures

Abbreviations

AHAB	Airborne Hydrography AB
ALB	Airborne Laser Bathymetry
ALS	Airborne Lidar System
AOP	Apparent Optical Properties
ASPRS	American Society of Photogrammetry and Remote Sensing
ATLAS	Advanced Topographic Laser Altimeter System
ATM	Airborne Topographic Mapper
BEG	Bureau of Economic Geology
CHIR	Chiroptera Lidar System
CORS	Continuously Operating Reference System
DEM	Digital Elevation Model
DOM	Dissolved Organic Matter
EM	Electromagnetic
EPA	Environmental Protection Agency
GHz	Gigahertz
GI	Geo-Informatics
GNSS	Global Navigation Satellite Systems
GPS	Global Positioning System
IHO	International Hydrographic Organization
IMU	Inertial Movement Unit
INS	Inertial Navigation System
ISODATA	Iterative Self Organizing Data Analysis
kHz	Kilohertz
LLSS	Leica Lidar Survey Suite
LVIS	Land Vegetation Ice Sensor
MABEL	Multiple Altimeter Beam Experimental Lidar
MDPI	Multidisciplinary Digital Publishing Institute
MHz	Megahertz
MIR	Mid-Infrared Range
MPIA	Multiple Pulses in the Air
MSL	Mean Sea Level
MW	Megawatts
NASA	National Aeronautics and Space Administration
NDWI	Normalized Difference Water Index
NIR	Near-infrared
NOAA	National Oceanic and Atmospheric Administration
NTU	Nephelometric Unit
QA	Quality Assurance
QC	Quality Control
PDOP	Position Dilution of Precision
RGT	Regional Ground Track
RMSE	Root Mean Squared Error
SDB	Satellite Derived Bathymetry

SPEAR	Spectral Processing Exploitation and Analysis Resource
SWIR	Short Wave Infrared Range
SWQM	Surface Water Quality Monitoring
TCEQ	Texas Commission on Environmental Quality
TIN	Triangulated Irregular Network
TVU	Total Vertical Uncertainty
TxDOT	Texas Department of Transportation
UAS	Unmanned Aerial Systems
UAV	Unmanned Aerial Vehicle
USV	Autonomous Surface Vehicle
USGS	United States Geological Survey
UT Austin	The University of Texas at Austin
UTM	Universal Transverse Mercator
VIS	Visible Infrared Spectrum

Acknowledgements

I would first like to thank my supervisor, Dr. Anders Knudby, who made pursuing a doctoral study a possibility for me. His wealth of remote sensing knowledge, compassion for learning, and dedication to his students, and his passion to advancing the science, coupled with an endless positive energy, made this chapter of my life a true learning and growing experience. I am also thankful and indebted to my committee members, Dr. Luke Copland, Dr. Michael Sawada, Dr. Christopher Hopkinson and Dr. Christopher Parrish for their insightful feedback and contributions to this thesis.

This thesis would not be possible without the support of my employer, the Bureau of Economic Geology, the University of Texas at Austin. A special thanks to Dr. Jeff Paine, who supported my studies without any hesitation and provided encouragement and feedback whenever possible. I also would like to extend my gratitude to Dr. Ken Wisian and Dr. Michael Young and to all members of the Near Surface Observatory group. I learned a lot from all of you.

To all members, past and present of the Shallow Water Earth Observation Laboratory at the University of Ottawa, thank you for sharing your friendship, knowledge and expertise and I look forward to continuing to contribute to online group meetings.

Unwavering appreciation goes to my family and my friends. Thank you for encouraging me to stay focused and curious and keep moving forward, even when times are difficult and discouraging. My mother Bingül Saylam, my father Ahmet Saylam, my sister Görkem, my brother-in law Hakan, and my nephew Yiğit. Your support and your positive thoughts made this happen. It was a long journey, and a great chapter in life, and we walked it together.

To my dear friends in Canada, in Türkiye, in the U.S., and elsewhere in the world. You all know yourselves. We are all connected, we are a family, and we all support each other. Your friendship at all levels is never forgotten. Thank you to you all. Merci beaucoup à vous tous. Hepinize çok teşekkür ederim.

Chapter One: Introduction

1.1. Geomatics and Remote Sensing

Geomatics is a derivative geodesic science field (matics: from “informatics”) adopted in the early 1980s in Canada (Paradis, 1981). Geomatics incorporates the increasing use and popularity of advanced electronics, optics and computing technologies to revolutionize land survey activities and the representation of large amounts of georeferenced data (Gagnon and Coleman, 1990). In 2004, the International Standards Organization, Technical Committee 211 (Committee, 2004) defined Geomatics as “the science discipline concerned with the collection, distribution, storage, analysis, processing, and presentation of geographic data or geographic information.” According to Gomarasca (2009), geomatics is a “neologism”, and the use of terminology has become increasingly widespread; however, not universally accepted or understood correctly. The disciplines and techniques that constitute geomatics are vast, and the information (data) acquired is defined within its own framework and the defined accuracy.

Remote sensing enables information retrieval of objects and measuring targeted surfaces from a distance using propagated electromagnetic (EM) energy and is a subfield of geomatics. Passive (e.g., multispectral and hyperspectral sensors) and active remote sensing techniques (e.g., synthetic aperture radar and light detection and ranging) measure EM reflected or emitted by target surfaces, allowing detection and characterizing features through their variable spectral response (Khorram and others, 2012; Thenkabail, 2018).. Currently, most remote imaging systems use a charge-coupled device and a metal-oxide semiconductor that convert the light energy into electrons and record the radiometric intensity values (McGlone and others, 2004).. On the contrary, information acquired using active sensors do not rely on ambient light reflected off the target, but instead measure the reflected part of radiation emitted by the sensors themselves. While this allows active sensors to operate under a greater variety of conditions (e.g. at night), the quality of the data can still be influenced by environmental conditions and disturbance from the atmosphere (Clark and Rilee, 2010; Janssen, 2004).

This PhD thesis research focuses on the use of lasers (light amplification by stimulated emission of radiation) for lidar (light detection and ranging). Operated from a variety of platforms, particularly airborne, lidar systems (ALS) can generate vast amounts of three-dimensional data with high planimetric accuracy, using artificially produced and emitted laser pulses (Dong and Chen, 2017; Petrie and Toth, 2018). The common ALS systems use gas lasers, solid-state lasers, and semi-conductor lasers. For most ranging, profiling, and scanning operations, *neodymium*-doped yttrium aluminum garnet; ($Nd{:}Y_3Al_5O_{12}$,) or “Nd:YAG” lasers are preferred due to their high output capability. These lasers are typically optically pumped, use a flash-diode and they can operate either in a pulsed (discrete) or in continuous modes. The high intensity pulses can be "frequency-doubled" to generate a green or "visible" wavelength output, which is a process of two photons interacting, and combined to generate a new photon with twice the energy (Killinger, 2014; Risk and others, 1989).

In addition to airborne lidar, this research is concerned with the measurements of an orbiting observatory, ICESat-2. Launched on September 15, 2018, the observatory orbits the Earth at 6.9 kilometers per second at an altitude of 496 km, completing an orbital cycle in approximately 94 minutes. The Advanced Topographic Laser Altimeter System (ATLAS) onboard ICESat-2 carries a photon-counting lidar system with multiple transmitters, operating with 532 nm wavelength. The ground tracks are spaced approximately 3.3 km apart, and the observatory completes a full cyclic orbit in 91-days (1387 orbits). Although the U.S. National Aeronautics and Space Administration (NASA) designed the ATLAS sensors principally for the use of cryospheric studies, pilot studies revealed seafloor depth measurement of up to 40 m in relatively transparent waters and its potential for bathymetric measurements (Parrish and others, 2019; Kacimi and Kwok, 2020; L. A. Magruder and others, 2024; Petty and others, 2020) and updated the operational objectives to accommodate a variety of science fields (Markus and others, 2017; Palm and others, 2018).

1.2. Airborne lidar systems

An ALS integrates a laser power unit, a scanner mirror, transmitting and receiving units, a navigational and positional unit (GNSS/INS), a digitizer, on-board storage, and an operator interface. Each pulse footprint is tagged with seven parameters of locational information: time, latitude, longitude, elevation, roll, pitch, and yaw. The INS system records data with 200 Hz, and the GNSS unit was configured to update recordings at 2 Hz. The data swaths on the target surfaces are generated by rotation of the scanning mirror; they can be in sawtooth (Z-shaped, oscillating), parallel (rotating) or in elliptical (nutating, Palmer) shapes. Onboard electronics measure the time-of-flight (TOF) duration of a lidar beam travelling from the transmitter to the target surface and back to the receiver (pulse echo). In a pulsed method (Equation 1-1), R_d is the slant distance, c is the speed of light (~3×10^8 m/sec) and t_s equals to the TOF duration.

$$R_d = (c \times t_s)/2 \qquad \text{(Equation 1-1)}$$

A relatively new technology, an ALS with green-wavelength capability (515-532 nm) have enabled surveying the depths of relatively shallow and transparent waters, referred to as *airborne lidar bathymetry* (ALB, Figure 1-1, Guenther, 2007; Kinzel and others, 2007). The term “bathymetry” refers to the measurement and mapping of the depths and shapes of underwater terrain. The science field focuses on measuring the physical features of a water body; in the same context that a topographic map represents the three-dimensional features of hard surfaces and terrain, a bathymetric map describes the topography of the bottom surfaces of rivers, lakes, and oceans.

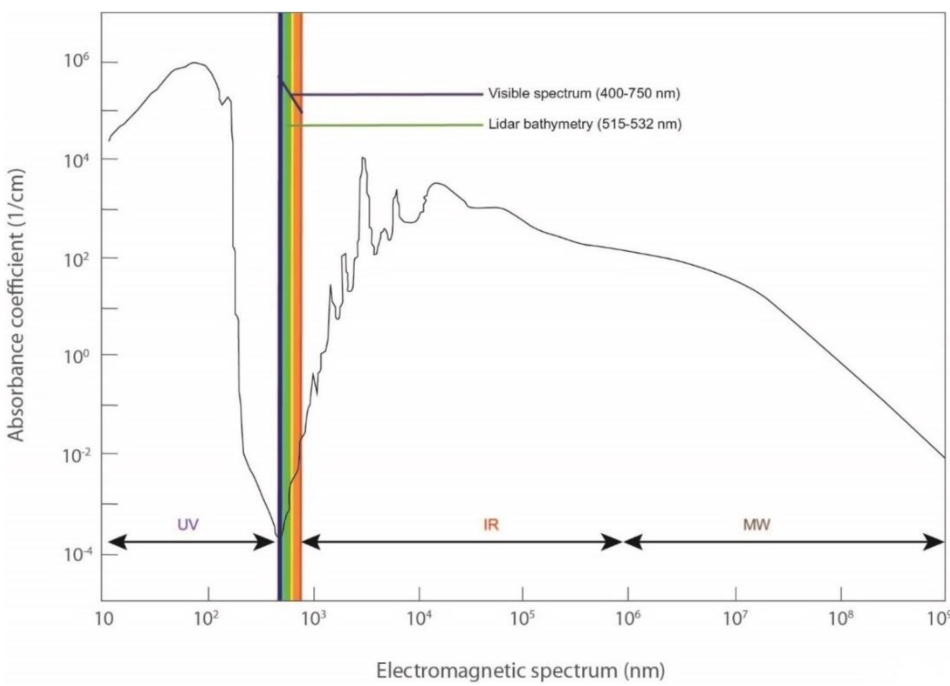

Figure 1-1. Representation of electromagnetic spectrum and indicating the functional lidar bathymetry optical range: 515-532 nm. (modified after Beć and Huck, 2019). The absorbance coefficient determines the maximum depth that a particular wavelength can penetrate a medium before it is attenuated.

Earlier ALB systems were cumbersome to operate, requiring large aircraft and specially trained operators. Over the years, systems have become more compact and intuitive to operate, and operating costs have decreased considerably. They have proven to be a versatile, cost-effective, and detailed method of shallow water mapping compared with other remote-sensing technologies such as sonar or satellite imaging (Casal and others, 2020; Mandlburger, 2021).

Emitted from an ALB, light beams travel through the air/water interface and propagate in the water-column until they reach and illuminate the bottom. While traversing the water, the beams slow and their amplitude decreases due to refraction and scattering. If a beam does not attenuate entirely, it reflects from the bottom and the backscatter is recorded by the receiver. The digitizer records the entire travel in a "waveform" fashion, indicating the water surface, bottom, and all other interactions with distinctive amplitude changes (Figure 1-2). Waveforms, with their potential to provide information about the depth and bottom characteristics of a water body, are a valuable source of information. They can be extracted and processed independently to validate surface properties and depths output from ALB manufacturer applications. Data are classified according to their pulse return order and their sampling amplitude as recorded.

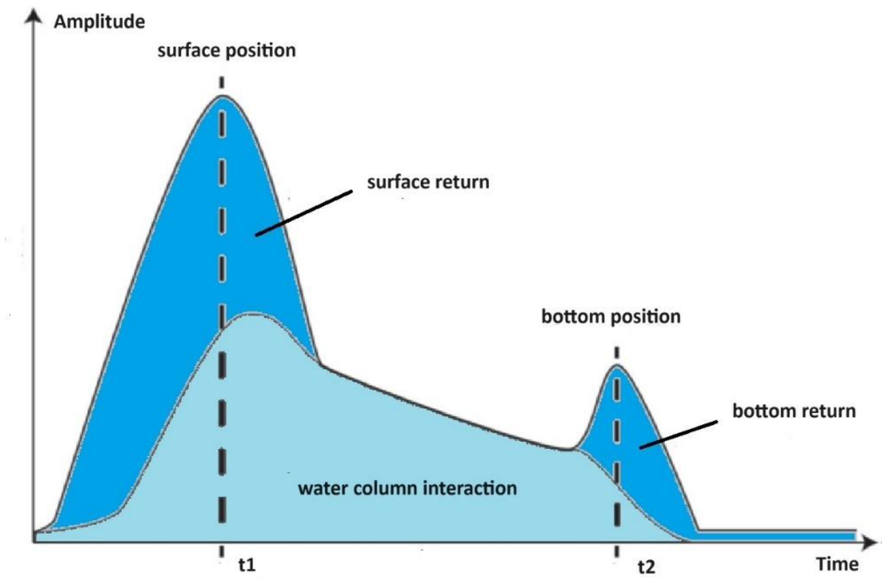

Figure 1-2: Conceptual representation of a green wavelength waveform. Delta (Δt) represents the time difference between the peaks ($t_2 - t_1$) when a pulse is propagating in the water column.

Depths are calculated by computing the time difference (delta time, Δt) between the backscattering peaks of surface and bottom (*t1* minus *t2*) registered in a waveform, which represents the total time when a pulse enters, propagates, and leaves a water column. The digitizer calculates the resulting time differences and considers errors and other variabilities recorded in a backscatter such as the electronic timing delays, artifacts in the water column, and the speed of light in water (C_w) slowing to 2.25×10^8 m/s. In Equation 1-2, d_m equals to the distance travelled (in meters) and n is the refractive index of the water (e.g., n=1.33 to 1.34) at 20° degrees Celsius, which varies with the water temperature (T), the salinity (S, ‰) and the wavelength of the emitted beam (e.g., λ=515 nm). The data processing application computes the surface representation with the n value, (Equation 1-3), therefore, users need to sample water and measure temperature and salinity, at certain locations. The digitizer decoding speed (frequency, f) is represented in gigahertz (GHz), and the duration (t_d) of each sample is calculated using the interval frequency (Equation 1-4). The Leica Chiroptera I and 4X systems used in this PhD research have an identical digitizer speed of f=1.8 GHz, which translates to ~12 cm of distance for each time sample in the vacuum, and ~9 cm while propagating in the water (n=1.34). In some cases, amplitude peaks in a waveform may not be distinctive or present (Allouis and others, 2010), and if a bottom position is not evident, we may assume that light pulse was attenuated while propagating in the water column because of excessive depth or transparency issues, or the water was too shallow for the digitizer to resolve the returning pulse echoes from the water surface and bottom, respectively. For instance, Chiroptera-I required a minimum of 10 time samples between the waveform peaks to distinguish them, which equaled to ~47 cm of depth (Saylam and others, 2017).

$$d_m = \frac{C_w \, \Delta t}{2nf} \qquad \text{(Equation 1-2)}$$

$$n(S,T,\lambda) = n_0 + (n_1 + n_2 T + n_3 T^2)S + n_4 T^2 + \frac{n_5 + n_6 S + n_7 T}{\lambda} + \frac{n_8}{\lambda^2} + \frac{n_9}{\lambda^3} \qquad \text{(Equation (1-3)}$$

$$t_d = \frac{1}{f} \times \Delta t \qquad \text{(Equation 1-4)}$$

Contrary to green-wavelength beams, near-infrared beams are either reflected by the water surface or absorbed in the first few centimeters of the water columns, so they can indicate the location of the water surface more precisely. In transparent and shallow waters, processing algorithms combine and approximate surface elevations using NIR, and green wavelength returns. Using solely green wavelength beams to detect the water surface may be misleading and may not be acceptable for constructing accurate hydrographic models due to the linear air/water interface combination mixed with volumetric backscattering energy in a waveform (Guenther and others, 2000). Therefore, to prevent any uncertainty, in this PhD research, NIR and green wavelength beams were used in conjunction, and where applicable surface elevations were validated with either in-situ methods or with waveform analysis.

1.3. Rationale for the research

The spatial accuracy of ALS derived products (i.e. digital elevation model) is determined by statistical comparisons between established control surfaces or other features with precise locational information. Typically, the errors that influence topographic measurements are caused by instrument electronics misalignments and can be largely corrected with a proper calibration procedure (Maas, 2003).

Nevertheless, any positional biases that propagate directly into the constructed elevation models due to mistakes (e.g., GNSS survey mishaps, system installation issues) may have important consequences, in some circumstances leading to scope and budget creeps or project failures. Therefore, a detailed and documented mission planning is critical for all types of airborne lidar missions (Saylam, 2009). Additional errors can be caused by data handling and improper transformations; however, such errors can typically be detected and corrected during the data processing stage and are not a focus of this research.

Various articles discuss quality control measures for airborne lidar used exclusively in topographic measurements (e.g., Aguilar and Mills, 2008; Csanyi and Toth, 2007; Vosselman, 2012). In addition, a number of governing agencies have published standards to follow when reporting horizontal and vertical accuracies of ALS derived topographic products (Flood, 2004; Kaufmann, 2019). However, quality control measures for ALB are often vague and do not adequately translate to each unique survey scenario. One exception is the standards published by the International Hydrographic Organization (IHO), which the "S-44 Edition 6.1.0" publication defined the maximum allowable total vertical uncertainty (TVU) for hydrographic surveys (IHO, 2020). $TVU_{max}(d) = \sqrt{a^2 + (b\ x\ d)^2}$ calculates the acceptable vertical uncertainty, where *a* is the coefficient that does not vary with the depth, *b* is the coefficient that changes with depth, and *d* is the depth. For instance, at 10 m depth, *a*=0.5 m, *b*= 0.013 m, and TVU_{max} = 0.52 m, at 2-sigma (95%) confidence level for the Order 1b. However, IHO uncertainty standards does not represent a particular survey method, rather they were compiled to cover common hydrographic survey methods, often in deeper waters where boat navigation and charting is critical.

1.4. Research objectives and questions.

The PhD thesis provides a scientific approach to understanding and modeling the practical and theoretical limitations of bathymetric airborne lidar surveys, demonstrating the significance of validating heights and depths with supplementary survey methods in locations with varying and dynamic environmental conditions. Each chapter of the thesis presents a case study with a unique survey scenario, where a different validation method was executed, highlighting the influence of varying environmental conditions on lidar bathymetry. Building on each case study, the PhD thesis identifies the research questions, presents the proposed methodology and the available materials, and depicts the research tasks and practices to generate results. Specifically, the PhD thesis provides answers to the following questions with each case study:

- [Chapter 2] In water reservoirs with almost ideal conditions, is there a need to confirm the water surface and bottom elevations generated by the ALB technology? What is the impact of submerged vegetation and varying bottom properties on the bathymetric results? Does waveform analysis provide a feasible method for depth validation where bottom conditions vary, and in-situ measurements are limited? Can we evaluate the waveform samples for normality and spatial autocorrelation?

- [Chapter 3] In water columns with submerged and floating vegetation, what are the challenges of mapping the river bottom using an ALB system? How can we address the potential ALB data gaps in stream bathymetry? Can we measure the river bottom with a geophysical instrumentation, particularly with a ground penetrating radar? What kind of dielectric adjustments and sampling do we need to correct the radio wave propagation? Can we validate the accuracy of all measurements before we merge them?
- [Chapter 4] Can we measure the bottom of a hypersaline lagoon with varying levels of turbidity using ALB technology? What are the potential benefits of conducting pixel reflectance analysis in bathymetric mapping? What are the implications of conducting in-situ campaigns and measuring transparency, salinity, temperature, and sonar depths, and how do these measurements apply to height (depth) validation? Is satellite-derived bathymetry a feasible technology to complement ALB measurements, and can we compare and quantify SDB to ALB in varying environmental conditions? What are the limitations, and the lessons learned?
- [Chapter 5] Can we measure the sea ice in the Arctic Ocean with an ALB system and compare the measurements to those of ICESat-2 ATLAS data products? How can we validate the lidar system calibration in the Arctic? What are the geophysical height constraints that apply to lidar datasets, and why are the modifications necessary? Since perfect correspondence is not possible between an orbiting and an airborne altimeter, can we theoretically modify and align the location of airborne lidar datasets to match those of ICESat-2 measurements? Can we validate the ICESat-2-derived melt ponds and lead (fracture) depths in the height domain?

1.5. References

Aguilar, F.J., Mills, Jon. P., 2008. Accuracy assessment of lidar-derived digital elevation models. The Photogrammetric Record 23, 148–169. https://doi.org/10.1111/j.1477-9730.2008.00476.x

Allouis, T., Bailly, J.-S., Pastol, Y., Le Roux, C., 2010. Comparison of Lidar waveform processing methods for very shallow water bathymetry using Raman, near infrared and green signals. Earth Surface Processes and Landforms 35, 640–650. https://doi.org/10.1002/esp.1959

Beć, K.B., Huck, C.W., 2019. Breakthrough Potential in Near-Infrared Spectroscopy: Spectra Simulation. A Review of Recent Developments. Front. Chem. 7, 48. https://doi.org/10.3389/fchem.2019.00048

Casal, G., Hedley, J.D., Monteys, X., Harris, P., Cahalane, C., McCarthy, T., 2020. Satellite-derived bathymetry in optically complex waters using a model inversion approach and Sentinel-2 data. Estuarine, Coastal and Shelf Science 241, 106814. https://doi.org/10.1016/j.ecss.2020.106814

Clark, P.E., Rilee, M.L., 2010. Remote sensing tools for exploration: observing and interpreting the electromagnetic spectrum. Springer, New York; London.

Committee, T., 2004. ISO/TC 211: Geographic information / Geomatics — Qualification and certification of personnel - Withdrawn. (Technical report No. 35.240.70), IT applications in science. ISO, Geneva, Switzerland.

Csanyi, N., Toth, C.K., 2007. Improvement of Lidar Data Accuracy Using Lidar-Specific Ground Targets. Photogrammetric Engineering & Remote Sensing 73, 385–396. https://doi.org/10.14358/PERS.73.4.385

Dong, P., Chen, Q., 2017. Lidar Remote Sensing and Applications. CRC Press, Boca Raton.

Flood, M., 2004. ASPRS guidelines. Vertical accuracy reporting for lidar data. (Guidelines). American Society of Photogrammetry and Remote Sensing.

Gagnon, P., Coleman, D.J., 1990. Geomatics an integrated, systemic approach to meet the needs for spatial information. CISM journal 44, 377–382. https://doi.org/10.1139/geomat-1990-0033

Gomarasca, M.A., 2009. Basics of geomatics. Springer, Dordrecht; London.

Guenther, G. C., Cunningham, A. G., LaRocque, P. E., & Reid, D. J. (2000). Meeting the accuracy challenge in airborne bathymetry (ADA488934; pp. 1–29). National Oceanic Atmospheric Administration/Nesdis Silver Spring MD.

Guenther, G.C., 2007. Airborne Lidar bathymetry (Manual No. 2), Digital elevation model technologies and applications: the DEM users manual. American Society of Photogrammetry and Remote Sensing.

IHO, 2020. International Hydrographic Organization, Standards for Hydrographic Surveys (Special publication No. S-44 Edition 6.0.0). International Hydrographic Bureau, Monaco.

Janssen, L.L.F., 2004. Principles of remote sensing: an introductory textbook. ITC, Enschede.

Kacimi, S., Kwok, R., 2020. The Antarctic sea ice cover from ICESat-2 and CryoSat-2: freeboard, snow depth, and ice thickness. The Cryosphere 14, 4453–4474. https://doi.org/10.5194/tc-14-4453-2020

Kaufmann, J.E., 2019. USGS Lidar Base Specification.

Khorram, S., Nelson, S.A.C., Koch, F.H., van der Wiele, C.F., 2012. Remote Sensing, Springer Briefs in Space Development. Springer US, Boston, MA. https://doi.org/10.1007/978-1-4614-3103-9

Killinger, D.K., 2014. Lidar (light detection and ranging), in: Laser Spectroscopy for Sensing. Elsevier, pp. 292–312. https://doi.org/10.1533/9780857098733.2.292

Kinzel, P.J., Wright, C.W., Nelson, J.M., Burman, A.R., 2007. Evaluation of an Experimental Lidar for Surveying a Shallow, Braided, Sand-Bedded River. Journal of Hydraulic Engineering 133, 838–842. https://doi.org/10.1061/(ASCE)0733-9429(2007)133:7(838)

Maas, H.G., 2003. Planimetric and height accuracy of airborne laser scanner data: User requirements and system performance, in: Proceedings of the 49th Photogrammetric Week. Wichmann verlag, pp. 117–125.

Magruder, L.A., Farrell, S.L., Neuenschwander, A., Duncanson, L., Csatho, B., Kacimi, S., Fricker, H.A., 2024. Monitoring Earth's climate variables with satellite laser altimetry. Nat Rev Earth Environ 5, 120–136. https://doi.org/10.1038/s43017-023-00508-8

Mandlburger, G., 2021. Bathymetry from Images, LiDAR, and Sonar: From Theory to Practice. PFG s41064-021-00153–0. https://doi.org/10.1007/s41064-021-00153-0

Markus, T., Neumann, T., Martino, A., Abdalati, W., Brunt, K., Csatho, B., Farrell, S., Fricker, H., Gardner, A., Harding, D., Jasinski, M., Kwok, R., Magruder, L., Lubin, D., Luthcke, S., Morison, J., Nelson, R., Neuenschwander, A., Palm, S., Popescu, S., Shum, C., Schutz, B.E., Smith, B., Yang, Y., Zwally, J., 2017. The Ice, Cloud, and land Elevation Satellite-2 (ICESat-2): Science requirements, concept, and implementation. Remote Sensing of Environment 190, 260–273. https://doi.org/10.1016/j.rse.2016.12.029

McGlone, J.C., Mikhail, E.M., Bethel, J.S., Mullen, R., American Society for Photogrammetry and Remote Sensing (Eds.), 2004. Manual of photogrammetry, 5th ed. ed. American Society for Photogrammetry and Remote Sensing, Bethesda, Md.

Palm, S., Yang, Y., Herzfeld, U., 2018. ICESat-2 Algorithm Theoretical Basis Document for the Atmosphere, Part I: Level 2 and 3 Products.

Paradis, M., 1981. De l'arpentage à la géomatique. The Canadian Surveyor 35, 262–268. https://doi.org/10.1139/tcs-1981-0036

Parrish, C. E., Magruder, L. A., Neuenschwander, A. L., Forfinski-Sarkozi, N., Alonzo, M., & Jasinski, M. (2019). Validation of ICESat-2 ATLAS Bathymetry and Analysis of ATLAS's Bathymetric Mapping Performance. Remote Sensing, 11(14), 1634. https://doi.org/10.3390/rs11141634

Petrie, G., Toth, C.K., 2018. Introduction to Laser ranging, profiling, and scanning, in: Topographic Laser Ranging and Scanning: Principles and Processing. Taylor & Francis, CRC Press, Boca Raton.

Petty, A.A., Kurtz, N.T., Kwok, R., Markus, T., Neumann, T.A., 2020. Winter Arctic Sea Ice Thickness From ICESat-2 Freeboards. JGR Oceans 125, e2019JC015764. https://doi.org/10.1029/2019JC015764

Risk, W.P., Pon, R., Lenth, W., 1989. Diode laser pumped blue-light source at 473 nm using intracavity frequency doubling of a 946 nm Nd:YAG laser. Appl. Phys. Lett. 54, 1625–1627. https://doi.org/10.1063/1.101394

Saylam, K., 2009. Quality assurance of Lidar systems: mission planning, in: American Society of Photogrammetry and Remote Sensing Conference. Presented at the ASPRS 2009, Curran Associates, Baltimore, Maryland, pp. 9–13.

Saylam, K., Brown, R.A., Hupp, J.R., 2017. Assessment of depth and turbidity with airborne Lidar bathymetry and multiband satellite imagery in shallow water bodies of the Alaskan North Slope. International Journal of Applied Earth Observation and Geoinformation 58, 191–200. https://doi.org/10.1016/j.jag.2017.02.012

Saylam, K., Hupp, J., Andrews, J., Averett, A., Knudby, A., 2018. Quantifying Airborne Lidar Bathymetry Quality-Control Measures: A Case Study in Frio River, Texas. Sensors 18, 4153. https://doi.org/10.3390/s18124153

Thenkabail, P., 2018. Remote Sensing Handbook - Three Volume Set, 1st ed. CRC Press. https://doi.org/10.1201/b19355

Vosselman, G., 2012. Automated planimetric quality control in high accuracy airborne laser scanning surveys. ISPRS Journal of Photogrammetry and Remote Sensing 74, 90–100. https://doi.org/10.1016/j.isprsjprs.2012.09.002

Chapter Two: Quantifying Airborne Lidar Bathymetry Quality-Control Measures: A Case Study in Frio River, Texas

2.1. Introduction

Airborne Lidar Bathymetry (ALB) is a technology for characterizing the depths of shallow-water bodies in transparent waters from an airborne platform using a scanning and pulsed light beam. The Bureau of Economic Geology (the Bureau) at The University of Texas at Austin owns and operates a Leica AHAB “Chiroptera I” ALB system and has access to a survey aircraft with varying mission capabilities (Figures 2-1 and 2-2). For data collection, Chiroptera uses a near-infrared (NIR) wavelength (1,064 nm) for topographic and a green-wavelength (515 nm) for bathymetry. The effective range is 400 to 500 m for the bathymetric scanner, which acquires data with pulsed signals. The topographic scanner enables surveys up to 1,500 m above ground level and can record pulses up to 400 kHz at lower altitudes. Both scanners direct the light beam at a fixed incident angle to 14° at fore and aft, and 20° to each side, creating an elliptical pattern on the surface (Palmer scanner). Advantages of this elliptical scanning pattern include the capability to map sloped surfaces such as cliffs and building facades, and to measure water surfaces with more uniform amplitudes. For visual-analysis purposes, Chiroptera integrates a 50-megapixel Hasselblad medium-format camera, which acquires imagery simultaneously with lidar data. At ALB survey altitudes, ground-sampling distance of an image is approximately 6 cm, producing details of the survey location features.

Figure 2-1. Leica AHAB Chiroptera I.

Figure 2-2. AHAB Chiroptera was installed in a Texas Department of Transportation (TxDOT) owned and operated Cessna 206 aircraft.

In recent years, use of ALB systems for hydrographic surveying of shallow waters has proved to be a versatile, cost-effective, and detailed method compared to other remote-sensing technologies such as sonar and satellite imaging (Ebrite and others, 2001; Guenther and others, 2002). The Bureau has been involved in airborne lidar surveys since 2000 (Paine and others, 2004, 2005) and has completed hundreds of ALB survey hours, covering areas larger than 9,000 km^2 at diverse locations and conditions. For all projects, specific quality-management, and quality-control (QC) methods were applied to achieve the most consistent and precise final products (Saylam and others, 2018). QC practices take place during and after the data acquisition phase to ensure that final products provide the desired level of quality. For ALB surveys, QC practices involve routine in-situ checks and supplementary surveys with other available technologies such as sonar and global navigation satellite system (GNSS). Because the quality of the lidar-derived surface models relies heavily on the accuracy of the lidar system components, it is essential to have accurate calibration parameters, and the magnitude of random and systematic errors should be budgeted carefully (Habib, 2009).

Various articles discuss topographic lidar QC measures (e.g., Aguilar and Mills, 2008; Csanyi and Toth, 2007; Vosselman, 2012); however, only a limited number note ALB methods and discuss comparisons with other relevant technologies, providing recommendations (e.g., Gao, 2009; Guenther and others, 2000; McKean and others, 2014). It is critical to understand and quantify the expected ALB survey accuracies, which rely heavily on environmental conditions and specific system capabilities. The International Hydrographic Organization (IHO) is the only organization that defines depth measuring standards and states the maximum allowed total vertical uncertainty (TVU) at 2-σ confidence requirements at certain depths, particularly for marine charting applications (IHO, 2008). Current ALB systems in the market cannot achieve depths to 100 m, however, they meet or exceed the Order 1 (b) requirements for depths shallower than 10 m (Saylam and others, 2018). However, this study is concerned with inland waters and uses other survey methods and in-situ measurements to investigate uncertainties associated with lidar bathymetry.

Overall, bathymetric surveys allow us to measure the depth of water bodies and understand the underwater terrain properties to support applications such as contour modeling, flood inundation, and leakage. Several bathymetric river surveys were completed in recent years using ALB technology (Hilldale and Raff, 2008; Kinzel and others, 2013; Legleiter, 2012; Mandlburger and others, 2013; Pan and others, 2015; Saylam, 2016); these studies demonstrated the practice as a viable and detailed method for shallow-water mapping. Because the geomorphology of rivers varies, success of an ALB survey relies on environmental aspects and conditions, especially if the survey location includes riparian areas with overhanging trees and submerged vegetation in the water column. Earlier studies demonstrated enhanced modeling and filtering and provided guidance to optimize modeling methods with potentially difficult river surveys (Mandlburger and others, 2013; McKean and others, 2009, 2014). In this study, throughout the river, we identified accessible locations with substantial water storage (pools) and approached certain areas with multiple flight lines and different headings, to minimize the shadow effect caused by overhanging riparian zone vegetation. We conducted in-situ measurements and applied relevant QC measures to validate ALB measurements and to correctly characterize the complex geomorphology of a river with a densely vegetated riparian and aquatic zone.

In this study, we defined the study objectives as follows:

- In inland water reservoirs with almost ideal conditions, do we need to confirm the water surface and bottom elevations measured by the ALB technology?
- What is the impact of submerged vegetation and varying bottom properties on the bathymetric results? Can we validate lidar bathymetry with other survey methods where lidar was not feasible?
- Can we use an external algorithm to validate depths with available waveform samples? Does an external waveform analysis provide a feasible method for depth validation where bottom conditions vary, and in-situ measurements were limited?
- Can we confirm the normality of the datasets and spatially correlate measurements to each other for further validation? What are the applicable statistical methods?

2.2. Materials and methods

2.2.1. Study area.

Frio River flows from northeast Real County, Texas, in a southeasterly direction for about 400 km, traversing Uvalde, Medina, Frio, La Salle, McMullen, and Live Oak counties, where northern sections of the river wind through the scenic Frio Canyon in the Texas Hill Country. The river passes through limestone canyons lined with a variety of tree species. Upper sections of the river, north of U.S. Route 90, are picturesque; overhanging trees provide a shaded setting for recreational activities and help to maintain an ecologically rich and diverse environment. Springs along the river provide valuable recharge along the outcrop portion of the Edwards Aquifer. The river empties into the Nueces River, contributing freshwater inflow to Nueces and Corpus Christi bays in the central Texas Gulf Coast. Because of recent drought conditions, the U.S. Geological Survey (USGS) gage (08195000, Frio River at

Concan) reported less discharge and lower gage height levels at lower sections of the river. For the month of April, since 1925, USGS gage recorded mean monthly discharge rate of 2.6 m^3/sec; however, in April 2018, the mean discharge rate was less than 1 m^3/s, and a drought trend continued in the following months (Figure 2-3). USGS also reported a gage height at 1.06 m, which was 7 cm lower than the average of the previous 19 years of measurements. Such lower water levels were an environmental concern and the reason for funding the study; however, these conditions contributed to possible lower turbidity levels and shallower water-column depths-an advantage for an ALB survey.

The aquatic and riparian habitats of the Frio River support an exceptionally diverse assemblage of invertebrates, fish, birds, weeds, and plants of the Edwards Plateau (Norris and others, 2005). Figure 2-4 presents the topography of the survey location and the designated 15 pools with substantial water storage as identified, in sequence from north to south. Researchers had access to these pools with a kayak and were able to complete an in-situ campaign for QC purposes (Figures 2-5 and 2-6).

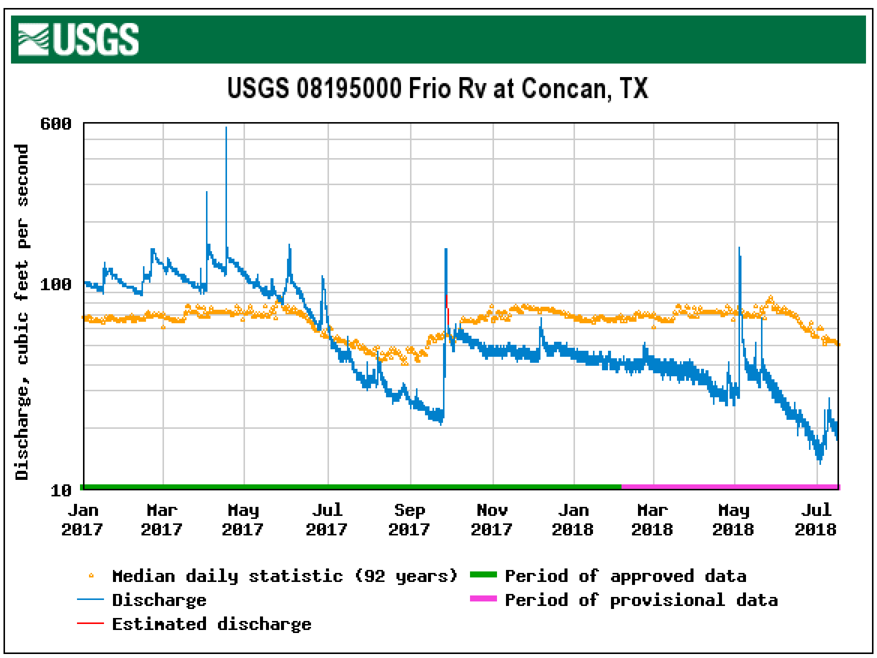

Figure 2-3. 2017 and 2018 discharge rates as measured by USGS gage at Concan, Texas location. The drought condition as a declining trend is visible in the graph, beginning by October 2017.

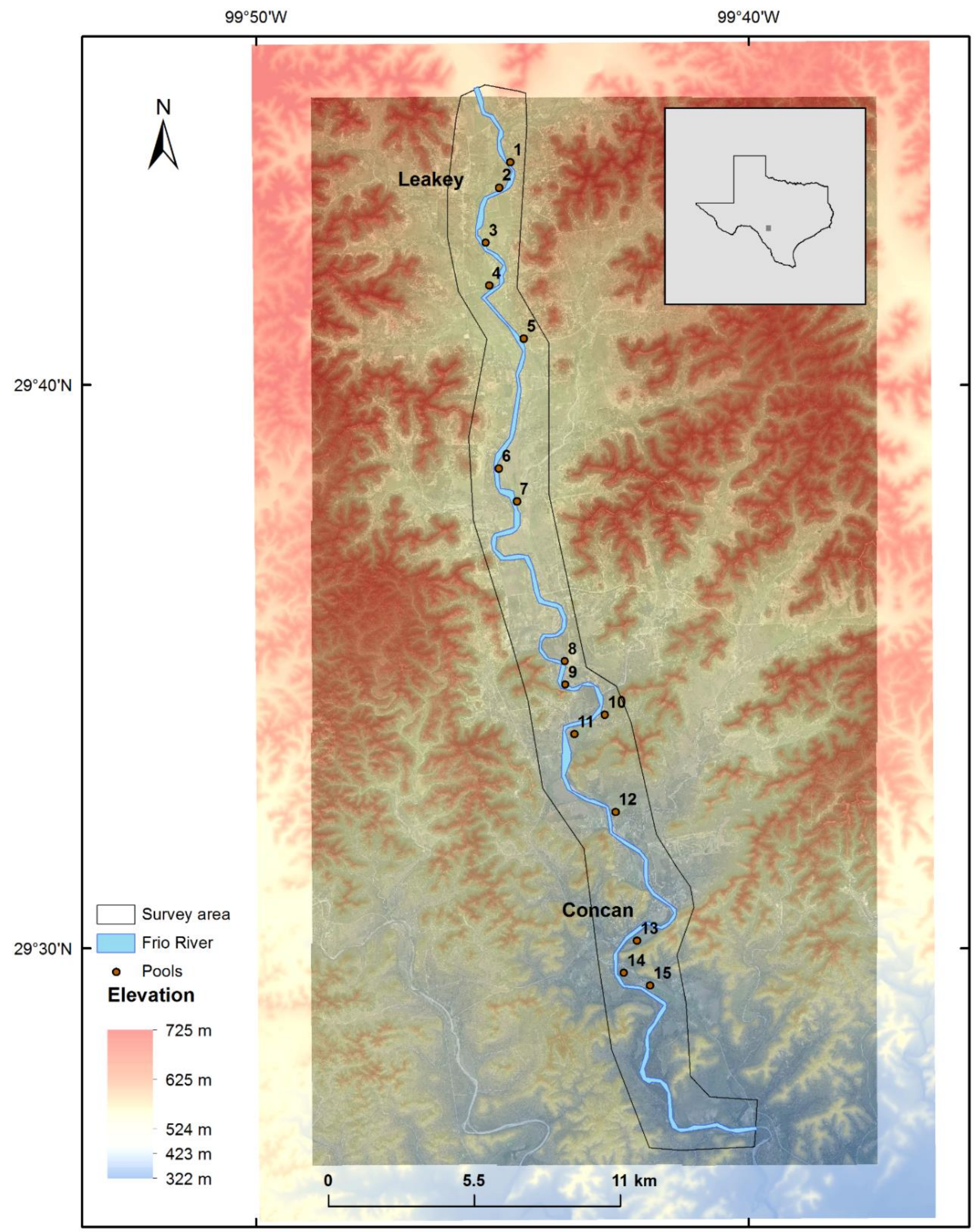

Figure 2-4. Frio River study area. Pools are numbered in sequence from one to fifteen, north to south. These locations were selected due to easier accessibility, and they hold substantial amounts of water.

Figure 2-5. Frio River and its riparian zone vegetation. Most of the river was surrounded by overhanging trees that limited the GNSS signal coverage.

Figure 2-6. Diverse submerged assemblage, which created challenges for lidar and sonar measurements.

2.2.2. GNSS control network.

Acquiring checkpoints with multi-channel GNSS receivers during ALB surveys was critical for lidar system calibration purposes. The positional quality of these measurements directly influences the final product accuracy. We used the Continuously Operating Reference System (CORS) to refine static GNSS measurements, which is an active GNSS network, operated by local agencies and overseen by the National Oceanic and Atmospheric Administration (NOAA). In the U.S., the public can access these stations and their datasets online, free of charge. Some of the more than 2,000 stations nationwide can have custom sampling rates (e.g. 1, 5, 10 seconds) with requests to their maintaining agency. We accessed TxDOT-maintained TXUV (Texas Uvalde) and TXLE (Texas Leakey) stations, sampling data at 1-s intervals. Table 2-1 illustrates the accuracy findings of TXUV and TXLE stations at all directions (latitude, longitude, and elevation), as measured and averaged in 2018. We measured the mean *Z* (vertical) bias at less than 1 cm during field work and airborne missions using these base stations.

Table 2-1. CORS stations TXUV and TXLE, positional accuracies as reported in 2018.

Reference station	Latitude	Longitude	Ellipsoidal height (H, m)	Mean accuracy (N, cm)	Mean accuracy (E, cm)	Mean accuracy (Z, cm)
TXUV	29°12' 01.86729	99°49' 37.57853	262.570	0.07	0.04	0.84
TXLE	29°44' 21.58283	99°45' 40.5039	478.402	1.57	-0.01	-0.41

2.2.3. Lidar system calibration.

Because Chiroptera's NIR- and green-wavelength scanners function independently, it is important to understand and minimize common offset errors. Positional accuracy of the lidar returns is the result of refining the offset measurements of system components and specific mounting parameters. Airborne lidar systems are equipped with manufacturer provided applications that optimize boresight angles by evaluating overlapping lidar datasets. For interested readers, studies describe the mathematical relationship and the importance of correct boresight angles (e.g., Csanyi and Toth, 2007; Habib, 2009; Mallet and Bretar, 2009). Shin and others (2016) and discuss potential synchronization problems between different scanners for ALB surveys.

For the Frio River project, we acquired lidar data using NIR and green wavelengths at 500-m range over the Del Rio International Airport (DRT), in opposite and adjacent directions, and used Leica Lidar Survey Suite v2.4 (LSS) to compute and optimize roll, pitch, and yaw angles ($R_{\Delta\omega,\Delta\Phi,\Delta K}$) for horizontal (boresight) calibration. For slant-range correction (vertical bias), we acquired 182 checkpoints over the taxiway surface using a multi-channel GNSS receiver (Trimble R8) and used 174 of these in the vertical calibration process. Because lidar points do not coincide and overlap, and we assume no redundancy with lidar- and GNSS-derived datasets, we cannot assume 1:1 comparison. Therefore, we generated triangulated irregular network (TIN) surface patches that represented the mean elevation of lidar returns and compared the elevations to those of control points. We used the least-squares method and calculated the coefficient of determination (R^2), the root-mean-square-error (RMSE) and observed the normality between the datasets.

2.2.4. Airborne missions and data acquisition.

In April 2018, we acquired lidar data with 101 individual flight lines, covering an area of 80 km^2. Flight crew spent approximately 15 hr in the air, acquiring lidar data from both scanners concurrently with high-resolution imagery. Average ground speed was 120 knots. At flat terrain, NIR lidar data sampling averaged up to 26 points/m^2, and bathymetric returns averaged 1.65 points/m^2. Output of all point-cloud data resulted in approximately 5 billion points. We referenced all datasets to North American Datum 1983 (NAD83 2011) and epoch 2010.00 and were output in Universal Transverse Mercator (UTM) 14N, in metric units. Ellipsoidal elevations were based on NAVD88[1], and the GEOID12b model was used to convert them to orthometric (real-world) elevations. For ease of data processing and analysis,

[1] North American Vertical Datum of 1988: Leveling network affixed to a single origin point on the continent.

we divided the survey area into 1-km^2 blocks and separated lidar datasets into classes with different attributes.

Flight lines were separated from each other by 160–180 m, achieving an average of 40 percent overlap and a ground-swath width of 250 m. The overlap was a critical planning consideration, given that the ground altitude of the survey location varied; any lesser amount of overlap would have potentially created gaps between the strips as the swath narrowed at smaller ranges. Because of abrupt changes in the elevation of the terrain in the southern sections of the river, we experienced the "multiple pulses in the air" (MPIA) phenomenon while collecting NIR data in the area. The affected flight lines were re-flown at the same altitude, with the system configured to use a slightly lower repetition rate (240 versus 260 kHz), which provided MPIA-free data. Nevertheless, performing a manual check of the terrain would ensure that the selected flight and scanner parameters do not exceed the system's operating limitations. To avoid MPIA, range (R) and pulse repetition rate (p) should be carefully selected. Equation 2-1 defines the mathematical relationship with C = speed of light and (s) as the fractional margin of safety.

$$R = \left(\frac{C}{2 \times p}\right) \times (1 - s) \qquad \text{(Equation 2-1)}$$

2.2.5. Waveform analysis.

Waveforms, with their potential to provide information about water-column properties and bottom characteristics of a water body, are a valuable source of data. In simple terms, an ideal waveform is composed of two distinctive peaks, representing the water-surface ($t1$) and bottom ($t2$). Number of samples (time signals. Δt), slope, and amplitude of backscatter provide information about the water depth, diffuse attenuation, and bottom properties (refer to Section 1-2, Figure 1-2). In slow-flowing rivers and still lakes, where water is mostly calm, transparent, and shallow, NIR beam reflections from the surface can be very weak and difficult to detect, and the green wavelength beams might not detect the surface at all. In such cases, the LSS surface-detection algorithm builds an interpolated surface, using all available returns from both scanners, which can introduce small biases. Because of such uncertainties, bathymetric waveform analysis is an active area of research; recent studies are available to the interested reader. Eren and others (2018) discussed a novel approach to identify water-bottom characteristics by studying backscatter amplitude. Richter and others (2017) examined the diffuse attenuation in the water column and presented an experimental approach for correcting turbidity effects. Zhao and others (2018) proposed a method of decomposing raw waveforms, Gaussian, triangle, and Weibull functions.

Chiroptera samples up to 1,024 times in a single waveform but we suggest acquiring data with a lesser sampling rate (e.g., 512) because of storage issues, especially for larger surveys. In this study, we analyzed the waveform samples using MATLAB v17, which is a commercial application package but other statistical applications (e.g., R, GNU Octave) are free of charge. We built an external algorithm to validate the depths, where applicable, as an alternative in-situ method. We selected two flight lines from different pools and output waveform samples in discrete return form and saved them in binary format. The MATLAB algorithm identified the water surface and bottom peaks by finding local maximums on a smoothed waveform. The filter smoothens data by replacing each sample with the average of neighbouring points, defined in a specific time span. Using the algorithm, it was possible to compute depths by calculating total discrete time signals (*Δt)* between the backscattering surface and bottom peaks (t_1 and t_2) and compare to the discrete return depths generated by LSS. Using LSS, we created 5x5 m blocks at selected sampling locations and exported the binary waveform information into the algorithm.

Furthermore, the algorithm required the refraction index value as the only variable (*n*), which relies on water temperature, salinity, and the specific light wavelength. Chiroptera uses 515 nm, specifically. Speed of light and digitizer sampling frequency (f_s = 1.8 GHz) are constant values to compute the backscatter travel distance (Equation 2-2). Each time signal (sample) corresponded to an estimated depth of ~9 cm with Chiroptera's current digitizing configuration.

$$d_m = \frac{C\ \Delta t}{2 n f_s} \qquad \text{(Equation 2-2)}$$

2.2.6. Sonar surveys

In shallow and transparent waters, waveform information indicates the surface and bottom positions with strong peaks; however, these may become less significant and difficult to distinguish in very shallow or wavy waters (Allouis and others, 2010) and may appear as noise-like. Furthermore, various other environmental conditions may influence the outcome of an ALB survey, making in-situ campaigns and sonar surveys beneficial or necessary (Saylam and others, 2018). In such challenging conditions, sonar surveys may provide essential depth information, as well as additional means to confirm the lidar bathymetry. In Frio River, we had access to 8 of 15 pools for sonar surveys, and we planned to have additional measurements on sections with overhanging riparian vegetation potentially blocking the laser. However, this was not an ideal situation, because the quality of GNSS signals were degraded, and influenced the accuracy of the positional information negatively. In addition, due to the ongoing drought, the river flow and overall depth was degraded, and occasional pools were not connected to each other. Therefore, we chose to use a kayak instead of a boat and mounted the sonar unit and powered it with a battery-powered trolling engine. This was an ideal platform because of its mobility and capability of maneuvering in tight and shallow areas of the river (Figure 2-7).

The sonar unit, a Garmin EchoMap 74dv, featuring a dual-frequency sonar transducer (50-200 KHZ) with an effective depth range of 36 cm to 700 m in freshwater bodies. It sampled positional data at a rate of 5 Hz with a built-in GPS-only interface. In the lab environment at UT Austin, we evaluated the unit and observed a vertical standard deviation of 2.7 cm at 11.8 m depth at freshwater. We further investigated the sonar for its horizontal positional accuracy that applied to the soundings, without applying any post corrections. Of all positions, the mean offset was less than 1 m for longitude, and ~2 m for latitude from a control point, which was adequate for basic positional information purposes in slow flowing river conditions (Figure 2-8). Because Frio River was shallow and mostly calm, and GNSS positional accuracy was degraded, we did not consider rotational angle adjustments for roll, pitch, and yaw information with sonar measurements.

We acquired approximately 10,600 sonar measurements in conjunction with the airborne lidar data acquisition missions. Scheduling airborne and sonar surveys at the same time to ensure similar environmental conditions was critical for the mission.

Figure 2-7. Kayak with sonar equipment.

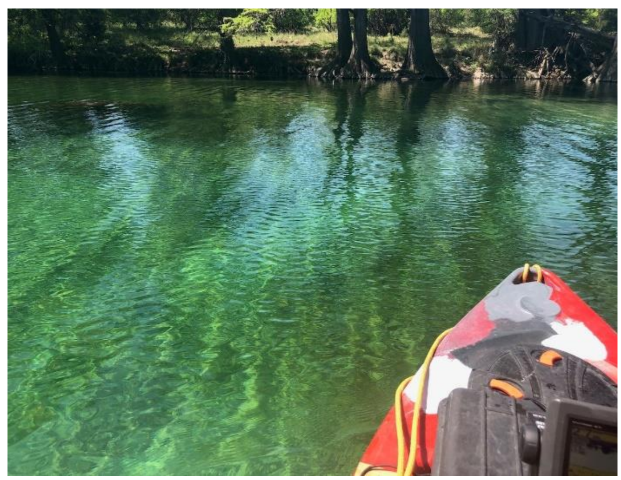

Figure 2-8. Calm, shallow and transparent waters of Frio River

2.2.7. Water-surface and bottom heights confirmation

We measured water-surface and bottom elevations at accessible locations with adequate pool depths throughout the river using a multi-channel GNSS receiver (Trimble R8) attached to a 2 m pole. As a practice, measuring water-surfaces heights on the river was difficult; therefore, we surveyed multiple locations at the water’s edge, averaging the elevations that was representative of an entire pool. For bottom measurements, we used rock or hard surfaces to prevent the survey rod from sinking into the bottom. Water-surface measurements were required to confirm the accuracy of ALB-derived surfaces, and we conducted measurements concurrent with airborne missions. We measured water-surfaces at 28 locations using a GNSS receiver, and differentially corrected the measurements. We conducted 40 water-bottom measurements and compared these heights to bathymetric lidar-derived elevations. In our computations, we subtracted lidar-derived bottom elevations (h_L) from differentially corrected GNSS (h_g) bottom measurements to calculate the height difference ($d_Z = h_L - h_g$). Here, we did not measure the depths, rather compared the bottom elevations.

2.2.8. Water-transparency measurements.

Water transparency and understanding its influence on lidar bathymetry is a challenging task for an ALB survey. Because organic and other suspended material scatters and attenuates light-beam energy, describing water-column conditions in quantitative terms is a good practice. Instead of specified requirements, ALB surveys have advised values indicating transparency and turbidity. The Secchi depth, which indicates the maximum depth at which a black-and-white circular disk (Figure 2-9) can be observed when progressively lowered into a water body, is not a definite predictor of ALB survey performance, but rather a surrogate to calculating the diffuse attenuation coefficient (Preisendorfer, 1986). ALB systems vary with their expectant depth performance, and AHAB expects Chiroptera-I to measure depths at 1.5 times the Secchi depth when benthic zone reflectance conditions are greater than 15 percent. Several empirical relationships have been developed between Secchi depth (Z_{SD}) and diffuse attenuation (K_D, m^{-1}) based on measurements in various water bodies, therefore, a varying coefficient value ($\alpha = K_D \times Z_{SD}$) has been reported in the range of ~ 1.3 to 2 (Lee and others, 2018). Interested readers can refer to articles that provide further information and discuss the effects of diffuse attenuation on ALB performance (e.g., Banic and Sizgoric, 1986; Churnside and others, 1998; Lee, 2005).

Turbidity is an expression of the optical property that causes light to be scattered and absorbed rather than transmitted in straight lines through the sample (Jethra, 1993; Suk and others, 1998). Expressed in nephelometric turbidity units (NTU) in the U.S., turbidity causes light to scatter in the water column, where particle size, shape, and composition may affect its amplitude (Baker and Lavelle, 1984; Bhargava and Mariam, 1991). In this project, we measured turbidity with a Hach 2100Q, a portable field turbidimeter (Figure 2-10) that complies with Environmental Protection Agency (EPA) method 180.11 and produces results between 0 and 1,000 NTU (O'Dell, 1993). As part of QC compliance, all turbidimeters require validation of manufacturer suggested calibration before and after each measuring session with factory-sealed samples. In Frio River, validation indicated a better-than-95-percent accurate observation.

In the Frio River project, we conducted turbidity and diffuse attenuation measurements throughout the river at various locations. Selection of these in-situ locations were important and required careful assessment of river flow, pool depth, riparian zone accessibility, bottom properties, and the adjacent private land authorizations. We sampled water conditions at selected locations and observed low turbidity levels, which was ideal for ALB surveys. In each sampling location, we conducted a minimum of three measurements and recorded the median readings. Because the river was mostly shallow and calm, we observed the Secchi disk at the water bottom as visible at all locations and expected lidar beams to map the bottom.

Figure 2-9. Freshwater Secchi disk.

Figure 2-10. Hach 2100Q field turbidimeter.

2.3. Results

2.3.1. System calibration.

In the calibration process, we converted the ellipsoidal elevations to orthometric heights using the GEOID2012B model. Results indicated a good fit for both scanners; median vertical bias was less than 2 cm, and the RMSE was smaller than 3 cm (Table 2-2). Figure 2-11 (a) illustrates the normal distribution of measurements for both scanners. The distribution for both scanner measurements to GNSS checkpoints was normal ($p < 0.004$) and statistically significant; however, slight skew occurred at locations where GNSS coverage was degraded. Figure 2-11 (b) shows the absolute median height difference, whereas the green-wavelength scanner generated ~2 cm lower heights compared to the NIR scanner, due to the larger beam divergence.

In addition, we analyzed the quality of GNSS post-processing solution results. Because we acquired static data to measure water-surfaces and bottoms, refining the horizontal and vertical accuracies was necessary. GNSS post-processing results revealed slightly high minimum versus maximum (range <

0.17 m) values, but we confirmed low standard-deviation values for horizontal and vertical solution (SD < 0.026 m, Figure 2-12) and normal distribution with high significance ($p < 0.005$) value.

Table 2-2. Vertical-bias adjustment results after Chiroptera system calibration.

Lidar scanner	Number of samples	Sample range (m)	Median (m)	RMSE (m)	R^2
NIR	174	0.13	0.004	0.026	0.99
Green- wavelength	174	0.16	0.016	0.026	0.99

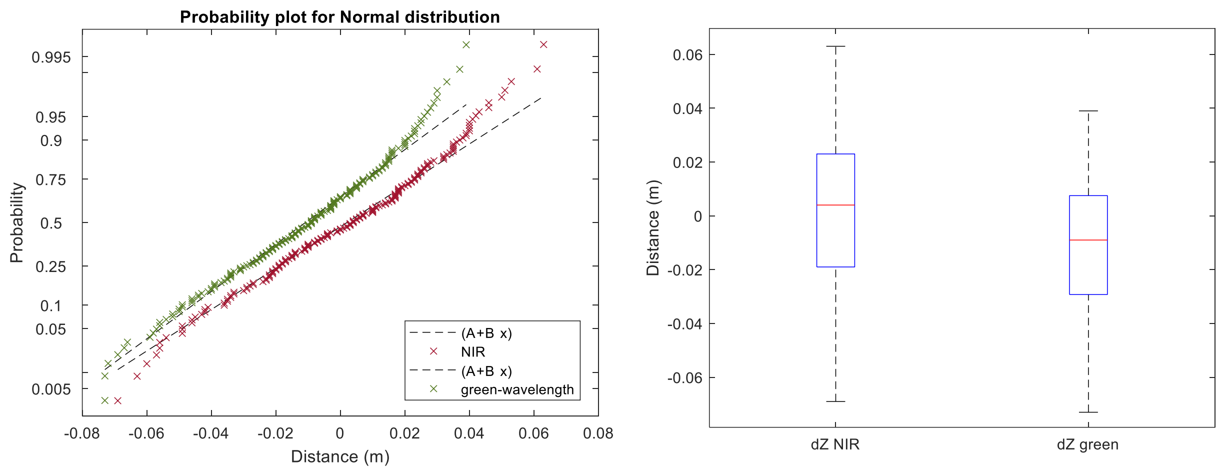

Figures 2-11 (a, b). Vertical and boresight adjustment of Chiroptera scanners; GNSS checkpoints versus lidar-derived surface patch elevations produced a normal distribution, with a few outliers in the areas with degraded GNSS coverage. The boxplots illustrate the lidar-derived surface patch median height values comparison to the GNSS checkpoint elevations.

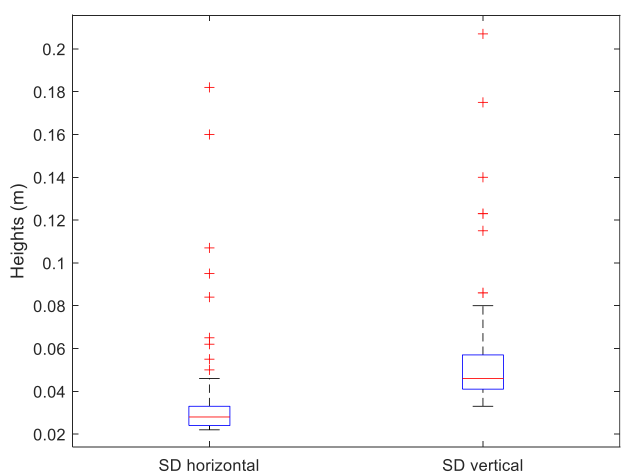

Figure 2-12. Result of GNSS post processing solution, applied to static water surface and bottom measurements. The horizontal and vertical outliers are visible in the figure.

2.3.2. Turbidity analysis.

For all observations, we measured the turbidity less than 1 NTU, calculated standard deviation less than 0.15, and the bottom was visible to the observer at all pools (Table 2-3). Under such conditions, diffuse attenuation and scattering was low, and we expected lidar beams to measure the pool bottom with sufficient backscatter amplitude.

Table 2-3. Turbidity and depth measurements at selected locations in the Frio River.

Sample	Pool	Location (latitude, longitude)	NTU (median)	SD (m)	Sonar depth (m)
1	2	29.724465, -99.749098	0.42	0.02	1.40
2	3	29.708657, -99.756977	0.66	0.15	1.38
3	3	29.706622, -99.755463	0.43	0.02	2.09
4	12	29.542181, -99.714676	0.44	0.03	1.73
5	12	29.538870, -99.713520	0.48	0.05	1.35
6	15	29.488645, -99.706318	0.59	0.03	2.06
7	15	29.488227, -99.702751	0.57	0.12	2.63
8	15	29.485601, -99.698762	0.76	0.04	1.78
9	8	29.583176, -99.729285	0.55	0.04	2.10
10	8	29.579488, -99.730900	0.46	0.06	1.11
11	9	29.576960, -99.728415	0.58	0.16	3.20
12	9	29.576916, -99.727918	0.39	0.03	1.90
		Avg.	0.54	0.07	1.90

2.3.3. Water-surface heights confirmation.

Frio River was shallow and transparent, and had minimal surface ripples; therefore, green wavelength returns were challenged to detect the surface correctly. LSS simulated the surface by using all available returns, from both scanners, and we expected minor variations in the data range. We subtracted the lidar-derived surface patch elevations from GNSS measurements and averaged the results. Of all pools measured, we computed a standard deviation of 0.05 m between the measurements, and the absolute mean difference was -0.054 m, RMSE was 0.06, and lidar-derived elevations were lower (Table 2-4). To further evaluate the results, we calculated the normality ($p=0.36$) and conducted Shapiro-Wilk test (0.96). The higher p-value indicated that the slight deviations were not statistically significant, and Shapiro-Wilk test result confirmed that the datasets were normally distributed, with only slight deviations (Figures 2-13 a, b).

Table 2-4. Water-surface measurement comparison to lidar-derived surface returns ($d_Z = h_L - h_g$).

Pool	Samples	Sampling range (m)	Mean dZ (m)	RMSE (m)
2	8	0.06	-0.09	0.1
8	6	0.12	-0.03	0.03
9	2	0.16	-0.1	N/A
12	4	0.07	-0.01	0.04
15	8	0.15	-0.04	0.07
		Avg.	-0.054	0.06

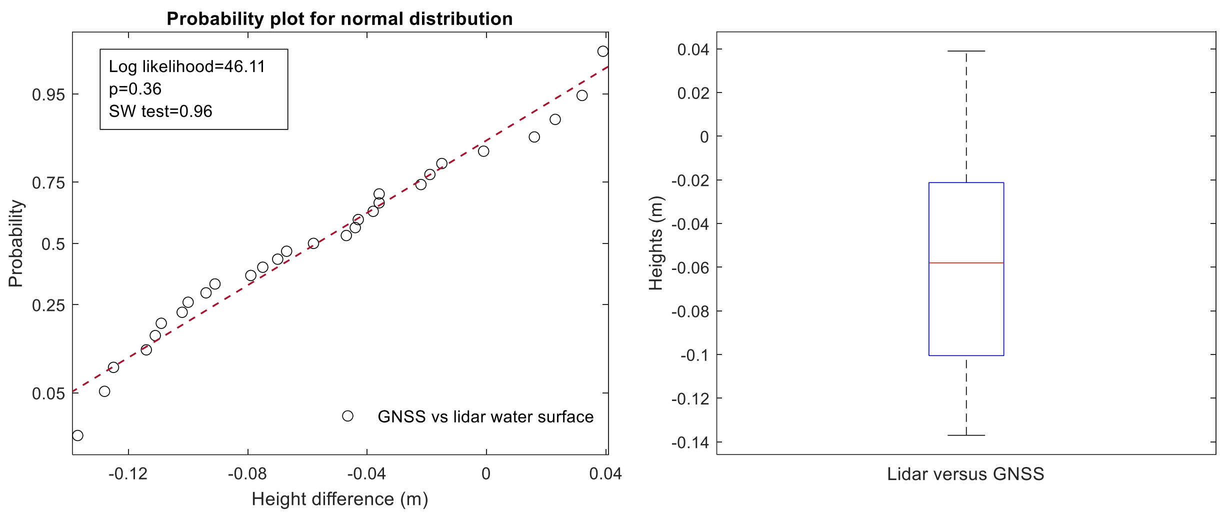

Figures 2-13 (a, b). Probability plot indicated normality for lidar and GNSS-derived water surface elevations, with slight deviation. Boxplot presents the median difference for all measurements compared (-0.054 m).

2.3.4. Water-bottom heights confirmation.

Water bottom heights comparison results showed a strong agreement to each other and a normal distribution, although lidar-derived elevations were slightly lower (Figures 2-14 a, b). Mean height bias was -0.01 m, and we computed RMSE at 0.08 m. The average coefficient of determination was $R^2 = 0.93$ and indicated a strong agreement (Table 2-5). To further evaluate the results, we calculated the normality of the measurements, the probability was significant (p=0.05), and the Shapiro-Wilk test confirmed normality (0.94). However, the p-value indicated that the deviation from normality was borderline (5%) and required caution.

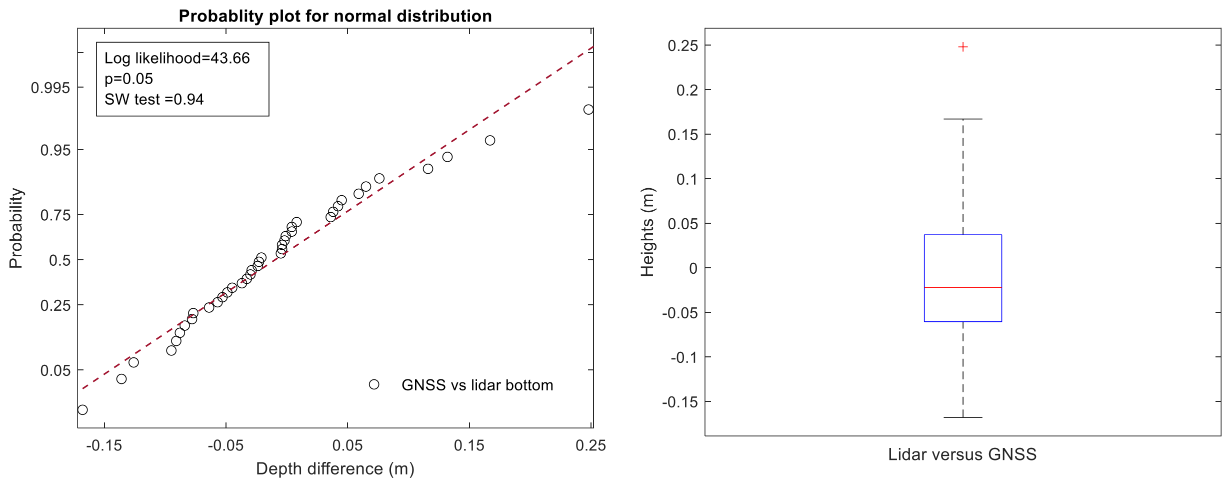

Figures 2-14 (a, b). Probability plot presented a normal distribution, and the boxplot indicated -0.02 m as the median height difference.

Table 2-5. Comparison of GNSS measured water-bottom elevations (in *height* domain, in ellipsoidal heights) to lidar-derived elevations ($d_Z = h_L - h_g$).

Pool	Number of samples	Mean lidar depth (m)	Mean GNSS depth (m)	Mean difference (m)	RMSE (m)	R^2
2	14	453.30	453.31	-0.01	0.06	0.96
3	11	446.41	446.42	-0.01	0.08	0.97
9	8	389.42	389.44	-0.02	0.05	0.92
12	7	367.70	367.71	-0.01	0.13	0.88
			Avg.	0.01	0.08	0.93

2.3.5. Waveform analysis.

At sampling location 1 (Pool 2), water was shallow and reflectance from the gravel bottom was high, resulting in strong backscatter amplitude. We sampled and averaged 22 waveforms, computing 25 samples between the surface and bottom peaks. We computed the overall depth at 1.56 m, and the algorithm indicated a 16-percent-deeper measurement compared to sonar depth (1.40 m). At location 12 (Pool 9), submerged vegetation and sand bottom caused a less reflective environment, producing a decreased backscatter amplitude; however, a more distinctive surface peak and a slope (between the peaks) was evident. We sampled and averaged 17 waveforms, computing 29 samples between peaks. The algorithm calculated the depth at 1.81 m, where water column was 9-percent-shallower compared to sonar recordings (1.90 m), caused by wider lidar pulses returning from submerged vegetation (Figure 2-15).

We investigated the waveform amplitudes for normality and conducted spatial autocorrelation testing using Moran's I (index) measure using the samples from FL6 and FL47. the probability (p=0.3) was identical, and Moran's I value was 0.93 and 0.92 (Figures 2-16 a, b). High and positive Moran's I value indicated strong autocorrelation and tendency towards clustering; however, the p-value suggested that the results could occurred by chance (30%). Therefore, from statistical perspective, we need to be cautious in interpreting the spatial clustering as statistically significant or having a non-random pattern (Figures 2-17 a, b).

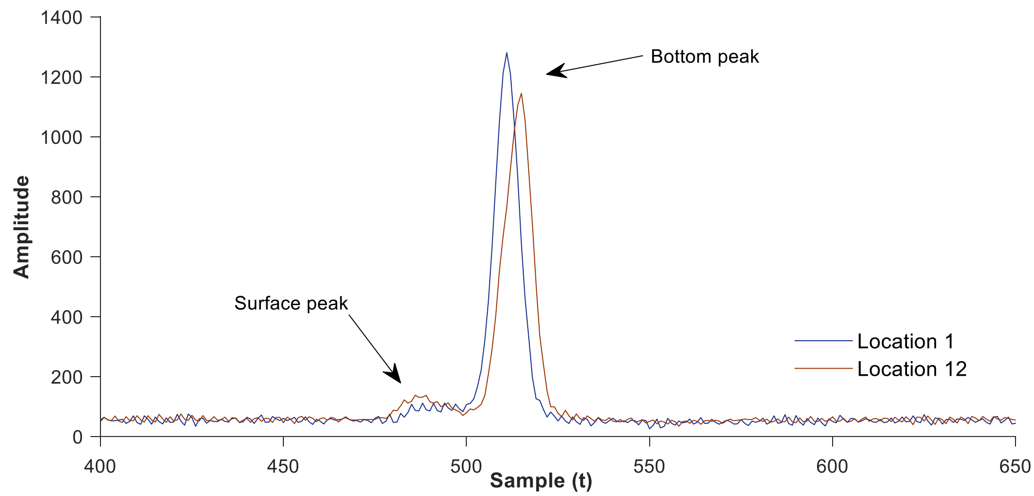

Figure 2-15. Averaged waveform amplitudes at sampling locations 1 and 12 (FL6 and FL47). The mean surface peak was weak, and the bottom backscatter was strong, indicating shallow and transparent water columns. The pool environmental characteristics were similar and sampling location 12 was deeper.

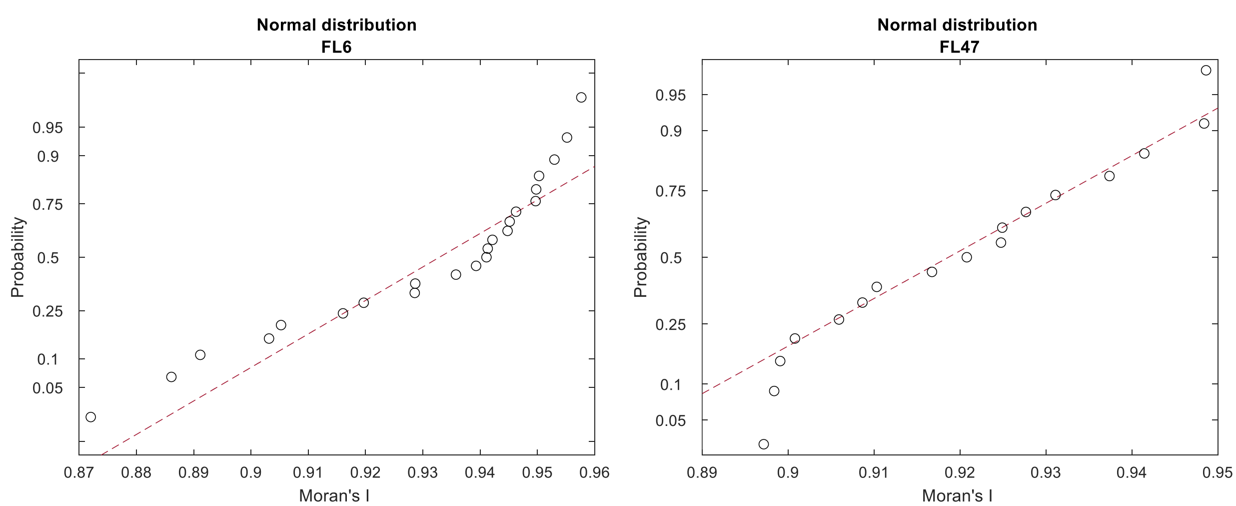

Figures 2-16 (a, b). Waveform samples generated identical normality (p=0.3) using Moran's indexing test. Although the average amplitude were similar, FL6 samples indicated deviation in the upper and lower percentiles, whereas FL47 samples generated deviation from normality in the lower percentiles.

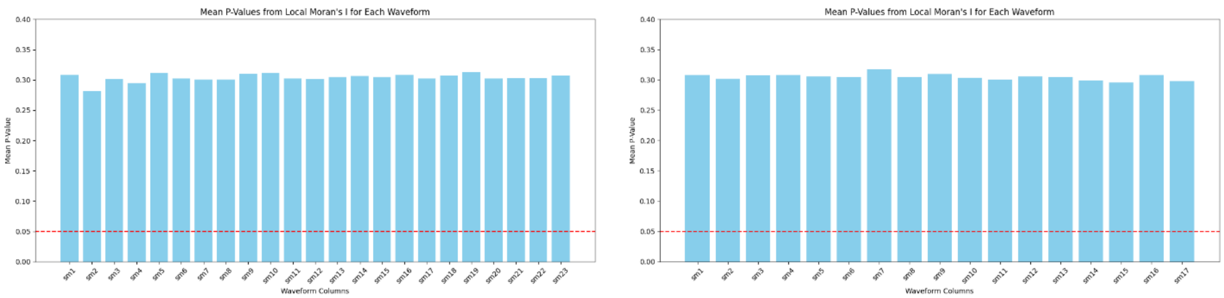

Figures 2-17 (a, b). Moran's Index value was ~0.93 for both waveform clusters, which indicated strong spatial autocorrelation.

2.3.6. Sonar measurements.

We evaluated the lidar bathymetry with sonar recordings at applicable locations. Measurements indicated 0.36 m as the shallowest and 4.67 m as the deepest water column. Mean depth of all measurements was 1.29 m. In the north, the pools were shallower, and depths increased with the river flow to south (Figure 2-18).

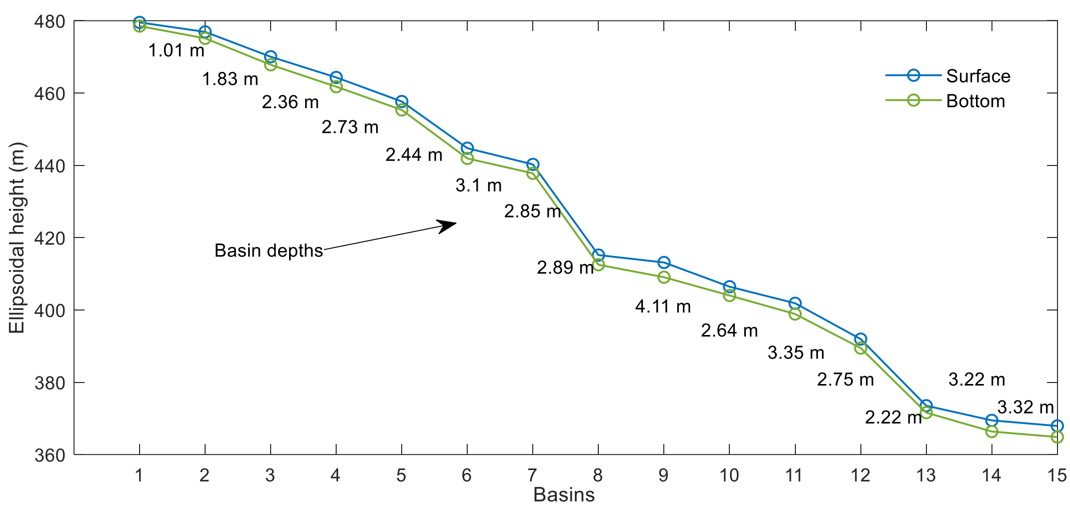

Figure 2-18. Sonar measurements in Frio River, and the maximum depths as measured. Pool #15 was the deepest with mean depth of 1.58 m and pool #12 was the shallowest at 0.91 m.

At all pools, sonar recordings to lidar bathymetry indicated a mean bias of 13 cm and RMSE was 28 cm (sonar measured deeper). The probability value varied for each pool, but we calculated an average p=0.018, which was evidence that datasets compared to each other were statistically significant. Further, we evaluated the skewness, indicating the asymmetry of data distribution to understand the normality of the datasets. If the skewness is lower than -1, or greater than 1, the data is highly skewed (Table 2-6).

Because sonar pulse beam was much narrower, it registered greater water depths at certain areas, especially in pools with submerged vegetation. This phenomenon was mostly evident in Pool 9, where lidar signals did not freely enter the water column, resulting in greatest sampling range and poor correlation at depths of 2 m and greater (Figures 2-19 a, b). Pool 8 findings indicated the lowest mean error and a good probability that lidar- and sonar-derived elevations matched each other in moderately vegetated pools (Figures 2-20 a, b). Evaluating the measurements in all pools, we used the Kernel density estimation plot (Figure 2-21), which is similar to a histogram, but uses a smoothing function to estimate univariate data (dZ) properties.

Further evaluating the datasets, the logarithmic likelihood (log likelihood) of lidar to sonar depths was smaller in pool 8 (-1142 vs -1173, -1708 vs 1937), suggesting a tighter fit to a normal distribution. In pool 8, the sigma (σ) values (0.498 and 0.507) were close to each other, indicating that the spread or variability in both datasets were similar; neither dataset had significantly more variability than the other. The small difference in the sigma value (0.009) represented that both datasets were consistent in terms of how much their values deviated from their respective means. In pool 9, the sigma values between the datasets were higher (0.613 and 0.693), and their difference was larger, suggesting the datasets deviated from each other significantly. The log likelihood values were larger in negative terms, and the difference (229) presented a loose fit to a normal distribution, particularly for the sonar measurements.

Table 2-6. Sonar-depths comparison to lidar-derived patch elevations at pool bottoms. Higher mean RMSE indicated datasets deviated from each other, caused by submerged vegetation and varying water bottom properties.

Pool	Number of samples	Sample range (m)	Mean (m)	RMSE (m)	*p (%)*	Skewness
3	1843	2.07	0.16	0.20	0.9	1.31
8	1584	1.60	0.04	0.20	1	-1.42
9	1840	4.56	0.23	0.48	2.6	1.97
12	2156	1.93	0.06	0.23	1	0.19
13	176	1.26	0.08	0.20	2.9	0.17
14	522	2.55	0.18	0.34	3	1.06
15	2479	3.04	0.16	0.33	1.3	0.1
		Avg.	0.13	0.28		

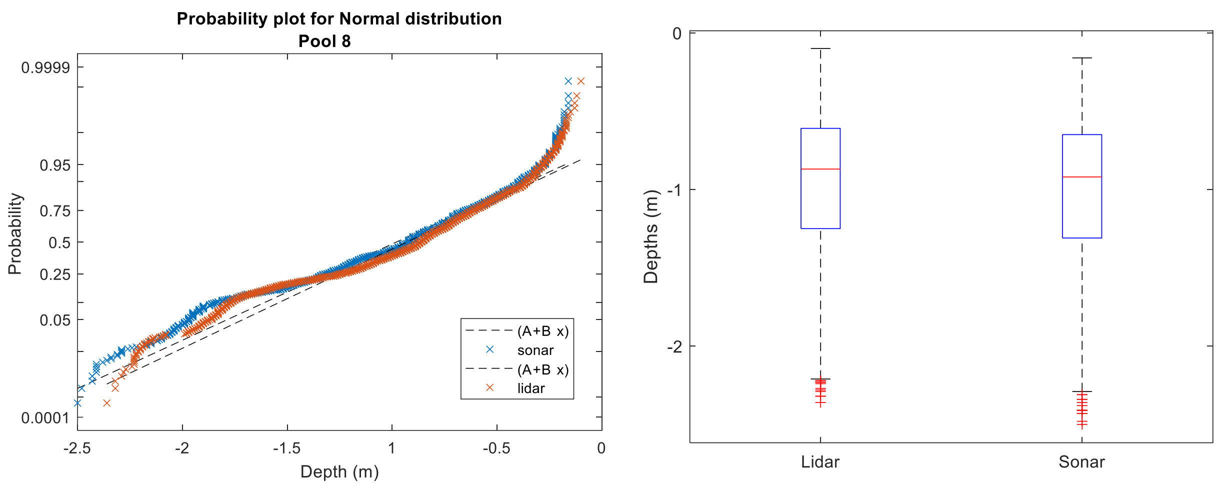

Figures 2-19 (a, b). Pool 8, lidar-derived elevation versus sonar-derived depths. The datasets were normally distributed, with slight skewness in the deeper parts. The boxplots presented the median measurements (4 cm difference) and a few outliers in depths greater than 2 m.

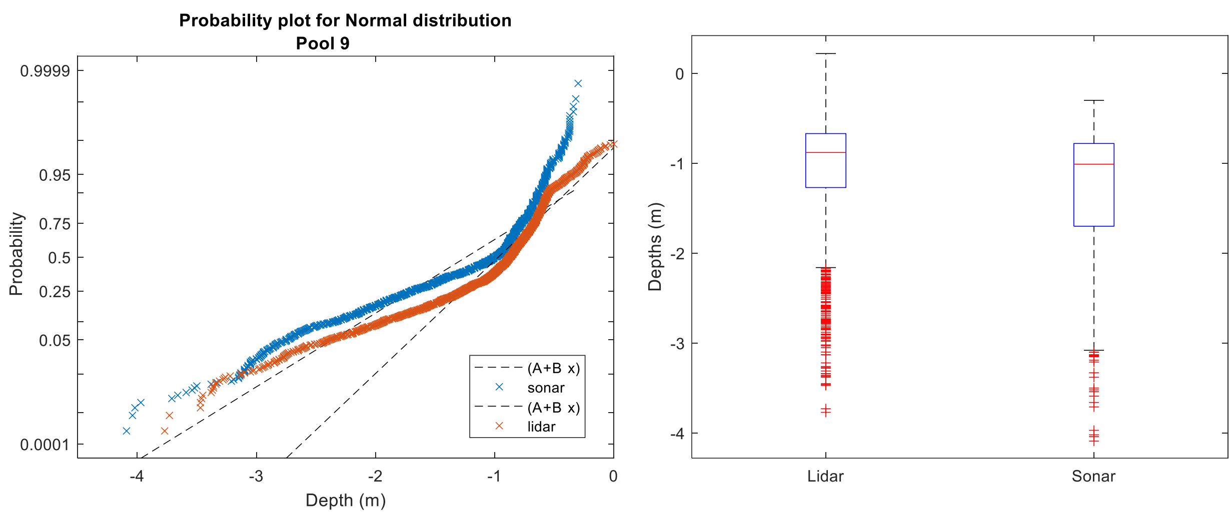

Figures 2-20 (a, b). In pool 9, datasets were skewed, and they deviated from each other, particularly at depths greater than 2 m. The environmental conditions were challenging, and the mean depth difference was high (23 cm). The boxplots indicated several outliers at deeper parts of the pool.

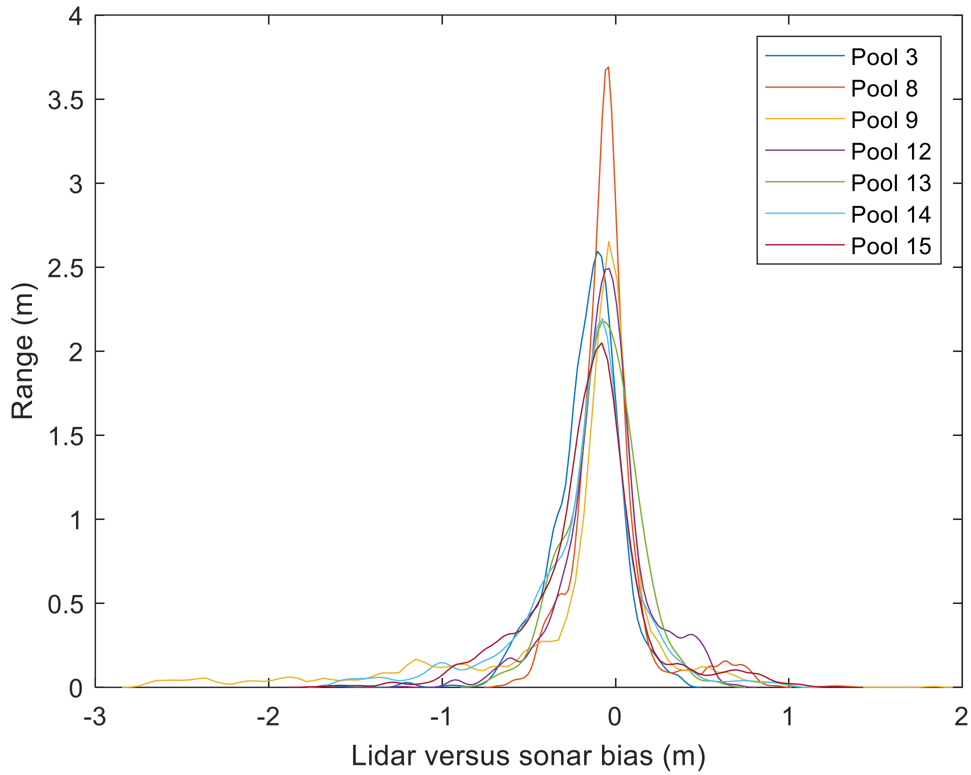

Figure 2-21. Kernel density plot of all pools presenting the measurement bias between lidar and sonar recordings. The absolute mean bias was 13 cm, where sonar recordings were deeper.

2.4. Discussion

In Frio River, we had limited access to the pools and in-situ locations. Because of the recent drought, the river flow was limited, the pools were shallow, and the heavy riparian zone degraded the GNSS signals quality required by the in-situ survey methods and limited lidar beams reaching to the pool areas. The principal study motivation was to investigate and validate the lidar bathymetry, where applicable, and introduce applicable in-situ methods to evaluate the data quality.

At shallow areas, one can estimate the depth by using a simple measuring device (e.g., marked rod with bubble level, or string with weight), but such measurements required positional information and may not be accurate at deeper and faster-flowing conditions. An unmanned surface vehicle (UAS) with tethered sonar may provide reliable bathymetry, but such surveys are localized, and they are restricted with dense aquatic vegetation, and difficult to navigate at locations with heavy riparian vegetation (Bandini and others, 2018). Therefore, the waveform algorithm introduced in this study was not complicated but enabled us with an external validation opportunity where needed. For both sampling locations (in pools 2 and 9), waveform analysis indicated a weak surface peak and a strong reflection from the bottom, which was an expected response for shallow and transparent water columns. In deeper and possibly less-transparent waters, we would expect the peaks to be reversed: surface peak amplitude is greater than bottom peak because of energy loss and scattering in the water column. The resultant bias (< 0.14 m) was in acceptable limits and can be improved in future research by investigating the depths generated by LLS application.

The comprehensive in-situ campaign presented here included validation of airborne lidar system calibration, water surface and bottom heights using GNSS surveys. Because GNSS signals were degraded at certain locations, the post-processing of static GNSS measurements were critical to improve the positioning accuracy. The solution was refined using the local CORS stations, and the mean vertical standard deviation was reported at 1 cm. However, the GNSS signals were degraded in the pools with heavy riparian zone vegetation and had an influence on the in-situ measurements. We measured the mean vertical bias ~5 cm for water surface heights, thus, the environmental conditions were challenging for the ALB to measure the surfaces faultlessly.

The quality of the sonar measurements varied with each pool. Overall, the measurements agreed with each other in 13 cm or less, and probability of a normal distribution was better than 2.9%. The heavy riparian zone with submerged vegetation influenced the accuracy of lidar and sonar measurements, and sonar measured deeper due to smaller pulse footprint. Other potential bias sources were the sonar transducer alignment, EM waves calibration and varying pool bottom reflectance may have contributed to the bias we calculated.

In Frio River study, we learned valuable lessons for consideration in the upcoming similar ALB studies. In general, river surveys require a comprehensive in-situ campaign in a dry-season with stable flow conditions, multiple airborne passes at different angles to eliminate or reduce shadow effects caused by trees, understanding and modeling of reflection and refraction effects, and creativity with deployment of ground truthing methods.

2.4. Conclusions

This study demonstrated and summarized quality-control measures applicable to ALB river surveys, and presented the efforts conducted in southwest Texas. Understanding the accuracy of lidar-derived bathymetric mapping products was essential, and we emphasized the importance of in-situ measurements and supplemental surveys for quantifying the quality of the measurements.

In the Frio River survey, the environmental conditions were varying and challenging to conduct a comprehensive airborne lidar survey and to validate the quality of the measurements. The river flow was low, and turbidity was minimal; however, the riparian zone vegetation limited the lidar beams reaching the river and influenced the GNSS geometry adversely. As a conclusion, we generated the following considerations to answer the study questions:

- In Frio River, water conditions were almost ideal (turbidity < 1 NTU); however, ALB measurements faced various other constraints. The study demonstrated that flow conditions, riparian zone vegetation, water column properties, and bottom characteristics influenced the quality of the measurements. Therefore, researchers need to evaluate and model the potential error sources and consider quantifying and documenting the biases in similar studies.
- The riparian zone vegetation had an impact on the quality of ALB measurements. Heavily canopied areas blocked lidar beams reaching the river, creating ‘shadow’ effects. Supplemental lidar data was acquired in these areas using additional flight lines at different angles, which inflated the project budget and extended the fieldwork schedule. In addition, the trees prevented acquiring spread-out GNSS geometry and degraded the precise positional information required by the in-situ measurements.
- To overcome some of these challenges, we built an external waveform analysis application and analyzed samples from applicable locations. The algorithm validated ALB where other typical methods were not feasible or limited. Results generated a good agreement to sonar recordings (< 14 cm).
- We evaluated the ALB measurements with GNSS and sonar recordings, where applicable. Our analysis indicated varying levels of agreement, reflecting each pool’s environmental conditions. However, correspondences generated normality and results were statistically significant. Further, we evaluated the waveform samples and results produced strong spatial autocorrelation. Normality tests suggested additional data samples to generate a more robust agreement.

In summary, we believe that observing near-ideal water conditions may not be sufficient to complete inland ALB surveys in confidence. Other environmental constraints required careful assessment, and we recommend investigating potential error sources and model biases. As demonstrated in this study, waveform samples may confirm depths as an in-situ method and can provide valuable information about water column and bottom characteristics where in-situ measurements are not feasible.

2.5. References

Aguilar, F.J., Mills, J.P., 2008. Accuracy assessment of lidar-derived digital elevation models. The Photogrammetric Record 23, pp. 148-169. https://doi.org/10.1111/j.1477-9730.2008.00476.x

Allouis, T., Bailly, J.-S., Pastol, Y., Le Roux, C., 2010. Comparison of lidar waveform processing methods for very shallow water bathymetry using Raman, near infrared and green signals. Earth Surface Processes and Landforms 35, pp. 640-650. https://doi.org/10.1002/esp.1959

Baker, E.T., Lavelle, J.W., 1984. The effect of particle size on the light attenuation coefficient of natural suspensions. Journal of Geophysical Research 89, pp. 8197-8203. https://doi.org/10.1029/JC089iC05p08197

Bandini, F., Lopez-Tamayo, A., Merediz-Alonso, G., Olesen, D., Jakobsen, J., Wang, S., Garcia, M., Bauer-Gottwein, P., 2018. Unmanned aerial vehicle observations of water surface elevation and bathymetry in the cenotes and lagoons of the Yucatan Peninsula, Mexico. Hydrogeology Journal pp. 1-16. https://doi.org/10.1007/s10040-018-1755-9

Banic, J., Sizgoric, S., 1986. Scanning lidar bathymeter for water depth measurement, in: Cruickshank, J.M., Harney, R.C. (Eds.), pp. 187-195. https://doi.org/10.1117/12.938673

Bhargava, D.S., Mariam, D.W., 1991. Light penetration depth, turbidity and reflectance related relationship and models. ISPRS Journal of Photogrammetry and Remote Sensing 46, pp. 217-230. https://doi.org/10.1016/0924-2716(91)90055-Z

Churnside, J.H., Tatarskii, V.V., Wilson, J.J., 1998. Oceanographic lidar attenuation coefficients and signal fluctuations measured from a ship in the Southern California Bight. Applied Optics 37, pp. 3105-3112. https://doi.org/10.1364/AO.37.003105

Csanyi, N., Toth, C.K., 2007. Improvement of lidar Data Accuracy Using lidar-Specific Ground Targets. Photogrammetric Engineering and Remote Sensing 73, pp. 385-396. https://doi.org/10.14358/PERS.73.4.385

Ebrite, S., Pope, B., Lillycrop, W.J., 2001. A multi-agency solution for coastal surveys - SHOALS in the Pacific. Marine Technol. Soc, pp. 1204-1211. https://doi.org/10.1109/OCEANS.2001.968284

Eren, F., Pe'eri, S., Rzhanov, Y., Ward, L., 2018. Bottom characterization by using airborne lidar bathymetry (ALB) waveform features obtained from bottom return residual analysis. Remote Sensing of Environment 206, pp. 260-274. https://doi.org/10.1016/j.rse.2017.12.035

Gao, J., 2009. Bathymetric mapping by means of remote sensing: methods, accuracy, and limitations. Progress in Physical Geography 33, pp. 103-116. https://doi.org/10.1177/0309133309105657

Guenther, G.C., Cunningham, A.G., LaRocque, P.E., Reid, D.J., 2000. Meeting the accuracy challenge in airborne bathymetry (No. ADA488934), pp. 1-29. National Oceanic Atmospheric Administration/Nesdis Silver Spring MD.

Guenther, G.C., Lillycrop, W.J., Banic, R.J., 2002. Future advancements in airborne hydrography. International Hydrographic Review, New series 3, pp. 67-90.

Habib, A., 2009. Accuracy, quality assurance and quality control of lidar data, in: Topographic Laser Ranging and Scanning: Principles and Processing. Taylor and Francis, Boca Raton, FL, pp. 269-294.

Hilldale, R.C., Raff, D., 2008. Assessing the ability of airborne lidar to map river bathymetry. Earth Surface Processes and Landforms 33, pp. 773-783. https://doi.org/10.1002/esp.1575

Hodúl, M., Bird, S., Knudby, A., Chénier, R., 2018. Satellite derived photogrammetric bathymetry. ISPRS Journal of Photogrammetry and Remote Sensing 142, pp. 268-277. https://doi.org/10.1016/j.isprsjprs.2018.06.015

IHO, 2008. IHO Standards for Hydrographic Surveys (Special publication No. 44), pp. 1-36. International Hydrographic Bureau, Monaco.

Jethra, R., 1993. Turbidity measurement. ISA Transactions 32, pp. 397-405. https://doi.org/10.1016/0019-0578(93)90075-8

Kinzel, P.J., Legleiter, C.J., Nelson, J.M., 2013. Mapping river bathymetry with a small footprint green lidar: applications and challenges. JAWRA Journal of the American Water Resources Association 49, pp. 183-204. https://doi.org/10.1111/jawr.12008

Lee, Z., Shang, S., Du, K., Wei, J., 2018. Resolving the long-standing puzzles about the observed Secchi depth relationships: Resolving puzzles about Secchi depth relationships. Limnology and Oceanography pp. 1-16. https://doi.org/10.1002/lno.10940

Lee, Z.-P., 2005. Diffuse attenuation coefficient of downwelling irradiance: An evaluation of remote sensing methods. Journal of Geophysical Research 110, pp. 1-9. https://doi.org/10.1029/2004JC002573

Legleiter, C.J., 2012. Remote measurement of river morphology via fusion of lidar topography and spectrally based bathymetry. Earth Surface Processes and Landforms 37, pp. 499-518. https://doi.org/10.1002/esp.2262

Mallet, C., Bretar, F., 2009. Full-waveform topographic lidar: State-of-the-art. ISPRS Journal of Photogrammetry and Remote Sensing 64, pp. 1-16. https://doi.org/10.1016/j.isprsjprs.2008.09.007

Mandlburger, G., Pfennigbauer, M., Pfeifer, N., 2013. Analyzing near water surface penetration in laser bathymetry - A case study at the River Pielach. ISPRS Annals of Photogrammetry, Remote Sensing and Spatial Information Sciences II-5/W2, pp. 175-180. https://doi.org/10.5194/isprsannals-II-5-W2-175-2013

McKean, J., Nagel, D., Tonina, D., Bailey, P., Wright, C.W., Bohn, C., Nayegandhi, A., 2009. Remote Sensing of Channels and Riparian Zones with a Narrow-Beam Aquatic-Terrestrial Lidar. Remote Sensing 1, pp. 1065-1096. https://doi.org/10.3390/rs1041065

McKean, J., Tonina, D., Bohn, C., Wright, C.W., 2014. Effects of bathymetric lidar errors on flow properties predicted with a multi-dimensional hydraulic model: lidar bathymetry and hydraulic models. Journal of Geophysical Research: Earth Surface 119, pp. 644-664. https://doi.org/10.1002/2013JF002897

Norris, C.W., Mounton, D.W., El-Hage, A., Bradsby, D., 2005. Ecologically Significant River and Stream Segments of Region L (South Central) Regional Water Planning Area (No. WRTS-2005-01), pp. 1-75, Sport Fish and Wildlife Restoration. Texas Parks and Wildlife Department, Austin, Texas.

O'Dell, J.W., 1993. Method 180.1: Determination of turbidity by nephelometry (No. Revision 2.0). Office of Research and Development, pp. 1-8, U.S. Environmental Protection Agency, Cincinnati, OH.

Paine, J.G., White, W.A., Smyth, R.C., Andrews, J.R., Gibeaut, J.C., 2005. Combining EM and lidar to Map Coastal Wetlands: An Example from Mustang Island, Texas. Environment and Engineering Geophysical Society, pp. 745-756. https://doi.org/10.4133/1.2923527

Paine, J.G., White, W.A., Smyth, R.C., Andrews, J.R., Gibeaut, J.C., 2004. Mapping Coastal Environments with lidar and EM on Mustang Island, Texas, U.S. The Leading Edge 23, pp. 894-898. https://doi.org/10.1190/1.1803501

Pan, Z., Glennie, C., Hartzell, P., Fernandez-Diaz, J., Legleiter, C., Overstreet, B., 2015. Performance assessment of high resolution airborne full waveform lidar for shallow river bathymetry. Remote Sensing 7, pp. 5133-5159. https://doi.org/10.3390/rs70505133

Preisendorfer, R.W., 1986. Secchi disk science: visual optics of natural waters: Secchi disk science. Limnology and Oceanography 31, pp. 909-926. https://doi.org/10.4319/lo.1986.31.5.0909

Richter, K., Maas, H.-G., Westfeld, P., Weiß, R., 2017. An Approach to Determining Turbidity and Correcting for Signal Attenuation in Airborne Lidar Bathymetry. PFG – Journal of Photogrammetry, Remote Sensing and Geoinformation Science 85, pp. 31-40. https://doi.org/10.1007/s41064-016-0001-0

Saylam, K., 2016. A tale of two airborne lidar scanners- lower Colorado River basin survey. Lidar Magazine 6, pp. 34-37.

Saylam, K., Hupp, J., Averett, A., Gutelius, B., Gelhar, B., 2018. Airborne Lidar bathymetry: Assessing quality assurance and quality control methods with Leica Chiroptera examples. International Journal of Remote Sensing, pp. 2518-2542, https://doi.org/10.1080/01431161.2018.1430916

Saylam, K., Hupp, J.R., Aaron, R.A., 2017. Quantifying the bathymetry of the lower Colorado River basin, Arizona, with airborne Lidar. Presented at the IGTF ASPRS 2017 Annual Conference, Baltimore, Maryland, pp. 1-11.

Shin, M.S., Yang, I.T., Lee, D.H., 2016. A Study on Airborne Lidar Calibration and Operation Techniques for Bathymetric Survey. Journal of Korean Society for Geospatial Information System 24, pp. 113-120. https://doi.org/10.7319/kogsis.2016.24.2.113

Suk, N.S., Guo, Q., Psuty, N.P., 1998. Feasibility of using a turbidimeter to quantify suspended solids concentration in a tidal saltmarsh creek. Estuarine, Coastal and Shelf Science 46, pp. 383-391. https://doi.org/10.1006/ecss.1997.0284

Traganos, D., Poursanidis, D., Aggarwal, B., Chrysoulakis, N., Reinartz, P., 2018. Estimating Satellite-Derived Bathymetry (SDB) with the Google Earth Engine and Sentinel-2. Remote Sensing 10, 859. https://doi.org/10.3390/rs10060859

Vosselman, G., 2012. Automated planimetric quality control in high accuracy airborne laser scanning surveys. ISPRS Journal of Photogrammetry and Remote Sensing 74, pp. 90-100. https://doi.org/10.1016/j.isprsjprs.2012.09.002

Zhao, X., Zhao, J., Zhang, H., Zhou, F., 2018. Remote Sensing of Suspended Sediment Concentrations Based on the Waveform Decomposition of Airborne Lidar Bathymetry. Remote Sensing 10, 247. https://doi.org/10.3390/rs10020247

Chapter Three: Multi-Sensor Approach to Improve Bathymetric Lidar Mapping of Semi-Arid Groundwater-Dependent Streams: Devils River, Texas

3.1. Introduction

Remote sensing technology uses active or passive propagated signals (e.g., light pulses, electromagnetic radiation) to enable acquisition of information about objects from distances. Remotely sensed data have spectral, spatial and temporal properties, and they include positional information acquired by global navigation satellite system (GNSS) (Khorram and others*,* 2012; Thenkabail, 2018). Since the late 1960s, traditional aerial photographic systems have been replaced with airborne and spaceborne sensors capable of acquiring data at different spatial, spectral, temporal, and radiometric resolutions, providing the means for a variety of analytical opportunities.

Airborne and satellite-based remote sensing approaches show great promise for characterizing aquatic ecosystems (Dauwalter and others*,* 2017; Mouw and others*,* 2015). One such approach is light detection and ranging (lidar), an active, non-imaging, remote sensing technology that uses an artificial light source commonly falling in the optical spectrum between 0.5 and 1.6 µm. The applications and usage of lidar technology have increased since the 1960s and cover a wide range of military, civilian, and scientific activities (Höfle and Rutzinger, 2011; Karp and Stotts, 2012; Killinger, 2014). A typical non-stationary lidar system is composed of a laser scanner, transmitting, and receiving units, a GNSS receiver, an inertial navigation system (INS), a digital storage unit, a digitizer, and an operator interface. These system components emit pulsed or continuous laser energy and with each pulse measure, the distance travelled between the transmitter, the target surface, and back to the receiver. Onboard electronics digitize the received electromagnetic (EM) energy and record the amplitude, the geographic location, and various other information.

Airborne lidar bathymetry (ALB) is a derivative of lidar technology, and utilized for mapping shallow and transparent bodies of water and shorelines from an airborne platform (Guenther, 2007; Muirhead and Cracknell, 1986). A typical ALB system uses two laser transmitters: a near-infrared (NIR, 1064 nm) wavelength to detect water surfaces, and a visible (green, 515–532 nm) wavelength to measure water depths. In theory, green wavelength beams emitted from an airborne laser transmitter traverse the air–water interface and propagate in the water until reaching and illuminating the bottom. The light beams slow while traveling in the water column, and their energy (amplitude) attenuates due to refraction and scattering. If a beam is not attenuated entirely, it reflects from the bottom, and the backscatter reaches the receiver. A digitizer records the reflected amplitude in a waveform fashion, indicating the surface, bottom, and all other major interactions, including noise. Contrary to green wavelength beams, depending on the turbidity levels and surface characteristics, NIR beams are either absorbed immediately beneath the water surface or reflect off, indicating the surface location (Figure 3-1).

In recent years, researchers have completed inland bathymetric surveys using ALB technology. In doing so, they have demonstrated this technology's versatility and accuracy (Hilldale and Raff, 2008; P. Kinzel and Legleiter, 2019; Legleiter, 2012; Saylam, Brown, and others, 2017). Here, we use the term "inland" to refer to specific ecosystem types, such as lakes, reservoirs, rivers, ponds, swamps, and wetlands. The term also represents ecological and hydrologic environments of diverse shapes and sizes and various physical, chemical, and optical properties (Ogashawara and others, 2017). In fluvial and karst environments, the conditions and aquatic properties vary, presenting an accuracy challenge for airborne lidar bathymetry (Saylam, Hupp, Andrews, and others, 2018). Therefore, it is essential to conduct in-situ measurements to quantify bathymetric expectations (Lague and Feldmann, 2020; Saylam, Hupp, Averett, and others, 2018). Variations in water transparency, depth, and other environmental conditions may limit or prevent measurement, affecting the modeling of the backscatter amplitude and the shape of the recorded waveform. Cottin and others, (2009) and Eren and others, (2018) investigated waveform shapes, backscatter amplitudes, and attempted to model the bottom properties. For river surveys, Allouis and other, (2010) and Pan and others, (2015) studied the waveform shape, modifying it via decomposition and deconvolution methods and comparing their findings to in-situ depth measurements.

The study addresses the possible data gaps in the stream bathymetry caused by environmental conditions. A seamless bottom map is required to parameterize physical stream-flow models to assess aquatic habitat conditions under a range of stream-flow conditions. In addition to thermal and hydrologic data collection, accurate stream bathymetry is critical to hydraulic model development. To map the stream bathymetry, we conducted an extensive airborne lidar survey campaign and performed supplementary measurements to build a seamless map of the river bottom and immediate surroundings. As a novel approach, we used an unconventional hydrographic survey instrument, we used a ground penetrating radar (GPR) to characterize the depth and river bedrock where surface or submerged vegetation prevented other active sensors such as lidar and sonar from accurately measuring its depth. A GPR is a high-resolution imaging sensor that uses electromagnetic waves to interpret near-surface geophysics. Literature has cited various environmental uses for GPRs, such as development of hydrogeologic models of the subsurface (Knight, 2001), identifying groundwater levels and mapping aquifers (Doolittle and others, 2006) and exploring groundwater contamination (Benson, 1995).

The study proposed a detailed evaluation of the pools by Dolan Falls because of their significant role in habitat conservation of the Devils River minnow. Specifically, we aimed to address the following study questions:

- In water columns with submerged and floating vegetation, what are the challenges of mapping the bottom with an ALB system? How can we address the potential ALB data gaps in stream bathymetry?
- Can we detect the river bedrock with a ground penetrating radar? What kind of dielectric adjustments and sampling do we need to correct the radio wave propagation? Can we validate GPR readings with another survey method?
- Can we validate the accuracy of heights and depths measured with different survey methods? Can we merge all datasets to build a seamless bottom map? What are the accepted biases?

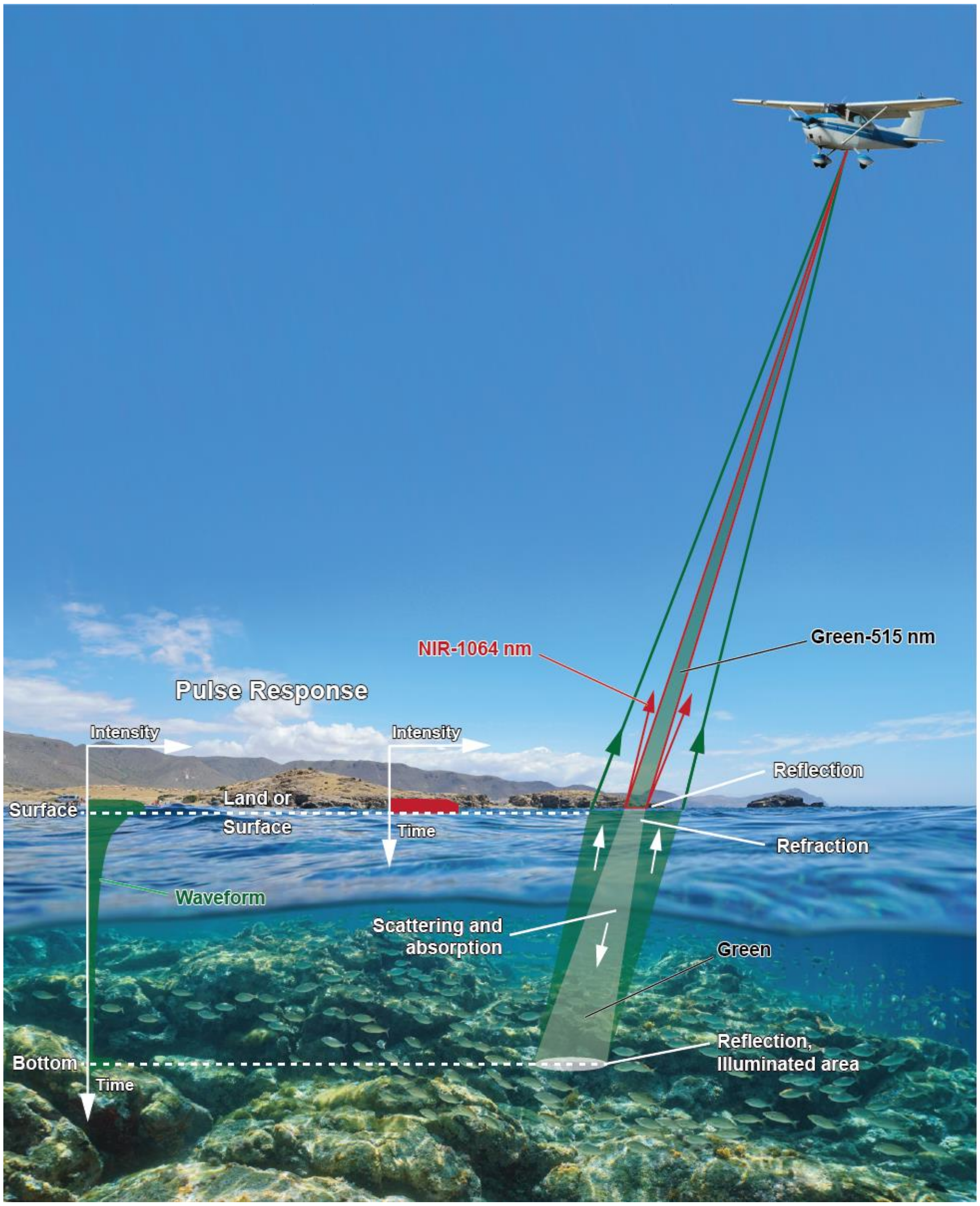

Figure 3-1. Scattering and refraction occur when light beams traverse through the air–water interface. Near infrared (NIR) beams are absorbed either at the surface or in the immediate water column, whereas some reflect to the receiver and indicate the water surface. Distances (range) from the surface and bottom can be computed by measuring the flight duration of the pulses and adjusting the varying speed of light in air and water.

3.2. Materials and Methods

In this study, we generated integrated bathymetric measurements of Devils River using a variety of survey methods. We acquired airborne lidar datasets using a Leica Airborne Hydrography AB (AHAB)

Chiroptera-I system with a maximum effective range of 500 m above the water surface. The system acquired and recorded green-wavelength data with a pulse rate of 35 kHz in a waveform format. A near-infrared scanner produced lidar pulses at 260 kHz—optimum speed at an average survey altitude of 450 m. The Chiroptera-I has two integrated cameras: a medium-format 50-megapixel (MP) Hasselblad camera (red-green-blue, RGB) for orthophoto production, and a lower-resolution camera (video graphics array; VGA) to assist airborne missions and data processing.

The Chiroptera-I is rated as a shallow (i.e., depth penetration to 15 m in transparent waters) mapping system. The pulse power and energy are lower (0.062 MW and 0.12 mJ) than a typical deep-channel (i.e., depth penetration to 30 m) ALB system, such as the Leica HawkEye III (0.72 MW and 2.3 mJ). The beam divergence of each pulse is between 0.5 and 3.0 mrad (NIR, green). The Chiroptera-I uses two Palmer scanners (nutating pattern) to distribute lidar pulses in an elliptic pattern; the maximum incident angle is ± 14° fore and aft and ± 20° toward the edges (Figure 3-2). There are advantages of using a Palmer scanner, such as generating uniform point distribution, reduced shadow effects, and the capability to map sloped surfaces with multiple view angles. Additionally, the nutating pattern eliminates excessively high amplitude returns coming off from the surface at nadir angles, which can be harmful to the sensitive system electronics.

To have higher chances of depth measurement and easier navigation with a boat, we completed GPR surveys in October with lesser vegetation presence due to seasonal changes. GPR surveys are common in seismic and near-surface profiling of bedrock (Busato and others, 2016; Słowik, 2011), emitting electromagnetic pulses in the microwave band of the radio spectrum (UHF/VHF) and detecting layer boundaries or objects in the subsurface with different permittivity. EM waves are discharged and received by an antenna mounted immediately above the water surface and are recorded when the instrument is in the rover (moving) mode. Because EM waves do not travel at a constant speed through distinct types of material or through the water column, the accurate propagation velocity needs to be calculated based on the electrical and magnetic properties of the survey environment. The relative permittivity of the soil, rock, water, and air vary greatly. Typically, EM waves travel 30 cm/ns in a vacuum and 3.3 cm/ns in freshwater (Carrick Utsi, 2017).

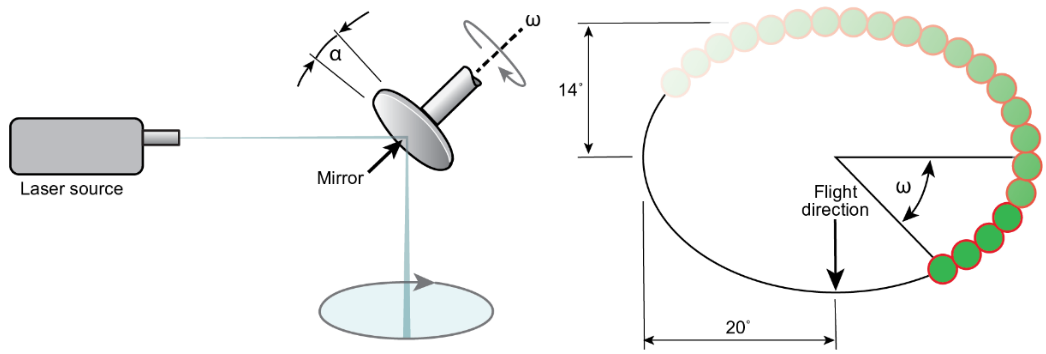

Figure 3-2. A representation of the Palmer scanner and its elliptical scanning pattern of Leica AHAB Chiroptera-I sensors.

3.2.1. Study Site

Devils River is a semi-arid karst stream in southwestern Texas in which most discharge originates as spring flows and distributed groundwater inflows (Green and others, 2014). The river is pristine due to its remote and rugged location, bordering primarily by large intact ranch lands and protected natural areas, which minimizes pollution from human and animal waste (S. Robertson and others, 2019). Riparian vegetation includes stands of Mexican white oak (*Quercus polymorpha*) and American sycamore trees (*Platanus occidentalis*); upland areas are dotted with scrub juniper (*Juniperus*) and mesquite (*Prosopis velutina*). The study area is comprised of important pool mesohabitats with a diversity of hydrologic habitats, supporting 28 species of fish (M. S. Robertson and Winemiller, 2003). The protected Devils River minnow (*Dionda diaboli*) is classified as a federally threatened species. *D. diaboli* is a minnow species (family *Cyprinidae*) with a distribution limited to tributaries of the middle Rio Grande in Texas and Coahuila, Mexico, with adults reaching 5-6 cm in length. Texas Parks and Wildlife Department (TPWD) biologists are working with conservation and research partners to develop and execute a multidisciplinary research program to collect the scientific evidence needed to inform management of *D. diaboli* and other species of interest to state and federal conservation efforts. This includes data collection to support development of a robust two-dimensional hydraulic fish habitat model, enabling resource managers to understand the declines in spring flow and surface water discharges that affect habitats for imperiled fish and mussel species. Findings would allow for data-driven revisions to current instream flow recommendations for Devils River. As part of this research program, researchers used an infrared camera mounted to an UAV to acquire stream surface temperature, identify spring discharge, and characterize stream and spring water mixing (Abolt and others, 2018). Additionally, in-stream stage and temperature measurements were acquired to quantify spring inputs and identify seasonal trends in thermal regime affecting target species (Caldwell and others, 2020).

We defined the pool mesohabitat areas upstream of Dolan Falls as “upper basin” and the area downstream of the falls as “lower basin.” The pool of the upper basin includes areas with dense submerged variable-leaf watermilfoil (*Myriophyllum heterophyllum*) and emergent American water willow (*Justicia americana*), which pose challenges for lidar and sonar. Because of access issues to the watershed (98% is privately owned), in-situ measurements were limited and clustered by The Nature Conservancy’s Dolan Falls Preserve Area (29°53' N, 100°59' W). Figure 3-3 illustrates the entire study area and exemplifies upper and lower basins, the location of in-situ measurements (L1-11), GNSS base stations, and Dolan Falls.

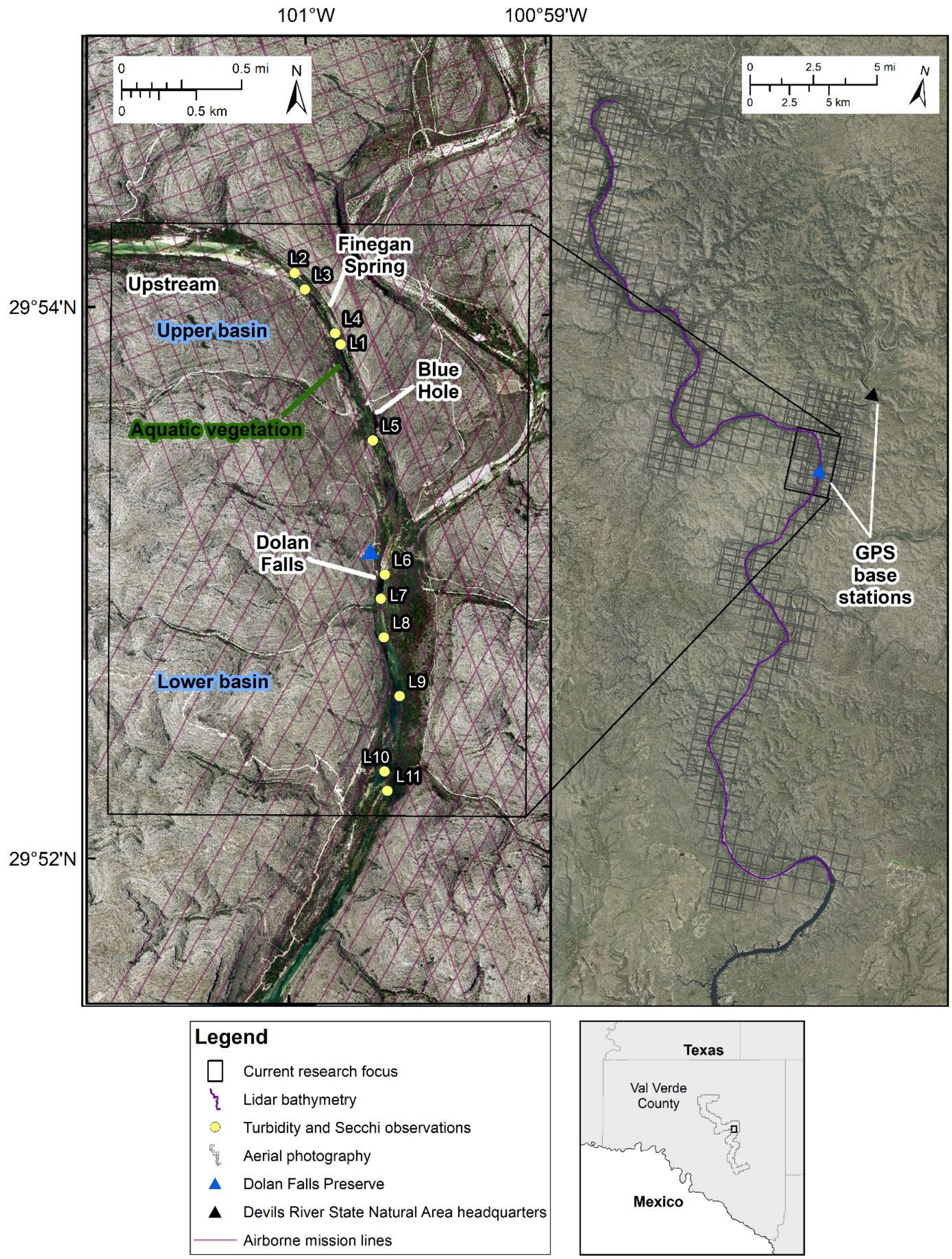

Figure 3-3. Survey area and the Devils River watershed by Dolan Falls. *In situ* locations are marked through L1-11, and purple lines indicate the airborne survey paths.

3.2.2. Data Acquisition

In March 2018, a Cessna 206 survey aircraft, owned and operated by the Texas Department of Transportation (TxDOT), spent approximately 30 hours over the survey site (Figures 3-4 a, b). The airborne survey consisted of 189 flight lines and covered an approximate area of 220 km^2. The NIR sensor produced an average point density of 10–12 per m^2 with an approximate flight speed of 120 knots. However, we computed an average ground-sampling density of 50 points per square meter, which was higher than usual due to flight lines overlapping each other, especially at river bend locations (previous section, Figure 3-3).

To comply with quality control procedures for ALB surveys (Saylam, Hupp, Averett, and others, 2018) and to build a continuous map of the river bottom, we acquired GNSS, sonar, and GPR data at pools upstream and downstream of Dolan Falls. Ground-truthing of river water surface and bottom elevations were completed using a multi-channel Trimble R8 GNSS global navigation satellite system (GNSS) receiver mounted to a variable height pole. We measured 29 water surface elevations and 487 bottom elevations and refined these static GNSS measurements differentially for higher accuracy. It was essential to measure the bottom elevations, particularly at locations with dense vegetation, to assist in building a seamless rasterized map. TIN patches were created (h_L) using all available water-bottom lidar returns (Classes 7 and 10) and were compared to GNSS-derived (h_g) surface (W_S) and bottom (W_B) elevations.

We used NovAtel GrafNav v8.4 application to improve the static positional information acquired by Chiroptera-I's integrated GNSS receiver. Initially, we refined the positions using only Texas Del Rio (TXDR), a continuously operating reference system (CORS) station in Del Rio, Texas (29°21'51" N, 100°53'58" W). However, because of the extended baseline (55 km) and to better comply with quality control procedures, we set up additional base stations (multi-channel Trimble R9 GNSS) closer to the survey location (CampTPWD: 29°56'27" N, 100°58'12" W; CampTNC: 29°53'7" N, 100°59'41" W). Because these local base stations were initially "floating" their locations were refined precisely using the Online Positioning User Service (OPUS) to be relative to the TXDR-CORS base station (orthometric height: 395.38 m versus 395.33 m, RMSE = 10 cm).

To augment spatial coverage of the bathymetric survey, we installed a consumer-grade Garmin EchoMap 74dv to a kayak and coupled it with a submerged GoPro HERO5 camera (Figure 3-5). Using the GoPro camera, we were able to distinguish bottom properties, wherever required. The sonar encompasses a dual-frequency transducer (200/50 kHz) with an effective range of 36 cm to 700 m in freshwater bodies, and the unit samples positional information at a frequency of 5 Hz (Figure 3-6). Prior to fieldwork, we evaluated the unit in a pool at Applied Research Laboratories (ARL), The University of Texas at Austin (30°23'05" N, 97°43'34" W). The equipment measured depths with a range bias of 2.7 cm (standard deviation to the mean) at a depth of 11.8 m. Because the sonar beam diameter is much narrower than the lidar pulse, we expected deeper measurement capability in areas with aquatic vegetation. For example, a green wavelength lidar pulse (4.75 mrad beam divergence, full angle) emitted at a range of 450 m will cover an area of 213 cm in diameter on the water surface, expanding to an area of approximately 411 cm in diameter at 5 m depth. However, the sonar transducer will generate a much smaller footprint of 15 cm in diameter at the same depth, increasing the likelihood of penetration through submerged vegetation (Westfeld and others, 2016).

For GPR surveys, we used a GSSI SIR-3000, coupled with a GSSI 200 MHz shielded monostatic antenna. The main purpose of using the GPR was to investigate the feasibility of EM waves passing through submerged aquatic vegetation and detecting the river bottom (Figure 3-7). The propagation of the GPR waves through different layers of materials or surfaces creates varying and distinctive resistivity in the frequency. The phase velocity (v) and attenuation constant (α) are the main parameters describing the EM wave propagation, and they both depend on the dielectric and conductivity (σ) properties of the medium. In theory, the lower the propagation (the higher the permittivity), the less the lateral dimension of the medium is resolved (Mancuso, 2012; Milsom and Eriksen, 2011). Because water is highly polarizable and has a higher degree of permittivity (ε), it absorbs EM waves quicker as the antenna frequency increases. Freshwater permittivity is commonly referenced as 80, attenuation constant (α) as 0.1 dB/m and conductivity (σ) as 0.5 mS/cm (Carrick Utsi, 2017; Sambuelli and Bava, 2012). EM velocities are referenced in cm/ns and frequencies in MHz; therefore, assuming a 200-MHz antenna and a water temperature of 20° Celsius, wavelength (λ) is 16.77 m and propagates (v) at 3.3 cm/ns. For optimum results, the GPR antenna should have no interference and should be clear of signal-blocking obstructions. Therefore, we mounted the instrument to a boat with a deflated rubber bottom, accounted for 1 cm offset from the water surface, and the operator did not carry any electronics onboard. We connected an external multi-channel Trimble R8 GNSS receiver to the GPR and synchronized the time between the instruments for all surveys. (Figure 3-8). We recorded 148 survey lines. Because GPR radio waves were continuous, we were able to extract returns at every 10 cm of forward motion and compared each measurement to the nearest lidar-derived TIN patch. Additional in-situ measurements, such as moisture and salinity content, are suggested in the presence of mixed materials (S. Robertson and others, 2019), but they are not considered critical in freshwater reservoirs such as the Devils Rivers watershed.

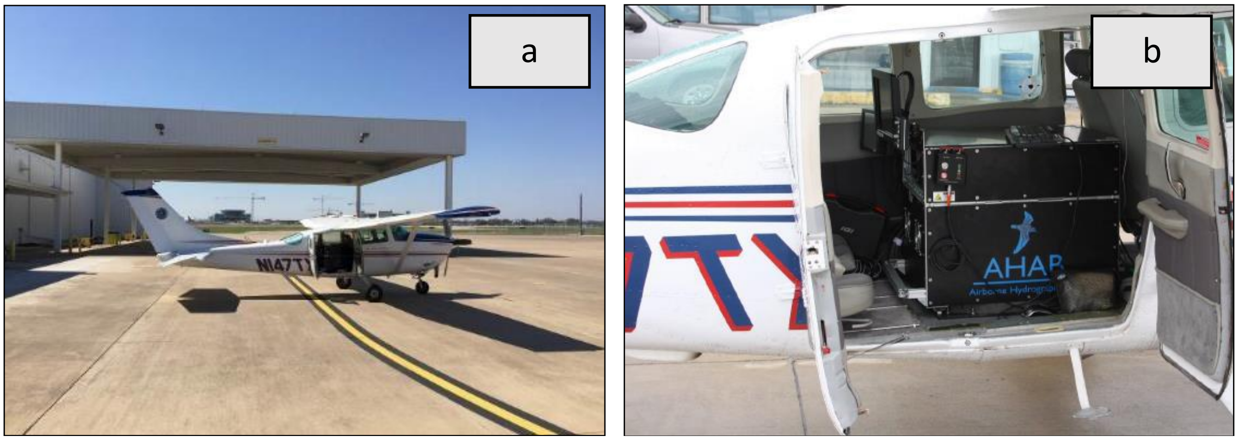

Figures 3-4. (a) TxDOT-owned Cessna 206 (aircraft registration N147TX) and (b) Leica AHAB Chiroptera-I installation.

Figure 3-5. River bottom captured with a submerged GoPro HERO5 camera.

Figure 3-6. Surveying stream depth using a dual-beam Garmin echosounder.


Figure 3-7. Dense submerged aquatic habitat in the upper basin.


Figure 3-8. GSSI SIR-3000 GPR mounted to an inflatable boat.

3.2.3. Optical Properties of Water

Light beams interact with constituents while traveling through the water column. Foremost, water in its purest form exhibits a complex absorption spectrum, and a significant amount of scattering occurs due to refractive index fluctuations (Jonasz and Fournier, 2007). The two fundamental IOPs of water are the absorption coefficient and the volume scattering function. Apparent optical properties (AOPs) depend on the medium and the geometric (directional) structure of the ambient light field. According to Smith and Baker (Smith and Baker, 1981), AOPs are particularly important when considering the penetration of radiant energy to varying depths. ALB uses green wavelengths (515–532 nm) because of the least water absorption (attenuation) (Figure 3-9).

In shallow waters and localized surveys, limnologists typically use conventional survey methods and refer to Secchi disk depth (Z_{sd}) to quantify water-column transparency. The diffuse-attenuation coefficient K_d (z, λ) is an important optical property. It defines the logarithmic depth derivative of ambient irradiance $E_d(z, \lambda)$, which comprises photons heading in downward and upward directions (Lee, 2005). K_d (or K_{PAR}) depends on the directional structure of the ambient light field and is classified as an AOP. It is determined in the photosynthetically active range of 400–700 nm.

Freshwater contains certain quantities of dissolved organic matter (DOM) and decayed vegetation that are responsible for temporal and spatial variability of optical properties. In the water column, these materials are the major cause of light and radio-wave absorption and scattering. Although there have been 21st-century advances in optical electronic instruments using tungsten light sources to measure water transparency and calculate K_d a popular, simple method is to use a 30-cm-diameter Secchi disk (Kitchener and others, 2017). The Secchi-disk depth (Z_{sd}, m) represents the maximum depth at which the disk is no longer observed as it is progressively lowered into a water column. Using a Secchi disk to determine K_d is simple: $K_d = \alpha / Z_{sd}$. However, this measurement is generalized and may not be accurate for large and multiple pools. (Lee and others (2005) defined the relationship between Z_{sd} and K_d and reported that α ranges between ~1.3 and 2.0, as observed in studies for over 90 years (Gallegos and others, 2011; Poole and Atkins, 1929). In this study, we assumed $\alpha = 1.6$ and $K_d < 1.5$ to calculate the theoretical depth measurability (D_{max}) of the Chiroptera-I as specified by the manufacturer (Leica AHAB, 2021).

A turbidimeter measures the loss of Intensity In the transmitted light resulting from scattering by DOM, which vary in shape, color, and reflectance and range from < 1.0 to 10s of micrometers in size. Researchers observe and report turbidity either in nephelometric turbidity units (NTU) or in formazin nephelometric units (FNU). In this study, we used a HACH 2100Q portable turbidimeter for observations in NTU, and the instrument calibration indicated compliance with the manufacturer recommendation (Supplementary Table S3-1). We sampled the river at an average depth of 1 m at 11 locations and replicated the practice three times in each location to comply with U.S. EPA 180.1 (O'Dell, 1993). We observed an average turbidity of 2.76 NTU, and the standard deviation of all readings was 0.42 NTU, which indicates suitability for lidar bathymetry (Saylam, Brown, and others, 2017).

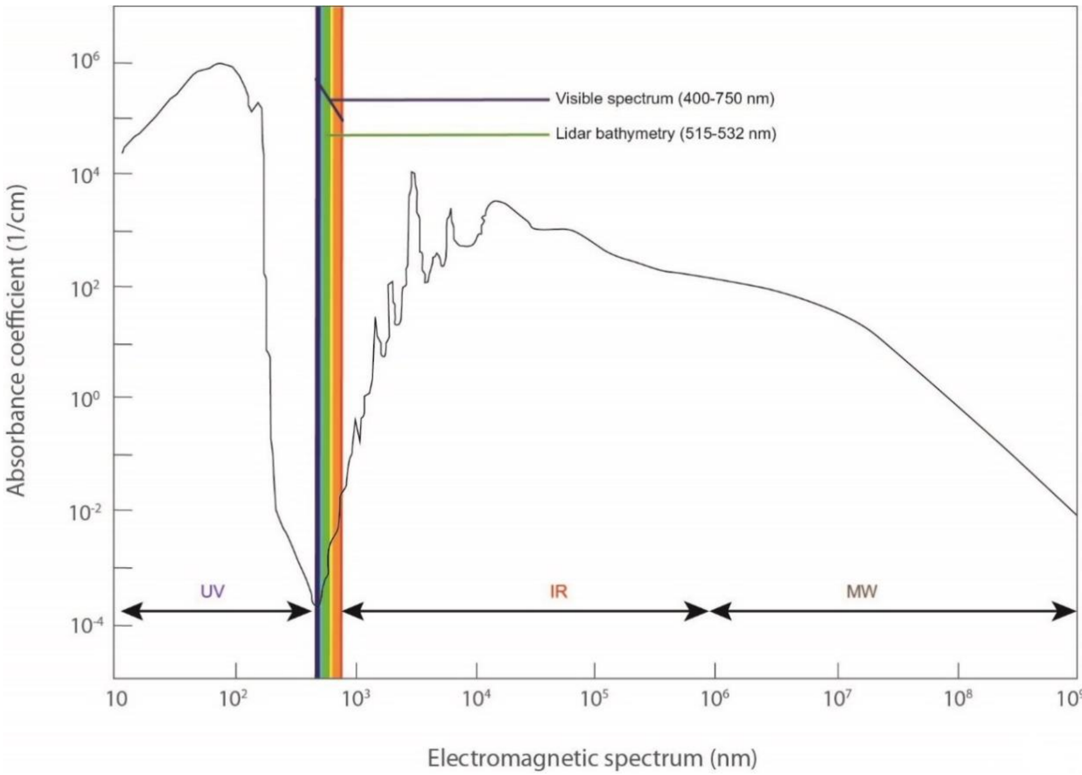

Figure 3-9. Graph indicating the minimal absorption coefficient in the 200–800 nm spectral region, attained in pure freshwater (modified after Beć and Huck [40]).

3.2.4. Data Analysis

Because most NIR beams get absorbed at the surface or in the immediate water column, only a few backscattering signals return to the receiver. Using a receiver with a high signal-to-noise error ratio, it is possible to detect and sort the returns and generate a representation of the water surface. The Chiroptera-I's manufacturer-supplied software, Lidar Survey Suite (LSS), outputs return to separate classes with respective wavelength type, shape, and amplitude. Class 0 includes returns from both wavelengths, and Class 5 stores solely green wavelengths. A previous study reported a robust goodness-of-fit between these classes (R^2 = 0.99) in the transparent and deep waters of the lower Colorado River Saylam, Hupp, and others*,* (2017). Conversely, in Laguna Madre (Saylam, Hupp, Averett, and others*,* 2018), which is a large, shallow lagoon in southern Texas, the goodness-of-fit between these classes declined (R^2 = 0.32) due to increased amounts of turbidity (2–10 NTU) and poor transparency (K_d > 2). Therefore, variance in environmental conditions represents one of the great challenges of ALB surveys, requiring frequent and localized in-situ measurements to predict measuring-depth performance.

As for water-bottom detection, LSS outputs two separate classes of green-wavelength return: regular (Class 7) and enhanced (Class 10). The latter output algorithm filters out weaker signals and

selects the returns omitted by the Class 7 algorithm that are recorded below an optimum threshold. In the Colorado River study, results revealed depth detection improved by an average of 0.81 m (9.2%) at less turbid conditions (0.4 NTU) and locations where Class 7 returns were extinguished.
Lidar point-cloud data were output in LAS v1.2 format, and we converted water-surface and water-bottom classes into text format (xyz) for analysis in MATLAB v17. LSS requires amplitude and backscatter thresholds to be optimized for accurate bathymetric datasets, especially at survey locations where environmental conditions are dynamic. To comply with quality assurance procedures, the field staff investigated the local conditions carefully and prepared supplemental information (e.g. pictures, field notes) to assist data analysts.

Point-to-point correspondence or comparison with lidar point-cloud datasets (Habib, 2009) or any other geospatial vector datasets is not assumed; therefore, we used the Delaunay triangulation algorithm (B Delaunay, 1932) to create surface patches of triangulated irregular networks (TIN) (Surface 1, Figure 3-10). In theory, the algorithm maximizes the minimum angles of triangles in the triangulation process by defining an empty circumcircle (P. Chew, 1989). Every TIN patch represented an averaged elevation computed from the returns that formed a triangle (Surface 2, Figure 3-10). We compared the TIN patches to sonar, GNSS, and GPR-derived elevations that registered proximity ($dS1_i$) of 1.0 m and excluded the returns at slopes (α) steeper than 45°. The vertical threshold (h) was set at 0.5 m to prevent the algorithm from picking up vegetation or other highly sloped surface returns. The selection of distance and angle thresholds were based on the percentage of matches algorithm was generating, and we evaluated different thresholds with evaluating coefficient of determination (R^2) and RMSE values. The outliers were not removed from the analysis, kept for validation, such as in the lower basin, Doolan Falls generated matches outside the limits at deeper locations, and they were included in the analysis.

All measurement elevations in this study were processed with reference to North American Vertical Datum 1988 (NAVD 88) and they were converted to North American Datum 1983 (NAD83-2011) with epoch 2010.00 for horizontal referencing. Datasets were projected to Universal Transverse Mercator (UTM) 14N coordinate system in units of meters. In the preliminary analysis stage, datasets were kept in ellipsoidal heights, and this is a recommended quality control procedure for a reason: the geographic positioning information acquired by most survey equipment (e.g., airborne lidar, sonar, GPR) requires conversions of ellipsoidal heights to real-world elevations (orthometric height), and the interpolation process can carry errors in extended baselines—particularly in river and shoreline surveys. It is considered good practice to transform elevations following the completion of vector data alterations (e.g., data cleaning, reclassifications) because most lidar and remote sensing projects require rasterized products in orthometric elevations. An average geoid height of −22.87 m was calculated using the GEOID12B model near Dolan Falls.

For GPR data analysis, it is possible to calculate the velocity (v) of an EM wave (C_{em}) in an insulator by factoring the permittivity (ε_w) into the speed of light (Equation (3-1)). The wavelength (λ) in any medium equals the velocity divided by the EM frequency (Equation (3-2)). We computed the *attenuation* coefficient (α) using the observed water-column conductivity (σ) and the calculated permittivity (Equation (3-3)). We adjusted the EM propagation in the water column by refining the permittivity value observed in situ water temperature (T) using Equation (3-4) as defined by Klein and Swift (Klein and Swift, 1977). Furthermore, we calibrated the GPR using point-source reflectors that produce "hyperbolas" in the data, which are caused by the cone shape of the antenna's radiation pattern. We fitted the hyperbolas with shapes of known velocity to the hyperbolas recorded at Devils River. Therefore, we were able to confirm wave velocities and compute the correct propagation through the water column (Serkan and Borecky, 2015).

Throughout Devils River, water temperature was recorded using the sonar transducer's thermometer, and we computed the median temperature to be 24.55° Celsius. Using an Aqua-TROLL 200 Data Logger, we measured the median conductivity at σ = 0.44 mS/cm and computed the attenuation coefficient at α = 0.08 dB/m (Equation (3-3)). The salinity was measured at ~300 mg/L (0.3 ppt), which was normal levels for typical freshwater rivers (<0.5 ppt). Because the river depth, discharge, and temperature vary, we expected to observe fluctuations in permittivity.

$$\nu = C_{em}/\sqrt{\varepsilon_w} \qquad \text{(Equation 3-1)}$$

$$\lambda = C_{em}/(f\sqrt{\varepsilon_w}) \qquad \text{(Equation 3-2)}$$

$$\alpha = 1.6\,\sigma/\sqrt{\varepsilon_w} \qquad \text{(Equation 3-3)}$$

$$\varepsilon_w T = 88.045 - 0.4147\,T + 6.295 \times 10^{-4} T^2 + 1.075 \times 10^{-5} T^3 \qquad \text{(Equation 3-4)}$$

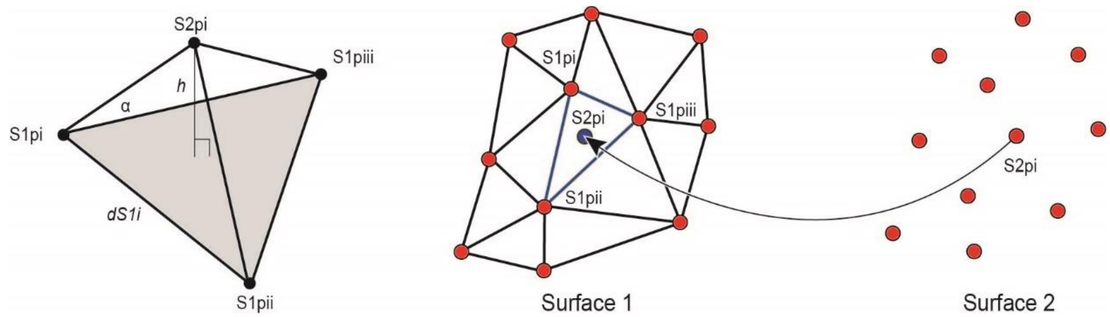

Figure 3-10. Conceptual representation of lidar, sonar, GNSS, and GPR-derived elevation comparisons using Delaunay triangulation and a point-to-patch relationship.

3.3. Results

3.3.1. Water Transparency and Turbidity

The river bottom was visible at five in-situ locations. Hence, we expected the lidar beams to measure the water bottom without complications. A quadratic relationship (Figure 3-11) was observed, and a high degree of coefficient of determination was computed between K_d and D_{max} ($R^2 = 0.99$, RMSE = 0.02 m). At other locations, Z_{sd} varied from 1.4 m to 2.9 m (Figures 3-12 a, b). We expected the lidar beams to attenuate rapidly in the less transparent waters. Table 3-1 illustrates the Z_{sd} and turbidity observations at all locations. AHAB claims that the Chiroptera-I can measure depths to 1.5 times the K_d, indicating the D_{max} capability (AHAB, 2020). To confirm this specification, we computed the theoretical $D_{max} = 2.72$ m by Dolan Falls (L6), where sonar readings indicated a depth of 5.77 m and lidar beams were attenuated at a depth of 2.65 m.

Table 3-1. Secchi-disk and turbidity measurements at Devils River. Areas with dense aquatic vegetation were excluded. VB indicates a visible river bottom.

In situ location	Latitude (N)	Longitude (W)	Secchi depth (Z_{sd}, m)	Sonar depth (m)	Turbidity (NTU)	K_d (m^{-1})	D_{max} (m)
L1	29°53'52"	100°59'50"	2.1	2.2	1.85	0.76	1.97
L2	29°54'08"	101°00'02"	1.4	2.0	3.35	1.14	1.31
L3	29°54'04"	100°59'59"	VB	1.1	2.86	NA	NA
L4	29°53'55"	100°59'51"	1.8	2.4	1.92	0.89	1.69
L5	29°53'32"	100°59'41"	VB	1.1	1.69	NA	NA
L6	29°53'03"	100°59'38"	2.9	5.8	1.31	0.55	2.72
L7	29°52'58"	100°59'38"	VB	1.0	1.46	NA	NA
L8	29°52'49"	100°59'38"	VB	1.8	6.14	NA	NA
L9	29°52'36"	100°59'33"	2.0	3.3	2.79	0.80	1.88

L10	29°52'20"	100°59'37"	1.6	2.4	2.86	1.00	1.50
L11	29°52'16"	100°59'36"	VB	1.5	4.13	NA	NA

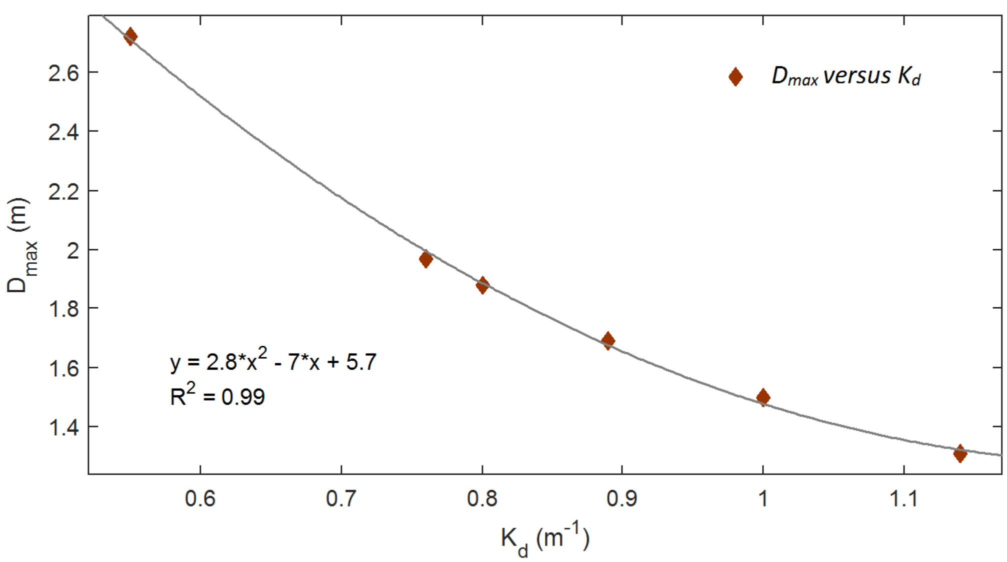

Figure 3-11. Quadratic relationship between K_d (m^{-1}) and D_{max} (m) in Devils River, indicating the lessening D_{max} in parallel to the escalation in K_d.

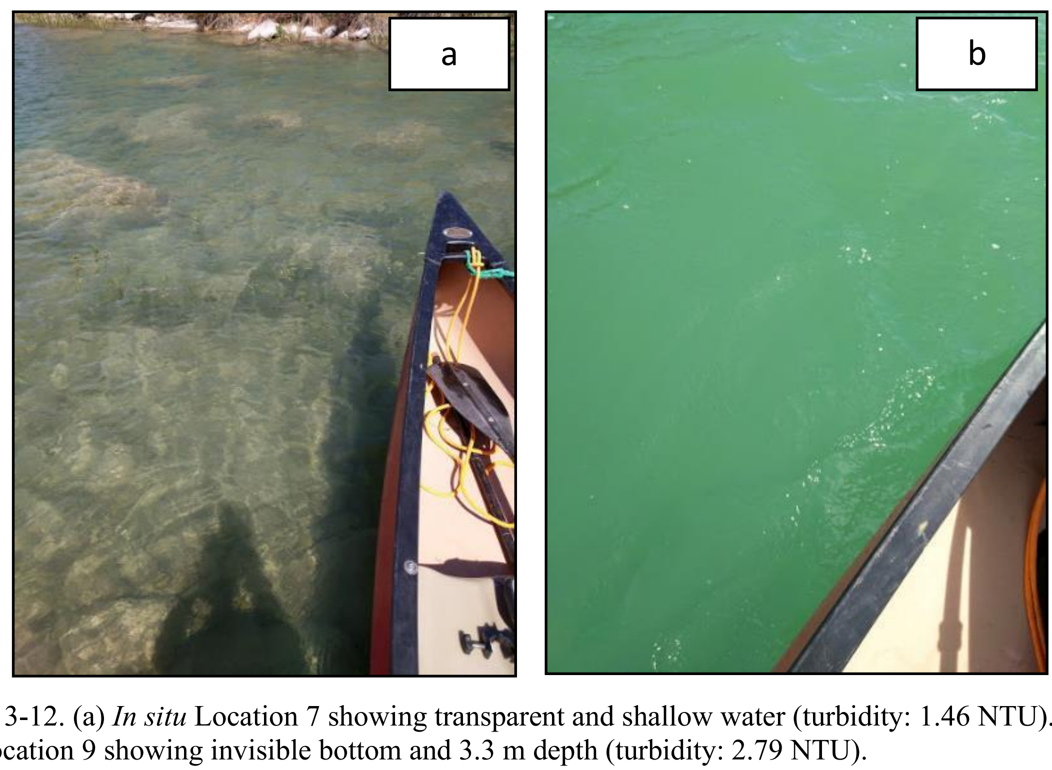

Figure 3-12. (a) *In situ* Location 7 showing transparent and shallow water (turbidity: 1.46 NTU). (b) *In situ* Location 9 showing invisible bottom and 3.3 m depth (turbidity: 2.79 NTU).

3.3.2. Water-Surface Detection Analysis

It is challenging to detect water surfaces accurately with airborne lidar, especially in riverine environments. In the Devils River project, we confirmed the surface representation with point-cloud datasets (Class 0 and 5). Because the Chiroptera-I emits NIR beams faster and with a narrower pulse width, fewer Class 0 returns are registered. It is expected that most NIR beams are absorbed by the immediate water surface and only a few reaches back to the receiver, especially in choppier and turbid waters.

In this analysis, we used Class 5 (green wavelength only) returns as the reference points to compute the point-to-patch relationship. TIN patches were formed by Class 0 returns (NIR and green wavelength), and each patch was compared to the nearest Class 5 return by using the least-squares method. Computations revealed that a higher degree of correspondence was evident in the lower basin due to less aquatic vegetation (Table 3-2). Furthermore, findings indicated that Class 0 returns characterized the water-surface elevations slightly higher than Class 5 returns (Supplementary Figure S3-1). Figure 3-13 illustrates the "noisy" nature of Class 5 returns compared to Class 0 output (Standard deviation = 10 cm versus 3 cm) in the lower basin, where NIR beams reflected off and penetrated the water column up to 0.19 m of median surface representation.

Table 3-2. Class 0 (CL0)-derived TIN patch elevations versus Class 5 (CL5) returns, indicating the surface representation. In the upper basin, CL5 registered fewer returns due to dense aquatic habitat.

Basin	CL0/CL5 Sample ratio	Number of Patches	Sample Range (m)	Mean Elevation Difference (m)	Standard Deviation (m)
Upper	1:37	32339	1.87	0.085	0.16
Lower	1:11	100063	1.02	0.094	0.10

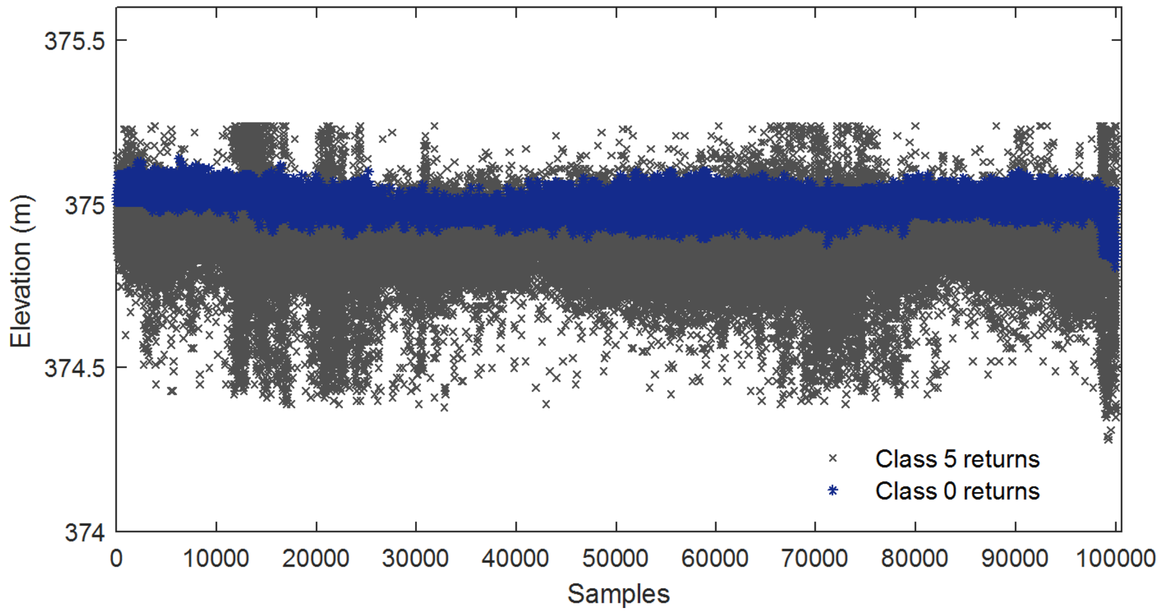

Figure 3-13. Representation of Class 0 (NIR + green) versus Class 5 (green wavelength only) returns, indicating the water-surface detection challenges in inland pools. Note the "noisy" characteristic of Class 5 returns; indicating the median surface is 9 cm lower than Class 0 returns.

3.3.3. GNSS Quality Control

We conducted eight missions to complete airborne data acquisition. In four of these, we merged TXDR and CampTPWD base-station solutions using GrafNav application to achieve a closer baseline (mean = 40.2 km) and a more precise differential solution. The application can support up to 32 base stations. An average of 99.34% quality-one (Q1) resolution was achieved for all missions (Supplementary Table S3-2). Positional dilution of precision (PDOP), which specifies the error propagation and measurement precision of satellite geometry (Spilker Jr. and others, 1996), averaged at 1.61 out of 10 scale (1-best, 10-worst). Further, we conducted a forward/reverse separation analysis to estimate the robustness of solutions and achieved RMSE of 1 cm for horizontal separation (easting and northing) and 5 cm for vertical separation.

Primarily, the CampTNC base station was used to differentially correct the static in-situ measurements. We analyzed the expected bias applicable to horizontal and vertical accuracies by computing the median standard bias and outliers in the differential solutions for 26–27 June 2019 (Supplementary Materials, Figure S3-2). Findings revealed a comparable horizontal and vertical bias for both days (2.5 cm and 4.1 cm). The probability plot indicates normal distribution. However, vertical solution has a higher probability to include outliers that are greater than 5 cm for both days (Supplementary Figure S3-3).

3.3.4. Lidar Bathymetry versus GNSS Measurements

ALB measurements revealed a robust coefficient of determination ($R^2 = 0.86$) to GNSS-derived river bottom elevations; however, only a fraction of measurements (21%) was compared due to aquatic vegetation blocking the lidar beams. Overall, GNSS measured 0.03 m deeper than lidar bathymetry (Table 3-3), due to circumference discrepancies between the measuring rod and the lidar beam at the water bottom. We measured the vertical bias at 0.12 m (RMSE). The q-q plot illustrates a normal distribution, and p=0.027 indicates strong evidence to reject the null hypothesis (< 5%), meaning the result was statistically significant, and the boxplot illustrated a few outliers in depths greater than ~ 1.5 m (Figure 3-14 a, b). In our computations, GNSS-derived elevations indicated a higher probability of deeper measurement in the shallower areas of the river compared to lidar TIN patch elevations (Supplementary Figure S3-4).

Table 3-3. Lidar-derived (h_L) water-bottom (W_B) patch elevations compared to GNSS measurements (h_g).

Surface	Samples	Sample range (m)	Mean difference (d, m) ($d_Z = h_L - h_g$)	RMSE (m)	*p* (%)
Bottom	102/487	0.82	−0.03	0.12	2.7

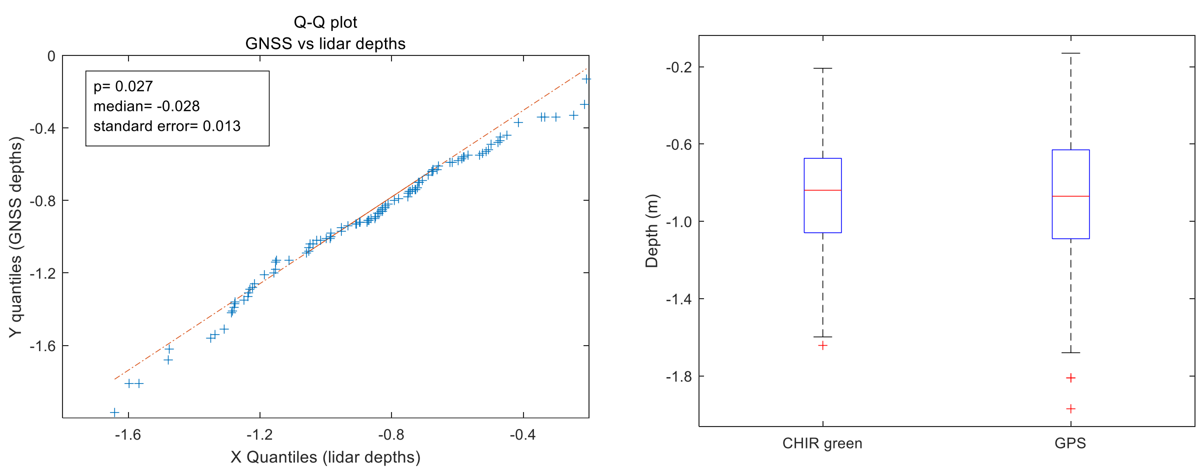

Figures 3-14 (a, b). The q-q plot illustrates a normal distribution (p=0.027), with slight skewing in depths greater than 1.2m. The boxplots present the median values and the quartiles, with a few outlier measurements in the greater depths.

3.3.5. Lidar Bathymetry versus Sonar

We processed a total of 13,720 sonar measurements in the upper and lower basins, which came out to a mean depth of 1.26 m and 2.0 m, respectively. Sonar measured the shallowest depth as 36 cm and the deepest depth as 7.87 m at the plunge pool by Dolan Falls. The density plot shows the distribution of all sonar measurements, revealing the distinctive aquatic and geomorphologic characteristics of each basin and the significant effects caused by Dolan Falls and other environmental factors (Supplementary Figure S3-5).

We compared sonar measurements to lidar-derived (W_B) TIN patch elevations using the least-squares algorithm. The computations matched 7240 sonar measurements (52.77%) to TIN patches that were within the defined thresholds (refer to Section 2.4). In the upper pool, results indicated a strong coefficient of determination (R^2 = 0.78, standard deviation =0.27 m, and p=0.007) due to its more uniform and shallower pool structure. Mean elevation difference computed between the datasets was slightly higher in the upper basin due to the presence of aquatic vegetation and occasional boulders in the river bottom (11 cm versus 9 cm), as visualized in the GoPro camera images. In the lower basin, a lesser determination of coefficient was observed (R^2 = 0.72), standard deviation =0.39 cm and p=0.016). Nevertheless, the mean elevation difference was lower, and sample range was higher due to fewer amounts of aquatic vegetation existence and the deep area by the Dolan Falls (Table 3-4, Figures 3-15 and 3-16). The plunge pool by Dolan Falls was visible in the regression and normality plots, where lidar returns matched with sonar recordings at depths to ~3 m, which was close to the theoretical maximum depth limitation computed (2.72 m).

Table 3-4. Lidar-derived TIN patch elevations versus sonar measurements for the upper and lower basins by Dolan Falls.

Basin	Degrees of Freedom	Sample Range (m)	Mean Elevation Difference (cm)	RMSE (m)	R^2	p (%)
Upper	4910	2.75	11	0.27	0.78	0.7
Lower	2330	5.54	9	0.41	0.72	1.6

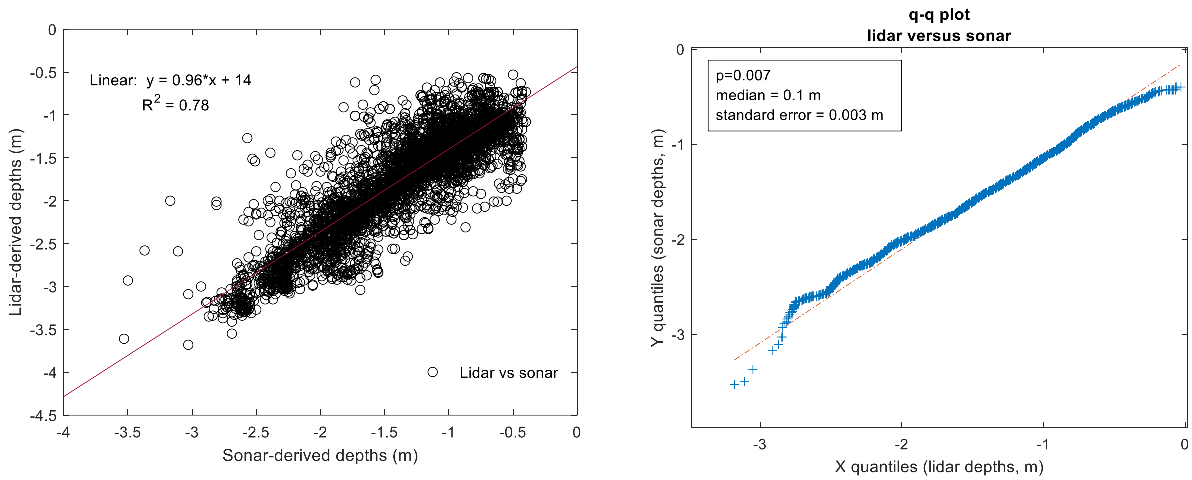

Figures 3-15 (a, b). In the upper pool, the regression plot generated a strong agreement between lidar and sonar measurements at depths to ~2.5 m (R^2=0.78). The q-q plot indicated a normal distribution with a low standard error (0.003 m) and p-value (0.007), which indicates a very strong correspondence and a statistically significant correspondence.

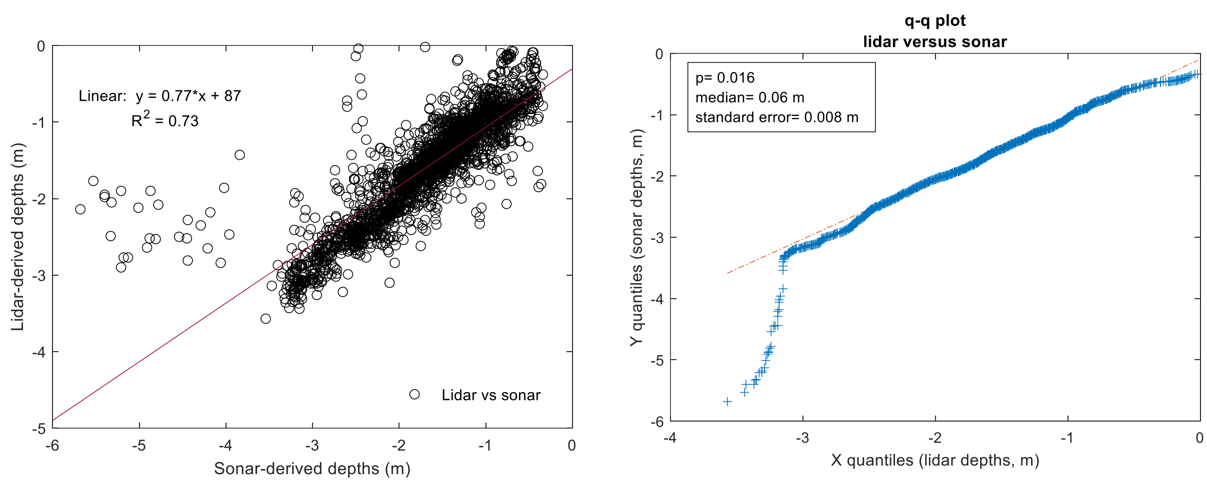

Figure 3-16 (a, b). In the lower pool, the regression plot illustrated a lesser level of agreement between lidar and sonar measurements due to the plunge pool area by Dolan Falls, where lidar returns did not penetrate to depths greater than ~3 m (R^2=0.73). The q-q normality plot indicated a similar result, where the skewness from normality occurred past ~3 m. However, the standard error (0.006 m) and the p-value (0.016) was small and indicated the significance for the correspondence.

3.3.6. Ground Penetrating Radar

Due to dense submerged vegetation and other environmental challenges, the least-squares algorithm did not match 57% of lidar measurements (634 samples out of 1113) with a GPR measurement (refer to Section 2.4), using the threshold values. Preliminary regression results revealed an average depth bias of 5 cm and RMSE of 16 cm using the literature suggested fresh-water EM propagation rate of v = 3.3 cm/ns. Signal discontinuity caused by temperature and permittivity variability was evident, particularly in the deeper areas. Of all GPR measurements taken, the deepest was 3.11 m, which confirms the depth limitations of using a 200-MHz antenna (Milsom and Eriksen, 2011). Using the in-situ measured values, we adjusted the water-column permittivity (ε), and as a result, EM waves propagated quicker in the water column (v = 3.38–3.7 cm/ns), especially in the deeper parts of the river, and generated an improved fit to lidar measurements. The probability of a normal distribution was similar (p=0.09 and 0.1) and agreement between the datasets was statistically significant (Table 3-5, Figure 3-17). We plotted the regression, and the coefficient of determination did not change (R^2=0.92); however, the function (f(x)) has improved, indicating a stronger agreement (Figure 3-18 a). In addition, the q-q normality plot illustrated a low standard error (0.01 m) and a strong indication of a normal distribution (p=0.033) and a statistically significant agreement (Figure 3-18 b).

As an example, and for visual confirmation, GPR measurements at survey line #117 were output and compared to lidar bathymetry after the propagation adjustments were completed. It was evident that lidar and GPR measurements matched at locations with no vegetation or less vegetation. On a normal "B-scan" (Figure 3-19), the horizontal axis represents distance, and the vertical scale is in two-way reflection time, which we converted to depth. As expected, submerged vegetation blocked lidar beams in the water column, and EM waves propagated through the medium, indicating the bedrock with distinctive amplitude in the waveform.

Table 3-5. GPR measurements compared to lidar TIN patches, indicating the mean and maximum depth discrepancies with initial and final EM velocity coefficients.

EM velocity (cm/ns)	Permittivity (ε)	Median Depth Difference (m)	Sample Range (m)	Mean Depth lidar/GPR (m)	RMSE (m)	R^2	p (%)
3.3	80	0.05	2.44	-1.99/-1.77	0.16	0.92	0.9
3.7	78.4	0.05	2.73	-1.99/-1.99	0.18	0.92	1

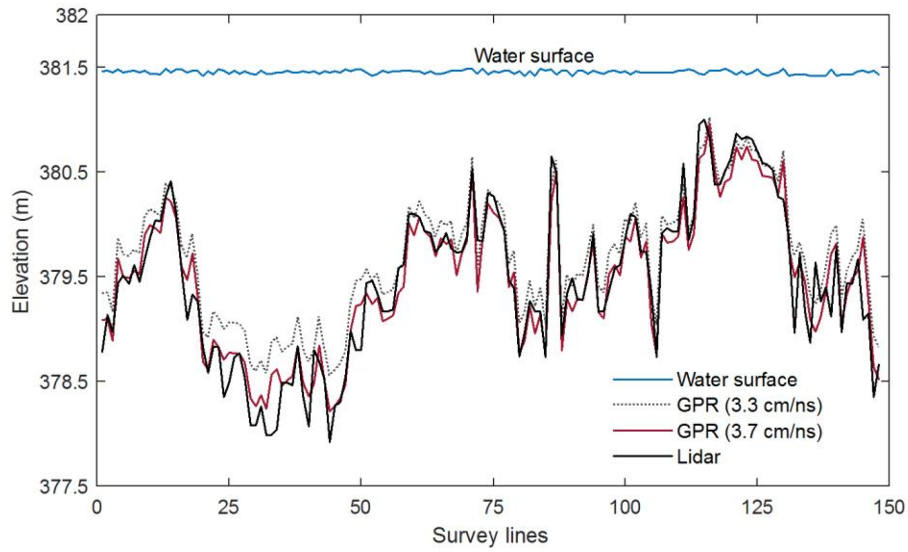

Figure 3-17. GPR measurements compared to lidar TIN surface patches using the least-squares method.

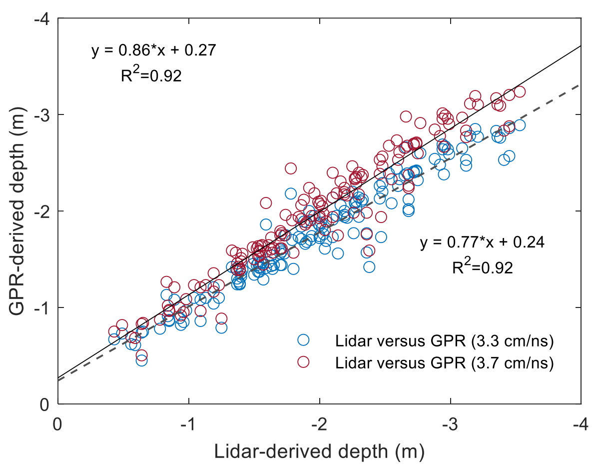

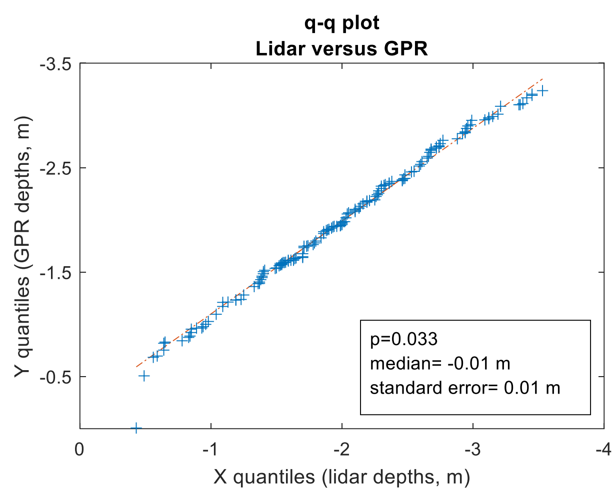

Figure 3-18 (a, b). Solid linear-fit line revealing an improved regression function between lidar and GPR-derived depths (3.3 cm/ns versus 3.7 cm/ns) using the adjusted EM propagation. The q-q plot illustrates the normal distribution of the lidar and GPR measurements matched with each other.

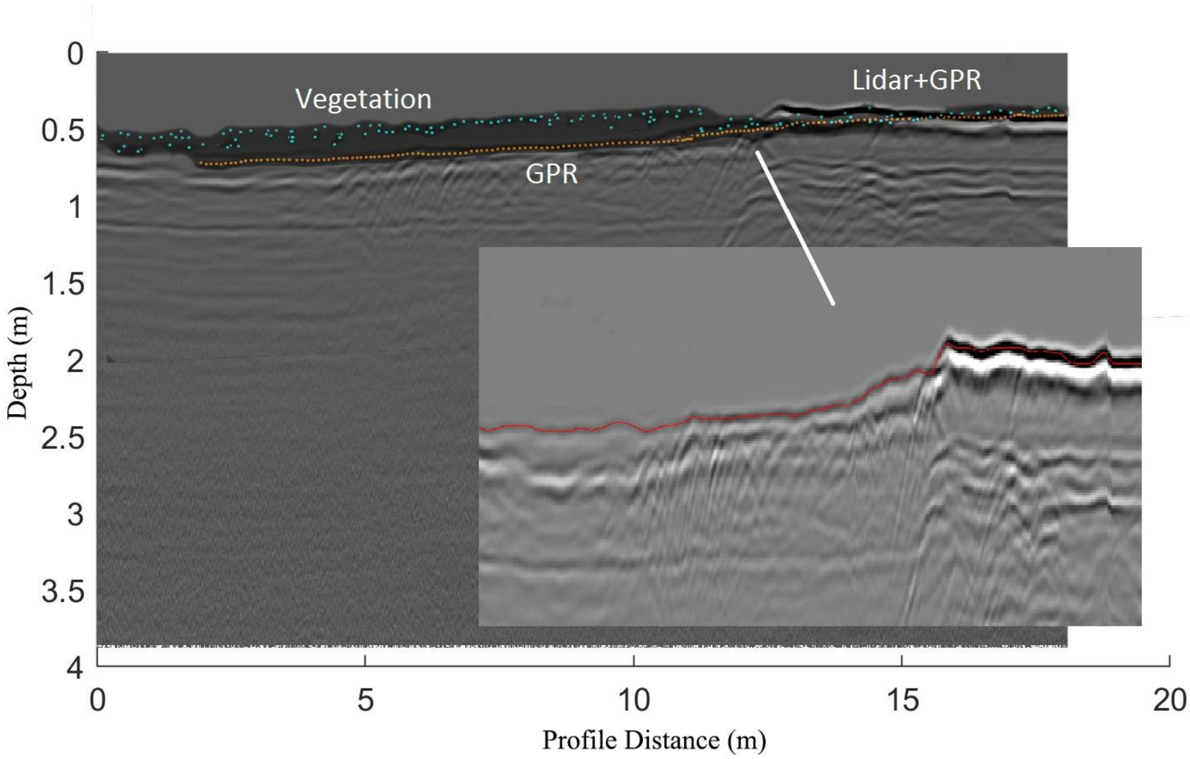

Figure 3-19. GPR EM “B-scan” representing survey line #117, after the propagation speed was adjusted using the in-situ measurements. Lidar pulses (blue) were blocked by submerged vegetation, and GPR wavelengths (orange) penetrated to measure the riverbed.

3.4. Discussion

In this study, we confirmed the vertical bias of remotely sensed measurements to one another before generating a complete stream bathymetric map of Devils River by the Dolan Falls Preserve area. In inland pools, especially in fluvial karst environments, conditions can be challenging and typically have a dynamic nature. The results depicted in this study revealed that mapping with airborne lidar technology is accurate and comprehensive; however, complementary surveys and in-situ measurements are required to validate potential biases and to complete bottom mapping.

In the upper basin by Dolan Falls, aquatic vegetation limited airborne lidar and sonar beams from measuring depths; therefore, we applied a novel approach and conducted GPR surveys to increase the likelihood of measuring the river bedrock. GPR data acquisition and analysis was the decisive step in this study due to uncertainties surrounding the vertical biases and completeness of data measured in such survey locations. Therefore, initial efforts (Figures 3-20 a–c) in this study confirmed the mean vertical bias of lidar bathymetry against post-processed GNSS measurements (11 cm RMSE) and dual-beam sonar measurements (27 cm RMSE). Our final efforts validated the GPR measurements with comparison to the TIN surface patches generated from lidar vector datasets (~17 cm RMSE). Overall, the mean vertical difference was computed less than 10 cm compared to all datasets. Figure 3-20 d illustrates the combined depth map of the upper basin by Dolan Falls where aquatic vegetation interfered with lidar and sonar measurements.

Using GPR as a novel depth measuring method, our research efforts primarily focused on detecting the bedrock at locations with dense aquatic vegetation. The foremost concern was the measurement reliability caused by excessive depths and the environmental conditions influencing the water-column permittivity. Prior to the Devils River survey, University of Texas at Austin researchers conducted a demonstration survey in Austin, Texas. Barton Springs pool had similar depths and bedrock characteristics to Devils River, allowing the researchers to investigate the suitability of using GPR throughout Devils River. Preliminary results revealed that a 200-MHz antenna was suitable for measuring depths up to 3 m, confirming GPR would be suitable for the Devils River study. A slower frequency antenna may generate deeper measurements but produce fewer details. We may advise researchers to have antennas with different gains at disposal, especially traveling to remote locations for similar bedrock surveys. In addition, installation of the GPR antenna on the boat requires critical attention. Potential electromagnetic interferences should be minimized, and the antenna should be mounted as close to the water surface as possible.

Other influences of EM attenuation, such as varying levels of salinity, turbidity, and bottom reflectance, may have an impact on the quality of the remotely sensed data. In the Devils River survey, the water was calm and shallow with minimal turbidity. Therefore, we did not require inertial measurements to correct positional information acquired from sonar and GPR. However, for choppier and more turbulent conditions, using an inertial measurement unit (IMU) coupled with a multi-frequency GNSS is advisable to prevent random angle bias in depth measurements from a boat. For instance, a 3° antenna angle, compared to the nadir angle, equals an additional 16 cm at a depth of 3 m.

Still, there are uncertainties in using active remote sensing technologies for bathymetric surveys. Because of differences in platform heights (airborne and on a boat), the sensitivity and capacity of electronics, and varying beam divergence and angles, minor discrepancies should be expected. Overall, the Devils River study findings revealed that these technologies could complement each other, and the potential biases should be investigated and documented. Remote sensing hardware manufacturers provide specific training and support, and we recommend collaboration before and during mapping efforts. To avoid costly re-measurements, researchers may follow previously confirmed and established in-house quality control and quality assurance procedures. For this purpose, researchers may consider implementing the U.S. Geological Survey's recently released lidar base specifications (version 2.1) for all products used in conjunction with their 3D Elevation Program (3DEP), which is a nationwide effort (Kaufmann, 2019). Various federal and local organizations have also published their procurement standards and specified quality control procedures to be followed prior to data and product acceptance (e.g., Texas Strategic Mapping Program, StratMap). For inland ALB surveys, passive remote sensing technologies (e.g., satellite or airborne spectral imaging), can be highly beneficial for predicting environmental conditions in which in-situ measurements may be inadequate or not feasible. There is a variety of tools available. Researchers should investigate the spatial and spectral resolutions of their project requirements and available budget prior to purchasing products. A new and exciting update to the repertoire of tools for civilian use is the no-cost data availability of NASA's Ice, Cloud, and Land Elevation Satellite 2 (ICESat-2), which became operational in September 2018. The satellite carries a photon-counting lidar unit with a 10-KHz scanner operating with green-wavelength energy. Recent articles have demonstrated its versatility with nearshore (Forfinski and Parrish, 2016; Parrish and others, 2019) and reservoir studies (Y. Li and others, 2019). Therefore, we believe the hydrographic remote sensing community may benefit from a study that compares the survey technologies demonstrated in this article to depths measured by ICESat-2 for quality control purposes, especially at karst riverine environments. Theoretically, positive comparison results would reduce the labor-intensive in-situ efforts, especially at remote locations. Additionally, due to the routine orbiting of the satellite, researchers can investigate temporal changes in project locations against the impacts of varying environmental conditions.

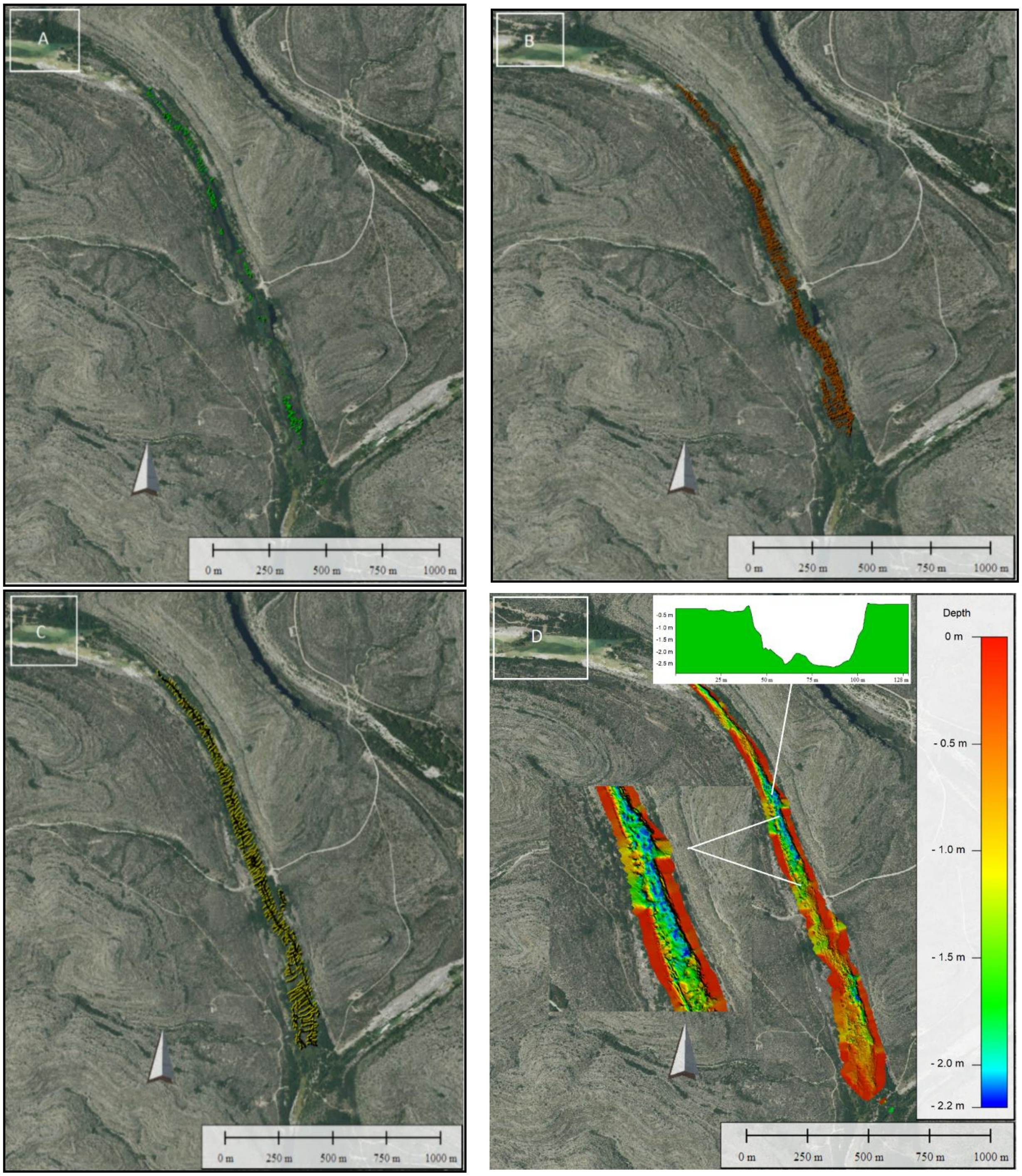

Figure 3-20. Maps showing upper basin depths measured using (**a**) GNSS, (**b**) sonar, and (**c**) GPR, and (**d**), a final depth map with all measurements combined.

3.5. Conclusions

In Devils River, our foremost goal was to measure the river's depth with airborne lidar, and supplement lidar datasets using other hydrographic survey methods, as necessary. We confirmed the possibility of combining datasets sourced from different sensors, and the feasibility of using GPR for measuring depths while aquatic vegetation was present. The quantification methods demonstrated in this study can be exhaustive and complicated. However, they are required to understand the biases before merging datasets with each other to build a seamless bottom map.

Therefore, we constructed our study questions based on the following assumptions: the probability of measuring the riverbed through submerged aquatic vegetation and quantifying the potential biases before merging all datasets. Our study revealed the following conclusions to answer the study questions as identified in the introduction:

- In water columns with submerged aquatic vegetation, airborne lidar bathymetry is not able to measure the riverbed. Sonar technology, with its smaller beam footprint can be complementary to lidar; however, heavy vegetation limits depth recordings. In this study, we demonstrated that use of GNSS and GPR was beneficial at locations where lidar and sonar beams were blocked.
- As a novel approach, we installed a ground penetrating radar with a 200 MHz antenna on a boat with deflated bottom. We were able to measure the bedrock underneath the submerged vegetation, to a maximum depth of ~3 m. In situ measurements such as measuring temperature and the water column conductivity was required to adjust the EM waves propagation speed, and the calibrated measurements matched lidar bathymetry in good confidence. The absolute mean height (depth) difference was similar, and RMSE was smaller than 0.18 m. Matched measurements were normally distributed and statistically significantly.
- We validated the GNSS, sonar, lidar and GPR measurements to each other. Agreement was strong, and the mean vertical difference was computed less than 10 cm compared for all datasets.

In this study, our principal motivation was to evaluate the feasibility of using a ground penetrating radar to map the bedrock where other remote sensing methods were not able. We successfully demonstrated that GPR waves can penetrate through the submerged vegetation and measurements can be fused with other datasets to build a seamless bottom map. This was a novel approach for GPR use, and we believe researchers can benefit from this study and apply the lessons learned in similar future studies.

Supplementary Materials

Table S3-6. [Supplementary materials] A priori calibration results of Hach 2100q field turbidimeter.

Predefined sample (NTU)	Measurement (NTU)	Bias (%)
10	9.87	-1.3
20	19.6	-2
100	104	4

Table S3-7. [Supplementary materials] Summary of post-processing of airborne missions concluded using TXDR and CampTPWD base stations.

Date	Stations	PDOP (RMSE)	Solution quality (%)	Positional accuracy (m, RMSE)			Forward/Reverse Separation (m, RMSE)		
			Q-1	E	N	H	E	N	H
3/20/2018	CampTPWD TXDR	1.83	98.5	0.017	0.022	0.047	0.011	0.007	-0.02
3/21/2018-A	CampTPWD TXDR	1.81	99.3	0.013	0.018	0.037	0.007	0.013	0.017
3/21/2018-B	CampTPWD TXDR	1.61	99.9	0.017	0.018	0.04	0.01	0.007	0.02
3/22/2018-A	TXDR	1.18	99.6	0.014	0.018	0.038	0.009	0.013	0.03
3/22/2018-B	CampTPWD TXDR	1.67	99.6	0.017	0.018	0.042	0.023	0.009	0.056
3/29/2018	TXDR	1.67	99.2	0.019	0.021	0.05	0.018	0.017	0.12
3/30/2018-A	TXDR	1.34	99.5	0.016	0.02	0.045	0.006	0.006	0.024
3/30/2018-B	TXDR	1.74	99.1	0.021	0.022	0.051	0.022	0.026	0.12
Avg.		1.61	99.34	0.02	0.02	0.04	0.01	0.01	0.05

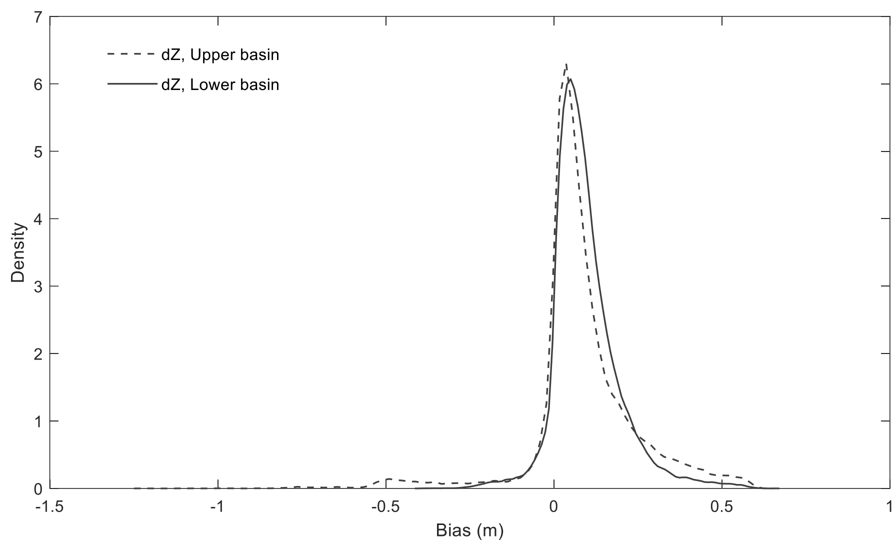

Figure S3-1. [Supplementary materials] Distribution of Class 0 versus Class 5 for surface representation.

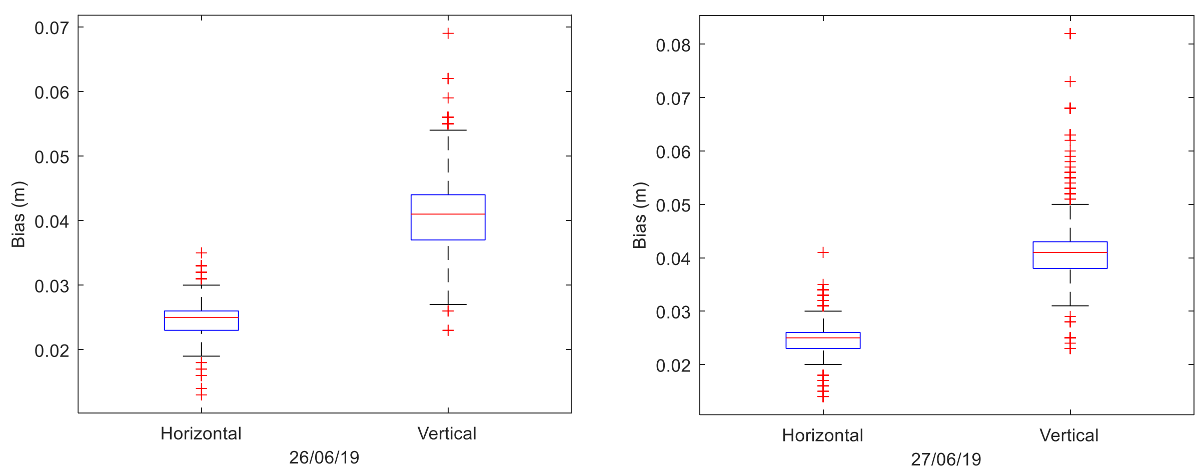

Figure S3-2. [Supplementary materials] Median horizontal and vertical accuracy bias in differential solution using CampTNC base station: (a) 26 June 2019, (b) 27 June 2019.

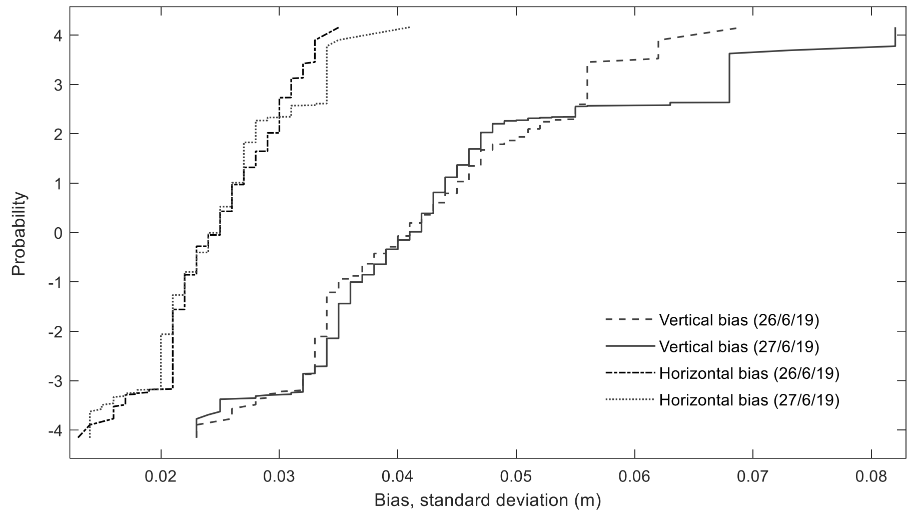

Figure S3-3. [Supplementary materials] The plot indicates the probability of positional bias present in the differential solution that is applicable to localized measurements.

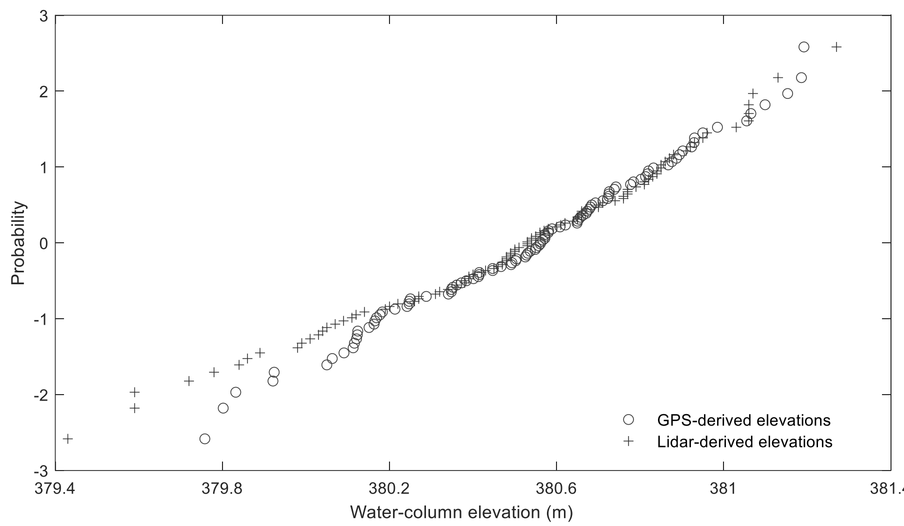

Figure S3-4. [Supplementary materials] GNSS-derived elevations have lower variance and higher probability of normal distribution compared to TIN patch elevations.

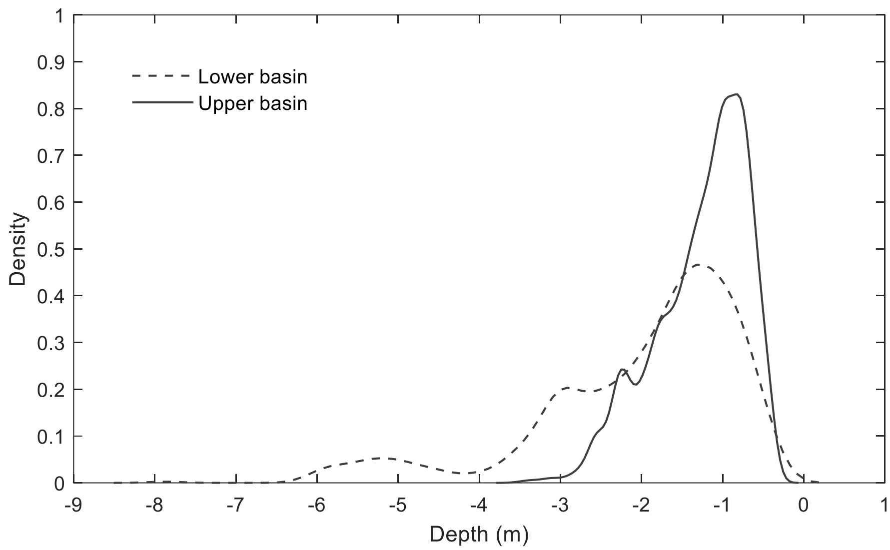

Figure S3-5. [Supplementary materials] Density plot indicates the distribution of sonar-derived depths in the upper and lower basins by Dolan Falls.

Acknowledgments

The authors would like to acknowledge all those who contributed and provided feedback: John Andrews, Tara Bongiovanni, Todd Caldwell, Chiraz Guessaier, Emily Harris, Doug King, Anders Knudby, Francine Mastrangelo, Jeff Paine and Kerem Yücel. Appreciation is extended to the Texas Department of Transportation (TxDOT) for their flight services. We extend our appreciation to the anonymous peer reviewers for their efforts and valuable comments.

3.6. References

Khorram, S.; Nelson, S.A.C.; Koch, F.H.; van der Wiele, C.F. *Remote Sensing*; Springer Briefs in Space Development; Springer US: Boston, MA, USA, 2012; ISBN 978-1-4614-3102-2.

Thenkabail, P. *Remote Sensing Handbook—Three Volume Set*, 1st ed.; CRC Press: Boca Raton, FL, USA, 2018; ISBN 978-1-4822-8267-2.

Mouw, C.B.; Greb, S.; Aurin, D.; DiGiacomo, P.M.; Lee, Z.; Twardowski, M.; Binding, C.; Hu, C.; Ma, R.; Moore, T.; and others Aquatic color radiometry remote sensing of coastal and inland waters: Challenges and recommendations for future satellite missions. *Remote Sens. Environ.* 2015, *160*, 15–30, doi: 10.1016/j.rse.2015.02.001.

Dauwalter, D.C.; Fesenmyer, K.A.; Bjork, R.; Leasure, D.R.; Wenger, S.J. Satellite and Airborne Remote Sensing Applications for Freshwater Fisheries. *Fisheries* 2017, *42*, 526–537, doi:10.1080/03632415.2017.1357911.

Höfle, B.; Rutzinger, M. Topographic airborne lidar in geomorphology: A technological perspective. *Zeit. Geo. Supp.* 2011, *55*, 1–29, doi:10.1127/0372-8854/2011/0055S2-0043.

Karp, S.; Stotts, L.B. *Fundamentals of Electro-Optic Systems Design: Communications, Lidar,* and *Imaging*; Cambridge University Press: Cambridge, UK, 2012; ISBN 978-1-139-10885-0.

Killinger, D.K. Lidar (light detection and ranging). In *Laser Spectroscopy for Sensing*; Baudelet, M., Ed.; Elsevier: Berkeley, CA, USA, 2014; pp. 292–312, ISBN 978-0-85709-273-1.

Muirhead, K.; Cracknell, A.P. Airborne lidar bathymetry. *Int. J. Remote Sens.* 1986, *7*, 597–614, doi:10.1080/01431168608954714.

Guenther, G.C. Airborne Lidar Bathymetry. In *Digital Elevation Model Technologies* and *Applications: The DEM Users Manual*; Maune, F.D., Ed.; American Society of Photogrammetry and Remote Sensing: Bethesda, MD, USA, 2007; pp. 253–320.

Hilldale, R.C.; Raff, D. Assessing the ability of airborne lidar to map river bathymetry. *Earth Surf. Process. Landf.* 2008, *33*, 773–783, doi:10.1002/esp.1575.

Kinzel, P.; Legleiter, C. sUAS-Based Remote Sensing of River Discharge Using Thermal Particle Image Velocimetry and Bathymetric Lidar. *Remote Sens.* 2019, *11*, 2317, doi:10.3390/rs11192317.

Legleiter, C.J. Remote measurement of river morphology via fusion of lidar topography and spectrally based bathymetry. *Earth Surf. Process. Landf.* 2012, *37*, 499–518, doi:10.1002/esp.2262.

Saylam, K.; Brown, R.A.; Hupp, J.R. Assessment of depth and turbidity with airborne lidar bathymetry and multiband satellite imagery in shallow water bodies of the Alaskan North Slope. *Int. J. Appl. Earth Obs. Geoinf.* 2017, *58*, 191–200, doi: 10.1016/j.jag.2017.02.012.

Ogashawara, I.; Mishra, D.R.; Gitelson, A.A. (Eds.) Remote Sensing of Inland Waters. In *Bio-Optical Modeling* and *Remote Sensing of Inl*and *Waters*; Elsevier: Berkeley, CA, USA, 2017; pp. 1–24, ISBN 978-0-12-804644-9.

Saylam, K.; Hupp, J.; Andrews, J.; Averett, A.; Knudby, A. Quantifying Airborne lidar Bathymetry Quality-Control Measures: A Case Study in Frio River, Texas. *Sensors* 2018, *18*, 4153, doi:10.3390/s18124153.

Lague, D.; Feldmann, B. Topo-bathymetric airborne lidar for fluvial-geomorphology analysis. In *Developments in Earth Surface Processes*; Elsevier: Berkeley, CA, USA, 2020; Volume 23, pp. 25–54, ISBN 978-0-444-64177-9.

Saylam, K.; Hupp, J.R.; Averett, A.R.; Gutelius, W.F.; Gelhar, B.W. Airborne lidar bathymetry: Assessing quality assurance and quality control methods with Leica Chiroptera examples. *Int. J. Remote Sens.* 2018, *39*, 2518–2542, doi:10.1080/01431161.2018.1430916.

Knight, R. (2001). Ground Penetrating Radar for Environmental Applications. *Annual Review of Earth and Planetary Sciences*, *29*(1), 229–255. https://doi.org/10.1146/annurev.earth.29.1.229

Doolittle, J. A., Jenkinson, B., Hopkins, D., Ulmer, M., & Tuttle, W. (2006). Hydropedological investigations with ground-penetrating radar (GPR): Estimating water-table depths and local ground-water flow pattern in areas of coarse-textured soils. *Geoderma*, *131*(3–4), 317–329. https://doi.org/10.1016/j.geoderma.2005.03.027

Benson, A. K. (1995). Applications of ground penetrating radar in assessing some geological hazards: Examples of groundwater contamination, faults, cavities. *Journal of Applied Geophysics*, *33*(1–3), 177–193. https://doi.org/10.1016/0926-9851(95)90040-3

Zhang, D.; Wu, W.; Lu, L.; Wu, M. Calibration Technology of Palmer Scanning Airborne Lidar with Vector Measurements. In Proceedings of the 2010 IEEE International Conference on Measuring Technology and Mechatronics Automation, Changsha, China, 13–14 March 2010; pp. 775–778.

Busato, L.; Boaga, J.; Peruzzo, L.; Himi, M.; Cola, S.; Bersan, S.; Cassiani, G. Combined geophysical surveys for the characterization of a reconstructed river embankment. *Eng. Geol.* 2016, *211*, 74–84, doi: 10.1016/j.enggeo.2016.06.023.

Słowik, M. Reconstructing migration phases of meandering channels by means of ground-penetrating radar (GPR): The case of the Obra River, Poland. *J. Soils Sediments* 2011, *11*, 1262, doi:10.1007/s11368-011-0420-x.

Carrick Utsi, E. The Effect of Water and Air. In *Ground Penetrating Radar*; Daniels, D.J., Ed.; Elsevier: Berkeley, CA, USA, 2017; pp. 39–50, ISBN 978-0-08-102216-0.

Green, R.T.; Bertetti, F.P.; Miller, M.S. Focused groundwater flow in a carbonate aquifer in a semi-arid environment. *J. Hydrol.* 2014, *517*, 284–297, doi: 10.1016/j.jhydrol.2014.05.015.

Robertson, S.; Wolaver, B.D.; Caldwell, T.G.; Birdsong, T.; Smith, R.; Hardy, T.; Lewey, J.; Joplin, J. A multidisciplinary approach to developing the science and public support needed to maintain instream flows in the Devils River Basin, Texas. In *Multispecies* and *Watershed Approaches to Freshwater Fish*

Conservation; Dauwalter, D.C., Birdsong, T.W., Garrett, G.P., Eds.; Symposium 91; American Fisheries Society: Bethesda, MD, USA, 2019; pp. 293–314.

Robertson, M.S.; Winemiller, K.O. Habitat Associations of Fishes in the Devils River, Texas. *J. Freshw. Ecol.* 2003, *18*, 115–127, doi:10.1080/02705060.2003.9663957.

Abolt, C.; Caldwell, T.; Wolaver, B.; Pai, H. Unmanned aerial vehicle-based monitoring of groundwater inputs to surface waters using an economical thermal infrared camera. *Opt. Eng.* 2018, *57*, 053113, doi:10.1117/1.OE.57.5.053113.

Caldwell, T.G.; Wolaver, B.D.; Bongiovanni, T.; Pierre, J.P.; Robertson, S.; Abolt, C.; Scanlon, B.R. Spring discharge and thermal regime of a groundwater dependent ecosystem in an arid karst environment. *J. Hydrol.* 2020, *587*, 124947, doi: 10.1016/j.jhydrol.2020.124947.

Westfeld, P.; Richter, K.; Maas, H.-G.; Weiß, R. Analysis of the effect of wave patterns on refraction in airborne lidar bathymetry. *ISPRS Int. Arch. Photogramm. Remote Sens. Spat. Inf. Sci.* 2016, *XLI-B1*, 133–139, doi:10.5194/isprsarchives-XLI-B1-133-2016.

Milsom, J.; Eriksen, A. *Field Geophysics: The Geological Field Guide Series*; 4th ed.; Wiley: Hoboken, NJ, USA, 2011; ISBN 978-0-470-74984-5.

Mancuso, S. (Ed.) *Measuring Roots: An Updated Approach*; Life sciences; Springer: Berlin/Heidelberg, Germany, 2012; ISBN 978-3-642-22066-1.

Sambuelli, L.; Bava, S. Case study: A GPR survey on a morainic lake in northern Italy for bathymetry, water volume and sediment characterization. *J. Appl. Geophys.* 2012, *81*, 48–56, doi:10.1016/j.jappgeo.2011.09.016.

Jonasz, M.; Fournier, G.R. *Light Scattering by Particles in Water: Theoretical* and *Experimental Foundations*, 1st ed.; Elsevier, Academic Press: Amsterdam, The Netherlands, 2007; ISBN 978-0-12-388751-1.

Smith, R.C.; Baker, K.S. Optical properties of the clearest natural waters (200–800 nm). *Appl. Opt.* 1981, *20*, 177–184, doi:10.1364/AO.20.000177.

Lee, Z.-P. Diffuse attenuation coefficient of downwelling irradiance: An evaluation of remote sensing methods. *J. Geophys. Res.* 2005, *110*, 1–9, doi:10.1029/2004JC002573.

Kitchener, B.G.; Wainwright, J.; Parsons, A.J. A review of the principles of turbidity measurement. *Prog. Phys. Geogr. Earth Environ.* 2017, *41*, 620–642, doi:10.1177/0309133317726540.

Lee, Z.; Shang, S.; Du, K.; Wei, J. Resolving the long-standing puzzles about the observed Secchi depth relationships: Resolving puzzles about Secchi depth relationships. *Limnol. Oceanogr.* 2018, 2321–2336, doi:10.1002/lno.10940.

Poole, H.H.; Atkins, W.R.G. Photo-electric Measurements of Submarine Illumination throughout the Year. *J. Mar. Biol. Ass.* 1929, *16*, 297–324, doi:10.1017/S0025315400029829.

Gallegos, C.L.; Werdell, P.J.; McClain, C.R. Long-term changes in light scattering in Chesapeake Bay inferred from Secchi depth, light attenuation, and remote sensing measurements. *J. Geophys. Res.* 2011, 19, *116*, 19, doi:10.1029/2011JC007160.

AHAB *Bathymetric lidar Systems*; Airborne Hydrography AB: Jonkoping, Sweden, 2014; http://www.bshc.pro/media/documents/lidar2014/04_140527_AHAB_Bathymetric_lidar.pdf.

O'Dell, J.W. *Method 180.1: Determination of Turbidity by Nephelometry*; Office of Research and Development, U.S. Environmental Protection Agency: Cincinnati, OH, USA, 1993; pp. 1–8; Available online: https://www.epa.gov/sites/production/files/2015-08/documents/method_180-1_1993.pdf (accessed on 25 July 2020).

Beć, K.B.; Huck, C.W. Breakthrough Potential in Near-Infrared Spectroscopy: Spectra Simulation. A Review of Recent Developments. *Front. Chem.* 2019, *7*, 48, doi:10.3389/fchem.2019.00048.

Cottin, A.G.; Forbes, D.L.; Long, B.F. Shallow seabed mapping and classification using waveform analysis and bathymetry from SHOALS lidar data. *Can. J. Remote Sens.* 2009, *35*, 422–434, doi:10.5589/m09-036.

Eren, F.; Pe'eri, S.; Rzhanov, Y.; Ward, L. Bottom characterization by using airborne lidar bathymetry (ALB) waveform features obtained from bottom return residual analysis. *Remote Sens. Environ.* 2018, *206*, 260–274, doi:10.1016/j.rse.2017.12.035.

Allouis, T.; Bailly, J.-S.; Pastol, Y.; Le Roux, C. Comparison of lidar waveform processing methods for very shallow water bathymetry using Raman, near-infrared and green signals. *Earth Surf. Process. Landf.* 2010, *35*, 640–650, doi:10.1002/esp.1959.

Pan, Z.; Glennie, C.; Hartzell, P.; Fernandez-Diaz, J.; Legleiter, C.; Overstreet, B. Performance assessment of high resolution airborne full waveform lidar for shallow river bathymetry. *Remote Sens.* 2015, *7*, 5133–5159, doi:10.3390/rs70505133.

Saylam, K.; Hupp, J.R.; Aaron, R.A. Quantifying the Bathymetry of the Lower Colorado River Basin, Arizona, with Airborne Lidar; Presented at ASPRS conference, Baltimore, MD, USA, 2017; Volume 1, pp. 1–11.

Habib, A. Accuracy, quality assurance and quality control of lidar data. In *Topographic Laser Ranging* and *Scanning: Principles* and *Processing*; Thot, C.K., Shan, J., Eds.; Taylor and Francis: Boca Raton, FL, 2009; pp. 269–294, ISBN 978-1-4200-5142-1.

Delaunay, P.B. Sur la sphere vide—A la memoire de Georges Voronoi. *Bull. Acad. Sci. URSS* 1932; *6*, 793. Available online: http://galiulin.narod.ru/delaunay_.pdf (accessed on 25 July 2020)

P.; Chew, L. Constrained Delaunay triangulations. *Algorithmica* 1989, *4*, 97–108, doi:10.1007/BF01553881.

Klein, L.; Swift, C. An improved model for the dielectric constant of sea water at microwave frequencies. *IEEE Trans. Antennas Propagat.* 1977, *25*, 104–111, doi:10.1109/TAP.1977.1141539.

Serkan, S.; Borecky, V. Estimation Methods for Obtaining GPR Signal Velocity. In Proceedings of the Third International Conference on Advances in Civil, Structural and Environmental Engineering- ACSEE 2015; Institute of Research Engineers and Doctors, Zurich, Switzerland, 10–11 October 2015; pp. 43–47.

Spilker, J.J., Jr.; Axelrad, P., Parkinson, B.W., Enge, P. (Eds.) *Global Positioning System: Theory* and *Applications, Volume I.*; American Institute of Aeronautics and Astronautics: Washington, DC, USA, 1996; ISBN 978-1-56347-106-3.

Milsom, J., Eriksen, A., 2011. Field geophysics, 4th ed. ed, The geological field guide series. Wiley, Hoboken, NJ.

Kaufmann, J.E. USGS Lidar Base Specification. 2019. Available online: https://www.usgs.gov/media/files/lidar-base-specification-version-21 (accessed on 25 July 2020).

Forfinski-Sarkozi, N.A.; Parrish, C.E. Active-Passive Spaceborne Data Fusion for Mapping Nearshore Bathymetry. *Photogramm Eng. Remote Sens.* 2019, *85*, 281–295, doi:10.14358/PERS.85.4.281.

Parrish, C.E.; Magruder, L.A.; Neuenschwander, A.L.; Forfinski-Sarkozi, N.; Alonzo, M.; Jasinski, M. Validation of ICESat-2 ATLAS Bathymetry and Analysis of ATLAS's Bathymetric Mapping Performance. *Remote Sens.* 2019, *11*, 1634, doi:10.3390/rs11141634.

Li, Y.; Gao, H.; Jasinski, M.F.; Zhang, S.; Stoll, J.D. Deriving High-Resolution Reservoir Bathymetry from ICESat-2 Prototype Photon-Counting lidar and Landsat Imagery. *IEEE Trans. Geosci. Remote Sens.* 2019, *57*, 7883–7893, doi:10.1109/TGRS.2019.2917012.

Zhang, D., Wu, W., Lu, L., Wu, M., 2010. Calibration Technology of Palmer Scanning Airborne Lidar with Vector Measurements, in 2010 International Conference on Measuring Technology and Mechatronics Automation. Presented at the 2010 International Conference on Measuring Technology and Mechatronics Automation (ICMTMA 2010), IEEE, Changsha City, China, pp. 775–778. https://doi.org/10.1109/ICMTMA.2010.688

Chapter Four: Analysis of Depths Derived by Airborne Lidar and Satellite Imaging to Support Bathymetric Mapping Efforts with Varying Environmental Conditions: Lower Laguna Madre, Gulf of Mexico

4.1. Introduction

Remote sensing is the science of gathering information about an object without physical contact. In recent years, the use of active remote sensing technologies from different platforms (orbiting satellites, aircraft, or Unmanned Airborne Vehicles) has become increasingly popular to measure the topography of hard surfaces (Höfle and Rutzinger, 2011; Lohani and Ghosh, 2017) or the depths of shallow and transparent waters (Guenther, 2007; Mandlburger, 2021). As a result, projects investigated and used the technology for coastal applications such as shoreline mapping, erosion, and change detection (Brock and Purkis, 2009; Klemas, 2011; Paine and others, 2017; Toure and others, 2019).

In dynamic coastal and fluvial inland water reservoirs, it is challenging to measure depths because of electromagnetic energy (EM) scattering from the water surface and the rapid amplitude degradation in the water column. Several studies revealed the challenges of bottom mapping with varying levels of water quality in coastal and inland waters using satellite imaging and measuring pixel reflectance (Caballero and Stumpf, 2019; Dogliotti and others, 2015; Garg and others, 2017). However, only a few investigated the combined use of airborne lidar and satellite imaging technologies. For instance, Ji and others introduced a feature-based data fusion model (Ji and others, 2022), and Yeu and others evaluated and enhanced the accuracy of satellite altimeter bathymetry using airborne lidar and multi-beam sonar on transparent, coastal waters of western Korea using a gravity-geologic model (Yeu and others, 2018).

In 2017, the Bureau of Economic Geology (BEG) at The University of Texas at Austin (UT Austin) acquired topographic and bathymetric airborne lidar data over Lower Laguna Madre, a hypersaline lagoon in south Texas. Previously, using an airborne lidar system, BEG researchers completed projects on the Gulf Coast, mapping the shallow seafloor along the Gulf of Mexico and the Pacific Coast (Paine and others, 2017) and investigating bottom morphologies along various river sheds in the southern US (Saylam and others, 2020; Saylam and others, 2018). The principal research motivation was to investigate the feasibility of measuring the lagoon bottom with airborne lidar and quantify lidar bathymetry's accuracy with applicable survey and in-situ methods. We need to emphasize that remote sensing methods used in this study are familiar; however, their application in challenging and varying coastal environments to complement and validate each other is important to the remote sensing community and has not been studied or documented in detail.

For this purpose, we prepared a control surface with GNSS observed checkpoints, collected dual-frequency sonar readings, observed transparency with a Secchi disk, and sampled turbidity in nephelometric measurements from a boat. Furthermore, we studied satellite imaging pixel reflectance and conducted passive and optical satellite-derived bathymetry (SDB) to measure the lagoon depths.

We aimed to address the following research questions in detail:

- Can we measure the bottom of a shallow and hypersaline lagoon with varying environmental conditions using an airborne lidar system? What are the theoretical and practical limitations of using an airborne lidar system in Laguna Madre?
- Is it feasible to confirm the accuracy of lidar bathymetry with sonar in Laguna Madre? How do they complement each other in a lagoon with varying environmental conditions? How do we calibrate sonar wavelengths to record accurate depths?
- Can we distinguish varying water quality using satellite pixel reflectance analysis? What are the potential benefits of conducting quantitative pixel reflectance analysis that is applicable to Laguna Madre?
- Is SDB a feasible methodology to measure the depths of a lagoon with varying environmental conditions? Can we compare and quantify SDB to lidar bathymetry?

4.2. Materials and methods

4.2.1. Project Location

In Texas, Lower Laguna Madre is a hypersaline (i.e., saltier than seawater) lagoon that is physiographically divided into two subunits (McManus, 1990). Upper Laguna Madre is separated from the lower section by a canal and partial land bridge, which was constructed from dredged material during the building of the Gulf Intracoastal Waterway (Tunnell and Judd, 2002). To the south, Lower Laguna Madre borders Mexico and covers an area larger than 800 km^2 (310 mi^2). The lagoon waters are transparent and shallow in the southeast and northern sections, and water quality changes with northerly winds that carry sedimentation from sand dunes and discharge freshwater streams. The lagoon has a unique seagrass ecosystem, protected by the Atascosa National Wildlife Refuge area in the north and by Padre Island on the Gulf Coast. Here, seagrass beds serve as essential nursery areas for various Gulf of Mexico species, such as supplying food and shelter for Redhead Ducks (*Aytha americana*). Because of seagrass' essential role in supporting fish and wildlife resources, studies have attempted to map the lagoon using remote sensing technologies (Dubin and others, 2018; Webster and others, 2015).

4.2.2. In-Situ Campaign

In 2017, an in-situ campaign was conducted in three distinct areas clustered in the southern portion of the lagoon, where it was possible to observe water transparency, depth, and turbidity (Appendix A). We sampled water with a turbidimeter and measured transparency with a Secchi disk. In the north, access to the lagoon was restricted due to private lands and the absence of public roads. We observed that in-situ Area-1 was shallow, transparent, and registered the least amount of turbidity content, in-situ Area-2 had varying turbidity and transparency, and in-situ Area-3 recorded the highest turbidity concentration (Figures 4-1 a, b).

(**a**)

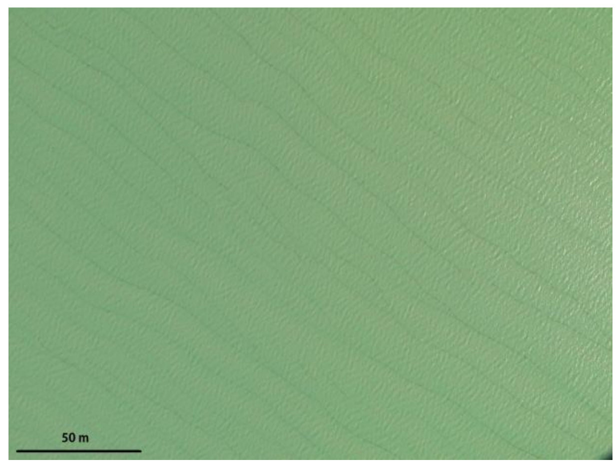

(**b**)

Figure 4-1. (**a**). Aerial image of Area-1. The turbidity was low, the lagoon was shallow, and the bottom was visible for observations. (**b**). Aerial image of Area-3. Turbidity and floating vegetation created challenges for bottom measuring.

We completed the sonar surveys on three dates where atmospheric conditions influencing the lagoon conditions were similar: calm and no precipitation. Survey dates 01/05 (Area-1), 05/05 (Area-2), and 12/05 (Area-3) were executed coincidently with airborne lidar data acquisition, and depths were measured using a dual-frequency transducer (200/50 kHz) sonar. We mounted the sonar unit onto a kayak and towed it throughout the lagoon with a power boat with an onboard observer. The sonar transducer was submerged with the operator in the kayak, and the resulting 6 cm was added to the recorded heights.

The sonar measured the lagoon bottom every two seconds, and the observer manually triggered the unit (*waypoints*) various times at each specified location where additional turbidity and water transparency measurements were sampled.

The sonar unit was calibrated in the lab environment, in the freshwater tank (UT Austin, Advanced Research Laboratories), producing depth measurements with a standard deviation of 2.7 cm at 11.8 m depth, which is acceptable for shallow-classified airborne lidar mapping systems (P. J. Kinzel and others, 2007). In salt waters, sound waves propagate faster and require additional adjustment for salinity (S), water temperature (T), and depth (z). In Lower Laguna Madre, the typical salinity is 35.3 parts per thousand (ppt) (Estrada, 2018), and we confirmed this value with the Texas Commission on Environmental Quality (TCEQ) stations (IDs: 13446 and 13447). These stations reported an average of 36.1 ppt and 38.6 ppt for all 2017 samplings. Figure 4-2 illustrates the survey location, in-situ areas, tide gauges, and TCEQ reference stations.

We recorded the water-column temperature using the sonar transducer, where the mean temperature varied (24.7, 23.4, and 26.2 °C), depending on the location and the survey day. Because the depth varied at each in-situ location, we used the mean value in the empirical formula (Equation (4-1)) to calculate the speed of sound in the water using coefficients (a_1–a_n) (Medwin, 1975). Computations revealed that sound waves propagated with different velocities for each survey day (1533.9, 1530.7, and 1537.5 m/s) in Lower Laguna Madre, which required an adjustment of 1/0.963–0.967 for sonar readings. Because the lagoon was calm and shallow, and the rocking movement with the kayak was minimal, we did not consider rotational adjustment (attitude) of sonar readings. Additionally, the sonar transducer was mounted in the middle of the boat, where the angles caused by the rocking movements would be minimal. However, because 10 degrees of boat roll would equal 3 cm of additional ranging in a 2 m water column, we recommend an inertial movement unit (IMU) sensor integration for rotational adjustment of sonar recordings in deeper and choppier waters.

$$c(T,S,z) = a_1 + a_2T + a_3T^2 + a_4T^3 + a_5(S-35) + a_6z + a_7z^2 + a_8T(S-35) + a_9Tz^2 \qquad \text{(Equation 4-1)}$$

Figure 4-2. Lower Laguna Madre in southern Texas and in-situ locations (TCEQ reference stations, NOAA tide gauges, and BEG observation areas). The yellow polygon indicates the extent of the airborne survey area (1600 km^2).

4.2.3. Tide and Datum Adjustments for Bathymetry

The National Oceanic and Atmospheric Administration (NOAA) reported a daily average of 23 cm of tides in the Port Isabel gauge (Station ID# 8779770: latitude 26°3.7′N, longitude 97°12.9′W), observed in the last 19 years. The Port Mansfield gauge (Station ID# 8778490: latitude 26°33.5′N, longitude 97°25.5′W), in May 2017 alone, recorded 44 cm of tidal range, and the mean surface height was 0.19 m, mean sea level (MSL). The Port Isabel gauge recorded a 90 cm tidal range for the same period, and the mean surface height observed was 0.12 m MSL. Because of its proximity to in-situ locations, we used the tide observations reported in Port Isabel station (in MSL) to adjust satellite bathymetry (0.29 m in 01/05/2017, 20:00 GMT and 0.24 m in 05/05/2017, 20:00 GMT). Because lidar and sonar measurements were completed in conjunction, no tidal adjustments were required to compare these datasets. For consistency purposes, all ellipsoidal heights in this study (e.g., lidar, GNSS, and sonar) were converted to orthometric heights (real-world elevations) using the GEOID2012B model, representing MSL elevations.

In addition to in-situ observations, TCEQ provided depth measurements through the SWQM program. We selected five operational SWQM reference stations that were scattered throughout the lagoon for uniformity (TCEQ IDs: 13446, 13447, 13448, 13449, and 14870). Depths provided in these stations represent the distance from the surface during observation and were adjusted to MSL heights. Because Lower Laguna Madre is a dynamic environment and depths vary with time, we considered the depth results in the *height* domain. Therefore, the depths mentioned in this study refer to the height measurements in the water column as perceived by a particular survey method and may not represent the lagoon bottom, particularly in areas with high turbidity.

4.2.4. Vector Data Analysis

Because point-to-point correspondence is not assumed with lidar point cloud datasets (Habib, 2009), we used the Delaunay triangulation algorithm (B Delaunay, 1932) to create surface patches of Triangulated Irregular Networks (TIN) for comparison purposes to other survey methods (e.g., sonar and GNSS). There are other algorithms to construct TIN surfaces (e.g., Distance Ordering, Region Growing). However, the Delaunay triangulation algorithm was preferred because of superior uniform modeling, automation capabilities, and statistical consistency with previous studies (Saylam and others, 2020; Saylam, Hupp, Andrews, and others, 2018).

This study used point cloud (vector) lidar datasets to construct the TIN surface patches. The process maximized the smallest angles of triangles by defining an empty circumcircle and selecting the shortest distance of all points (h) to minimize the interior angle of all triangles, where the triangles were equiangular. A surface patch was created by defining a set of circumcircles (e.g., 1 m radius), and an average height was compared to a particular height measured by the other applicable survey methods (e.g., sonar and GNSS). The algorithm picked the lidar returns that registered in the user-defined proximity (e.g., $dS1i$ = 1 m) and excluded the returns registered at slopes greater than the defined (e.g., α = 45°) angle. The vertical threshold (e.g., h = 0.5 m) was adjusted to prevent the algorithm picking up returns from erroneous features that may represent heights (or depths) incorrectly. This was an essential practice in the lagoon survey, where lidar returns picked submerged and floating vegetation and registered as bottom peaks in the waveform.

4.2.5. Airborne Lidar Bathymetry and System Calibration

Airborne lidar bathymetry (ALB) is an active remote-sensing technology for mapping inland reservoirs and shorelines with shallow and transparent waters. A typical ALB system integrates a laser power unit, scanner mirrors, transmitting and receiving units, a Global Satellite Navigation System / Inertial Navigation System (GNSS/INS) unit, a digitizer, onboard storage, and an operator interface. We used an ALB system manufactured by Airborne Hydrography AB (AHAB) of Sweden named "Chiroptera," which uses a near-infrared and a green-wavelength for data collection. In May 2017, using Chiroptera, we acquired 60 h of in-flight time over the lagoon with a Partenavia P68-C (N88N) fixed-wing aircraft. Table 4-1 presents the system settings.

Table 4-1. Chiroptera system settings in the Lower Laguna Madre survey.

Item	1064 nm	515 nm
Pulse repetition rate (PRF)	100–300 kHz	36 kHz
Average lidar point density	10 points/m2 (+side overlap)	2 points/m2 (+side overlap)
Average flight altitude	400–600 m	
Swath width and overlap rate	250–300 m/30% overlap	
Average aircraft survey speed	110–130 knots	

ALB relies on recording a waveform representing the observed amplitude of backscattered energy from each transmitted laser pulse. Depths are calculated by computing the time difference (Δt) between the distinctive peaks in the waveform that represent the water surface ($t1$) and bottom ($t2$). The post-processing software (Leica Lidar Survey Suite, LLSS v2.40) calculates the time differences between these peaks. Additionally, the application considers the properties of the waveform, accounting for electronic timing delays, interactions with the water column, and the speed of light traveling in the air and in the water column.

During raw data processing, LLSS produced point cloud datasets in which each return is assigned a numerical class. These classes were derived from the original waveform, set by user backscatter thresholds, and they represent a position in three-dimensional space, identifying a specific type of surface as illuminated by the laser beam. For the bathymetric analysis, we used specific data classes, which required detailed processing, cleaning, and analysis (sample illustrations: Appendix B). In detail, these data classes and their positions were calculated in the following manner:

- Class 0 returns represent the water surface synthetically and they are interpolated using a proprietary AHAB algorithm. The NIR channel measurements estimate the water surface's elevation, and the algorithm uses the synthetic surface to inform the selection of peaks in the green channel waveform.
- Class 5 returns represent the water surface and are calculated by picking out the first strong peak from the green channel waveform without using data from the NIR channel.
- Class 7 returns represent a reflective surface in the water column and are calculated by selecting a second strong peak from the waveform.
- Class 10 returns represent a reflective surface in the water column and are calculated using peaks of lower amplitude than those used in Class 7. The weaker peaks are selected using a proprietary algorithm to improve the lidar system's depth-measuring capability by discarding peaks created by low or moderate turbidity levels.

In Equation 4-2, d_m is the distance traveled in meters, n is the refractive index of the water, C_w is the speed of light in the water, and f is the digitizer sampling rate in gigahertz (GHz). The refractive index changes with water temperature (T), salinity (S, ‰), and the wavelength of the emitted beam (λ). To estimate the irregularity in refractive index value, we used a tool built into LLSS v2.4 that computes the surface representation using the refraction equation (Equation (4-3)) (Quan and Fry, 1995). This equation determined each refraction coefficient (n_0 to n_9) using the least-squares method to match the terms as a function of wavelength, salinity, and temperature at a given atmospheric pressure (Roswell and Halikas, 1976). We considered the water temperature as 25 °C (T), typical for May; therefore, S = 35‰, and n = 1.343.

$$d_m = \frac{C_w \, \Delta t}{2nf} \quad \text{(Equation 4-2)}$$

$$n(S,T,\lambda) = n_0 + (n_1 + n_2T + n_3T^2)S + n_4T^2 + \frac{n_5 + n_6S + n_7T}{\lambda} + \frac{n_8}{\lambda^2} + \frac{n_9}{\lambda^3} \quad \text{(Equation 4-3)}$$

It is possible to compute the duration of each sample (t_d) by dividing the time difference (Δt) by the system sampling rate (f) (Equation 4-4). We can also calculate the vertical spacing between the lidar pulses traveling in space and the water column. Assuming the refraction is constant, such as in a vacuum (n = 1), each sample represents a spacing of 0.167 m. In seawater, with the addition of a higher refraction index and the slowing light propagation, the sample spacing decreases, e.g., n = 1.342, and the spacing equals 0.0931 m between the samples.

$$t_d = \frac{1}{f} \times \Delta t \quad \text{(Equation 4-4)}$$

The accuracy of the lidar-derived measurements relies on the calibration of individual system components. The eccentricity and misalignment between the laser mirrors, the inertial movement unit (IMU), and the GNSS antenna must be determined precisely. The process requires collecting height measurements of a flat surface using a geodetic grade GNSS receiver and comparing these heights to lidar measurements. For this purpose, we surveyed the Port Isabel-Cameron County airport (KPIL) taxiway using a Trimble R8 receiver. Static GNSS checkpoints were post-processed to improve their positioning using a TxDOT (Texas Department of Transportation) maintained TXLN (Texas Laguna Madre, 26°5”41.6392′N, −97°18”02.4998′W) NOAA-CORS (National Oceanic and Atmospheric Administration-Continuously Operating Reference System) base station. All datasets used in this study were referenced to the North American Datum 1983 (NAD83) update 2011, epoch 2010.00, and coordinates were computed in Universal Transverse Mercator (UTM 14N), in units of meters.

4.2.6. Satellite Imagery and Pixel Reflectance Analysis

Satellites with high-resolution imaging sensors can capture information on large areas, allowing identification of various features. Because Lower Laguna Madre is dynamic, and airborne lidar measurements were acquired in May and June, we downloaded imagery acquired solely in May and June

2016-2019 for temporal study purposes. We omitted 2020 imagery due to clouds blocking in-situ measurement locations.

The European Space Agency operates the Sentinel series satellites, and the Payload Data Ground Segment unit processes Level-1C (L1C) products and outputs radiometrically and geometrically corrected top-of-atmosphere images. L1C products are composed of 100 × 100 km tiles, including cloud masks and European Centre for Medium-Range Weather Forecasts information (total ozone column, water vapor, and MSL pressure). Every L1C product registers information with wavelength bands 1 to 9 (442 to 864 nm). Bands 2-blue, 3-green, 4-red, 5-red edge, and 8-NIR (492, 559, 664, 704, and 832 nm) were essential to this study because of their capability to distinguish the differences in pixel reflectance values, emphasizing the boundary between land and water (Mondejar and Tongco, 2019). The spatial resolution varied with each band: 10 m per pixel for bands 2 to 4 and 8 and 20 m for band 5. Table 4-2 summarizes the sensing time, date, tile numbering, and other specifics of the downloaded imagery.

Table 4-2. Details of Sentinel-2A L1C imagery used in the study.

Date	Sensing Time (UTC)	Tile	Sun Elevation (Degrees)	Sun Azimuth (Degrees)	Cloud Coverage (%)
12/05/2016	17:11:44	T14RPQ	72	113.6	20
12/05/2016	17:11:44	T14RPP	72.3	111.1	24
16/06/2017	17:15:05	T14RPQ	72.9	96.9	6
16/06/2017	17:15:05	T14RPP	73	94	6
17/05/2018	17:10:16	T14RPQ	72.4	110.5	0
17/05/2018	17:10:16	T14RPP	72.8	107.9	0
27/05/2019	17:16:29	T14RPQ	73.1	104.5	25
27/05/2019	17:16:43	T14RPP	73.3	101.6	16

Analysis of EM radiation recorded from underwater reflectance and optics may supply essential information about quality, depth, and other distinctive properties of water. Therefore, we studied optical information and used algorithms to estimate bathymetry (Ashphaq and others, 2021). The blue-green and NIR wavelengths can distinguish the varying concentrations of suspended particulate matter in the water (Gernez and others, 2015; Saylam and others, 2017). Previous studies indicated that Band 4 (665 nm) can distinguish the chlorophyll-A absorption, and Band 5 (705 nm) relates to the vegetation monitoring and turbidity patterns in shallow lagoons (Delegido and others, 2011; Sebastiá-Frasquet and others, 2019). In this study, the principal motivation was to distinguish the water clarity and transparency and locate the in-situ locations that reflect the environmental characteristics of the lagoon. Because the lagoon was only accessible in the south, we identified these locations by analyzing the reflectance properties and selected areas that indicated different conditions.

The ENVI Spectral Profile Tool was used to analyze the radiance recorded at each pixel. Our objective was to distinguish the areas with high turbidity; nevertheless, the pixel radiance values helped us to identify the features surrounding the lagoon (e.g., vegetation and dunes). Areas with clouds have exceedingly high reflectance values, and we generated masks to exclude these areas from further analysis. To plot the results, we used ENVI's Iterative Self Organizing Data Analysis (ISODATA) clustering algorithm, an unsupervised classification tool that iteratively clusters pixels to the nearest class (Ahmad and Sufahani, 2012). The algorithm does not require *a priori* knowledge of the surfaces. Instead, it computes the mean radiance values by reclassifying the pixels until the difference between them is less than the threshold (e.g., 2%) or the maximum number of iterations, ten by default, is achieved. The process is similar to K-*means* clustering, which has advantages for fast converging datasets and a simple implementation process (Yuan and Yang, 2019). Further, we conducted a Normalized Difference Water Index [NDWI = (green − NIR)/(green + NIR)] analysis to build a surface map by mounting the areas of interest [35]. Typically, NDWI analysis can detect moisture changes in vegetation (Kaplan and Avdan, 2017), and we used the algorithm to exclude cloudy and vegetated areas as identified by the ISODATA analysis. The band reflectance was normalized (0–1) using the ENVI Band Math tool because the scaling factor normalizes the images to reduce radiometric differences across non-surface effects (de Carvalho and others, 2013).

4.2.7. Satellite-Derived Bathymetry

We studied satellite-derived bathymetry that utilizes ocean optics and algorithms to estimate depths (Saylam, Brown, and others, 2017). Water-leaving radiance is the backscatter upwelling after traversing the air/water interface and recording subsurface volumetric and bottom information. Previous studies developed the bottom albedo-independent bathymetric algorithm that accurately distinguishes bottom types such as sand, rock, and vegetation up to 15 m depth under ideal atmospheric and water conditions (Favoretto and others, 2017; Stumpf and others, 2003).

The principal motivation was to compare and quantify the resultant satellite bathymetry to lidar measurements and study the compatibility, particularly in the in-situ areas. The satellite imagery's varying turbidity, excessive shallow depths, and coarse grid spacing (20 m) were expected to adversely influence the bathymetric quality and completeness. Therefore, we assessed the comparison algorithm threshold values (e.g., $dS1i$ = 5 m) and included more measurements in the computations. We must emphasize that satellite bathymetry was adjusted with local tides to match lidar measurements and observed MSL values were extracted from heights (*depths*).

The Spectral Processing Exploitation and Analysis Resource (SPEAR) algorithm in the Relative Water Depth (RWD) tool in ENVI v5.5 allows analysts to understand bathymetric properties using the blue, green, and NIR bands (2, 3, 4, and 8). In this study, in-situ measurements were required to generate absolute results; therefore, we input depth values into 06/2017 imagery, which included a combination of TCEQ station observations and sonar waypoints, all relative to MSL. With the SPEAR algorithm, the satellite imagery was preprocessed with creating vector polygons to mask erroneous features such as boats, islands, and clouds. The images were normalized (0-1), pansharpened and resampled to 20 m grid for haze removal, following a Log Ratio Transform (LRT) algorithm application. The LRT approach in the RWD algorithm uses an empirical formula (Stumpf and others, 2003) to compute water depth independently of the base albedo, where each band is assumed to absorb water differently.

4.3. On-Site Analysis

We conducted preliminary data processing activities immediately after each airborne data acquisition mission. Decimated (e.g., 1/100) vector datasets were output to confirm lidar swath coverage and height measurements.

Previously, in the Colorado River study (Saylam, Hupp, and others, 2017), where water was deeper (up to 12 m) and transparent, we observed an increase in Chiroptera's bathymetric capability by 0.8 m (9.2%) using the Class 10 algorithm. In Lower Laguna Madre, where water was shallower than 3.35 m, the on-site analysis revealed a 41.2% depth measuring increase using the same algorithm (Table 4-3). In contrast, our analysis indicated a reduced correlation between Classes 0 and 5 (*water surface*) with increasing turbidity (Table 4-4). Naturally, escalating turbidity scattered Class 5 pulses, generating a less consistent surface representation. Therefore, we used Class 0 returns to define the water surface that averaged heights derived from returns of both wavelengths.

Additionally, we analyzed the influence of turbidity on the bathymetric capability of Chiroptera by studying the in-situ observations (Appendix A). We converted the turbidity measurements to logarithmic values, and the findings indicated a linear relationship ($R^2 = 0.82$) between the maximum measurable depth (theoretical, D_{max}) and escalating turbidity at locations where the bottom was not visible to the observer (Figure 4-3).

Table 4-3. Bathymetric class data output (Classes 7 and 10) comparison to sonar recordings at BEG-observed in-situ locations.

In-Situ Area	Number of Measurements (Class 7/10)	Mean Sonar Depth (m, MSL)	Mean Lidar Depth (m, MSL) (Class 7/10) (Class 7/10)	Standard Deviation (m) (Class 7/10)	Bathymetric Improvement. (%)
1	256/130	−1.35	−1.28/−1.57	0.14/0.23	23
2	381/140	−1.43	−1.42/−1.78	0.17/0.38	20.2
3	551/272	−1.84	−1.35/−1.84	0.62/0.63	41.2

Table 4-4. Turbidity and surface class data output (Classes 0 and 5) comparison. Escalating turbidity levels scattered Class 5 returns and adversely influenced root-mean-square error (RMSE) values.

In-Situ Area	Mean Turbidity (NTU)	Number of Returns (Class 0/5)	Median Difference (m) (Class 0 to 5)	RMSE (m) (Class 0 to 5)	R^2
1	2.7	528/173	−0.07	0.03	0.94
2	8.6	907/653	−0.09	0.06	0.65
3	10.5	806/420	−0.11	0.08	0.32

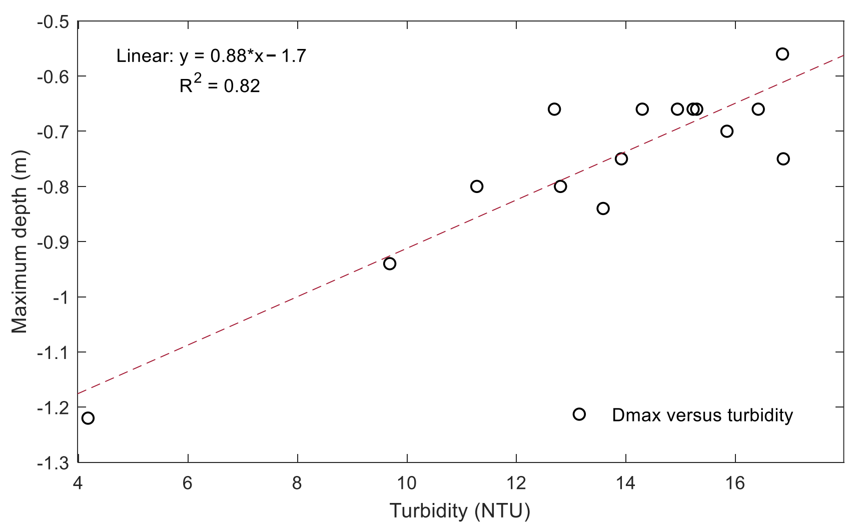

Figure 4-3. The influence of increasing turbidity on the theoretical bathymetric capability (maximum depth: D_{max}) of Chiroptera is a linear relationship ($R^2 = 0.82$).

4.4. Results

4.4.1. ALB System Calibration

Using the *least-squares* statistical method, we compared 448 ground GNSS checkpoint elevations to lidar derived surface TIN patches (Savitzky and Golay, 1964). For both scanners, the correlation produced a strong agreement ($R^2 > 0.95$). Each scanner's median height bias and RMSE were less than 2.8 cm. Findings revealed a minor height bias between the scanners (<4 cm), caused by NIR and green wavelength pulses registering different surface heights due to beam divergence differences (Table 4-5, Figure 4-4).

Table 4-5. Chiroptera ALB system height calibration results.

Scanner	Number of Samples	Data Range (m)	Median (m)	RMSE (m)	R^2
NIR (1064 nm)	448	0.14	0.025	0.025	0.96
Green (515 nm)	448	0.17	−0.013	0.028	0.95

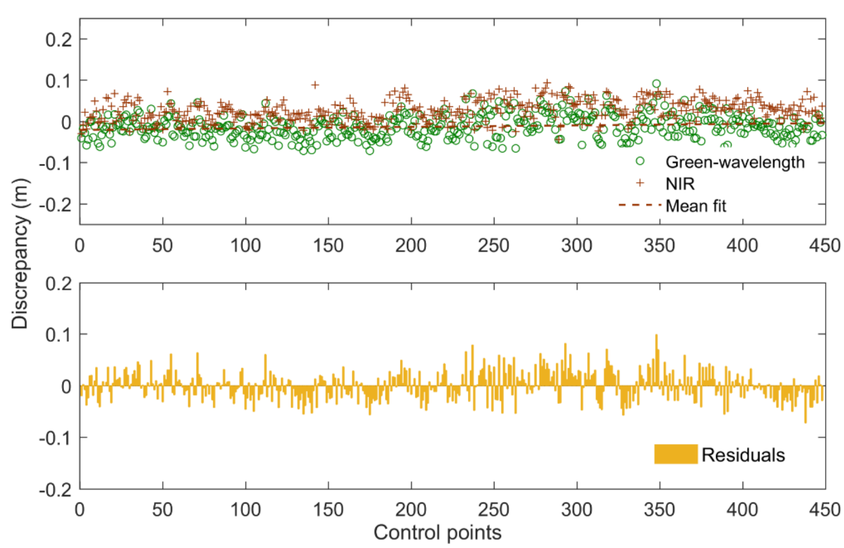

Figure 4-4. Comparison of heights as measured by each Chiroptera scanner. Results indicated a median bias of less than 4 cm measured from an altitude of 500 m.

4.4.2. Pixel Reflectance

Six ISODATA classes of pixel reflectance (1-low, 2-mixed, 3-moderate-low, 4-moderate-high, 5-high, and 6-unclassified/cloud) were generated, which was in line with the Alaskan North Slope study (Saylam and others, 2017). The classifications were based on 2% spectral variability, and results omitted excessive turbid and unclassified/cloud areas using masking polygons. Table 4-6 presents the pixel count (%) of each image as the result of ISODATA classification, and the maps illustrate the dynamic nature of the lagoon by indicating the water quality variations (Figures 4-5 a–d). Interpreting the results and predicting the temporal changes that occurred over the years is possible, and these variations can uncover potential geomorphological changes such as subsidence or coastal erosion. Additionally, results may highlight the need to update local charts and coastal geology maps.

We can assume the following statements by examining the findings:

- In 2016, the average reflectance values were the lowest; therefore, the overall water quality was higher. Furthermore, the moderate-high and high reflectance classes indicated the lowest pixel counts (3.54%), confirming higher water quality, particularly in the southwestern parts of the lagoon (Figure 4-5 a).
- In 2017, the low reflectance classes were least significant (1.05%), while the mixed reflectance class registered (6.02%) as the most substantial, translating to the lowest water quality of all years analyzed (Figure 4-5 b).
- In 2018, pixel count was lower in moderate-high and high reflectance classes (5.22%), which translated to lower water quality. However, water quality has increased visibly in the northern parts of the lagoon (Figure 4-5 c).
- In 2019, the low reflectance class registered the highest pixel count (4.33%), resulting in the most suitable conditions for SDB analysis (Figure 4-5 d).

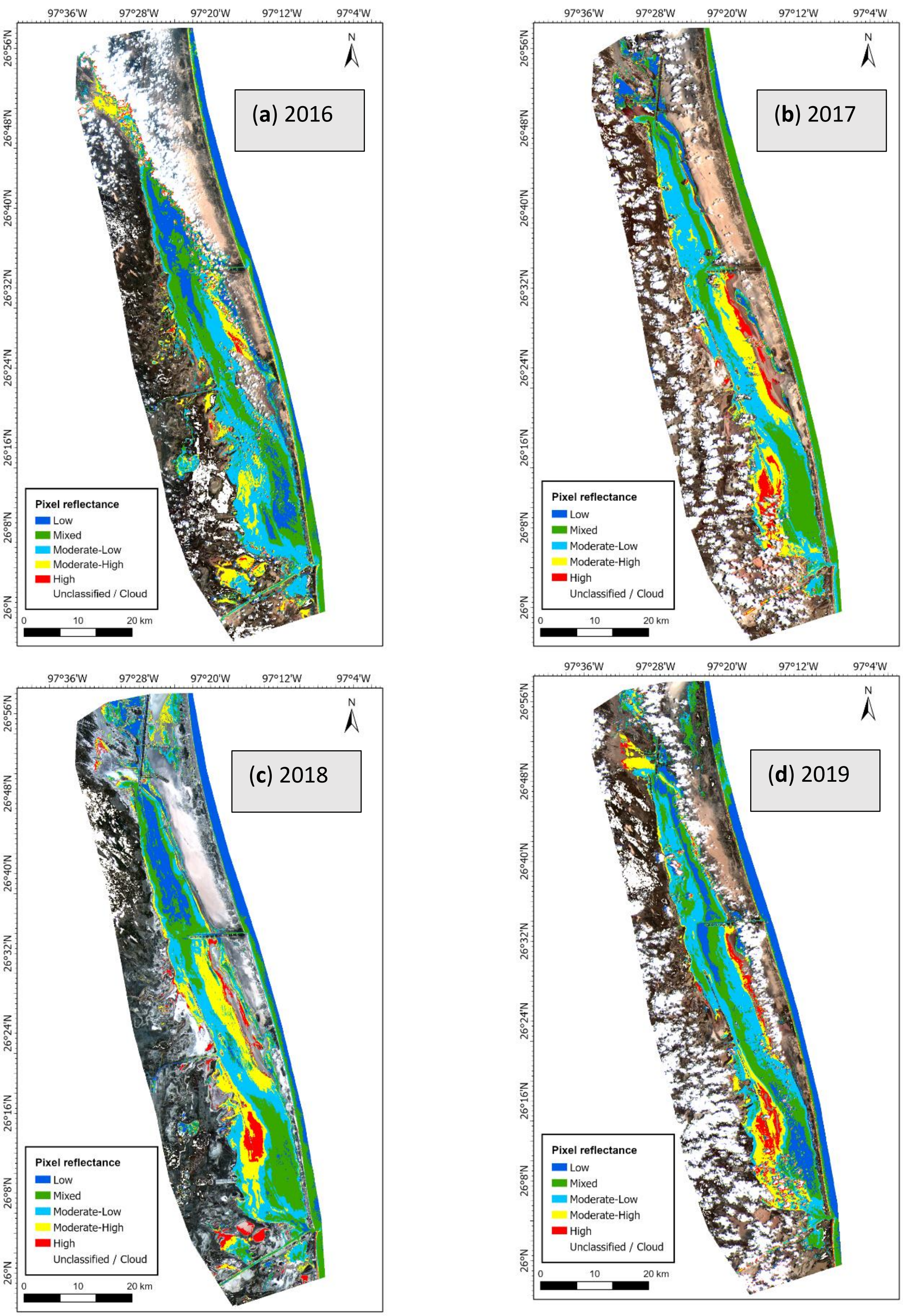

Figure 4-5. (a–d) Pixel reflectance as recorded with Sentinel-2A L1C Band 5, classified using ENVI v5.5 ISODATA algorithm.

Table 4-6. Pixel reflectance count (%) of Lower Laguna Madre imagery, classified by ENVI's ISODATA algorithm. N/A indicates the areas outside the study area.

Imagery	Pixel Reflectance Count (%)						
	1-Low	2-Mixed	3-Moderate-Low	4-Moderate-High	5-High	6-Unclassified/Cloud	N/A
2016	4.16	5.79	6.11	2.97	0.58	0.09	80.31
2017	1.05	6.02	5.58	3.18	1.05	0.04	83.07
2018	3.94	5.68	5.51	4.08	1.14	0.14	79.50
2019	4.33	4.91	5.37	2.66	1.18	0.09	81.47

4.4.3. Lidar Bathymetry

Chiroptera measured the lagoon bottom deepest at 3.35 m in Area-1 and 4.25 m on the northeastern edge of the survey area, at the Gulf coastline. Lidar measurements indicated the mean depth of the lagoon was no more than 0.61 m, where 42.65% of the depths registered were between 0.4 m and 1.2 m, and only 1.07% of measurements were deeper than 2 m (Figure 4-6).

We completed the lidar data acquisition campaign in approximately 60 flight hours. Due to the tides, surface datasets revealed height differences of 0.84 m (lowest = −0.28 m MSL, highest = 0.56 m MSL) in two weeks. The mean surface height was 0.04 m, and the standard deviation was 0.18 m throughout the data acquisition campaign. Surface height variation aligned with the 0.9 m tide range that was observed at the Port Isabel gauge in May 2017 (Figure 4-7).

We must emphasize that lagoon bottom measurements shallower than 0.4 m may not represent the true bottom due to the environmental limitations imposed by turbidity and the waveform sampling capability of Chiroptera's digitizer. Particularly in moderately turbid sections of the lagoon, a considerable number of lidar beams penetrated the water column slightly. However, beams were scattered and reflected to the receiver by suspended material before reaching the bottom, causing very shallow depths or no depths to be registered. Therefore, measurements greater than 0.4 m (>51%) have a higher probability of being accurate and represent the actual lagoon bottom (Figure 4-8).

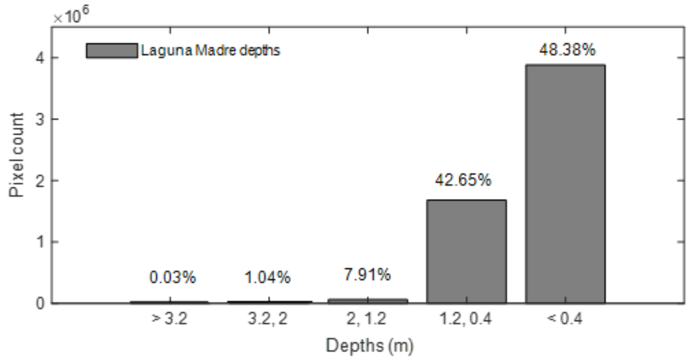

Figure 4-6. Lidar bathymetry of the entire lagoon. The mean depth was 0.61 m, and 42.65% of all measurements were between 0.4 and 1.2 m.

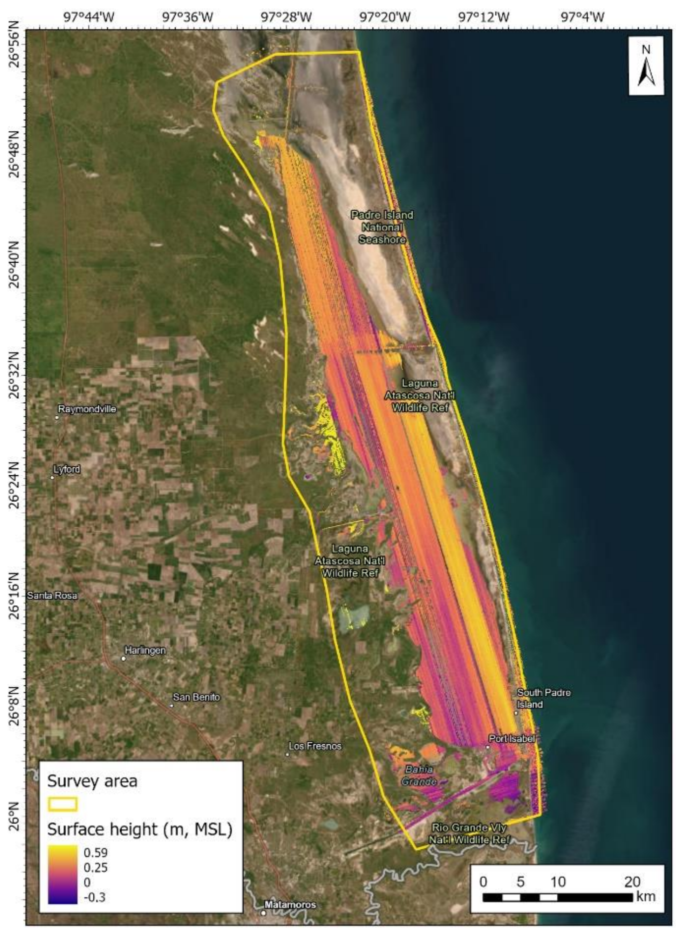

Figure 4-7. Surface elevation variation during airborne data acquisition campaign. The mean height was 0.04 m, and the standard deviation was 0.18 m.

Figure 4-8. Lagoon bottom as measured with Chiroptera. 51% percent of the lagoon depths were greater than 0.4 m.

4.4.4. Lidar Bathymetry versus Sonar

The varying levels of turbidity and transparency influenced lidar and sonar measurements, especially in the southwestern and northern sections. A comparison of depths indicated that sonar (d*S*) recorded deeper versus lidar (d*L*) in all in-situ areas, and the mean difference was greater at locations with higher turbidity, which exposed a limitation of lidar bathymetry. In Area-1, lagoon was transparent, and the bottom had mixed properties, where sonar would naturally have deeper penetration due to smaller footprint. In Area-2, we observed moderate levels of turbidity, and algorithm matched reduced number of returns to sonar recordings. In Area-3, where turbidity was the highest, lidar returns were scattered and attenuated rapidly, either on the immediate surface or in the water column, resulting in fewer matches between the measurements (Table 4-7). Investigating the results further, we can consider the following statements for each of the in-situ areas:

- In Area-1, the water was shallow, the bottom was visible to the observer, and we sampled the lowest turbidity (2.7 NTU). Initially, the comparison algorithm returned poor correspondence efficiency (5%) in matching sonar to lidar measurements because of the sparse nature of sonar recordings. Therefore, we increased the distance of circumcenter triangle coverage (default $dS1i$ = 1 m) of lidar TIN patches to 5 m and the height (h) tolerance to 1 m (default = 0.5 m). We kept the slope angle at the default setting (45°). As a result, the algorithm efficiency increased, and the matching rate improved (55%). The correspondence produced a linear relationship, where returns deeper than 1 m were scattered (R^2 = 0.68). In this location, the average height for lidar/sonar was −0.87/−0.92 m MSL and the deepest measurement was −1.83 m MSL (Figures 4-9 a, b).
- In Area-2, the lagoon bottom was partially visible, and we observed varying Secchi disk depths (0.6–0.9 m). Overall, turbidity increased (8.6 NTU), and the comparison algorithm matched fewer sonar to lidar measurements (40%), producing less dependable matches, particularly in depths shallower than 1 m, indicating the increased turbidity. The mean lidar depth was −1.09 m MSL, and the sonar measured 14 cm deeper (−1.23 m MSL). The correspondence between the measurements was linear but produced a less favorable agreement (R^2 = 0.38, Figures 4-10 a, b).
- In Area-3, deeper bottom and poor water quality were observed. The Secchi disk depths were recorded between 0.7 and 1.3 m, and we sampled turbidity at 10.5 NTU; hence, lidar beam amplitudes were insufficient to measure the lagoon bottom. With default threshold parameters, the comparison algorithm produced unreliable results; consequently, we applied looser values to the experiment ($dS1i$ = 10 m) and the algorithm included more legitimate matches. As a result, the matching efficiency dropped (8%) and generated a linear agreement (R^2 = 0.71). The mean lidar depth was −1.14 m MSL, and sonar measured deeper at −1.39 m MSL (Figures 4-11 a, b).

Table 4-7. Sonar versus lidar bathymetry comparison at in-situ locations.

In-Situ Area	Mean Turbidity (NTU)	Comparison Parameters (dSli, h, Slope Angle)	Matching (%)	Mean Depth (dL/dS, m, MSL)	Difference (dL-dS, m)	RMSE (m)	R^2
1	2.7	5/1/45	55	−0.87/−0.92	−0.05	0.15	0.68
2	8.6	5/1/45	40	−1.09/−1.23	−0.14	0.18	0.38
3	10.5	10/1/45	8	−1.14/−1.39	−0.25	0.27	0.71

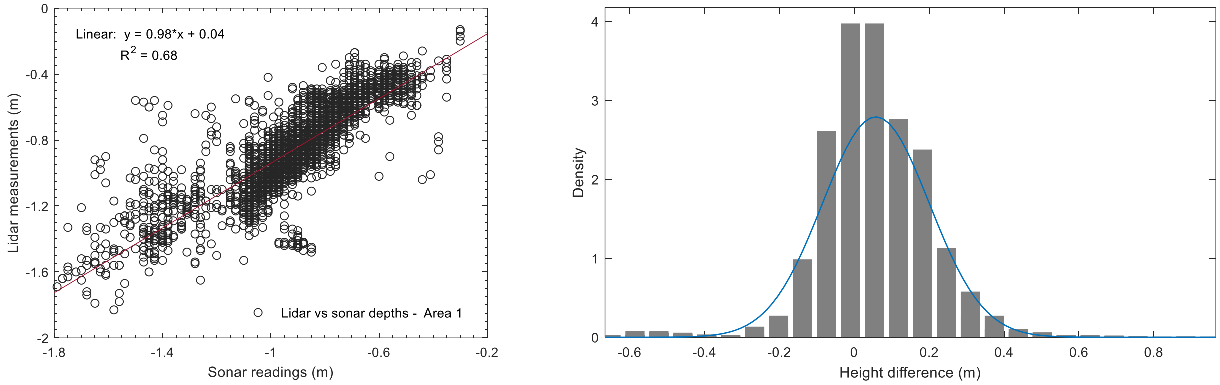

Figures 4-9. (a, b). In Area-1, lidar and sonar heights produced a linear agreement ($R^2 = 0.68$), indicating higher turbidity levels in depths greater than 1 m. The sonar-recorded slightly deeper compared to lidar measurements (dZ = 5 cm).

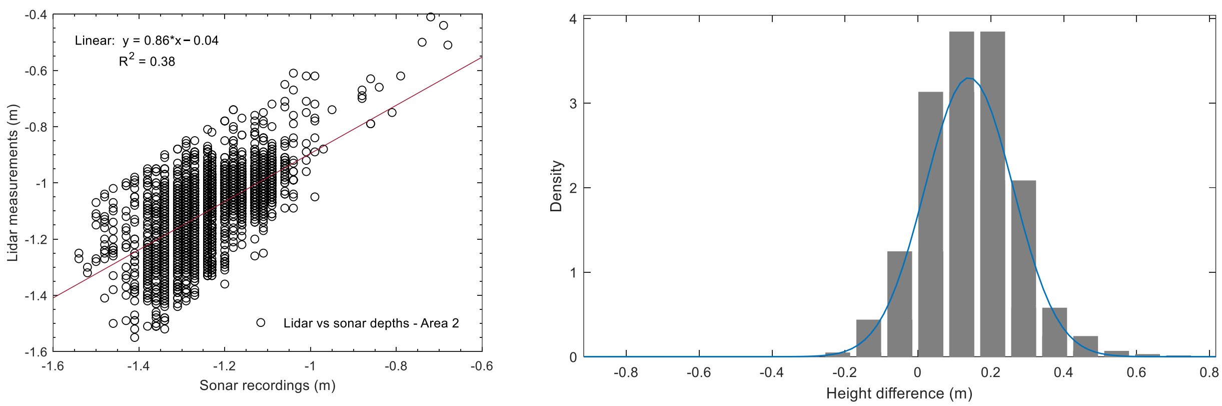

Figures 4-10. (a, b). In Area-2, turbidity was high in depths shallower than 1 m (mean = 8.6 NTU), scattering and attenuating lidar pulses, influencing the correspondence between lidar and sonar measurements adversely ($R^2 = 0.38$). The mean height difference was 14 cm.

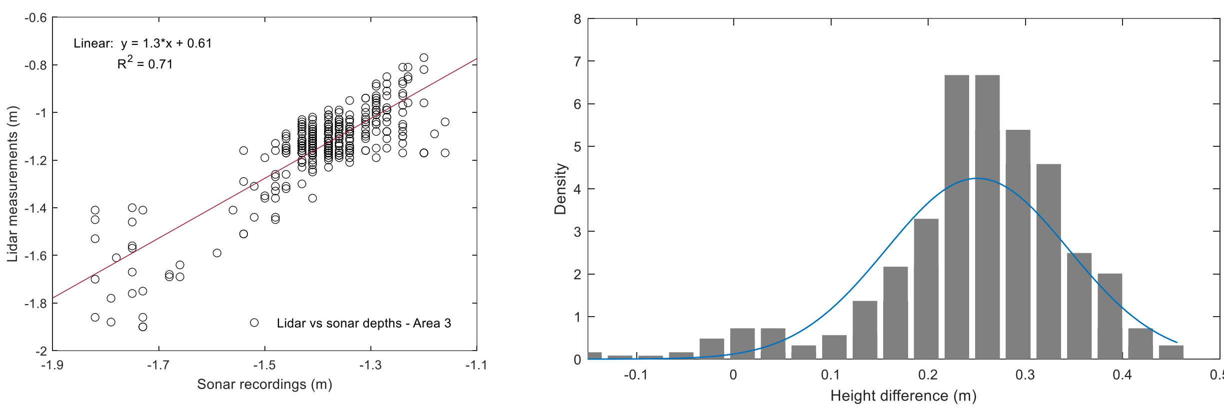

Figures 4-11. (a, b): In Area-3, turbidity was the highest (mean = 10.5 NTU) and increased with depth. Fewer sonar and lidar measurements were matched (8%) because of loose algorithm thresholds. The mean height difference increased to 25 cm, improving the regression, and generating a bi-modal distribution ($R^2 = 0.71$).

4.4.5. Satellite-Derived Bathymetry versus Lidar Bathymetry

We compared the SDB findings to lidar measurements at in-situ locations in Area-1 and Area-2 and omitted those in Area-3 because the location was blocked with excessive clouds. Because SDB measurements were coarse, the matching process did not produce a reliable correspondence. Using a 5 m threshold, in Area-1, where turbidity was lower, mean satellite bathymetry was 13 cm deeper compared to lidar measurements (−0.99 m versus −0.86 m MSL), and using a 10 m threshold, the mean difference was reduced to 11 cm. In Area-2, where turbidity and depths increased, we observed mean heights matching each other within 0.02 m (Table 4-8). To visualize the relationship further, we plotted sample height profiles and produced histograms (Figures 4-12 and 4-13). In both in-situ locations, SDB produced linear measurements with a low standard deviation (0.03 m), where lidar measurements were scattered, and produced a higher standard deviation (0.16 m). We calculated the RMSE between the measurements at less than 0.15 m.

Studying the SDB results and their correspondence to lidar measurements at both in-situ locations, we can assume that the optical technology has depth-resolving limitations in shallow waters with varying turbidity. However, results suggested that SDB correlated adequately with lidar measurements, indicating the depth coarsely, and can be an effective method to evaluate the feasibility of conducting an expensive and comprehensive airborne lidar survey campaign.

Table 4-8. Comparison of SDB to lidar measurements in 2017. Area-3 was covered with clouds (N/A) and was excluded from the study.

In-Situ Area	Pixel Reflectance Category	Mean Turbidity (NTU)	Comparison Parameters (*dSli*, *h*, Slope Angle)	Correlation (%)	Mean ALB (m, MSL)	Mean SDB (m, MSL)	Mean Difference (d*L*-d*S*, m)	RMSE (m)
1	1-Low	2.7	5/0.5/45	46	−0.86	−0.99	−0.13	0.15
1	1-Low	2.7	10/0.5/45	66	−0.88	−0.99	−0.11	0.14
2	2-Mixed	8.6	5/0.5/45	42	−1.06	−1.05	0.01	0.14
2	2-Mixed	8.6	10/0.5/45	61	−1.06	−1.04	0.02	0.15
3	N/A	10.5			N/A			

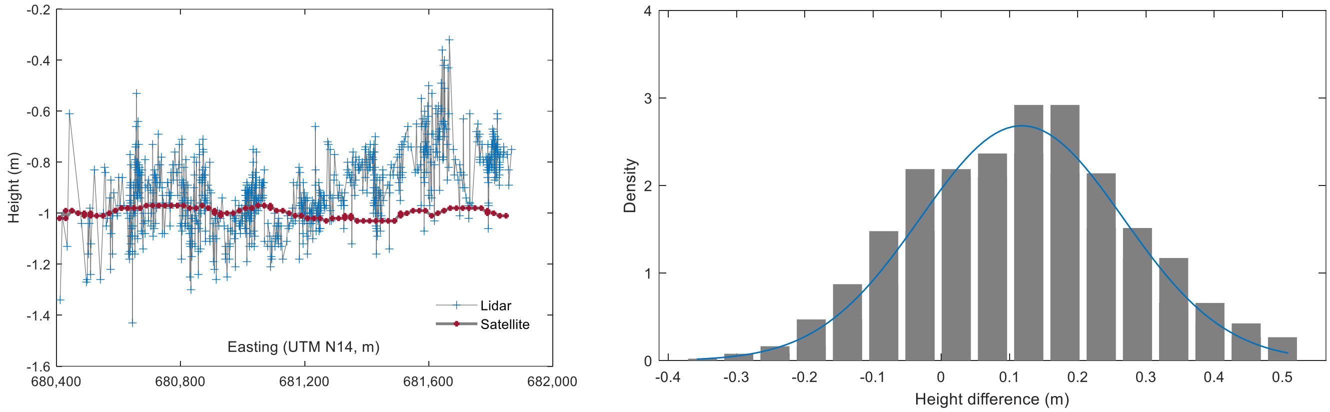

Figures 4-12. (a, b). SDB versus lidar bathymetry in 2017 in Area-1. Measurement differences produced a skewed distribution and SDB measured deeper than lidar (mean difference < 13 cm).

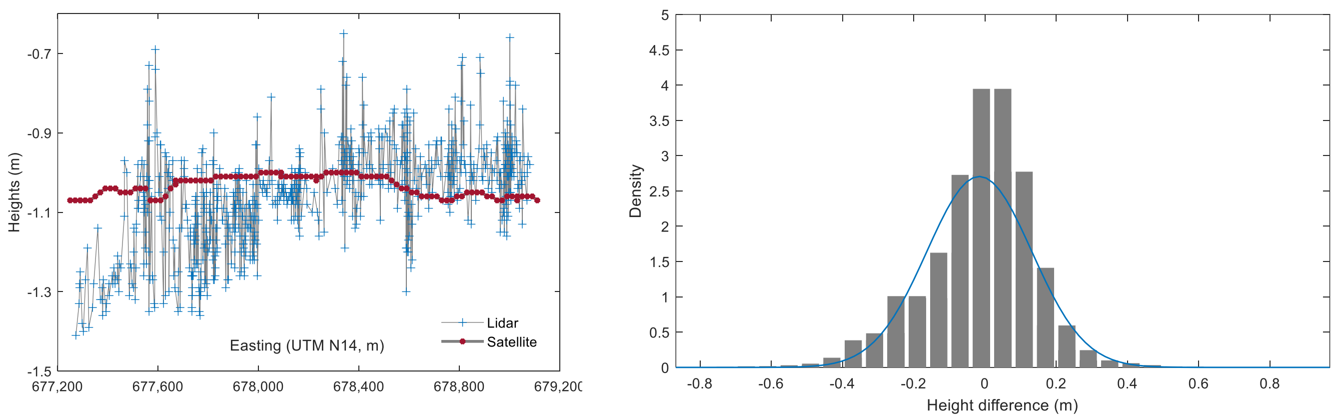

Figures 4-13. (a, b). SDB versus lidar depths in 2017 in Area-2. Turbidity increased, and the confidence between the measurements declined (<61%), particularly in areas deeper than 1 m.

4.5. Discussion

In this study, we acquired, processed, and analyzed remotely sensed datasets of Lower Laguna Madre and investigated the depths in the *height* domain. Our objective was driven by a desire to further understand and quantify the quality-control aspects of airborne lidar bathymetry with applicable survey methods, as we previously demonstrated at inland water reservoirs (Saylam and others, 2020; Saylam and others, 2018).

In Laguna Madre, we conducted an extensive in-situ campaign to understand and classify the water conditions and the expectant ALB depth measurement performance. We investigated 4-years of satellite imaging that were captured in the same time frame of lidar data acquisition and conducted pixel reflectance analysis to generate spatial masks, distinguishing land and water boundaries. Further investigating the reflectance findings, we were able to classify areas that were impacted by persistent and elevated levels of turbidity. We established in-situ locations in the south end of lagoon using the reflectance analysis results and identified areas that represented slightly different environmental conditions. This practice helped us to apply in-situ measurement findings to lagoon in general, where access in the north was restricted and not feasible. Therefore, we demonstrated that in large and remote survey locations where in-situ measurements may not be practical or sufficient to cover all areas, a preliminary satellite imaging pixel reflectance analysis can provide a cost-effective means of establishing localized in-situ locations, representative of all areas.

In our study, we found that higher levels of turbidity (>2.7 NTU) reduced the correspondence between sonar and lidar measurements and negatively impacted the confidence in lidar readings. Although this may be an expected finding, the turbidity levels that adversely affect lidar bathymetry performance have not been thoroughly documented in the literature. Additionally, by observing transparency with a Secchi disk, we were able to calculate the diffuse attenuation coefficient and correlate turbidity levels with the theoretical maximum depths achievable by the first-generation Chiroptera lidar system. The western coastal waters of the Gulf of Mexico are turbid due to currents and winds that carry sediment from river discharges (Shideler, 1984). Understanding and documenting the limitations of ALB usage is thus critical for coastal and estuarine studies along the Gulf Coast. The newer Chiroptera-series ALB systems generate stronger green-wavelength pulses and, with larger beam divergences, are likely to marginally increase depth penetration performance in similar environmental conditions.

Laguna Madre was large and environmental conditions varied quickly. Because lidar and satellite imagery were not acquired concurrently, depths would vary with tides. To align all measurements with each other, we converted lidar measurements to real world heights using the GEOID12B model, adjusted all depths to MSL, and applied tide corrections. An essential part of this study was to compute optical satellite imaging bathymetry and compare the findings to lidar depths. ENVI's SPEAR algorithm was trained using the TCEQ and sonar depths where it was applicable, and the depth comparison was applied to two in-situ locations with transparent and moderate-turbidity levels, where lidar bathymetry was studied. SDB results revealed similar and uniform depths, where lidar was detailed and more receptive to the changes in depth and turbidity levels. The absolute mean depth difference between the technologies was not high (< 13 cm) and due to the linear form of SDB results, the RMSE did not fluctuate (~14 cm). There are studies that investigated the affect of turbidity in SDB performance (Caballero and Stumpf, 2023; McCarthy and others, 2022), and they revealed the limitations at deeper coastal waters. Because Laguna Madre was shallow, the depth difference was marginally smaller.

Lidar bathymetry versus sonar depth comparison revealed adequate results that exceeded the Special-Order 1b standards set by the International Hydrographic Organization (total vertical uncertainty < 0.26 m, depths shallower than 10 m, (IHO, 2020). Complying with Special Order 1a requires measuring a cubic target in the water column, and future research may explore the option of a more comprehensive accuracy assessment in a location with similar environmental conditions. Additionally, as discussed in this study, particularly in deeper waters, the use of a sonar unit with attitude information recording may increase confidence in the measurements.

ALB technology is effective and detailed for mapping the bottoms of shallow, transparent waters, with numerous studies documenting its use in coastal regions with calm, stable conditions. An earlier study discussed challenges of conducting lidar surveys in areas like Laguna Madre (Pastol, 2011); however, more recent studies using newer-generation ALB systems in more challenging environmental conditions are limited. Nevertheless, in this study, we investigated the practical challenges and technological limitations, confirming that ALB technology was unable to measure 48% of the lagoon bottom, highlighting a significant limitation of the methodology.

4.6. Conclusions

In conclusion, we addressed doubts concerning the reliability of water bottom measurements using airborne lidar and optical imaging methods to support bathymetric mapping efforts in a hyper-saline lagoon in southern Texas. Overall, we conclude the following as the answers to our research questions outlined in the introduction:

- Measuring the lagoon bottom with airborne lidar has practical and theoretical limitations. The technology was unable to measure 48% Laguna Madre depths. Its use is costly and, therefore, more suitable for coastal areas with more favorable environmental conditions. We recommend that researchers carefully assess local conditions, plan missions accordingly and adjust survey areas as needed before undertaking data acquisition campaigns.
- *In-situ* campaigns are an essential practice of mapping with airborne lidar bathymetry. As demonstrated, we recommend careful planning and executing in-situ campaigns with airborne missions. Sonar surveys are invaluable to confirm the bottom (or *depth*) measurements attained by airborne lidar; however, sonar units require calibration to align with the survey location's environmental conditions.

- Our study highlights the need to conduct satellite imaging analysis before surveying estuaries and oceanic areas using an airborne lidar system applicable to large inland water reservoirs. Analysts can estimate and modify their survey requirements with the resultant pixel reflectance analysis and predict the areas with different water quality characteristics for establishing in-situ locations, representative of the areas with access restrictions.
- Airborne lidar bathymetry is more detailed compared to SDB. Coarse grid sampling of satellite bathymetry limited a comprehensive depth comparison and cross-use of datasets. However, the study results indicated adequate agreement between the measurements, particularly in the transparent sections of the lagoon.

In Lower Laguna Madre, the water conditions were variable, and depths were shallow for effective airborne lidar mapping efforts. Our study indicated that 51% of the lagoon was in acceptable limits of bathymetric mapping (deeper > 0.4 m). However, we should emphasize that even in transparent water conditions, shallower depths would push the theoretical and practical bottom mapping limitations of the technology. It is common that an ALB can map depths exceeding 40 m, and SDB is effective up to 20 m in ideal environmental conditions, and both technologies have proven their effectiveness. However, we intended to fill the gap in the literature that these technologies are not novel, but they have theoretical and practical limitations, particularly in dynamic estuaries and oceanic environments.

Acknowledgments

TWDB staff Caimee Schoenbaechler, Amin Kiaghadi, and Joey Thomas supplied valuable feedback. Aspen Helicopters of Oxnard, California, provided the survey aircraft and the aircrew. BEG researchers Tiffany Caudle and John Hupp participated in fieldwork and contributed to field data processing. Jackson School of Geosciences graduate student Shelby Short assisted with the article graphics. University of Ottawa faculty Anders Knudby provided valuable feedback. We thank all others who were involved and made this comprehensive study possible.

Abbreviations

UTM E	Universal Transverse Mercator–Easting (m)
UTM N	Universal Transverse Mercator–Northing (m)
Avg. NTU	Average measured turbidity in nephelometric turbidity unit
Secchi	Observed Secchi disk depth (m)
K_d	Diffuse attenuation coefficient
VB	Water bottom is visible to the observer.
WP	Waypoint location marked for a sonar measurement (observer-triggered measurement).
Avg. sonar depth	Average depth of all sonar measurements in a 1 m radius (automatically derived).
CL0	Lidar vector data, Class 0, surface, NIR + green wavelength.
CL7	Lidar vector data, Class 7, bottom, green wavelength, standard bathymetric algorithm.
CL10	Lidar vector data, Class 10, bottom, green wavelength, enhanced bathymetric algorithm.
N/A	Not Applicable.

Appendix 4A. Turbidity and Sonar Depth Measurements.

Table A4-9. [Appendix 4-A] *In situ* measurements

Location	Survey Area	Date	UTM E	UTM N	Reading 1	Reading 2	Reading 3	AVG NTU	Secchi (m)	*Kd*	WP SNR Depth (m)	Avg. SNR Depth (m)	Lidar Depth CL0–CL7 (m)	Lidar Depth CL0–CL10 (m)
2		2017-05-01	681,989.95	2,891,306.11	0.60	0.70	0.61	0.64	VB	N/A	1.49	1.13	1.06	N/A
3		2017-05-01	682,546.59	2,891,234.73	2.21	2.49	2.81	2.50	VB	N/A	1.85	1.83	1.08	2.16
4		2017-05-01	681,723.88	2,891,259.92	2.10	2.02	2.01	2.04	VB	N/A	1.26	1.29	1.34	1.53
5		2017-05-01	680,939.15	2,891,230.51	2.38	2.99	2.79	2.72	VB	N/A	1.38	1.38	1.42	1.50
6		2017-05-01	681,101.49	2,890,944.68	1.60	1.81	1.99	1.80	VB	N/A	1.35	1.38	1.40	1.47
7	1	2017-05-01	681,434.53	2,890,731.42	1.90	2.16	2.24	2.10	VB	N/A	1.38	1.30	1.23	1.41
8		2017-05-01	681,985.00	2,890,432.00	2.82	3.70	4.55	3.69	VB	N/A	1.33	1.33	1.37	1.47
9		2017-05-01	682,282.75	2,890,039.69	2.81	3.18	3.26	3.08	VB	N/A	N/A	1.27	1.34	1.59
10		2017-05-01	681,075.64	2,889,328.48	1.75	1.52	1.99	1.75	VB	N/A	1.19	1.22	1.11	1.40
11		2017-05-01	680,624.58	2,888,914.09	3.36	3.62	4.10	3.69	VB	N/A	1.28	1.33	0.05	N/A
12		2017-05-01	680,311.53	2,889,005.78	4.64	5.26	5.68	5.19	VB	N/A	1.45	1.44	1.44	1.63
13		2017-05-05	678,831.78	2,894,403.48	1.31	1.51	1.59	1.47	VB	N/A	1.28	1.25	1.37	N/A
14		2017-05-05	678,364.02	2,894,849.48	1.34	1.82	1.81	1.66	VB	N/A	1.19	1.21	1.35	1.38
15		2017-05-05	677,943.08	2,895,043.14	2.79	2.93	3.39	3.04	VB	N/A	1.23	1.23	1.13	N/A
16		2017-05-05	677,471.31	2,895,420.79	3.66	7.90	8.02	6.53	VB	N/A	1.40	1.40	1.49	1.63
17		2017-05-05	677,293.56	2,895,990.83	3.78	11.50	12.20	9.16	VB	N/A	1.26	1.42	N/A	1.85
18		2017-05-05	676,829.28	2,896,189.47	15.90	17.30	19.30	17.50	0.6	2.67	1.61	1.63	N/A	2.17
19	2	2017-05-05	677,032.68	2,897,036.17	10.20	15.50	16.40	14.03	0.7	2.29	1.52	1.53	N/A	1.97
20		2017-05-05	677,611.28	2,897,369.09	7.57	9.04	11.00	9.20	0.85	1.88	1.38	1.35	1.54	1.22
21		2017-05-05	677,341.54	2,898,209.33	4.27	4.95	5.52	4.91	VB	N/A	1.45	1.41	1.67	1.72
22		2017-05-05	676,915.17	2,897,588.56	8.69	11.50	12.30	10.83	0.7	2.29	1.57	1.54	1.27	1.59
23		2017-05-05	677,020.09	2,896,493.08	10.50	12.80	12.70	12.00	0.9	1.78	1.57	1.57	N/A	2.58
24		2017-05-05	676,501.32	2,895,309.69	14.00	18.90	19.70	17.53	0.8	2.00	1.66	1.67	N/A	N/A
25		2017-05-05	677,336.30	2,894,813.24	3.85	3.43	3.90	3.73	VB	N/A	1.42	1.42	1.51	1.73
26		2017-05-12	672,597.73	2,888,097.92	11.10	15.70	16.70	14.50	0.7	2.29	1.83	1.79	N/A	1.96
27		2017-05-12	673,745.52	2,887,921.14	11.10	17.10	21.70	16.63	0.7	2.29	1.97	1.97	N/A	2.04
28		2017-05-12	674,964.06	2,887,817.43	9.48	13.50	16.10	13.03	0.7	2.29	1.90	1.90	N/A	N/A
29		2017-05-12	676,179.75	2,887,926.15	8.91	11.90	12.10	10.97	0.85	1.88	2.13	2.15	N/A	N/A
30		2017-05-12	676,968.38	2,888,786.30	3.12	4.00	5.05	4.06	1.3	1.23	1.52	1.51	1.25	1.45
31	3	2017-05-12	675,270.36	2,888,720.85	9.03	15.80	19.00	14.61	0.7	2.29	1.92	1.94	N/A	N/A
32		2017-05-12	674,052.80	2,888,881.79	10.80	13.40	13.20	12.47	0.8	2.00	2.02	2.01	N/A	1.86
33		2017-05-12	674,961.02	2,889,283.61	15.20	15.00	16.50	15.57	0.75	2.13	2.06	2.02	N/A	N/A
34		2017-05-12	676,290.01	2,889,264.61	5.44	8.22	9.33	7.66	1	1.60	1.90	1.89	N/A	2.61
35		2017-05-12	676,841.89	2,889,261.02	1.80	2.80	3.09	2.56	VB	N/A	1.59	1.55	1.33	1.51
36		2017-05-12	677,419.18	2,889,228.25	2.47	3.33	4.08	3.29	VB	N/A	1.59	1.54	1.33	1.48

Appendix 4B. Lidar Bathymetry Waveform Classes

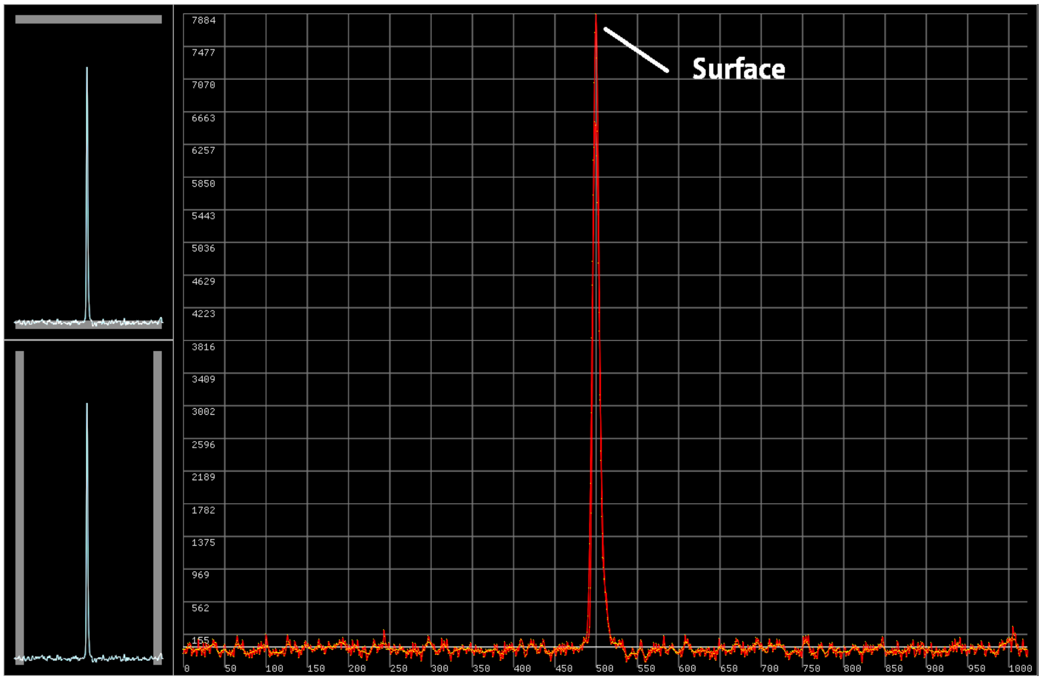

Figure S4-A1. Class 0. Synthetic water surface is interpolated using a proprietary algorithm. A strong NIR backscatter surface peak estimates the elevation of the water surface, confirmed by the immediate peaks in the green wavelength.

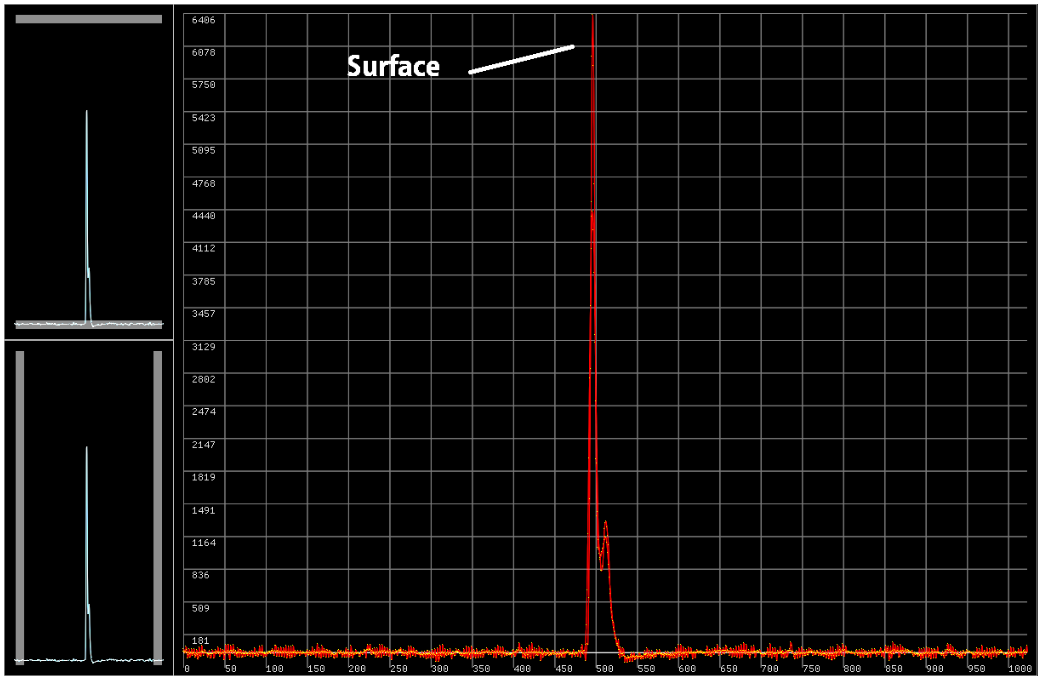

Figure S4-A2. Class 5. Water surface represented by the first strong backscatter peak from the green wavelength waveform, without the use of an NIR channel.

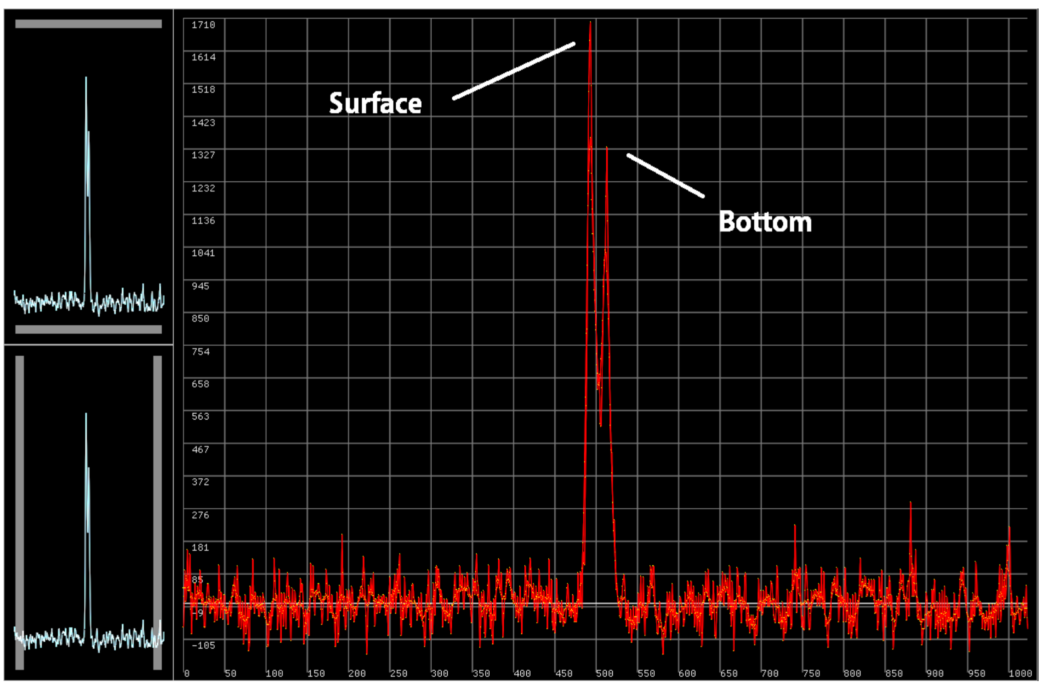

Figure S4-A3. Class 7. Last return originating from a reflective backscatter surface (or the bottom) in the water column and calculated by a strong peak in the waveform.

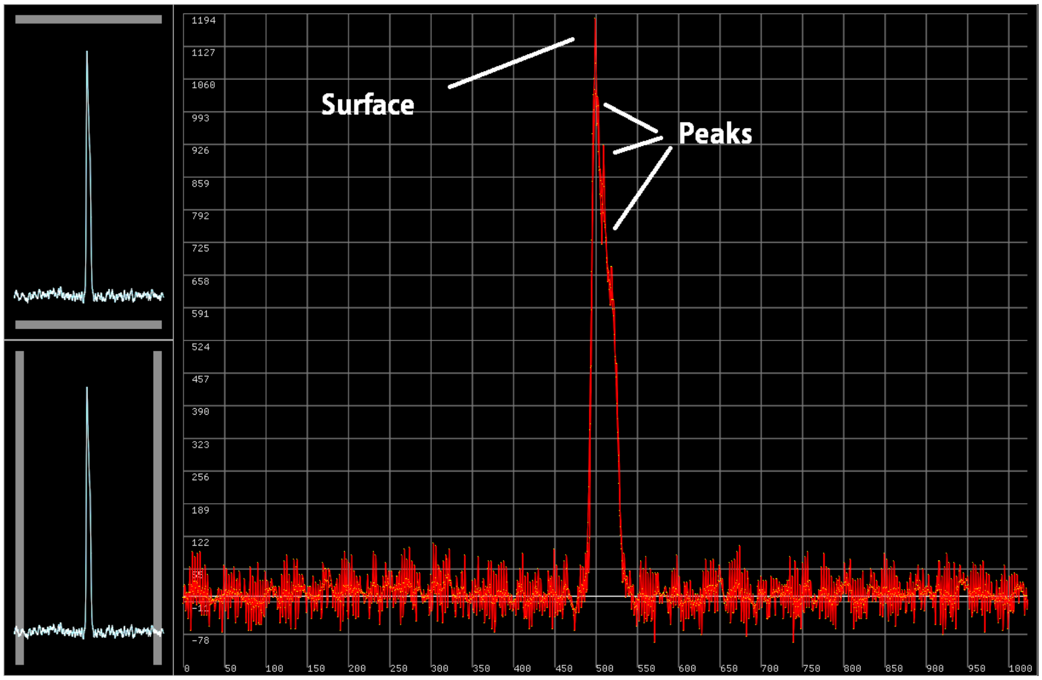

Figure S4-A4. Class 10. A reflective surface (or bottom) detected in the water column and calculated using peaks of lower amplitude than those used in Class 7.

4.7. References

Höfle, B.; Rutzinger, M. Topographic Airborne lidar in Geomorphology: A Technological Perspective. *Z. Für Geomorphol.* 2011, *55*, 1–29. https://doi.org/10.1127/0372-8854/2011/0055S2-0043.

Lohani, B.; Ghosh, S. Airborne lidar Technology: A Review of Data Collection and Processing Systems. *Proc. Natl. Acad. Sci. India Sect. A Phys. Sci.* 2017, *87*, 567–579. https://doi.org/10.1007/s40010-017-0435-9.

Guenther, G.C. *Airborne Lidar Bathymetry*; Digital elevation model technologies and applications: The DEM user's manual; American Society of Photogrammetry and Remote Sensing: Pennsylvania State University Press, University Park, PA, 2007; pp. 253–320.

Mandlburger, G. Bathymetry from Images, lidar, and Sonar: From Theory to Practice. *PFG–J. Photogramm. Remote Sens. Geoinf. Sci.* 2021, 89, 69–70. https://doi.org/10.1007/s41064-021-00153-0.

Brock, J.C.; Purkis, S.J. The Emerging Role of Lidar Remote Sensing in Coastal Research and Resource Management. *J. Coast. Res.* 2009, *10053*, 1–5. https://doi.org/10.2112/SI53-001.1.

Klemas, V. Beach Profiling and Lidar Bathymetry: An Overview with Case Studies. *J. Coast. Res.* 2011, *277*, 1019–1028. https://doi.org/10.2112/JCOASTRES-D-11-00017.1.

Paine, J.G.; Caudle, T.L.; Andrews, J.R. Shoreline and Sand Storage Dynamics from Annual Airborne LIDAR Surveys, Texas Gulf Coast. *J. Coast. Res.* 2017, *333*, 487–506. https://doi.org/10.2112/JCOASTRES-D-15-00241.1.

Toure, S.; Diop, O.; Kpalma, K.; Maiga, A. Shoreline Detection Using Optical Remote Sensing: A Review. *ISPRS Int. J. Geo-Inf.* 2019, *8*, 75. https://doi.org/10.3390/ijgi8020075.

Dogliotti, A.I.; Ruddick, K.G.; Nechad, B.; Doxaran, D.; Knaeps, E. A Single Algorithm to Retrieve Turbidity from Remotely Sensed Data in All Coastal and Estuarine Waters. *Remote Sens. Environ.* 2015, *156*, 157–168. https://doi.org/10.1016/j.rse.2014.09.020.

Garg, V.; Senthil Kumar, A.; Aggarwal, S.P.; Kumar, V.; Dhote, P.R.; Thakur, P.K.; Nikam, B.R.; Sambare, R.S.; Siddiqui, A.; Muduli, P.R.; and others Spectral Similarity Approach for Mapping Turbidity of an Inland Waterbody. *J. Hydrol.* 2017, *550*, 527–537. https://doi.org/10.1016/j.jhydrol.2017.05.039.

Caballero, I.; Stumpf, R.P. Retrieval of Nearshore Bathymetry from Sentinel-2A and 2B Satellites in South Florida Coastal Waters. *Estuar. Coast. Shelf Sci.* 2019, *226*, 106277. https://doi.org/10.1016/j.ecss.2019.106277.

Ji, X.; Yang, B.; Tang, Q.; Xu, W.; Li, J. Feature Fusion-Based Registration of Satellite Images to Airborne lidar Bathymetry in Island Area. *Int. J. Appl. Earth Obs. Geoinf.* 2022, *109*, 102778. https://doi.org/10.1016/j.jag.2022.102778.

Yeu, Y.; Yee, J.-J.; Yun, H.; Kim, K. Evaluation of the Accuracy of Bathymetry on the Nearshore Coastlines of Western Korea from Satellite Altimetry, Multi-Beam, and Airborne Bathymetric lidar. *Sensors* 2018, *18*, 2926. https://doi.org/10.3390/s18092926.

Saylam, K.; Hupp, J.; Andrews, J.; Averett, A.; Knudby, A. Quantifying Airborne Lidar Bathymetry Quality-Control Measures: A Case Study in Frio River, Texas. *Sensors* 2018, *18*, 4153. https://doi.org/10.3390/s18124153.

Saylam, K.; R. Averett, A.; Costard, L.; D. Wolaver, B.; Robertson, S. Multi-Sensor Approach to Improve Bathymetric Lidar Mapping of Semi-Arid Groundwater-Dependent Streams: Devils River, Texas. *Remote Sens.* 2020, *12*, 2491. https://doi.org/10.3390/rs12152491.

McManus, J. Hydrodynamics of Estuaries Edited by Bjorn Kjerfve, Vol II Estuarine Case Studies, CRC Press, 1988. No. of Pages: 125. *Earth Surf. Process. Landf.* 1990, *15*, 384–385. https://doi.org/10.1002/esp.3290150411.

Tunnell, J.W.; Judd, F.W. (Eds.) *The Laguna Madre of Texas* and *Tamaulipas*, 1st ed.; Gulf Coast studies; Texas A&M University Press: College Station, TX, USA, 2002; ISBN 978-1-58544-133-4.

Dubin, J.T.; Ballard, M.S.; Lee, K.M.; McNeese, A.R.; Sagers, J.D.; Venegas, G.R.; Rahman, A.F.; Wilson, P.S. Compressional and Shear in Situ Measurements in the Lower Laguna Madre. *J. Acoust. Soc. Am.* 2018, *143*, 1712–1712. https://doi.org/10.1121/1.5035575.

Webster, T.; McGuigan, K.; Crowell, N.; Collins, K.; McDonald, C. *Acquisition* and *Processing of Topo-Bathymetric Lidar for Isle Madame in Support of the World Class Tanker Safety Initiative*; NSCC Applied Geomatics Research Group: Middleton, NS, USA, 2015; pp. 1–56.

Kinzel, P.J.; Wright, C.W.; Nelson, J.M.; Burman, A.R. Evaluation of an Experimental lidar for Surveying a Shallow, Braided, Sand-Bedded River. *J. Hydraul. Eng.* 2007, *133*, 838–842. https://doi.org/10.1061/(ASCE)0733-9429(2007)133:7(838).

Estrada, J. *Investigating the Effects of Nutrient Limitation, Light,* and *Salinity upon Seagrass Cover in the Lower Laguna Madre*; GIS in Water Resources; The University of Texas at Austin: Austin, TX, USA, 2018; p. 11.

Medwin, H. Speed of Sound in Water: A Simple Equation for Realistic Parameters. *J. Acoust. Soc. Am.* 1975, *58*, 1318–1319.

Habib, A. Accuracy, Quality Assurance and Quality Control of Lidar Data. In *Topographic Laser Ranging* and *Scanning: Principles* and *Processing*; Taylor and Francis: Boca Raton, FL, USA, 2009; pp. 269–294; ISBN 978-1-4200-5142-1.

Boris, Delaunay, Sur la sphere vide— *Izv. Akad. Nauk SSSR, Otdelenie Matematicheskii i Estestvennyka Nauk*, *7, pp* 793-800, 1934

Quan, X.; Fry, E.S. Empirical Equation for the Index of Refraction of Sea Water. *Appl. Opt.* 1995, *34*, 3477. https://doi.org/10.1364/AO.34.003477.

Roswell, A.; Halikas, G. *The Index of Refraction of Seawater*; University of California San Diego, Scripps Institution of Oceanography: La Jolla, CA, USA, 1976; p. 121.

Mondejar, J.P.; Tongco, A.F. Estimating Topsoil Texture Fractions by Digital Soil Mapping—A Response to the Long-Outdated Soil Map in the Philippines. *Sustain. Environ. Res.* 2019, *29*, 31. https://doi.org/10.1186/s42834-019-0032-5.

Ashphaq, M.; Srivastava, P.K.; Mitra, D. Review of Near-Shore Satellite Derived Bathymetry: Classification and Account of Five Decades of Coastal Bathymetry Research. *J. Ocean Eng. Sci.* 2021, *6*, 340–359. https://doi.org/10.1016/j.joes.2021.02.006.

Saylam, K.; Brown, R.A.; Hupp, J.R. Assessment of Depth and Turbidity with Airborne Lidar Bathymetry and Multiband Satellite Imagery in Shallow Water Bodies of the Alaskan North Slope. *Int. J. Appl. Earth Obs. Geoinf.* 2017, *58*, 191–200. https://doi.org/10.1016/j.jag.2017.02.012.

Gernez, P.; Lafon, V.; Lerouxel, A.; Curti, C.; Lubac, B.; Cerisier, S.; Barillé, L. Toward Sentinel-2 High Resolution Remote Sensing of Suspended Particulate Matter in Very Turbid Waters: SPOT4 (Take5) Experiment in the Loire and Gironde Estuaries. *Remote Sens.* 2015, *7*, 9507–9528. https://doi.org/10.3390/rs70809507.

Delegido, J.; Verrelst, J.; Alonso, L.; Moreno, J. Evaluation of Sentinel-2 Red-Edge Bands for Empirical Estimation of Green LAI and Chlorophyll Content. *Sensors* 2011, *11*, 7063–7081. https://doi.org/10.3390/s110707063.

Sebastiá-Frasquet, M.-T.; Aguilar-Maldonado, J.A.; Santamaría-Del-Ángel, E.; Estornell, J. Sentinel 2 Analysis of Turbidity Patterns in a Coastal Lagoon. *Remote Sens.* 2019, *11*, 2926. https://doi.org/10.3390/rs11242926.

Gerald L. Shideler. (1984). Suspended Sediment Responses in a Wind-Dominated Estuary of the Texas Gulf Coast. *SEPM Journal of Sedimentary Research*, *Vol. 54*. https://doi.org/10.1306/212F84E5-2B24-11D7-8648000102C1865D

Caballero, I., & Stumpf, R. P. (2023). Confronting turbidity, the major challenge for satellite-derived coastal bathymetry. *Science of The Total Environment*, *870*, 161898. https://doi.org/10.1016/j.scitotenv.2023.161898

McCarthy, M. J., Otis, D. B., Hughes, D., & Muller-Karger, F. E. (2022). Automated high-resolution satellite-derived coastal bathymetry mapping. *International Journal of Applied Earth Observation and Geoinformation*, *107*, 102693. https://doi.org/10.1016/j.jag.2022.102693Ahmad, A.; Sufahani, S.F. Analysis of Landsat 5 TM Data of Malaysian Land Covers Using ISODATA Clustering Technique. In Proceedings of the 2012 IEEE Asia-Pacific Conference on Applied Electromagnetics (APACE), Melaka, Malaysia, 11–13 December *2012*; IEEE: Melaka, Malaysia, 2012; pp. 92–97.

Yuan, C.; Yang, H. Research on K-Value Selection Method of K-Means Clustering Algorithm. *J* 2019, *2*, 226–235. https://doi.org/10.3390/j2020016.

Wang, X.; Ling, F.; Yao, H.; Liu, Y.; Xu, S. Unsupervised Sub-Pixel Water Body Mapping with Sentinel-3 OLCI Image. *Remote Sens.* 2019, *11*, 327. https://doi.org/10.3390/rs11030327.

Kaplan, G.; Avdan, U. Object-Based Water Body Extraction Model Using Sentinel-2 Satellite Imagery. *Eur. J. Remote Sens.* 2017, *50*, 137–143. https://doi.org/10.1080/22797254.2017.1297540.

de Carvalho, O.; Guimarães, R.; Silva, N.; Gillespie, A.; Gomes, R.; Silva, C.; de Carvalho, A. Radiometric Normalization of Temporal Images Combining Automatic Detection of Pseudo-Invariant Features from the Distance and Similarity Spectral Measures, Density Scatterplot Analysis, and Robust Regression. *Remote Sens.* 2013, *5*, 2763–2794. https://doi.org/10.3390/rs5062763.

Favoretto, F.; Morel, Y.; Waddington, A.; Lopez-Calderon, J.; Cadena-Roa, M.; Blanco-Jarvio, A. Testing of the 4SM Method in the Gulf of California Suggests Field Data Are Not Needed to Derive Satellite Bathymetry. *Sensors* 2017, *17*, 2248. https://doi.org/10.3390/s17102248.

Stumpf, R.P.; Holderied, K.; Sinclair, M. Determination of Water Depth with High-Resolution Satellite Imagery over Variable Bottom Types. *Limnol. Oceanogr.* 2003, *48*, 547–556. https://doi.org/10.4319/lo.2003.48.1_part_2.0547.

Saylam, K.; Hupp, J.R.; Aaron, R.A. Quantifying the Bathymetry of the Lower Colorado River Basin, Arizona, with Airborne Lidar; presented at ASPRS conference: Baltimore, MD, USA, 2017; Volume 1, pp. 1–11.

Savitzky, A.; Golay, M.J.E. Smoothing and Differentiation of Data by Simplified Least Squares Procedures. *Anal. Chem.* 1964, *36*, 1627–1639. https://doi.org/10.1021/ac60214a047.

IHO. *International Hydrographic Organization, Standards for Hydrographic Surveys*; International Hydrographic Bureau: Monaco, Monaco, 2020; pp. 1–51.

Pastol, Y. (2011). Use of Airborne LIDAR Bathymetry for Coastal Hydrographic Surveying: The French Experience. *Journal of Coastal Research*, *62*, 6–18. https://doi.org/10.2112/SI_62_2

Chapter 5: Airborne lidar to verify ICESat-2 Arctic summer sea ice heights and melt pond bathymetry: Calibration and validation campaign, Greenland 2022

5.1. Introduction

In July 2022, researchers from the University of Texas at Austin (UT Austin) and NASA conducted an airborne lidar data acquisition campaign based in Pituffik Space Base (Pituffik SB, formerly Thule AB) in northwestern Greenland. The calibration and validation (Cal/Val 2022) campaign provided researchers with detailed lidar datasets of Arctic summer sea ice to verify ICESat-2 ATLAS segment heights and bathymetry during the summer melt season.

NASA developed the ICESat-2 (2018-present) observatory principally for cryospheric and climate change studies (Kacimi & Kwok, 2020; Magruder et al., 2024; Petty et al., 2020). ICESat-2 quickly became popular, and researchers applied its data products in studies across numerous disciplines, such as biomass and canopy volume estimation, reservoir bathymetry, and mapping of dune environments (Duncanson et al., 2020; Feng et al., 2023; Li et al., 2023; Rehman et al., 2023). The accuracy assessment of ICESat-2 ATLAS measured elevations in a cryospheric environment was completed earlier in Antarctica, using a network of ground-based global navigation satellite systems (GNSS) measurements (Brunt et al., 2019). Additionally, NASA-owned airborne altimeters, including the LVIS, have been deployed to support satellite altimetry missions and to validate measurements. However, measuring the Arctic Ocean surface elevations and the relevant melt pond depths was challenging with laser altimeters using only near-infrared (NIR) channel (Kwok et al., 2014; Yi et al., 2015). Nonetheless, NASA operated an experimental photon counting lidar system, the Multiple Altimeter Beam Experimental Lidar (MABEL), and the system demonstrated that raw photons include signals that can be extracted to indicate inland and near-shore water surfaces and depths (Jasinski et al., 2016; Ma et al., 2018; Parrish et al., 2019).

Advancements in airborne lidar technology enabled the measurement of ice and snow thickness (Deems et al., 2013). Researchers used the technology to measure the changes in subglacial lakes, analyze glacier surface motion, and assess radiation loading scaling issues over glacierized mountainous terrain (Hopkinson et al., 2001; Jóhannesson et al., 2013; Telling et al., 2017). These studies provided a foundation to support evaluating sea ice surface elevations, including melt pond depths, using an airborne lidar system and comparing measurements with those from ICESat-2.

However, flying over the Arctic Ocean with a conventional slow survey aircraft was not feasible. To address some of these challenges and experiment with a dual-wavelength airborne lidar system, a data acquisition campaign was executed in the summer of 2022, using NASA's Gulfstream V research aircraft (N95NA). Based in Pituffik SB, a Leica Chiroptera-4x (CHIR) airborne lidar system, equipped with separate green and NIR wavelength scanners (515 and 1064 nm), acquired sea ice measurements, supplemented by four-band high-resolution imagery. On the same platform, LVIS (1064 nm) was operated by NASA researchers concurrently with CHIR at lower altitudes, enabling cross-checking of sea ice heights and system calibration.

ICESat-2's ATLAS instrument has multiple beams, with the number of active beams and their power ratios varying. While optimized to measure changes in polar sea ice and land ice, the observatory collects elevation data over all surfaces. Surface-specific datasets are prepared by experts and disseminated with corresponding ATL prefixes (ATLAS products) from the nsidc.org website. In this study, we investigated ATL03 (global geolocated photon data) and ATL07 (Arctic/Antarctic Ocean sea ice elevation) products and identified the following research questions that were applicable to the Cal/Val 2022 campaign:

- Significant technical differences exist between the ICESat-2, CHIR, and LVIS. How can we compare and validate the sea ice heights recorded by ICESat-2 beams with CHIR and LVIS measurements? Which comparison method would yield the best results?
- Quantifying the accuracy of CHIR measurements is fundamental to the study. How do we calibrate CHIR system, and can we verify the calibration with ICESat-2 measurements on a coincident solid surface?
- LVIS and CHIR systems measured sea ice elevations from the same airborne platform using identical near-infrared wavelengths. The height comparison results would further validate the robustness of CHIR's calibration. How do we compare CHIR and LVIS measurements with each other?
- ICESat-2 and CHIR measurements must coincide spatially for accurate comparison. However, ideal coincidence is almost impossible due to logistical and environmental challenges. Therefore, can we modify the location of CHIR point cloud data swath theoretically to match that of ICESat-2 measurements?
- Melt ponds and fractures (leads) form on the sea ice, providing an opportunity to measure and investigate the depths (in the height domain) of ATL03 photons. How can we evaluate and compare ATL03 photon heights using CHIR's green wavelength lidar?

5.2. Materials and methods

5.2.1. CHIR airborne lidar system

Airborne lidar is an active, pulse-based remote-sensing technology for mapping topographic surfaces and depths of shallow water columns. CHIR uses a NIR (1064 nm) wavelength for topographic measurements and a green wavelength (515 nm) for bathymetry. Both scanners operate simultaneously, emitting laser pulses with an incidence angle of 14° to 20° using a Palmer scanner. Elliptical scanning provides an advantage in registering lidar returns on sloped and variable surfaces and measuring irregular sea ice surface elevations. NIR pulses reflect from the water surface, while the green wavelength pulses enter the water column ($t1$), where they slow and attenuate because of natural refraction and scattering. Pulses that do not fully attenuate reflect from the bottom ($t2$) or an object in the water column and the receiver records the entire travel time (Δt) as a waveform, recording the interactions with amplitude changes. Depths are calculated by computing the time difference ($t2$-$t1$) between the waveform peaks, where it is possible to calculate the number of samples and the duration using the digitizer sampling rate (f) (t_d=1/f x Δt). For a comprehensive explanation of CHIR depth computations, interested readers can refer to an earlier study (Saylam et al., 2023).

The positional accuracy of the airborne lidar-derived measurements depends on the determination of system component offset values, such as the eccentricity and misalignment between the scanner laser mirror, the inertial measurement unit (IMU), and the aircraft GNSS antenna reference locations. A boresight and range calibration requires a flat surface with no obstructions to determine roll, pitch, and yaw corrections, whereas a range calibration is the minimization of the recorded and the actual distance measured. The rigorous determination process requires surveying a flat surface using a multi-channel GNSS receiver. These measurements are compared to the lidar-derived triangular irregular network (TIN) surface patch heights using the least-squares regression method. The necessary corrections help to achieve an ideal system calibration (Savitzky & Golay, 1964; Saylam et al., 2018).

We adjusted CHIR system calibration parameters to the checkpoints established on July 10th, 2022, using a multi-channel GNSS receiver. A GNSS base station (BEGB) was setup for base-referencing purposes, and its geographical location was improved using Natural Resources Canada's (NRCan) precise point positioning system (N 76° 32' 12.9469", W 68° 49' 26.9045", H 37.969 m). To further validate the system calibration, we compared CHIR measurements to the ATL03 photon heights that registered on the Pituffik SB runway on 06/05/2021 (RGT-1109) with a strong beam (Figure 5-1). We used a ±0.5 m threshold from the GNSS checkpoints to remove extraneous photon heights that did not represent the tarmac surface (1466 of 6137 photons).

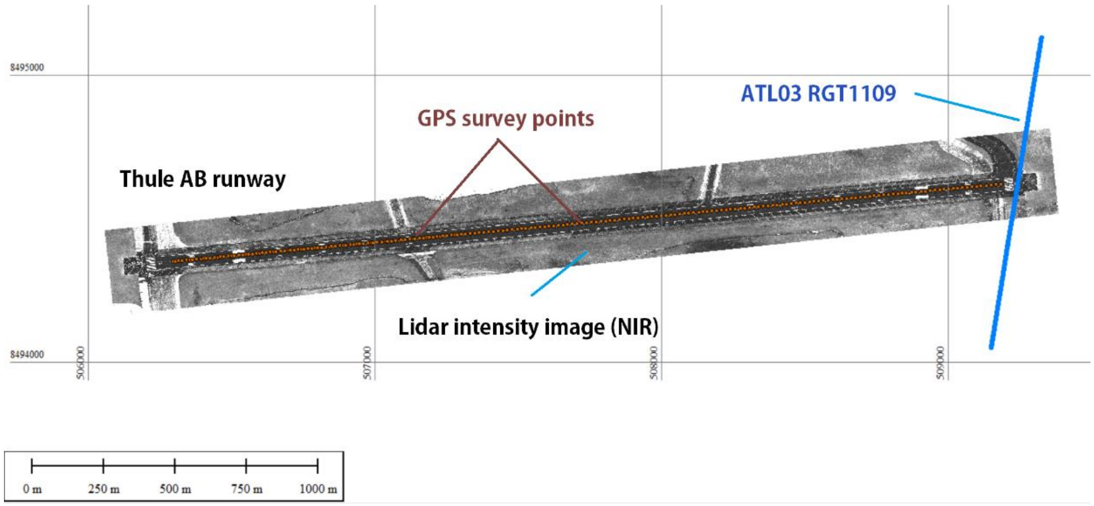

Figure 5-1: Illustration of CHIR NIR lidar intensity image and GNSS checkpoints, established on 10/07/2022. ICESat-2 registered ATL03 photon heights were recorded on the east end of the Pituffik SB runway on 06/05/2021.

5.2.2. ICESat-2

Launched on September 15, 2018, ICESat-2 orbits the Earth at 6.9 kilometers per second at an approximate altitude of 496 km, completing a cycle in approximately 94 minutes. The reference ground tracks (RGTs) are fictional trajectories on the Earth, and ICESat-2 acquires data along 1387 different RGTs, where each track follows the number of 91-day cycles in the mission (Neumann, et al., 2023). Tracks are referred to as “fictional” because the exact ground path that the observatory follows may not be the same with each pass, rather representing an idealized model, not the precise physical path. ICESat-2 transmitter samples the surface at 10 kHz, releasing approximately 20 trillion photons for each pulse, of which only a dozen is typically registered by the beryllium telescope (0.8 m in diameter) (Markus et al., 2017; Neumann et al., 2019). During the Cal/Val 2022 campaign, ICESat-2 ATLAS collected data with three pairs of beams, with an energy ratio of 1:4. The three ground tracks were approximately 3.3 km apart in the across-track direction. The strong and weak beams were separated by 90 m, each beam producing an overlapping (~70%) footprint of approximately 12 m in diameter (Figure 5-2) (Magruder et al., 2020). During the Cal/Val 2022 campaign, the strong (*r-series*) and weak (*l-series*) beam configurations were operational, accommodating disparate energy levels to meet diverse science objectives (Martino et al., 2019).

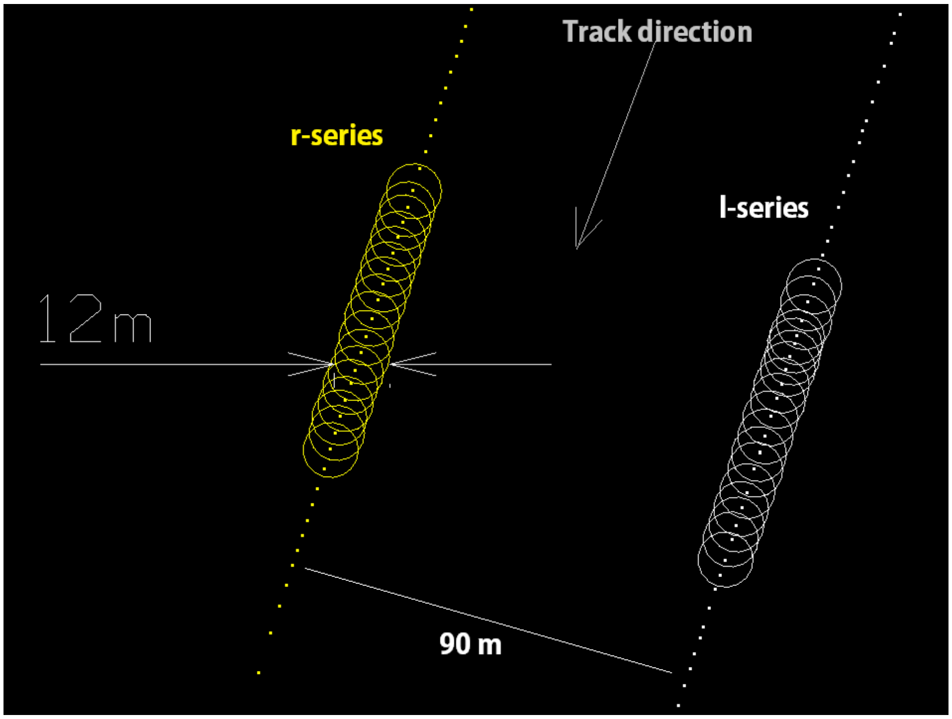

Figure 5-2: Representation of ICESat-2 strong (r-series) and weak (l-series) beam patterns and pulse footprints on the sea ice surface during the 07/26/2022 CHIR mission. The footprints were approximately 12 m in diameter, and they overlapped with each other by ~70%.

5.2.3. Land, Vegetation and Ice Sensor (LVIS)

The LVIS is an airborne scanning laser altimeter designed to operate at high altitudes (nominal altitude, 10 km), producing data swaths up to 2 km wide with 20 m diameter pulse footprints. The new instrument, LVIS-Facility (LVIS-F), began operations in 2017 using a 2.5 kHz scanner, replacing LVIS-Classic with a 1 kHz sensor built in 2010 (Blair et al., 1999). The LVIS-F can be equipped with different laser configurations to deliver specific beam characteristics; a laser type A (Fibertek laser, 1064.2 nm, 4 kHz) was used for the Cal/Val 2022 campaign. During the Cal/Val 2022 campaign, LVIS measured sea ice heights concurrently with CHIR at an altitude of 500 m, whereas LVIS data swath was 80 m wide and CHIR generated swaths of approximately 380 m.

A cross-check analysis would validate calibration for both systems because LVIS and CHIR operated concurrently from the same platform. Initially, we compared CHIR datasets with ellipsoidal heights to a decimated (1/100) LVIS dataset, classified with *z-low* waveform amplitude: the mean elevation of the lowest detected waveform sample. Further, we investigated the orthometric heights using the *z-maxamp* classification[2] that included the necessary geophysical height adjustments.

Table 5-1 compares the technical specifications of all altimeters used in the Cal/Val 2022 campaign. The orbital altitude of ICESat-2 varies, and the pulse footprint diameter at the surfaces were calculated at full angle.

Table 5-1. Comparison of ICESat-2 beams to LVIS and CHIR system specifications operating at 500 m altitude.

	ICESat-2	**LVIS**	**CHIR4X**
Technology	Photon counting	Linear detector	Linear detector
Platform	Orbital	Airborne	Airborne
Wavelength (nm)	532.27	1064.2	515, 1064
Operational altitude (km)	481-511	0.5 to 20	0.5 to 1.5
Velocity (km /h)	24,840	200-600	200-450
Pulse repetition frequency (kHz)	10	4	36-500
Beam divergence	21µRad	1.27 mRad	0.5 mRad (1064 nm) 4.2 mRad (515 nm)
Pulse footprint, altitude (in diameter)	~12 m, in orbit	0.63 m, 500 m	0.25 m (1064 nm), 2.1 m (515 nm), 500 m
Scanning pattern	Near-nadir only, fixed beam pattern	Raster, 6° degrees, half-angle	Elliptic, 20° degrees, half-angle

5.2.4. Study methodology

This study utilized CHIR airborne lidar system to map sea ice and compared the surface elevations and melt pond depths to those measured by ICESat-2 observatory. For this purpose, we followed the flowchart (Figure 5-3) methodology:

[2] LVIS data structure (LDS) 2.0.4. – level 1B geolocated LVIS waveforms: https://lvis.gsfc.nasa.gov/Data/DataStructure.html

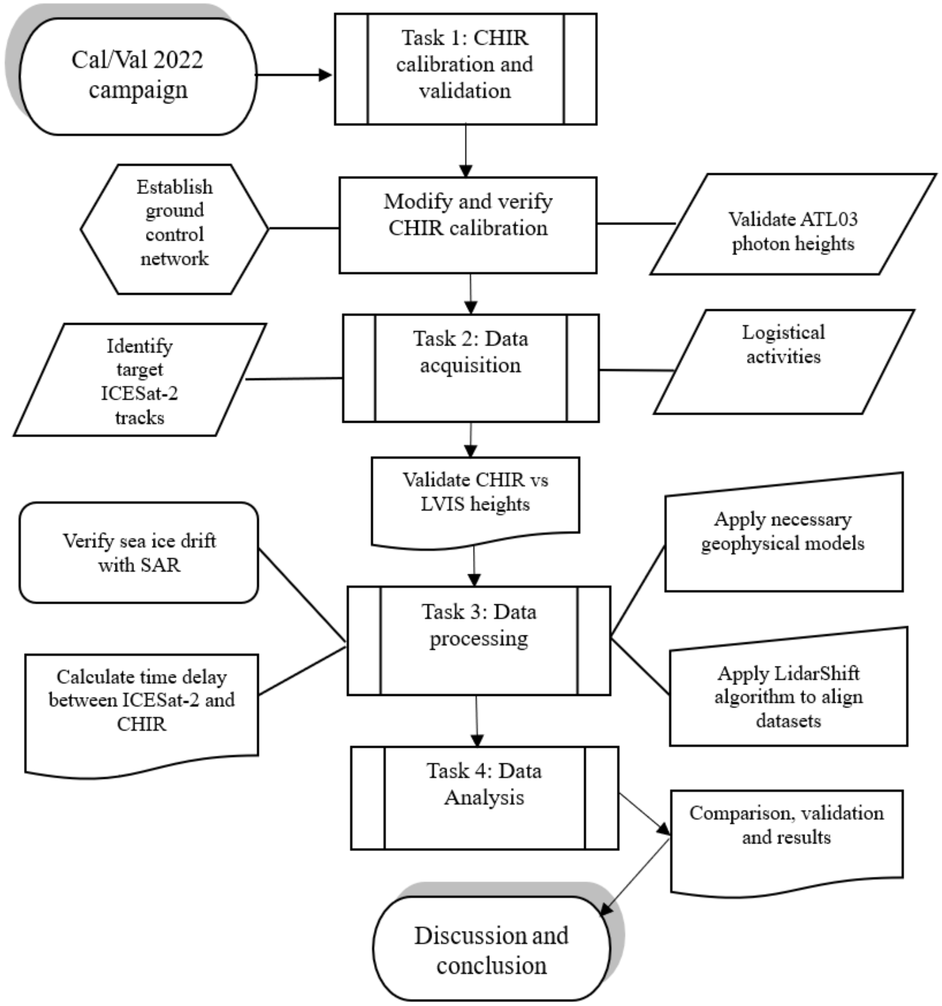

Figure 5-3: Study methodology flow chart.

5.2.5. Data acquisition campaign

CHIR and LVIS were installed onto a Gulfstream V (N95NA) aircraft at Ellington Field in Houston, Texas. This aircraft had a pressurized cabin and two glass viewports, where both instruments were mounted (Figures 5-4 a, b).

(a) (b)

Figures 5-4 (a, b): CHIR and LVIS were installed onto a Gulfstream V (N95NA) aircraft at Ellington Field in Houston, Texas. This aircraft had a pressurized cabin and two glass viewports, where both instruments were mounted.

Before each mission, we investigated ICESat-2 RGTs and calculated target survey locations in the Arctic Ocean. The greatest challenge was aligning the N95NA flight path with the ICESat-2 RGT to acquire coincident measurements because the ICESat-2 travels ~70 times faster than the N95NA. We, therefore, precisely calculated the distance from Pituffik SB to the target survey location in the Arctic Ocean, the flight time, the altitude, and the forecasted weather conditions.

Not all prospective missions were executed because of logistical and environmental challenges. During the 07/26/2022 RGT 531 mission, the time delay of CHIR was achieved to be the smallest (8m 26s to 38m 26s) and the overlapping ratio to ICESat-2 beams was the highest; therefore, data from this mission were selected for this study. The remaining mission data are available but considered out of scope of this study. Due to the excessive length of data swath lines (Flight line 1 and Flight line 2, ~100 km), we split these data swaths into shorter sections (~30 km) and segments (~3 km). Notably, this study analyzed the datasets in selected segments of FL1-C section, where CHIR and ICESat-2 beams recorded optimum overlapping of sea ice measurements. Figure 5-5 illustrates CHIR missions where sea ice measurements were collected. As a reference, the sampling point density of CHIR NIR sensor was ~ 1 pt/m^2, whereas the green-wavelength sensor generated 0.4 pt/m^2.

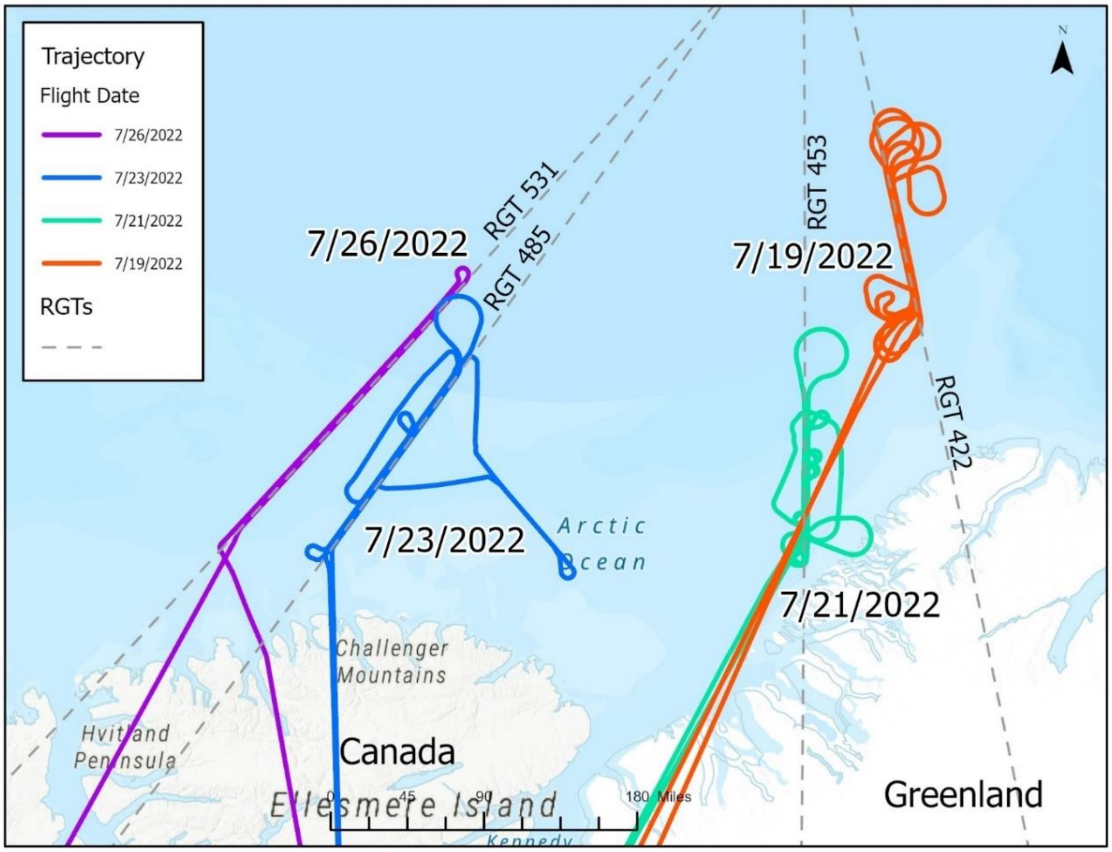

Figure 5-5: CHIR missions in the Arctic Ocean in July 2022. Colored lines indicate the flight trajectories as recorded by the aircraft's GPS, whereas the dashed lines indicate the respective ICESat-2 RGT.

5.2.6. Data products and geophysical height corrections

Comparisons to ICESat-2 ATLAS data products require geophysical height and tidal system adjustments, which include specific models for different products (Kwok et al., 2023). According to NASA, the tidal system refers to how the tidal effect is treated and applied to the solid earth tide model, inclusive of the geoid model. NASA addresses and refers to two tidal systems: the *mean-tide system* and the *tide-free system* (Figure 5-6). The non-periodic, zero frequency, or time-averaged deformation is termed as the *permanent tide*, and it is the cause of the Earth's shape to be slightly compressed at the poles and extended in the equatorial plane. The mean-tide system defines how any surface is measured in the real world, with the influence of the permanent tide present, whereas the tide-free system eliminates the permanent tide deformation from the shape of the Earth, both in terms of a direct (surface and crustal) response. (Robbins et al., 2022). The geoid and solid earth tides reported on ATL03 products are provided in a tide-free system.

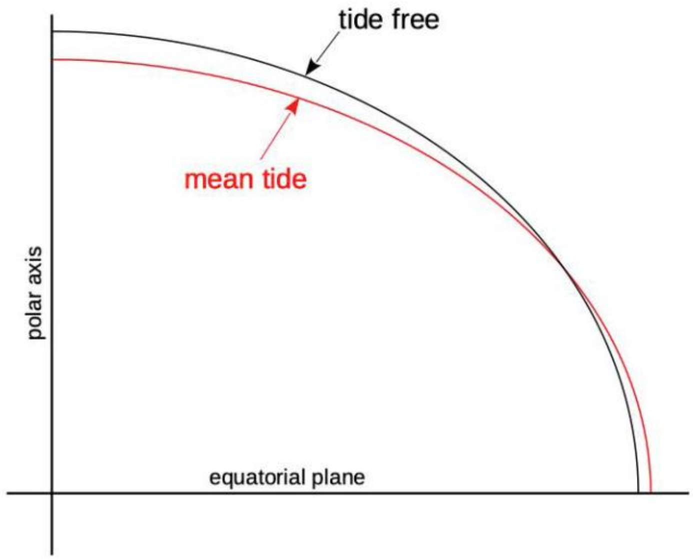

Figure 5-6: The geophysical concept of mean-tide versus tide-free systems illustrated along a meridian line (Robbins, J. and others, 2022).

The ATL03 photons are the standard ATLAS product and contain heights in the ITRF2014 reference frame (International Terrestrial Reference Frame-2014), while positional information is in the WGS-84 G1150 (World Geodetic System-1984) ellipsoid model. In 2024, NASA announced the reference frame switch to ITRF2020 for the data products published after November 2022. Level 2A (L2A) datasets contain information derived from the geolocated sensor data, such as ground elevation, highest and lowest surface return elevations, and other metrics describing the intercepted surface from the tagged photon event. Surface masks are built-in to reduce the volume of ATL03 products, and each photon event is classified as high, medium, or low confidence by generating histograms as a function of height (Neumann et al., 2020).

ATL07 datasets are reported in orthometric elevations and referenced to the mean sea surface (Kwok & Morison, 2016). Further, geophysical corrections in ATL07 products (h_{07_c}) include subtraction of all ATL03 corrections (h_{03_c}) and permanent mean sea surface (h_{mss}, range: -68 to +65 m), time-varying ocean tide (h_{ot}, range: ±6.2 m), long-period equilibrium tide (h_{lpe}, range: -7.1 to +6 cm), and the dynamic inverted barometer (IB) corrections (h_{ib_dyn}, range: -56 to +89 cm). NASA recently revised the IB adjustment and released version 006 (Robbins et al., 2022). Equation 5-1 summarizes the corrections that were applied to CHIR lidar datasets for optimum comparison to ATL07 products.

$$h_{07\_c} = h_{03\_c} - h_{mm} - h_{ot} - h_{lpe} - h_{ib\_dyn} \qquad \text{(Equation 5-1)}$$

5.2.7. Data analysis

We do not assume point-on-point correspondence with vector lidar data (Habib, 2009). Therefore, we used the Delaunay triangulation algorithm to generate TIN surface patches from lidar point cloud data, representing surface morphology (Delaunay, 1932). Several algorithms construct TIN surfaces (e.g., Distance Ordering, Region Growing); however, the Delaunay triangulation algorithm was preferred because of its superior uniform modeling, automation capabilities, and statistical consistency with previous studies (Saylam et al., 2018; Zhu et al., 2008). In summary, a TIN surface patch represents surfaces, created by triangulating a group of vector points selected from connecting and non-overlapping triangles. A patch defines a set of circumcircles (e.g., in 1 m radius) and user-defined proximities of horizontal and vertical distance thresholds (e.g., d=1 m, h=0.5m) and slope angle (e.g., α=45°). In this study, we used CHIR point cloud data to construct the TIN surface patches representing sea ice surfaces, and the average height of each patch was compared to the elevations measured by another survey method (e.g., LVIS, ATL07 segment heights).

5.2.8. Sea ice drift correction

Computation of sea ice drift (motion) was an essential element of this study, enabling CHIR lidar data swaths to align with those of ICESat-2 by compensating for the time difference between the sensors measuring a certain location. This process was required for ideal comparison of heights and depths. Wind is the dominant driver of sea ice motion variability, but ocean currents, tides, and ice freeboard also influence the speed and direction of drift. A popular method is to utilize satellite-based imaging sensor products (e.g., Special Sensor Microwave/Imager, Quick Scatterometer, Advanced Very High-Resolution Radiometer), operating in the optical and microwave range of the electromagnetic spectrum (Gui et al. 2020; Sandven et al. 2023). We investigated the Copernicus Arctic Sea Ice and Analysis Forecast (Phy-Ice-002), which incorporated a stand-alone sea ice model (Next Generation Sea Ice Model, neXtSIM) using Bingham-Maxwell Sea ice rheology (Bingham, 1922; Williams et al., 2021). For those missions (07/21 and 07/23/2022), CHIR lidar swath data overlapped with an adjacent opposite direction flight line, and we were able to calculate the drift metrics using vectorization between selected features. During the 07/26/2022 mission, CHIR did not record overlapping data due to N95NA flight time restrictions. The data swath lines (FL1 and FL2) were separated by approximately 3 km, following the ICESat-2 transmitter paths. As a result, we used the Copernicus neXtSIM model to estimate the drift bearing and the speed (Figures 5-7 a, b). The principal motivation was to estimate the initial sea ice drift values that would apply to the alignment algorithm.

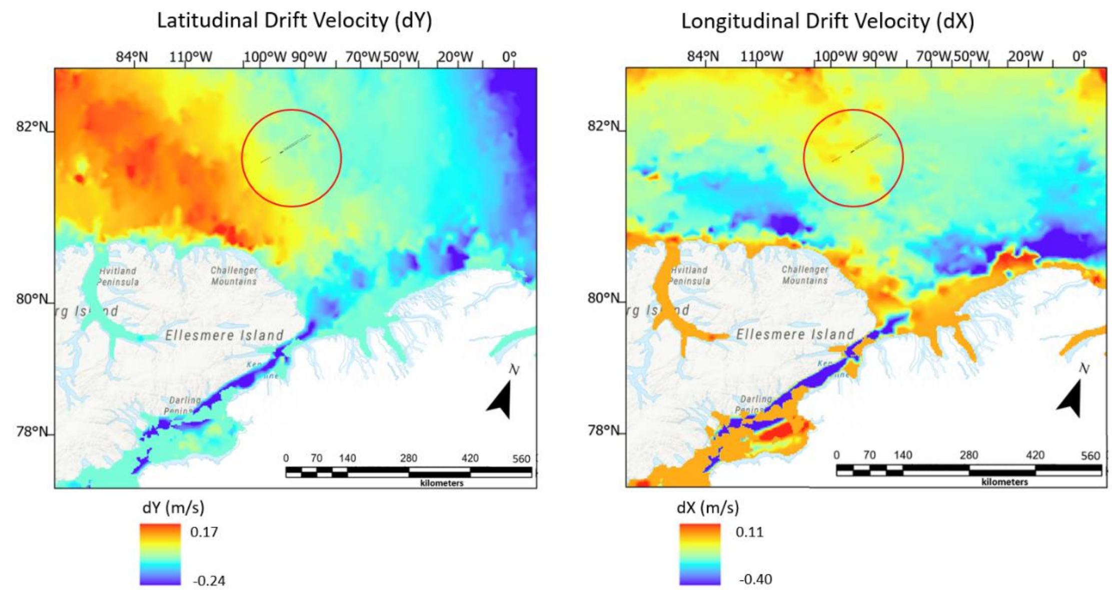

Figure 5-7 (a, b): Copernicus OSI-SAF product. Sea ice drift velocities were reported in m/s, representing estimated latitudinal and longitudinal information (in dY and dX). The circle indicates the location of the flight line (FL1), where CHIR lidar data were collected with the 07/26/2024 mission.

Preferring a more comprehensive approach, we developed an algorithm (*LidarShift*) that modified the position of each CHIR measurement (point) to a theoretical location to align with the specified ICESat-2 beam. There are studies that defined lidar point cloud strip alignment (Habib et al. 2009; Streutker et al. 2011) at stationary surfaces; however, our challenge was to compute an ideal location of correspondence where the surface moved in all directions, 18 to 70 m during the misalignment of sensors. Therefore, for each point, the time difference between CHIR and ICESat-2 observations reaching a location was iteratively computed for different combinations of drift speed and bearing at arbitrary intervals and increments (e.g., 0.002 m/s and 1-degree). During each iteration, the algorithm computed the mean elevation of point cloud data that registered within each ATL07 photon footprint (default=6 m radius, approximately 300 CHIR points). The linear regression tool within the Python *pandas* data analysis library (v.2.0.2) was used to compare values along the track. For the FL1C swath data, we identified three data segments (S12-14) that corresponded in full to the ICESat-2 beams, and we expected to have slight bearing and drift speed variability with each ~3 km segment. Shorter data swath segments (e.g., 1 km) may produce slightly different results, and this option may be investigated in future research.

Using the LidarShift algorithm, we computed the correction vectors (X_C and Y_C) with time difference (t), the speed (V), and the drift bearing (Θ). New coordinates for each point were exported in a text file, and alignment results were calculated for two sets of height values using the SciPy library (v.1.9.3) linear regression function (slope, intercept, r and p values, root-mean-square-deviation (RMSE), and standard error). The calculation results, drift speed and bearing shift were evaluated in each iteration, stored in the data structure and the next iteration with another set of parameters was executed. When all iterations in the user-specified threshold were completed, the new data structure containing the linear regression results was output with the arguments. The combination of drift speed and bearing that produced the highest *R*-squared and the lowest RMSE value was selected as the best alignment, and new CHIR lidar datasets were output. Interested readers can refer to Appendix (5-B) for a complete set of algorithm equations and download the Python algorithm from GitHub.

5.3. Results

5.3.1. Lidar system calibration

We compared CHIR lidar-derived TIN patch surface heights to GNSS checkpoints on the Pituffik SB runway. For both CHIR scanners, the absolute mean height difference was less than 0.01 m, and the coefficient of determination was R^2 =0.99. Further, we confirmed CHIR system calibration with ATL03 photon heights registered on the runway (Table 5-2 and Figures 5-8 a, b). The absolute mean height difference was smaller than 1 cm, equaling the GNSS survey results. The noticeably higher RMSE values were caused by the wider pulse width of ICESat-2, registering varying surface elevations.

Table 5-2. Comparison of CHIR measurements to ATL03 photon heights on the Thule AB runway (ICESat-2 RGT 1109 strong sensor, 06/05/2021).

CHIR Scanner (nm)	Samples	GNSS Threshold (m)	Mean dZ (m)	Median dZ (m)	RMSE (m)	R^2
515	1464	±0.5	-0.001	-0.01	0.198	0.99
1064			-0.008	-0.01	0.186	0.99

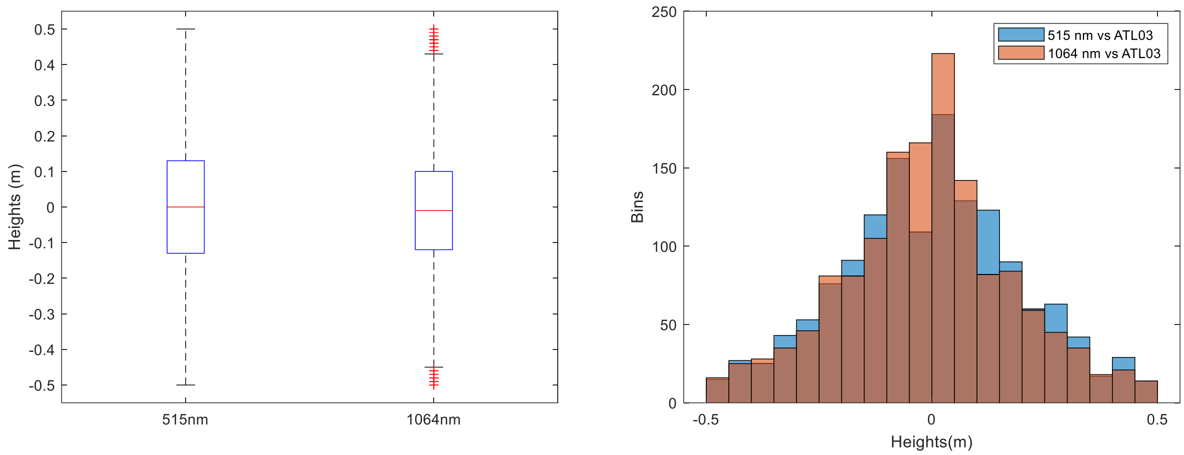

Figures 5-8 (a, b): Boxplot and histogram of ATL03 RGT 1109 photon heights compared to Pituffik SB runway CHIR NIR and green-wavelength measurements. The absolute mean height difference (dZ) was less than 1 cm.

5.3.2. CHIR versus LVIS heights

Height comparison between the CHIR and LVIS on a 31-km long sea ice data swath using *z-low* values of the waveform and ellipsoidal heights indicated $R^2 > 0.98$ and RMSE < 0.045 m. The absolute mean height difference (*dZ*) was less than 0.013 m, where LVIS heights were slightly lower. Comparing the *z-maxamp* of waveform values resulted in a higher number of matching measurements (> 90% versus 88%). The absolute mean height difference was less than 0.04 m, the coefficient of determination was similar ($R^2 > 0.98$), and RMSE < 0.047 m. We further investigated the normality of the measurements and evaluated bivariate spatial association using Lee's measure coefficient (~0.99; Lee, 2001). Interested readers can refer to the detailed results in Appendix (5-A).

5.3.3. Sea ice drift computation

Using the Copernicus neXtSIM model, we estimated the drift speed of the sea ice to be 0.035 m/s for the 07/26/2022 mission. The bearing of the data swath in the northwest direction (287 degrees) was questionable, particularly given the reported northerly winds at 13 km/h. We proceeded to use the LidarShift alignment algorithm by applying the calculated drift speed and an estimated bearing in the direction of the winds. Figure 5-9 shows an example of the algorithm's output applied to ATL07, FL1C-

S12 dataset. The ideal drift bearing and speed adjustment parameters were identified using the highest coefficient of determination (R^2), and the lowest RMSE value (Figure 5-10) between the datasets.

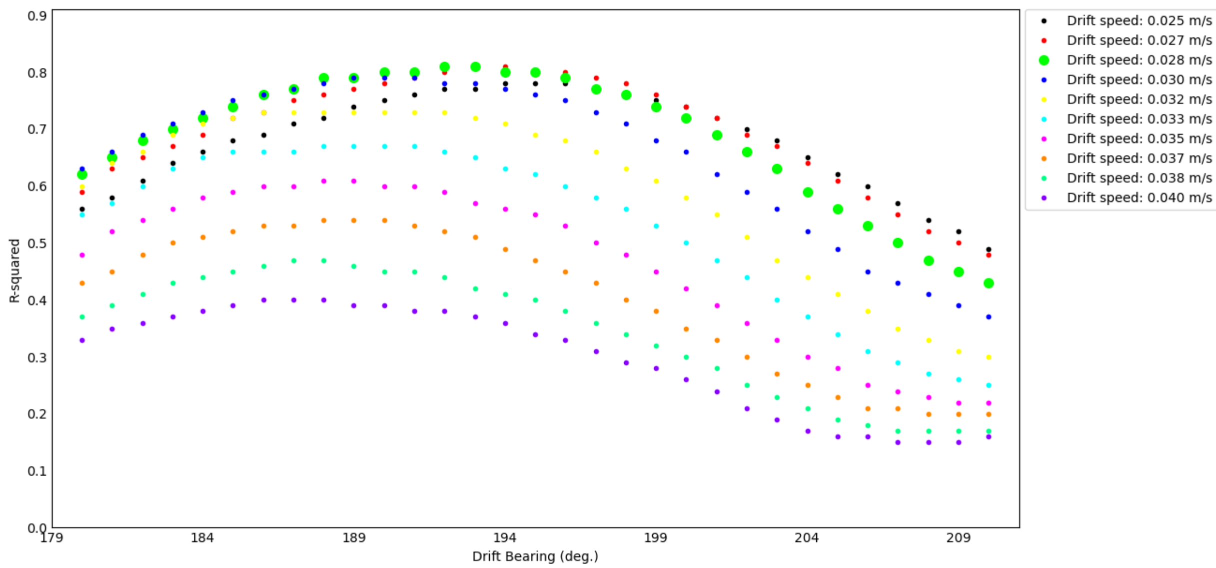

Figure 5-9. Linear regression comparison of ATL07 strong beam elevations and CHIR NIR heights. Each colored line represents an increment of drift speed (~0.002 m/s), with the highest coefficient of determination achieved at a drift speed of 0.028 m/s.

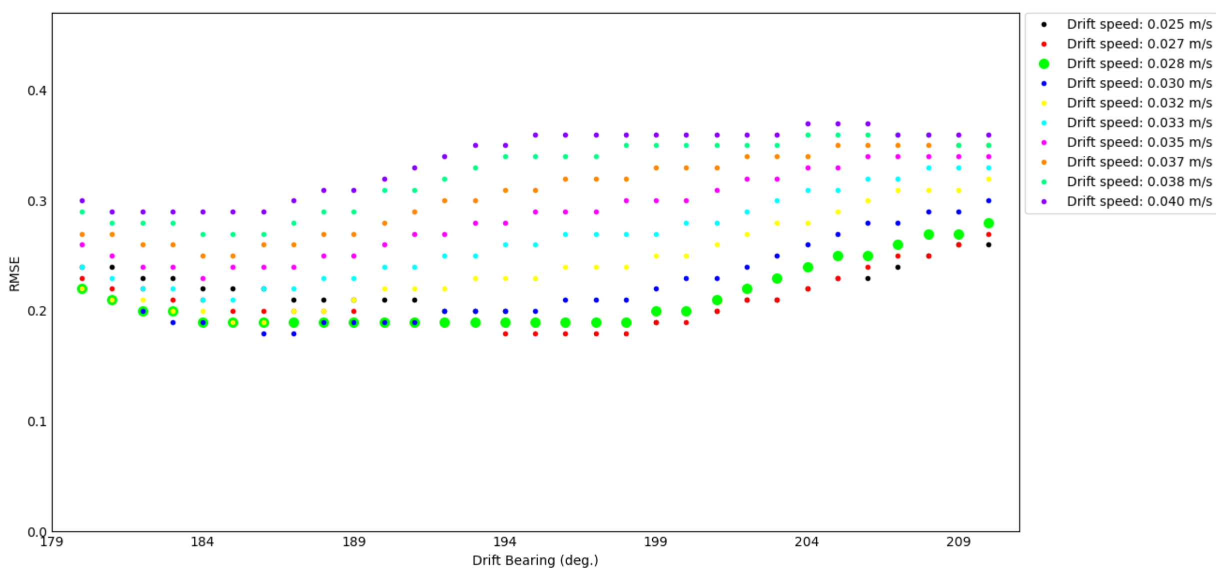

Figure 5-10. Linear regression comparison of ATL07 strong beam elevations and CHIR NIR heights. The lowest RMSE was achieved at a drift speed of 0.028 m/s, consistent with the coefficient of determination result.

5.3.4. CHIR NIR versus ATL07 segment heights

We investigated the FL-1C data swath segments 12 to 14, where overlapping CHIR and ICESat-2 ATLAS beam products were ideal. Before applying the drift adjustments, the height comparison generated high bias (RMSE= 0.25 m), and the agreement between the measurements was poor (R^2= 0.24), and the computations yielded more favorable results with a single beam comparison rather than combining the weak and strong beam products together (R^2=0.80 versus 0.69 and RMSE=0.17 versus 0.35). Table 5-3 presents the comparison results where the height agreement improved substantially (mean RMSE= 0.20 m, mean R^2=0.73), particularly for the ATL07 strong beam product using the *LidarShift* algorithm generated parameters. We output a cross-section of the dataset for visualization, showing that strong beam heights followed sea ice ridges and keels with higher accuracy compared to the weak beam product. Figures 5-11 (a-c) illustrate the plot of the original and adjusted CHIR data swath (green: original, blue: adjusted), where ATL07 strong and weak beam products were aligned ideally to CHIR data swath. Figures 5-12 (a-f) present the linear regression analysis for each data swath segment after drift adjustment was applied to the respective CHIR lidar dataset.

Table 5-3. Comparison of ATL07 segment heights versus CHIR NIR measurements after drift adjustment was applied.

Segment	Beam	Intercept	Drift speed (m/s)	Drift angle (deg.)	Mean height ATL07 (m)	Mean height CHIR (m)	dZ (m)	RMSE (m)	R^2
FL1C_12	strong	327	0.028	190	0.103	0.124	-0.021	0.20	0.80
FL1C_13	strong	328	0.030	186	0.133	0.126	0.007	0.27	0.66
FL1C_14	strong	338	0.028	187	0.060	0.000	0.060	0.13	0.73
				Avg.	0.099	0.083	0.015	0.20	0.73
FL1C_12	weak	307	0.028	190	0.132	0.093	0.039	0.22	0.59
FL1C_13	weak	319	0.030	186	0.063	0.005	0.058	0.16	0.57
FL1C_14	weak	314	0.028	187	0.034	-0.031	0.065	0.13	0.51
				Avg.	0.076	0.022	0.054	0.17	0.55

Figures 5-11. (a-c) Illustration of sea ice drift adjustment. The green data swath presents the original raster CHIR lidar data swath, and the blue data swath displays the adjusted vector CHIR lidar dataset (Figure 5-11-a). In the cross-section illustration, the ATL07 strong and weak beam measurements are illustrated with red and orange points. It is visible that strong beam sensor product agreed better with CHIR data swath, particularly with irregular height characteristics of sea ice, compared to the weak beam product (Figures 5-11 b, c).

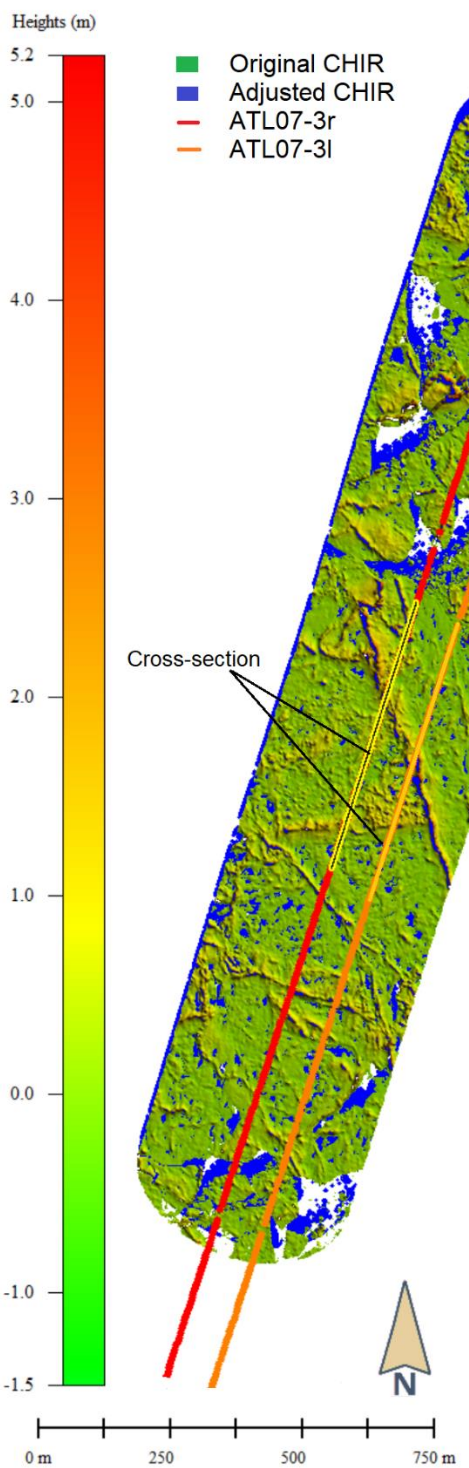

Fig. 5-11 a

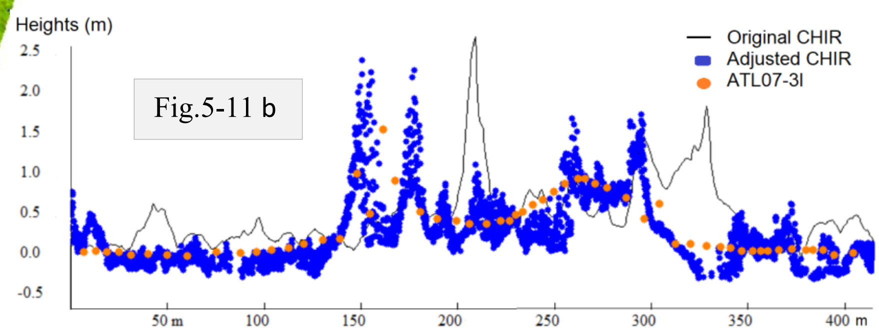

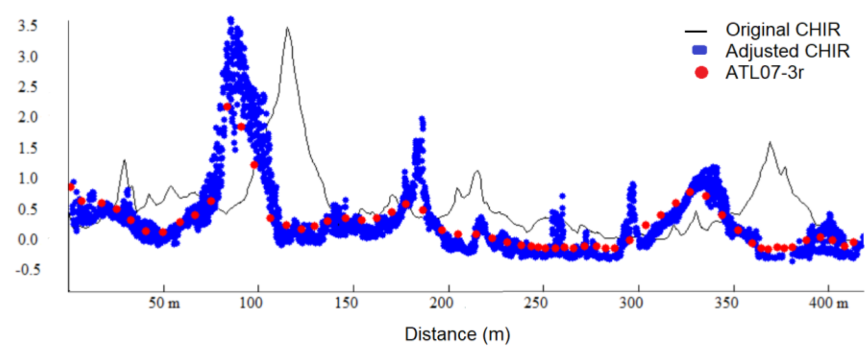

Fig. 5-11 c

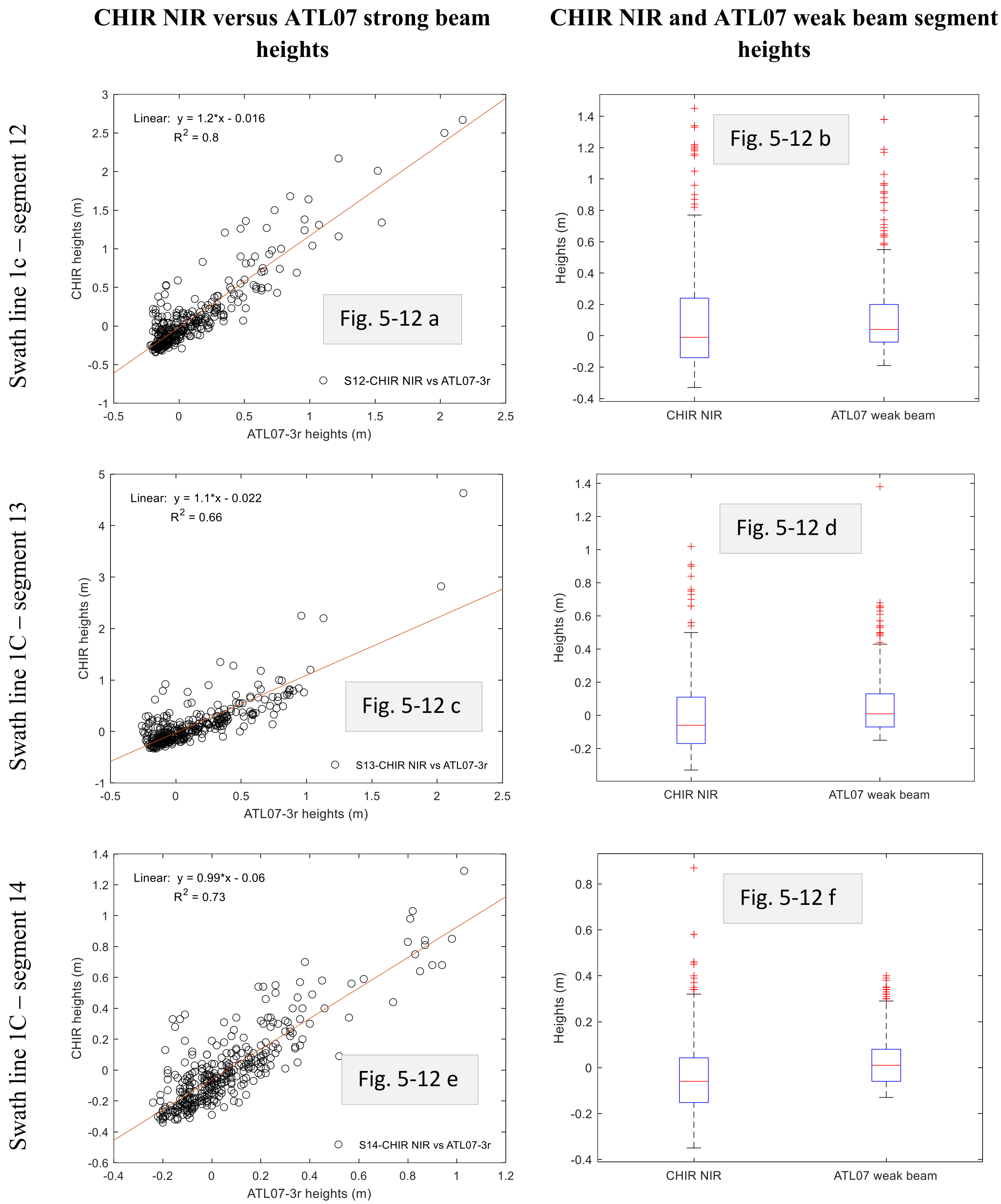

Figures 5-12. (a-f) Agreement of CHIR NIR heights and ATL07 strong beam segments and comparison of heights to the weak beam *after* LidarShift drift adjustment parameters were applied to the respective sea ice lidar data swath.

5.3.5. CHIR-green wavelength versus ATL03 photon heights

We investigated the ATL03 strong and weak beam products that corresponded with CHIR green wavelength lidar depths (in the height domain), particularly at melt ponds and where leads formed. For this purpose, we adjusted the green FL1C, segments 12-14 CHIR lidar data swath, using the identical drift speed and bearing parameters applied to the NIR datasets. We used CHIR NIR returns to distinguish the melt pond and sea ice surface elevations and compared the ATL03 photons and CHIR green wavelength returns registered below the surfaces. Because melt ponds are shallow, and ATL03 photons can be difficult to distinguish at reflective surfaces, we matched the measurements in a triangulated space (e.g., d=2 m, h=0.5 m, $slope$ = 45°). The preliminary investigation indicated that the weaker ATLAS beam registered insufficient bathymetric photons; therefore, we excluded these recordings from further analysis.

Table 5-4 presents the maximum depth, mean sea ice surface, and the mean height findings of each CHIR green-wavelength measurement matched with an ATL03 strong beam photon height. Expectantly, matched measurements indicated shallow depths, except where photons registered deeper heights in the leads. RMSE was 16 cm, and the mean height agreement was strong (R^2 = 0.84). The height difference was consistent across the segments, where ATL03 photons registered slightly deeper returns (0.01 m). Figures 5-13 (a-f) display the agreement (R^2) and the spread (boxplot) of ATL03 strong photon heights to the nearby CHIR measurements.

Table 5-4. CHIR bathymetry (*in height domain*) comparison to the ATL03 strong beam photon heights, recorded in ellipsoidal heights.

Sensor	Segment	Intercept	Valid	Outliers (%)	Minimum height (m)	Mean sea ice surface (m)	Mean height (m)	dZ (m)	RMSE (m)	R^2
CHIR ATL03	S12	192	165	14.06%	15.14 15.14	18.01	17.46 17.45	0.01	0.12	0.93
CHIR ATL03	S13	122	107	12.30%	15.49 15.49	17.97	17.56 17.56	0	0.21	0.79
CHIR ATL03	S14	106	99	6.60%	16.06 16.06	17.87	17.65 17.63	0.02	0.16	0.79
							Avg.	0.01	0.16	0.84

CHIR green wavelength versus ATL03 strong beam heights

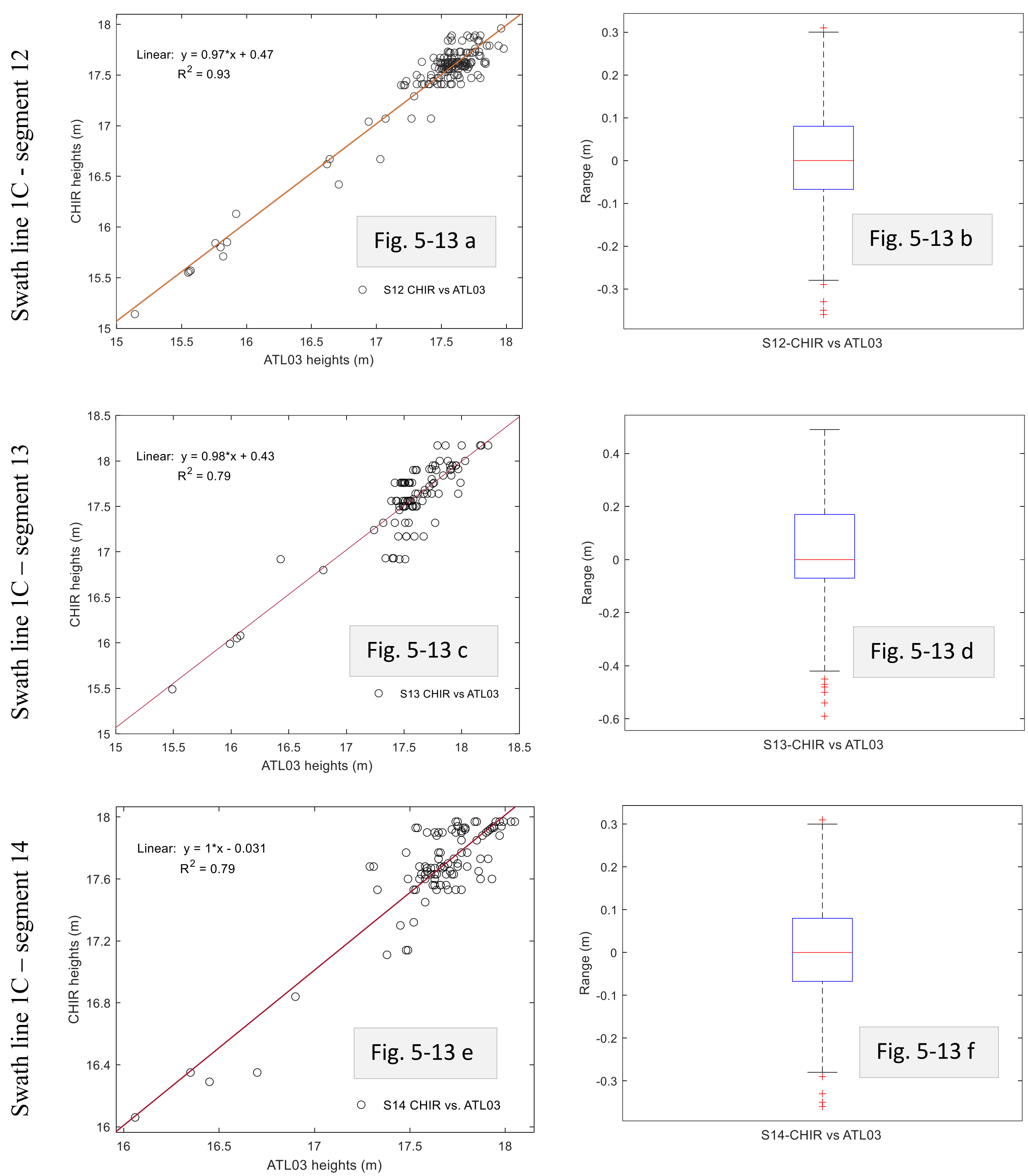

Figure 5-13. (a-f) Comparison of CHIR green-wavelength depths (in height domain) to ATL03 strong beam photon heights. The agreement between the measurements was strong (R^2=0.84), and the absolute mean height difference was 1 cm.

5.4. Discussion

NASA's Cal/Val 2022 campaign provided scientists with lidar point cloud datasets and high-resolution imagery to quantify ICESat-2 measurements of Arctic summer sea ice. The campaign was unique, and successful mission completion required the researchers to overcome technical, logistical, and environmental concerns, such as integrating CHIR with an uncharacteristic survey aircraft, planning around unpredictable and quickly changing weather conditions, and dealing with airspace access issues. Before the deployment in Greenland, CHIR-series altimeters had yet to measure sea ice; uncertainties existed, particularly regarding the methodology to quantify the data quality. We carefully prepared and executed a data acquisition campaign, following a thorough system calibration methodology. Observations at Pituffik SB runway using a GNSS-receiver and verification of CHIR system calibration to ATL03 photon heights at the same location provided confidence in the measurements. Further, LVIS and CHIR measured sea ice surfaces concurrently at lower altitudes, and the results showed a tight agreement, a minor height bias, and a normal distribution that confirmed the calibration cross-check between the airborne altimeters.

Mapping sea ice surfaces, measuring shallow depths with an airborne laser altimeter, and comparing it to ICESat-2 ATLAS products are not novel. Earlier efforts using the high-altitude MABEL and ATM systems were successful, and lessons learned helped to execute the 2022 campaign successfully (Forfinski & Parrish, 2016; Kwok & Kacimi, 2018). Unique to the Cal/Val 2022 campaign, we could map the sea ice concurrently with ICESat-2, and we constructed detailed TIN surface patches for a 1:1 height comparison using the least squares method. The novel LidarShift algorithm enabled us to align CHIR data swath closer to match the ICESat-2 beam measurements by computing the time difference and modifying each lidar point location to compensate for the sea ice drift. The analysis of Copernicus neXtSIM model provided us with an estimated drift speed to input to the algorithm and helped to predict the correct parameters. The point cloud data swath segments were approximately 3 km in length, and theoretically, we could split the swath to shorter segments and generate different correction parameters. We may investigate this possibility in future research; however, as demonstrated, the improved alignment between the measurements enabled assurance with our methodology, and we could compare and validate the sea ice heights and shallow depths to insignificant differences (bias). We confirmed the agreement between CHIR NIR and ATL07 sea ice surface heights to 0.015 m, where weak beam was visibly and quantitively less sensitive to the irregular sea ice surface heights (dZ=0.054 m).

The depth comparison in this study was based on the height domain. We accounted for CHIR green wavelength lidar and ATL03 photon heights registered below the mean sea ice and water surfaces. A more comprehensive depth analysis would include extracting ATL03 photon bathymetry of individual melt ponds and the occasional leads where measurements coincided. Naturally, sea ice melt ponds were shallow, had irregular shapes, and highly reflective bottom surfaces. These conditions differed from the locations with leads, where water was deep and dark (poor transparency), adversely impacting the bathymetric ability of the lidar systems. We recognize that both beams measured deeper water columns at other locations (Parrish et al., 2019; Tingaker & Ekelund, 2022) and earlier studies evaluated the ATL03 photon bathymetry (Lin et al., 2023; Ranndal et al., 2021) at other locations. However, in the Arctic Ocean, the environmental conditions were vastly different, and the sea ice was dynamic, requiring a novel approach that contrasted with the earlier bathymetric study conditions and validations methods that were conducted in the southern locations (Saylam et al., 2023).

Nevertheless, using the LidarShift algorithm, we could align and compare shallow depths in the height domain, which was 0.01 m in agreement. These results validated the accuracy and the robustness of ICESat-2 ATLAS data products, which is critical to sea ice community monitoring the changes in the polar regions and reducing the uncertainties in forecasting sea ice reduction and sea level rise worldwide.

5.5. Conclusion

In this study, we acquired, processed, aligned, and investigated sea ice lidar datasets using space and airborne-based altimeters. Our principal motivation was to validate the accuracy of ICESat-2 ATLAS measurements using an airborne lidar system. Because the sea ice was dynamic, and true alignment between the altimeters was almost impossible, we built an algorithm to compensate for the time offset between the systems and align the sea ice point cloud lidar dataset location to a theoretical position. The Cal/Val 2022 study concluded with answers to the research questions as defined in the introduction section:

1. CHIR system calibration was validated using precise multi-channel GNSS survey measurements. The absolute mean height difference was less than 1 cm for both scanning channels. We further validated the system calibration by comparing it to the ATL03 strong beam photon heights that registered on the same surface, where the mean difference was also less than 1 cm, measured in ellipsoidal heights.
2. LVIS and CHIR measurements, compared both to ellipsoidal and orthometric heights, had an elevated level of agreement ($R^2 > 0.98$) and a low bias in height measurements (RMSE=0.045 m), confirming the cross-check calibration.
3. To compare ICESat-2 and CHIR measurements, we developed the LidarShift algorithm, which modified the position and time stamp of each CHIR lidar point to match those of ICESat-2. This

algorithm iteratively adjusted CHIR lidar swath data for drift speed and bearing combinations within user-defined increments to optimize agreement with the ICESat-2 beam measurements.

a. Agreement of CHIR lidar data to ATL07 segment heights improved significantly after the application of optimum algorithm parameters (mean R^2=0.73, RMSE=0.20 m), compared to the original agreement (mean R^2 =0.24, RMSE =0.25). The mean height difference (*dZ*) of the strong beam product was 0.015 m, which was insignificant given the technological differences and the irregularity of sea ice surface heights.
b. Comparison to the weak beam slightly increased the height difference (*dZ*=0.054 m). The weaker beam was less sensitive to detect sloping and irregular sea ice surface heights.
c. The ATL03 photon heights agreed strongly with CHIR green wavelength heights (mean R^2=0.84, RMSE=0.16 m). The mean height difference was 0.01 m, where the ATL03 strong beam registered photon heights slightly deeper.

The Cal/Val 2022 study outlined the technical, logistical, and environmental challenges of acquiring coincident lidar data in the Arctic Ocean. It also highlighted the requirement to use the LidarShift algorithm to conduct optimum comparisons to ICESat-2 ATLAS data products. We believe the scientific sea ice and glaciology communities will benefit from the findings of the study, and the availability of CHIR lidar dataset, high-resolution four-band imagery, and the drift algorithm.

Data Availability Statement

The airborne lidar dataset used in this study is available to the public at Texas Data Repository. The physical address is: https://doi.org/10.18738/T8/MYOUUV

Researchers are encouraged to use the following citation (Saylam et al., 2024) in their studies.

The Python code (LidarShift) is available to the public in the GitHub domain: https://github.com/ut-beg/ICESat2LidarShift.

Acknowledgement

NASA funded the Cal/Val 2022 campaign with the contract GSFC22CA034. The authors would like to acknowledge all those who organized, participated, and helped to make NASA's Cal/Val 2022 campaign a reality: Tom Neumann, Lori Magruder, Michelle Hofton, David Rabine, Marco Bagnardi, Sinead Farrell, Helen Cornejo, and all others in the sea ice scientific community. Appreciation is extended to Pituffik SB staff for their welcoming hospitality, Leica Geosystems staff for their genuine interest, and Minnesota Public Radio staff Kerem Yücel for his assistance in the project. Special thanks are due to Anders Knudby, Luke Copland, Michael Sawada (University of Ottawa), Christopher Parrish (Oregon State University), Christopher Hopkinson (University of Lethbridge) and the Near Surface Observatory colleagues at the Bureau of Economic Geology for their valuable time and constructive feedback. We also extend our gratitude to the American Geophysical Union and to everyone who carefully reviewed and positively contributed to improve the quality our article during the peer-review process.

5.6. References

Bingham, E. C. (1922). Preliminary Methods of Measurement. In *Fluidity and Plasticity* (Vol. 2). McGraw-Hill.

Blair, J. B., Rabine, D. L., and Hofton, M. A. (1999). The Laser Vegetation Imaging Sensor: A medium-altitude, digitisation-only, airborne laser altimeter for mapping vegetation and topography. *ISPRS Journal of Photogrammetry and Remote Sensing*, *54*(2–3), 115–122. https://doi.org/10.1016/S0924-2716(99)00002-7

Brunt, K. M., Neumann, T. A., and Smith, B. E. (2019). Assessment of ICESat-2 Ice Sheet Surface Heights, Based on Comparisons Over the Interior of the Antarctic Ice Sheet. *Geophysical Research Letters*, *46*(22), 13072–13078. https://doi.org/10.1029/2019GL084886

B Delaunay. (1932). *Sur la sphere vide—A la memoire de Georges Voronoi*. Bulletin de Académie Science de L'URSS. http://galiulin.narod.ru/delaunay_.pdf

Deems, J. S., Painter, T. H., and Finnegan, D. C. (2013). Lidar measurement of snow depth: A review. *Journal of Glaciology*, *59*(215), 467–479. https://doi.org/10.3189/2013JoG12J154

Diamond, R., Sime, L. C., Schroeder, D., and Guarino, M.-V. (2021). The contribution of melt ponds to enhanced Arctic sea-ice melt during the Last Interglacial. *The Cryosphere*, *15*(11), 5099–5114. https://doi.org/10.5194/tc-15-5099-2021

Duncanson, L., Neuenschwander, A., Hancock, S., Thomas, N., Fatoyinbo, T., Simard, M., Silva, C. A., Armston, J., Luthcke, S. B., Hofton, M., Kellner, J. R., and Dubayah, R. (2020). Biomass estimation from simulated GEDI, ICESat-2 and NISAR across environmental gradients in Sonoma County, California. *Remote Sensing of Environment*, *242*, 111779. https://doi.org/10.1016/j.rse.2020.111779

Feng, T., Duncanson, L., Montesano, P., Hancock, S., Minor, D., Guenther, E., and Neuenschwander, A. (2023). A systematic evaluation of multi-resolution ICESat-2 ATL08 terrain and canopy heights in boreal forests. *Remote Sensing of Environment*, *291*, 113570. https://doi.org/10.1016/j.rse.2023.113570

Forfinski, N., and Parrish, C. (2016). *ICESat-2 bathymetry: An empirical feasibility assessment using MABEL* (C. R. Bostater, S. P. Mertikas, X. Neyt, C. Nichol, and O. Aldred, Eds.; p. 999904). https://doi.org/10.1117/12.2241210

Garcia-Soto, C., Cheng, L., Caesar, L., Schmidtko, S., Jewett, E. B., Cheripka, A., Rigor, I., Caballero, A., Chiba, S., Báez, J. C., Zielinski, T., and Abraham, J. P. (2021). An Overview of Ocean Climate Change Indicators: Sea Surface Temperature, Ocean Heat Content, Ocean pH, Dissolved Oxygen Concentration, Arctic Sea Ice Extent, Thickness and Volume, Sea Level and Strength of the AMOC (Atlantic Meridional Overturning Circulation). *Frontiers in Marine Science*, *8*, 642372. https://doi.org/10.3389/fmars.2021.642372

Gui, D., Lei, R., Pang, X., Hutchings, J. K., Zuo, G., & Zhai, M. (2020). Validation of remote-sensing products of sea-ice motion: A case study in the western Arctic Ocean. *Journal of Glaciology*, *66*(259), 807–821. https://doi.org/10.1017/jog.2020.49Habib, A., Bang, K. I., Kersting, A. P., & Lee, D.-C. (2009). Error Budget of Lidar Systems and Quality Control of the Derived Data. *Photogrammetric Engineering & Remote Sensing*, *75*(9), 1093–1108. https://doi.org/10.14358/PERS.75.9.1093

Hopkinson, C., Demuth, M., Sitar, M., and Chasmer, L. (2001). Applications of airborne lidar mapping in glacierised mountainous terrain. *IGARSS 2001. Scanning the Present and Resolving the Future.*

Proceedings. IEEE 2001 International Geoscience and Remote Sensing Symposium (Cat. No.01CH37217), *2*, 949–951. https://doi.org/10.1109/IGARSS.2001.976690

Jasinski, M. F., Stoll, J. D., Cook, W. B., Ondrusek, M., Stengel, E., and Brunt, K. (2016). Inland and Near-Shore Water Profiles Derived from the High-Altitude Multiple Altimeter Beam Experimental Lidar (MABEL). *Journal of Coastal Research*, *76*, 44–55. https://doi.org/10.2112/SI76-005

Jóhannesson, T., Björnsson, H., Magnússon, E., Guðmundsson, S., Pálsson, F., Sigurðsson, O., Thorsteinsson, T., and Berthier, E. (2013). Ice-volume changes, bias estimation of mass-balance measurements and changes in subglacial lakes derived by lidar mapping of the surface of Icelandic glaciers. *Annals of Glaciology*, *54*(63), 63–74. https://doi.org/10.3189/2013AoG63A422

Kacimi, S., and Kwok, R. (2020). The Antarctic sea ice cover from ICESat-2 and CryoSat-2: Freeboard, snow depth, and ice thickness. *The Cryosphere*, *14*(12), 4453–4474. https://doi.org/10.5194/tc-14-4453-2020

Kwok, R., and Kacimi, S. (2018). Three years of sea ice freeboard, snow depth, and ice thickness of the Weddell Sea from Operation IceBridge and CryoSat-2. *The Cryosphere*, *12*(8), 2789–2801. https://doi.org/10.5194/tc-12-2789-2018

Kwok, R., Markus, T., Morison, J., Palm, S. P., Neumann, T. A., Brunt, K. M., Cook, W. B., Hancock, D. W., and Cunningham, G. F. (2014). Profiling Sea Ice with a Multiple Altimeter Beam Experimental Lidar (MABEL). *Journal of Atmospheric and Oceanic Technology*, *31*(5), 1151–1168. https://doi.org/10.1175/JTECH-D-13-00120.1

Kwok, R., and Morison, J. (2016). Sea surface height and dynamic topography of the ice-covered oceans from CryoSat-2: 2011–2014. *Journal of Geophysical Research: Oceans*, *121*(1), 674–692. https://doi.org/10.1002/2015JC011357

Lee, S.-I. (2001). Developing a bivariate spatial association measure: An integration of Pearson's r and Moran's I. *Journal of Geographical Systems*, *3*(4), 369–385. https://doi.org/10.1007/s101090100064

Li, B., Xie, H., Tong, X., Liu, S., Xu, Q., and Sun, Y. (2023). Extracting accurate terrain in vegetated areas from ICESat-2 data. *International Journal of Applied Earth Observation and Geoinformation*, *117*, 103200. https://doi.org/10.1016/j.jag.2023.103200

Lin, Y., and Jensen Knudby, A. (2023). Global automated extraction of bathymetric photons from ICESat-2 data based on a PointNet++ model. *International Journal of Applied Earth Observation and Geoinformation*, *124*, 103512. https://doi.org/10.1016/j.jag.2023.103512

Ma, Y., Liu, R., Li, S., Zhang, W., Yang, F., and Su, D. (2018). Detecting the ocean surface from the raw data of the MABEL photon-counting lidar. *Optics Express*, *26*(19), 24752. https://doi.org/10.1364/OE.26.024752

Magruder, L. A., Farrell, S. L., Neuenschwander, A., Duncanson, L., Csatho, B., Kacimi, S., and Fricker, H. A. (2024). Monitoring Earth's climate variables with satellite laser altimetry. *Nature Reviews Earth and Environment*, *5*(2), 120–136. https://doi.org/10.1038/s43017-023-00508-8

Magruder, L., Brunt, K., and Alonzo, M. (2020). Early ICESat-2 on-orbit Geolocation Validation Using Ground-Based Corner Cube Retroreflectors. *Remote Sensing*, *12*(21), 3653. https://doi.org/10.3390/rs12213653

Markus, T., Neumann, T., Martino, A., Abdalati, W., Brunt, K., Csatho, B., Farrell, S., Fricker, H., Gardner, A., Harding, D., Jasinski, M., Kwok, R., Magruder, L., Lubin, D., Luthcke, S., Morison, J., Nelson, R., Neuenschwander, A., Palm, S., … Zwally, J. (2017). The Ice, Cloud, and land Elevation Satellite-2 (ICESat-2): Science requirements, concept, and implementation. *Remote Sensing of Environment*, *190*, 260–273. https://doi.org/10.1016/j.rse.2016.12.029

Martino, A. J., Neumann, T. A., Kurtz, N. T., and McLennan, D. (2019). ICESat-2 mission overview and early performance. In S. P. Neeck, T. Kimura, and P. Martimort (Eds.), *Sensors, Systems, and Next-Generation Satellites XXIII* (p. 11). SPIE. https://doi.org/10.1117/12.2534938

Neumann, T. A., A. Brenner, D. Hancock, J. Robbins, S. B. Luthcke, K. Harbeck, J. Lee, A. Gibbons, J. Saba, and K. Brunt. (2023). *ATLAS/ICESat-2 L2A Global Geolocated Photon Data, version 6* [dataset]. NASA National Snow and Ice Data Center DAAC. https://doi.org/10.5067/ATLAS/ATL03.006

Neumann, T. A., Martino, A. J., Markus, T., Bae, S., Bock, M. R., Brenner, A. C., Brunt, K. M., Cavanaugh, J., Fernandes, S. T., Hancock, D. W., Harbeck, K., Lee, J., Kurtz, N. T., Luers, P. J., Luthcke, S. B., Magruder, L., Pennington, T. A., Ramos-Izquierdo, L., Rebold, T., … Thomas, T. C. (2019). The Ice, Cloud, and Land Elevation Satellite – 2 missions: A global geolocated photon product derived from the Advanced Topographic Laser Altimeter System. *Remote Sensing of Environment*, *233*, 111325. https://doi.org/10.1016/j.rse.2019.111325

Parrish, C. E., Magruder, L. A., Neuenschwander, A. L., Forfinski-Sarkozi, N., Alonzo, M., and Jasinski, M. (2019). Validation of ICESat-2 ATLAS Bathymetry and Analysis of ATLAS's Bathymetric Mapping Performance. *Remote Sensing*, *11*(14), 1634. https://doi.org/10.3390/rs11141634

Petty, A. A., Kurtz, N. T., Kwok, R., Markus, T., and Neumann, T. A. (2020). Winter Arctic Sea Ice Thickness from ICESat-2 Freeboards. *Journal of Geophysical Research: Oceans*, *125*(5), e2019JC015764. https://doi.org/10.1029/2019JC015764

Ranndal, H., Sigaard Christiansen, P., Kliving, P., Baltazar Andersen, O., and Nielsen, K. (2021). Evaluation of a Statistical Approach for Extracting Shallow Water Bathymetry Signals from ICESat-2 ATL03 Photon Data. *Remote Sensing*, *13*(17), 3548. https://doi.org/10.3390/rs13173548

Rehman, K., Fareed, N., and Chu, H.-J. (2023). NASA ICESat-2: Space-Borne lidar for Geological Education and Field Mapping of Aeolian Sand Dune Environments. *Remote Sensing*, *15*(11), 2882. https://doi.org/10.3390/rs15112882

Robbins, J., Neumann, T. A., Kurtz, N. T., Brunt, K. M., Bagnardi, M., Hancock, D. W., and Lee, J. (2022). *ICE, CLOUD, and Land Elevation Satellite (ICESat-2) Project, ICESat-2 Data Comparison, User's Guide for Rel006* (Code: 615). Goddard Space Flight Center, NASA.

Savitzky, Abraham, and Golay, M. J. E. (1964). Smoothing and differentiation of data by simplified least squares procedures. *Analytical Chemistry*, *36*(8), 1627–1639. https://doi.org/10.1021/ac60214a047

Sandven, S., Spreen, G., Heygster, G., Girard-Ardhuin, F., Farrell, S. L., Dierking, W., & Allard, R. A. (2023). Sea Ice Remote Sensing—Recent Developments in Methods and Climate Data Sets. *Surveys in Geophysics*, *44*(5), 1653–1689. https://doi.org/10.1007/s10712-023-09781-0

Saylam, K., Briseno, A., Averett, A. R., and Andrews, J. R. (2023). Analysis of Depths Derived by Airborne Lidar and Satellite Imaging to Support Bathymetric Mapping Efforts with Varying Environmental Conditions: Lower Laguna Madre, Gulf of Mexico. *Remote Sensing*, *15*(24), 5754. https://doi.org/10.3390/rs15245754

Saylam, K., Hupp, J., Andrews, J., Averett, A., and Knudby, A. (2018). Quantifying Airborne Lidar Bathymetry Quality-Control Measures: A Case Study in Frio River, Texas. *Sensors*, *18*(12), 4153. https://doi.org/10.3390/s18124153

Saylam, K. (2024). Calibration and validation campaign 2022 ICESat-2, NASA and UT Austin [Dataset]. Texas Data Repository. https://doi.org/10.18738/T8/MYOUUV

Schutz, B. E., Zwally, H. J., Shuman, C. A., Hancock, D., and DiMarzio, J. P. (2005). Overview of the ICESat Mission. *Geophysical Research Letters*, *32*(21), L21S01. https://doi.org/10.1029/2005GL024009

Streutker, D. R., Glenn, N. F., & Shrestha, R. (2011). A Slope-based Method for Matching Elevation Surfaces. *Photogrammetric Engineering & Remote Sensing*, *77*(7), 743–750. https://doi.org/10.14358/PERS.77.7.743

Telling, J., Glennie, C., Fountain, A., and Finnegan, D. (2017). Analyzing Glacier Surface Motion Using lidar Data. *Remote Sensing*, *9*(3), 283. https://doi.org/10.3390/rs9030283

Tingaker, T., and Ekelund, A. (2022). Recent developments in airborne lidar bathymetry. In G. W. Kamerman and O. Steinvall (Eds.), *Electro-Optical Remote Sensing XVI* (p. 10). SPIE. https://doi.org/10.1117/12.2645180

Williams, T., Korosov, A., Rampal, P., and Ólason, E. (2021). Presentation and evaluation of the Arctic sea ice forecasting system neXtSIM-F. *The Cryosphere*, *15*(7), 3207–3227. https://doi.org/10.5194/tc-15-3207-2021

Yi, D., Harbeck, J. P., Manizade, S. S., Kurtz, N. T., Studinger, M., and Hofton, M. (2015). Arctic Sea Ice Freeboard Retrieval with Waveform Characteristics for NASA's Airborne Topographic Mapper (ATM) and Land, Vegetation, and Ice Sensor (LVIS). *IEEE Transactions on Geoscience and Remote Sensing*, *53*(3), 1403–1410. https://doi.org/10.1109/TGRS.2014.2339737

Zhu, Q., Zhang, Y., & Li, F. (2008). Three-dimensional TIN algorithm for digital terrain modeling. *Geo-Spatial Information Science*, *11*(2), 79–85. https://doi.org/10.1007/s11806-008-0043-6

Appendix 5A. LVIS versus CHIR heights comparison

Table 5A-1. LVIS (*z-low*) waveform heights versus CHIR NIR measurements in ellipsoidal heights. before geophysical height adjustments.

Swath line/ section	Intercept	Match (%)	LVIS mean height (m)	CHIR mean height (m)	dZ (m)	RMSE (m)	R^2
FL1-B	8634	87.77	17.539	17.544	-0.005	0.045	0.98
FL1-C	8749	88.89	17.820	17.833	-0.013	0.042	0.98

Table 5A-2. LVIS (*max-amp*) waveform heights versus CHIR NIR measurements in orthometric heights with identical geophysical height adjustments applied.

Swath line/section	Intercept	Match (%)	LVIS mean height (m)	CHIR mean height (m)	dZ (m)	RMSE (m)	R^2
FL1-B	8630	90.01	0.297	0.328	-0.031	0.047	0.98
FL1-C	8680	90.04	0.292	0.332	-0.040	0.047	0.98

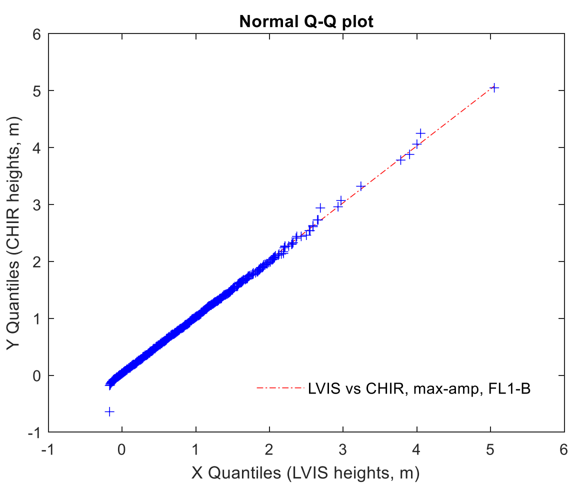

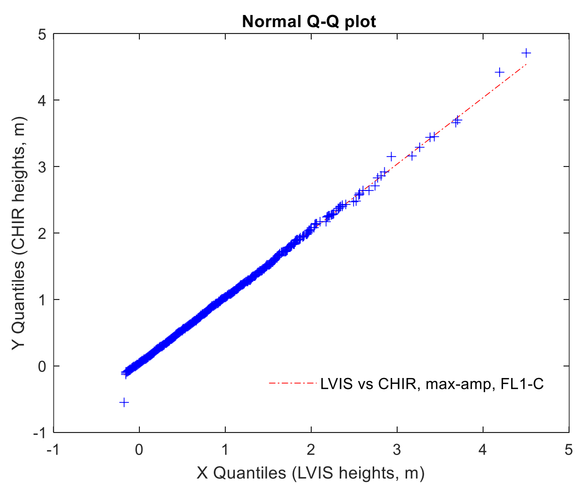

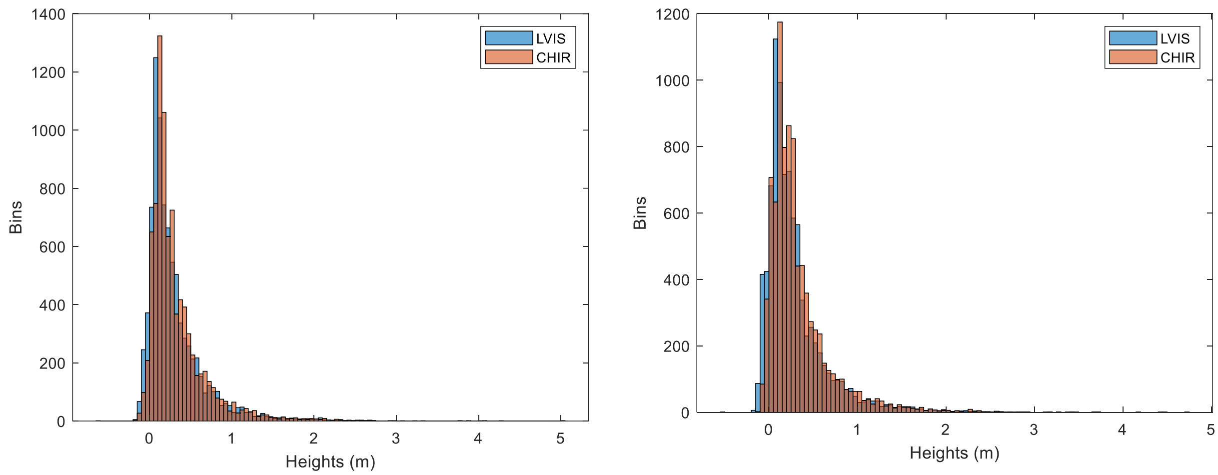

Figure S5-A1. [Supplementary materials] (a-d) Comparing the distribution of LVIS (*max-amp*) heights and CHIR NIR measurements (segments: FL-1B and FL1-C). Both sensor datasets are normally distributed (Lee's spatial autocorrelation = 0.99).

Appendix 5B. Sea ice drift computation

The physical location of the *LidarShift* algorithm: https://github.com/ut-beg/ICESat2LidarShift

The position of each CHIR lidar data point is adjusted to compensate for the drift of sea ice during the time delay between the ICESat-2 and CHIR passes. Below, we summarize the major formulas in the algorithm.

- Total time delay of ICESat-2 orbit is computed by subtracting the beginning time (*atl07t0*) from the end time (*atl07t1*).

$$atl07TotalTime = atl07t1 - atl07t0 \qquad \text{[Equation S5-B1]}$$

- Total time delay of the CHIR pass is computed by subtracting the beginning time (*CHIRt0*) from the end time (*CHIRt1*).

$$chiropteraTotalTime = CHIRt0 - CHIRt1 \qquad \text{[Equation S5-B2]}$$

- The drift bearing angle (*driftBearing*) is converted into radians, relative to the East.

$$driftPolarDirRad = (360\ + 90 - driftBearing\ ) \div \frac{360}{2\pi} \qquad \text{[Equation S5-B3]}$$

- The drift speed is converted to m/s.

$$driftMetersPerSecond = \frac{driftSpeedMetersPerMinute}{60}$$ [Equation S5-B4]

- Easting (*X*) and Northing (*Y*) components of the drift speed are computed.

$$driftXVel = \cos(driftPolarDirRad) \times driftMetersPerSecond$$ [Equation S5-B5]

$$driftYVel = \cos(drifPolarDirRad) \times driftMetersPerSecond$$ [Equation S5-B6]

- For each point in the dataset, the shift function is called. The function captures the location (*X, Y, Z*) and time (*t*) components of each point and computes the time since the beginning of CHIR pass for that moment in time.

$$timeSinceLineStart = t - chiropterat0$$ [Equation S5-B7]

- The fraction of the total time consumed on the CHIR pass is computed.

$$chiropteraTimeFraction = timeSinceLineStart \div chiropteraTotalTime$$ [Equation S5-B8]

- Time that ICESat-2 would have reached the same location (*atl07TimeOnTarget*) is computed.

$$atl07TimeOnTarget = atl07T0 + (atl07TotalTime * chiropteraTimeFraction)$$ [Equation S5-B9]

- The absolute difference in time between ICESat-2 reaching the point, and the CHIR deltaT (Δt).

$$deltaT = t - atl07TimeOnTarget$$ [Equation S5-B10]

- Easting (X) and Northing (Y) components of the sea ice drift occurred in deltaT are computed.

$$chiropteraDeltaX = deltaT \times driftXVel$$ [Equation S5-B11]

$$chiropteraDeltaY = deltaT \times driftYVel$$ [Equation S5-B12]

- New positional coordinates are computed for each point after the drift correction is completed and recorded in a text file.

$$xFinal = x - chiropteraDeltaX$$

$$yFinal = y - chiropteraDeltaY$$

$$zFinal = z$$

$$tFinal = t + deltaT$$ [Equation S5-B13]

Chapter Six: Conclusions

6.1. Summary of findings

The research included in this PhD thesis demonstrated scientific approaches to applying quality control aspects of airborne lidar systems to generate accurate topographic and bathymetric products. Lidar technology enables the measurement of target surfaces with detail and accuracy; however, conducting in-situ campaigns using an approach best suited to the impacting environmental conditions remain essential to ensure the quality of the data products. Often, a rigorous approach to execute quality control mechanisms in ALB surveys is overlooked or not deemed sufficiently necessary due to financial and scheduling constraints. There are published guidelines and standards for digital elevation products (Abdullah and others, 2023; Terziotti and Archuleta, 2020), particularly for topographic mapping; however, documentation and protocols to address lidar bathymetry quality control mechanisms are either vague or non-existent, failing to address the technology's improving nature. The hydrographic specifications refer to a particular program requirement or a specific hydrologic unit at a location, describing the needs that a contractor should comply when collecting and processing elevation data. Nevertheless, this PhD study applied the ALB technology in diverse locations, including rivers in fluvial southern regions, a shallow hypersaline lagoon, and the Arctic Ocean for mapping sea ice, and demonstrated the practical applications and the statistical methodology to validate the heights and depths acquired to build accurate mapping products. The airborne lidar community, particularly the bathymetric application users, will benefit from this study, and will have an understanding of the expected validation processes in similar survey locations.

In the Frio River study, in southwest Texas, where water conditions were almost ideal for mapping with an ALB system, the riparian environment posed challenges to the integrity of the in-situ campaign. The comprehensive waveform analysis validated the ALB measurements at these locations, where the satellite signals necessary for sonar and GPS measurements were blocked. In the Devils River, the research built upon knowledge gained from studying fluvial and karst riverbeds, and we used an ALB system to measure the riverbed and provide the necessary habitat for the endangered Devils River minnow. At certain locations, particularly where the fish often inhabit, measuring the riverbed with ALB and sonar was challenging due to submerged vegetation blocking the electromagnetic pulses. As a novel surveying method, a geophysical instrument, a ground-penetrating radar with a shielded monostatic antenna (200 MHz) was used from an inflatable boat. Adjusting the water column permittivity based on the water temperature allowed the radio waves to propagate more quickly, particularly in the deeper parts of the river. This adjustment improved the depth agreement between the ALB and radar measurements, resulting in an identical mean depth value. Nevertheless, the study demonstrated the possibility of seamlessly combining datasets sourced from different sensors—an ALB system, a dual-frequency sonar, a ground-penetrating radar, and a GNSS—to build a river bottom map. It also proved the feasibility of using a geophysical instrument to map shallow riverbeds with the correct calibration settings.

In Laguna Madre, a hypersaline and shallow lagoon in southern Texas, an ALB system was used to measure the bottom. The depth of the lagoon varied with tides, and water quality (turbidity) was influenced by the northerly winds that suspended sediment. The in-situ campaign was conducted in three clustered sections of the southern lagoon, each characterized by unique turbidity, depth, and other environmental conditions. In each in-situ section, sonar soundings were adjusted to match mean water temperature and salinity, and for the satellite-derived bathymetry analysis, tides were observed, and surface heights were adjusted to match the satellite sensing times prior to comparing them to ALB measurements. The pixel reflectance analysis enabled the classification of spectral variability, and excessively turbid locations were excluded from further analysis. The modified sonar recordings showed good agreement with ALB heights, and the resultant bias exceeded the Special-Order standards set by the International Hydrographic Organization. The study results demonstrated the practical and theoretical limitations of airborne lidar bathymetry in locations with varying environmental conditions. The comparison of heights derived from satellite imaging revealed compatibility challenges and limitations between the technologies, thereby filling a gap in the scientific literature.

Contrary to the southern fluvial and karst locations, in the summer of 2022, 11,000 km^2 of Arctic Ocean sea ice was mapped using an ALB system. The campaign was funded and organized by NASA and aimed to provide scientists with detailed lidar datasets of sea ice for various cryospheric research purposes. In this research, as continuation of the previous case studies completed in the south using an ALB system, the objective was to validate the ALB measurements with applicable methods and quantify sea ice heights and shallow melt pond bathymetry to those of ICESat-2 ATLAS products. Because sea ice is dynamic and achieving a 1:1 correspondence of satellite and airborne datasets in terms of time and location was not possible, an algorithm was introduced to adjust the location of airborne lidar measurements. The Python-based algorithm, *LidarShift*, iteratively adjusted the lidar data swath for drift speed and bearing combinations within a user-defined range and increments. Excessively long (~100 km) lidar data swaths were segmented to shorter sections, and heights were adjusted to the tide-free system, identical to the ICESat-2 ATL07 segments. The agreement of the lidar data swath to ATL07 segment heights improved significantly after application of algorithm parameters, proving to be an effective method of comparison. The absolute mean height difference was computed between the ALB measurements and the ATLAS sensors, and results demonstrated the superiority of the r-series sensor to l-series to map the undulating sea ice surface with the ATL07 product. The results also demonstrated a comparison of ATL03 photon heights to those of ALB green wavelength returns that registered lower than the mean sea ice surfaces. The absolute mean height difference was insignificant, and the agreement between the datasets was high, demonstrating a high-degree of measurement compatibility between ICESat-2 and airborne lidar bathymetry.

6.2. Contributions to knowledge

The research outlined in this PhD thesis has contributed to the knowledge of airborne lidar bathymetry in several ways, primarily related to the application of quality control mechanisms across diverse locations and environmental conditions. In detail, these aspects are outlined with each respective chapter:

- [Chapter 1] Introduction and the rationale for the research.
- [Chapter 2] The study presented the use of waveform analysis to validate airborne lidar bathymetry in situations where in-situ measurements may not be feasible due to varying and challenging environmental conditions.
- [Chapter 3] The study demonstrated the feasibility of using a ground-penetrating radar to measure the bottom of a riverbed with submerged vegetation, where airborne lidar pulses and sonar recordings were partially blocked.
- [Chapter 4] The study demonstrated the use of pixel reflectance analysis and demonstrated the practical and theoretical limitations of conducting airborne lidar bathymetry in shallow lagoon waters with varying environmental conditions by comparing depths and heights to sonar and satellite-derived bathymetry results.
- [Chapter 5] The study presented the use of airborne and orbiting altimeters to validate measurements of sea ice heights and depths and introduced a novel algorithm to adjust the lidar data swath of sea ice for the purpose of a 1:1 comparison.

6.3. Limitations

Scientific studies and commercial projects using airborne lidar technology and derived elevation models can be constrained by methodological, theoretical, practical, and logistical challenges. Some of these constraints that were applicable to the research presented in this thesis are outlined below:

- *Methodological and theoretical constraints*: Some studies outline the anticipated limitations and performance expectations of ALB (Guenther, 2007; Parker and Sinclair, 2012). However, these studies provide broad and general guidelines rather than location-specific methods for understanding the possible constraints in each unique data acquisition scenario. Case studies in this thesis demonstrated a modified approach to acquiring, analyzing, and investigating data quality by demonstrating the use of location-specific methods as outlined below:
    - [Chapter 2] The use of waveform analysis in the Frio River served as an unconventional and an effective quality control mechanism to validate airborne lidar measurements. GNSS and sonar were not feasible for validation due to the excessive riparian zone vegetation and varying bottom properties.
    - [Chapter 3] The use of a ground-penetrating radar to measure the bottom of a riverbed with submerged vegetation enabled validating and complementing the airborne lidar measurements. The calibration of radio waves propagation speed was critical and required multiple data acquisition campaigns in a challenging survey environment.
    - [Chapter 4] A pixel reflectance analysis using satellite-imagery helped to identify excessively turbid areas of the lagoon and the limits of the study, where a complete in-situ campaign was not feasible due the size and access restrictions.
    - [Chapter 5] Beside logistical and environmental challenges of conducting an airborne survey in the Arctic, the largest constraint was adjusting the airborne lidar data swath of sea ice, in terms of time and location, to match those of ICESat-2 for direct comparison purposes. An algorithm was introduced to address this challenge effectively.

- *Temporal constraints:* In each case study presented in this PhD research, the temporal constraints included the allocated project time, availability of funding, and the environmental conditions that influenced the outcomes. Specifically, in the Frio and Devils River case studies, seasonal rainfall variations impacted river water flow, reservoir depths, vegetation growth, and suspended matter concentration, thereby influencing the results of airborne lidar bathymetry. In the Laguna Madre study, wind conditions impacted turbidity levels and the amount of floating vegetation, directly affecting the comparison between ALB and satellite-derived bathymetry. In the Cal/Val 2022 study, wind speed and the direction influenced sea ice drift, and temperature variability impacted the sea ice integrity. Additionally, airborne lidar missions are sensitive to weather conditions such as rain, fog, low clouds, and wind direction and speed, all of which can significantly impact the feasibility of the missions and the quality of the resulting data.

- *Logistical and regulatory constraints:* In addition to varying and seasonal weather conditions, airborne lidar missions require careful regulatory coordination. While this may not be a significant constraint in sparsely populated areas (e.g., Frio and Devil River case studies), airborne campaigns near urban regions necessitated obtaining airspace permissions. In Laguna Madre [Chapter 4], each flight mission required detailed application submission to the local authority due to the proximity to international airspace and to avoid impacting local aerial surveillance and SpaceX operations. The Cal/Val 2022 campaign [Chapter 5] was based out of Thule Air Force Base in Greenland, necessitating a federal special permit for all operations, and requiring the research staff to obtain security clearance. In addition, access to the international airspace between the U.S., Canada, and Iceland required an application and consent from authorities. Furthermore, the use of an airborne lidar system required special permits and certifications from NASA, and prior to operations, approval from the Laser Safety Board was necessary.

6.4. Relevant future research directions

In conclusion, this study has investigated and demonstrated the necessary quality-control mechanisms for airborne lidar bathymetry, applicable across diverse locations with varying environmental conditions. As ALB technology matures, advanced methodologies, particularly in bathymetric lidar data processing and classification, are emerging and have gathered significant interest within the ALB scientific community. Mandlburger (2021) presented a deep neural network based on multispectral aerial imagery, trained with an ALB dataset for depth estimation. Janowski and others (2022) discussed advanced bathymetric lidar data classification that enhanced identifying water bottom properties, which could be purposeful in riverbed studies. Kogut and others (2022) introduced an automatic vector data classification of water surface, bottom, and bottom properties using neural network algorithm. These applications promise to introduce efficiency and automation to lidar data processing, reducing user interaction and decreasing the likelihood of human errors. Nevertheless, as demonstrated in this thesis, uncertainties caused by varying environmental conditions highlight the importance of coincident in-situ campaigns, adapting the collection of validation data to the unique requirements of each survey location, and critically assessing environmental conditions. These factors cannot be overlooked or deferred in any practical ALB application.

In addition, Tingaker and Ekelund (2022) discussed the availability of ALB datasets online, which are classified and disseminated in near real-time for maritime surveillance activities and hazard management. On a different scale, Szafarczyk and Toś (2022) contributed to the ALB literature by detailing the extent of coastal abrasion and sediment accumulation, as well as identifying underwater bottom relief forms, sunken wrecks, and underwater archaeological sites, using ALB data. Chen and others (2023) reviewed ALB datasets that provided a high spatial and temporal resolution view of plankton distribution and biological activities in oceanic environments. These studies expand and contribute to the range of issues that can be investigated using ALB technology and provide an understanding of emerging trends in the field. Furthermore, a recent study formally assessed the emerging airborne lidar trends (Pricope and Bashit, 2023) and reported that technologies such as Unmanned Aerial Systems (UAS) and airborne sonar are gaining prominence in the topographic and bathymetric research fields, and are poised to make contributions in the coming years, driven by advances in technology and miniaturization. For example, Mandlburger and others (2020) operated a UAS with dual-wavelength ALB capability and reported high spatial resolution and adequate depth performance and accuracy when the system was tested in a riverine environment. Interpreting all this, we can assume that the emerging technology is introducing automated data classification and analysis methods to reduce uncertainty and improve reliability, while computing hardware is becoming more compact, customizable, and less expensive to suit a variety of survey needs.

6.5. Conclusion statement

The theoretical and practical operating requirements of near-infrared-only airborne lidar technology are relatively straightforward, and necessary quality-control mechanisms have been developed over the years by the federal government agencies (e.g., USGS[3], ASPRS[4]). In contrast, airborne lidar

[3] USGS: United States Geological Survey (https://www.usgs.gov/)
[4] ASPRS: American Society of Photogrammetry and Remote Sensing (https://www.asprs.org/).

bathymetry is subject to a greater range of environmental conditions, as demonstrated throughout this thesis. The ALB system manufacturers and the scientific community are aware of the biases and the uncertainties that may be introduced by these conditions. The depth penetration capability or spatial resolution of a lidar system may not always be as advertised, e.g. when poor water transparency, excessive submerged vegetation or other factors adversely impact ALB survey results and data quality.

This PhD research demonstrated the necessity of completing in-situ campaigns and validating the data quality as applicable to each unique case study. Lessons learned and expertise gained from each study helped to execute a more comprehensive study with a better understanding of the expectations. The karst, fluvial and southern environments were vastly different from the Arctic Ocean; however, the ALB system configuration and the computing applications used in this research were almost identical and differences arose primarily from the in-situ campaigns. For instance, in the Frio River study, the environmental conditions were almost ideal for bathymetric lidar mapping of the entire riverbed. Unexpectedly, in several basins, the heavy riparian zone vegetation blocked the GNSS signals required for in-situ measurements, creating the need to conduct waveform analysis to validate the depths. In the Devils River survey, the use of a geophysical instrument typically employed for subsurface measurements required hardware and recording calibration, as well as several trials, to accurately measure depths underneath the submerged vegetation. In the Laguna Madre study, pixel reflectance analysis using satellite imagery and partitioning of in-situ locations helped manage airborne lidar datasets more efficiently for comparison to information derived from other surveys. And finally, in the Cal/Val 2022 campaign, height validation required cross-checking with other airborne and orbiting altimeter measurements for additional assurance, and development of a data shifting algorithm to maximize correspondence between the airborne lidar data and ICESat-2 ATLAS products.

This PhD research provides a comprehensive insight into airborne lidar bathymetry expectations at diverse locations and under varying environmental conditions and demonstrates how specific in-situ validation campaigns serve to improve and ensure ALB data quality. The expertise and knowledge gained from these case studies contributes to advancing the technology and guides the scientific community in its application of ALB technology across a wide range of environments.

6.6. References

Abdullah, Q., Heidemann, H. K., & Smith, D. (2023). The ASPRS Positional Accuracy Standards, Edition 2: The Geospatial Mapping Industry Guide to Best Practices. Photogrammetric Engineering & Remote Sensing, 89(10), 581–588. https://doi.org/10.14358/PERS.89.10.581

Chen, W., Chen, P., Zhang, H., He, Y., Tang, J., Wu, S., 2023. Review of airborne oceanic lidar remote sensing. Intell. Mar. Technol. Syst. 1, 10. https://doi.org/10.1007/s44295-023-00007-y

Guenther, G.C., 2007. Airborne Lidar bathymetry (Manual No. 2), Digital elevation model technologies and applications: the DEM users manual. American Society of Photogrammetry and Remote Sensing.

Janowski, L., Wroblewski, R., Rucinska, M., Kubowicz-Grajewska, A., Tysiac, P., 2022. Automatic classification and mapping of the seabed using airborne lidar bathymetry. Engineering Geology 301, 106615. https://doi.org/10.1016/j.enggeo.2022.106615

Kogut, T., Tomczak, A., Słowik, A., Oberski, T., 2022. Seabed Modelling by Means of Airborne Laser Bathymetry Data and Imbalanced Learning for Offshore Mapping. Sensors 22, 3121. https://doi.org/10.3390/s22093121

Mandlburger, G., 2021. Bathymetry from Images, lidar, and Sonar: From Theory to Practice. PFG s41064-021-00153–0. https://doi.org/10.1007/s41064-021-00153-0

Mandlburger, G., Pfennigbauer, M., Schwarz, R., Flöry, S., Nussbaumer, L., 2020. Concept and Performance Evaluation of a Novel UAV-Borne Topo-Bathymetric lidar Sensor. Remote Sensing 12, 986. https://doi.org/10.3390/rs12060986

Parker, H., Sinclair, M., 2012. The successful application of Airborne lidar Bathymetry surveys using latest technology, in 2012 Oceans - Yeosu. Presented at the OCEANS 2012 - YEOSU, IEEE, Yeosu, Korea (South), pp. 1–4. https://doi.org/10.1109/OCEANS-Yeosu.2012.6263588

Pricope, N.G., Bashit, M.S., 2023. Emerging trends in topo-bathymetric lidar technology and mapping. International Journal of Remote Sensing 44, 7706–7731. https://doi.org/10.1080/01431161.2023.2287564

Szafarczyk, A., Toś, C., 2022. The Use of Green Laser in lidar Bathymetry: State of the Art and Recent Advancements. Sensors 23, 292. https://doi.org/10.3390/s23010292

Terziotti, S., & Archuleta, C.-A. (2020). Elevation-derived hydrography acquisition specifications (Specifications 11-B11; Techniques and Methods). NGTOC Rolla.

Tingaker, T., Ekelund, A., 2022. Recent developments in airborne lidar bathymetry, in: Kamerman, G.W., Steinvall, O. (Eds.), Electro-Optical Remote Sensing XVI. Presented at the Electro-Optical Remote Sensing XVI, SPIE, Berlin, Germany, p. 10. https://doi.org/10.1117/12.2645180